Michael Schubert

High-Precision Torque Control of Inverter-Fed Induction Machines with Instantaneous Phase Voltage Sensing

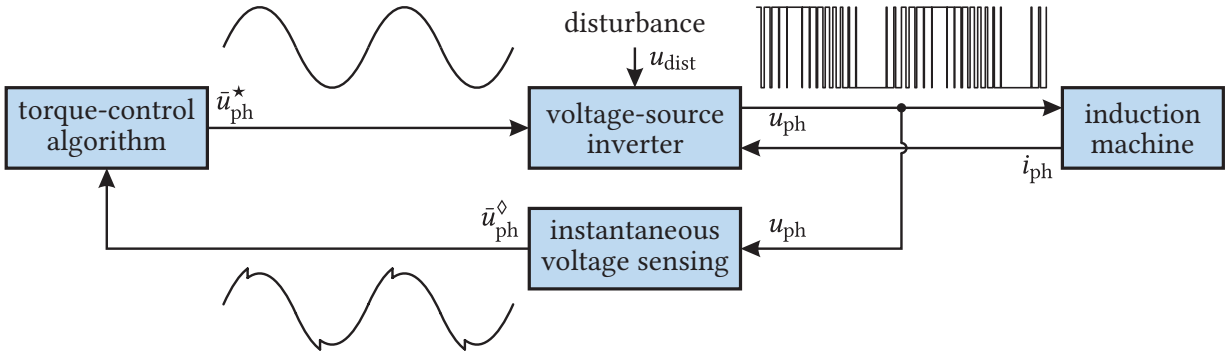

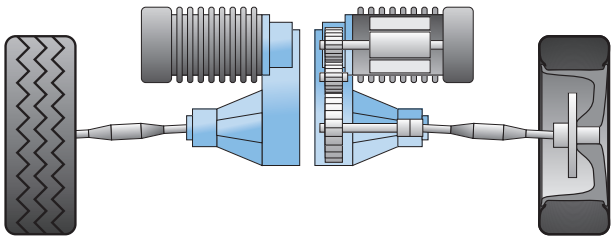

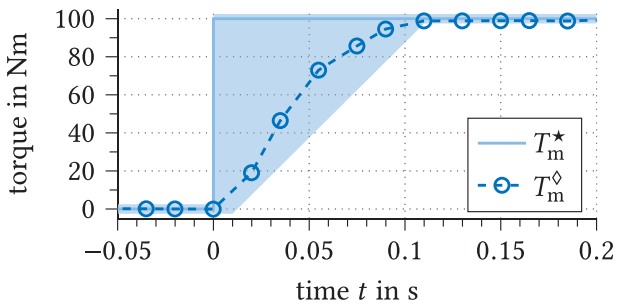

Aachener Beiträge des ISEA Band 118

High-Precision Torque Control of Inverter-Fed Induction Machines with Instantaneous Phase Voltage Sensing

Von der Fakultät für Elektrotechnik und Informationstechnik der Rheinisch-Westfälischen Technischen Hochschule Aachen zur Erlangung des akademischen Grades eines Doktors der Ingenieurwissenschaften genehmigte

Dissertation

vorgelegt von

Diplom-Ingenieur
Michael Schubert
aus Leverkusen

Berichter:
Univ.-Prof. Dr. Ir. Dr. h. c. Rik W. De Doncker
Univ.-Prof. Dr.-Ing. Axel Mertens

Tag der mündlichen Prüfung: 26. November 2018

Electronic Version
This dissertation is available online on the website of the university library:
`https://publications.rwth-aachen.de`

AACHENER BEITRÄGE DES ISEA
Vol. 118

Editor:
Univ.-Prof. Dr. Ir. Dr. h. c. Rik W. De Doncker
Director of the Institute for Power Electronics and Electrical Drives (ISEA)
RWTH Aachen University

ISSN 1437-675X

Institute for Power Electronics and Electrical Drives (ISEA)
Jägerstr. 17/19 • 52066 Aachen • Germany
Tel: +49 (0)241 80-96920
Fax: +49 (0)241 80-92203
post@isea.rwth-aachen.de

Vielen Dank...

Die vorliegende Dissertation entstand während meiner Tätigkeit als wissenschaftlicher Mitarbeiter am Institut für Stromrichtertechnik und Elektrische Antriebe (ISEA) der Rheinisch-Westfälischen Technische Hochschule (RWTH) Aachen.

Am ISEA wird seit jeher an elektrischen Traktionsantrieben für Straßenkraftfahrzeuge geforscht. Dabei ist eine experimentelle, prototypische Umsetzung stets obligatorisch. So wurde mir – in einer Zeit, in der die Elektromobilität auch kommerziell an Bedeutung gewinnt – die Ehre zuteil, ein elektrisches Traktionsantriebssystem für ein an der RWTH neu entwickeltes Elektrofahrzeug zu entwerfen, aufzubauen und hinsichtlich der Applikation einer übergeordneten Fahrdynamikregelung zu optimieren.

Es ist offensichtlich, dass die erfolgreiche Umsetzung eines solchen Projektes nicht das Werk eines Einzelnen darstellt, sondern eine enge Zusammenarbeit einer Vielzahl an Personen erfordert. An dieser Stelle möchte ich all jenen „Danke“ sagen, die mich bei der täglichen Arbeit am ISEA unterstützt und damit auch direkt oder indirekt zur Entstehung dieser Dissertation beigetragen haben.

Allen voran danke ich meinem Doktorvater Prof. Rik W. De Doncker, der mir die Möglichkeit gab, Teil seiner Forschungsgruppe am ISEA zu werden und mir stets vollstes Vertrauen entgegengebracht, sowie uneingeschränkte Freiheit bei der Arbeitsgestaltung gewährt hat. Ebenso danke ich Prof. Axel Mertens vom Institut für Antriebssysteme und Leistungselektronik (IAL) der Leibniz Universität Hannover für die freundliche Übernahme des Koreferats und das Interesse an meiner Arbeit.

Den Mitarbeitern der StreetScooter GmbH und FEV GmbH danke ich für die enge und unkomplizierte Zusammenarbeit im Projekt, sowie für die daraus entstandenen interessanten Herausforderungen, welche letztendlich die Grundlage für diese Arbeit geschaffen haben. Den Kollegen der AixControl GmbH danke ich für die schnelle Lösung von Problemen und den vielseitigen Hilfestellungen bei der Erstinbetriebnahme ihrer DSP/FPGA-Regelungsplattform XCP3100 am ISEA.

Das hervorragende Arbeitsklima am ISEA ist ein Nährboden für neue Ideen und innovative Problemlösungen. Der enge Austausch in der Gruppe, sowie die unzähligen fachlichen Diskussionen haben entscheidend zum Gelingen dieser Arbeit beigetragen. Jan Gottschlich danke ich für das Teilen seines Expertenwissens über analoge Schaltungen und störungsresistentes PCB-Design während unseren intensiven Kaffeepausen. Tobias Lange, Stefan Koschik und Martin Rosekeit bin ich durch ihre Soft- und Hardwarevorarbeiten, besonders hinsichtlich der Fahrzeugintegration und der funktionalen Sicherheit, zu großem Dank verpflichtet. Daniel Scharfenstein danke ich für seinen unermüdlichen Einsatz bei

der Portierung und Weiterentwicklung des ISEA Regelungs-Frameworks und Fang Qi für seine Arbeiten an der echtzeitfähigen, ortsaufgelösten thermischen Modellierung elektrischer Maschinen, welche eine präzise Kompensation des thermischen Widerstandsdrifts im Stator und Rotor der Asynchronmaschine ermöglichte.

Ein besonderer Dank gilt auch den Studenten und späteren Kollegen Vivien Grau, Matthias Gossen, Lars Jebe, Kshitij Girigoudar und Decheng Yan, die mir während ihrer Zeit als HiWi oder im Rahmen von Master- und Bachelorarbeiten eine große Hilfe waren.

Mit Bernhard Burkhart teile ich eine äußerst wertvolle gemeinsame Erfahrung als Gruppenleiter der Forschungsgruppe Elektrische Antriebe. Für seine bedingungslose Einsatzbereitschaft und seine effiziente Art, Aufgaben und Probleme anzugehen, bin ich ihm überaus dankbar. Ein großes „Dankeschön“ gehört auch meinen Oberingenieurskollegen Annegret Klein-Heßling und Markus Neubert, die mir gerade in den letzten Monaten durch ihren aufopferungsvollen Einsatz jenen zeitlichen Spielraum verschafften, der zum Fertigstellen dieser Arbeit nötig war.

Allen ISEAnern danke ich auch für die vielen heiteren Stunden bei der Arbeit, den Exkursionen und gemeinsamen Konferenzbesuchen, aber auch nach der Arbeit beim Segeln, Wandern, der Band oder Bahnfahrten der besonderen Art Richtung Süddeutschland. Ohne diese ausgleichende Komponente wäre es mir sicher erheblich schwerer gefallen bis zum Schuss durchzuhalten und mit voller Begeisterung diese Dissertation abzuschießen.

Nicht zuletzt möchte ich mich ganz besonders bei meiner Frau und Familie bedanken für das Verständnis und die Geduld der letzten Monate und Jahre, sowie für die stets uneingeschränkte Liebe und Unterstützung.

Aachen, im Dezember 2018 *Michael Schubert*

Contents

1 Introduction **1**
- 1.1 The MAs:Stab Electric Vehicle . . . 2
- 1.2 Objective and Outline of this Work . . . 4

2 Modeling of Induction Machine Drives **9**
- 2.1 The Dynamic Model of the Induction Machine . . . 9
  - 2.1.1 The Ideal Rotating Transformer Model . . . 10
  - 2.1.2 State-Space Representation of the Induction Machine Model . . . 12
  - 2.1.3 Extended Nonlinear IM Model . . . 15
- 2.2 Field-Oriented Torque Controllers . . . 25
  - 2.2.1 Efficiency Optimization – Field Weakening at Light Loads . . . 29
  - 2.2.2 The Direct Stator Field-Oriented Torque Controller . . . 33
  - 2.2.3 Operational Constraints and the Field-Weakening Region . . . 34
- 2.3 Output Voltage Distortion of Voltage-Source Inverters . . . 36
  - 2.3.1 Dead Time and Inverter Voltage-Drop Model . . . 36
  - 2.3.2 The Inverter Voltage Distortion Curve . . . 39
- 2.4 Summary . . . 41

3 Stator Flux-Linkage Observers **43**
- 3.1 Open-Loop Observers . . . 43
  - 3.1.1 Current Model . . . 43
  - 3.1.2 Voltage Model . . . 44
- 3.2 Closed-Loop Observers . . . 45
  - 3.2.1 Voltage-Model Observer with Current-Model Feedback . . . 46
  - 3.2.2 Full-Order Luenberger-Type Observer . . . 47
- 3.3 Discrete-Time Implementation . . . 53
  - 3.3.1 Discrete-Time Voltage and Current Model of the IM . . . 54
  - 3.3.2 Stator-Current Predictor . . . 56
- 3.4 Summary . . . 57

4 The Torque Accuracy of the IM Drive – Analysis and Optimization **59**
- 4.1 Sensitivity of the Controller to Nonlinear Effects . . . 59
  - 4.1.1 Induction Machine Parameter Deviation . . . 62
  - 4.1.2 Measurement-Feedback Distortion . . . 74
  - 4.1.3 Nonlinear Inverter Voltage Distortion . . . 81

4.1.4 Rejection of Higher-Order Harmonics by the Flux Observer . . . 82
4.2 Adaptive Compensation of Parameter Faults . . . 85
4.2.1 Stator- and Rotor-Resistance Estimation Methods . . . 86
4.2.2 Thermal Model Feedback Approach . . . 91
4.3 Measurement Results and Conclusions . . . 94
4.4 Summary . . . 96

5 Instantaneous Phase-Voltage Measurement 97
5.1 State-of-the-Art Methods for Stator Voltage Detection . . . 98
5.1.1 Reference Voltage with Feed-Forward Disturbance Compensator 98
5.1.2 Phase Voltage Measurement Techniques . . . 99
5.2 Instantaneous Measurement of the PWM Switching-Period Average Voltage 102
5.2.1 Theoretical Worst-Case Measurement Error Analysis . . . 103
5.2.2 Dimensioning of the Filter Time Constant . . . 106
5.2.3 Gate-Driver Integrated Hardware Implementation . . . 108
5.2.4 Experimental Verification and Conclusions . . . 110
5.3 Online Current and Voltage Sensor Offset Calibration based on Inverter Voltage Distortion . . . 117
5.3.1 Theoretical Approach for the Offset Calibration Algorithm . . . 118
5.3.2 Experimental Results and Discussion . . . 122
5.4 Online Semiconductor Condition Monitoring . . . 129
5.4.1 Implementation Details and Experimental Evaluation . . . 130
5.4.2 Monitoring of the MOSFET Junction Temperature and Resistance 132
5.5 Torque Control without dedicated Speed Transducer . . . 137
5.6 Summary . . . 140

6 Torque Dynamics of the Efficiency-Optimized Induction Machine Drive 141
6.1 Dynamics of the Direct SFO controller . . . 142
6.1.1 Experimental Results and Conclusions . . . 146
6.2 Dynamically-Optimized Current Sharing in FOC drives . . . 147
6.2.1 RFO Current Model of the IM in State-Space Representation . . . 148
6.2.2 MPC-based Trajectory-Optimization Algorithm . . . 149
6.2.3 Simulation Results and Trajectory-Planner Synthesis . . . 150
6.3 Summary . . . 156

7 Conclusions and Future Work 157
7.1 Open Issues and Future Work . . . 160

A Appendix 163
A.1 Mathematical Conventions . . . 163
A.1.1 Superscripts and Diacritical Marks . . . 163

A.1.2 Space Vector Arithmetic and Reference Frame Transformations . 163
A.2 Experimental Test Setups 165
A.2.1 Induction Machines under Test 166
A.2.2 Inverters under Test 168
A.2.3 Measuring Equipment 170
A.3 Inverter Control Framework 172
A.3.1 Structure of the FPGA Framework 173
A.3.2 Structure of the DSP Framework 173
A.4 Software-in-the-Loop Simulation Model 174
A.5 Observer Gain Selection 175
A.5.1 Proportional Observer Pole Placement 176
A.5.2 Left Shift Observer Pole Placement 176
A.5.3 Proportional Observer Pole Placement with Rotation 177
A.6 Special Case: Two Current Sensors 177
A.7 MPC Prediction Matrices 178

List of Abbreviations **181**

List of Symbols **185**

List of Figures **195**

List of Tables **203**

Bibliography **205**

Curriculum Vitae **221**

1 Introduction

Even though the internal combustion engine has dominated the market for individual road transportation throughout the last 100 years, electric vehicles (EVs) have always been around. From the early beginnings of electrically powered mobility in the 19th century, the major restriction that held EVs off the mass market was – and still is – the lack of affordable electrical energy storage with sufficiently high energy density to achieve an acceptable driving range.

In the meantime, driven by the electrification of railways and the increasing automation in industry, electrical drive systems have undergone several evolutionary developments. In the last decades, the availability of power-electronic converters [Sti+17] and the development of dynamic torque-control algorithms, such as field-oriented control (FOC) [Bla74] and dead-beat direct torque and flux control (DB-DTFC) [Ken01], made highly-dynamic electric propulsion with efficiencies above 95 % possible.

With the recent achievements in high-energy-density batteries, electric mobility becomes more and more suitable for the mass market of individual road transportation. Pushed by the political goals of exhaust emission reduction and a more sustainable energy supply, EVs have lately gained considerable importance in research and industry. While in terms of energy storage and charging infrastructure enormous technical challenges still exist, electrical traction drives already fulfill the ordinary requirements for automotive propulsion. Research and development therefore focus mainly on vehicle integration and the reduction of manufacturing costs, for example, by increasing the power density. Especially in terms of power consumption only marginal improvements of the driving range can be expected, as the aforementioned evolutionary developments have already pushed the efficiency of electrical drives to a very high level.

Nevertheless, electrical drive systems are currently undergoing important innovations. As a participant of the internet of things (IoT), the electrical drive becomes an intelligent device that communicates with its environment to support higher-level features. For example, in the scope of Industry 4.0, the drive can act as a sensor for monitoring the condition of connected mechanical systems such as the load or a gear box, or even the condition of the drive components, itself. With the concept of predictive maintenance and multi-sensor data fusion this offers substantial ecological and economic benefits.

In addition to that, in EVs, electrical drives offer regenerative braking and enable straightforward implementation of new advanced driver-assistance systems (ADAS) that make EVs more attractive than their conventional counterparts. Besides comfort functions, such as adaptive cruise control (ACC), this also includes safety-relevant features. By selective

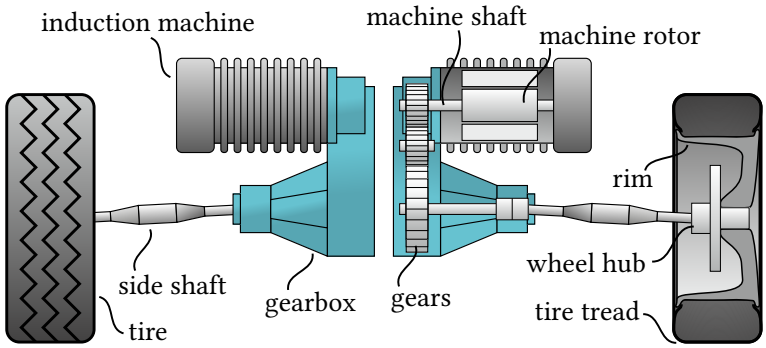

Fig. 1.1: Drive train of the electric vehicle with two independent electrical drives at the rear axle.

distribution of the propulsion force to the individual wheels, solutions like electronic stability control (ESC) can be implemented using only the electrical traction drives – mechanical braking is not required. This can be realized by application of multiple single-wheel drives instead of a single high-power drive, which is also advantageous in terms of an increased reliability and the generation of economies of scale.

The modular concept has been addressed at the *Institute for Power Electronics and Electrical Drives* (ISEA)[(i)] in the collaborative research project *modular drive train: stability with multiple drives* (MAs:Stab)[(ii)] which was funded by the German Federal Ministry for Economic Affairs and Energy. The majority of the research presented in this work has been conducted in the course of the MAs:Stab project.

1.1 The MAs:Stab Electric Vehicle

The goal of the MAs:Stab project was to investigate and demonstrate novel torque vectoring (TV) functions for EVs with a modular drive train consisting of multiple independent traction drives. Therefore, a two-seats EV – the StreetScooter C16 – was constructed and built by the project partners[(iii)]. Two independent single-wheel drives were mounted to the rear axle, as illustrated in Fig. 1.1. By dynamic torque distribution between the left and the right drive, a dynamic yawing moment can be applied to the vehicle. Photographs of the C16, taken at an electric mobility event and during a test drive, are shown in Fig. 1.2.

An overview of the TV functions developed and implemented by FEV is given in Fig. 1.3. By precisely controlling the torque difference of the left and right drive, the function of an electronic differential (a) is achieved. This way, the agility is increased, and the vehicle stability is significantly improved (b), for example during fast steering maneuvers. It also includes the compensation of disturbing forces on the chassis (c), such as wind, road banking or uneven road surfaces. Furthermore, the active stability control allows

[(i)] German name: Institut für Stromrichtertechnik und Elektrische Antriebe
[(ii)] original German title: Modularer Antriebsstrang: Stabilität bei Mehrfachantrieben
[(iii)] namely: RWTH Aachen University, StreetScooter, FEV, CP autosport, ABM Greiffenberger

(a) C16 at *Aachen goes electro 2014*

(b) test drive at project completion

Fig. 1.2: StreetScooter C16 with two independent single-wheel drives at the rear axle. During the test drive, the 3D-printed body parts were dismantled.

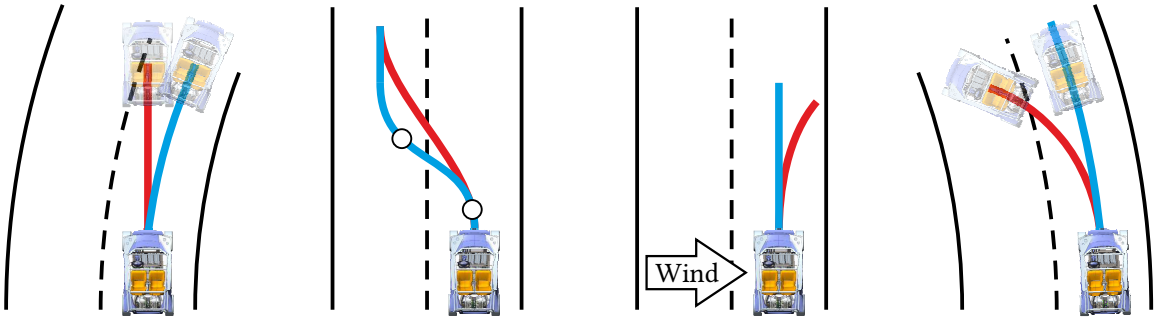

(a) Electronic differential with dynamic torque distribution between left and right rear wheel.

(b) Agility enhancement through a supporting yaw moment during fast steering maneuvers.

(c) Compensation of disturbing forces such as side wind and road banking by application of a yaw moment.

(d) Increased efficiency through enhanced regenerative braking with active control of the vehicle stability.

Fig. 1.3: New torque vectoring functions developed in the project MAs:Stab [Kra+17]. Blue trace with and red trace without torque vectoring.

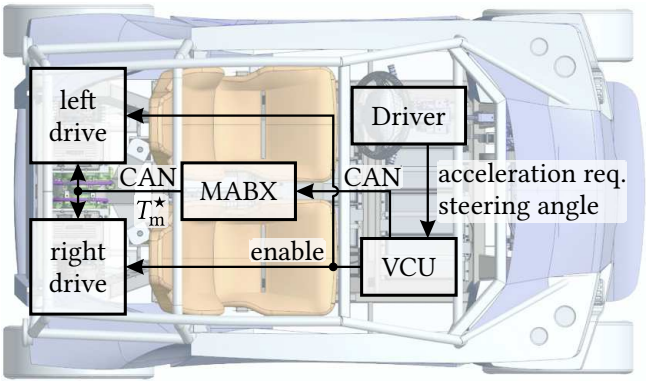

Fig. 1.4: Configuration of the drive system with higher-level torque-vectoring and stability control.

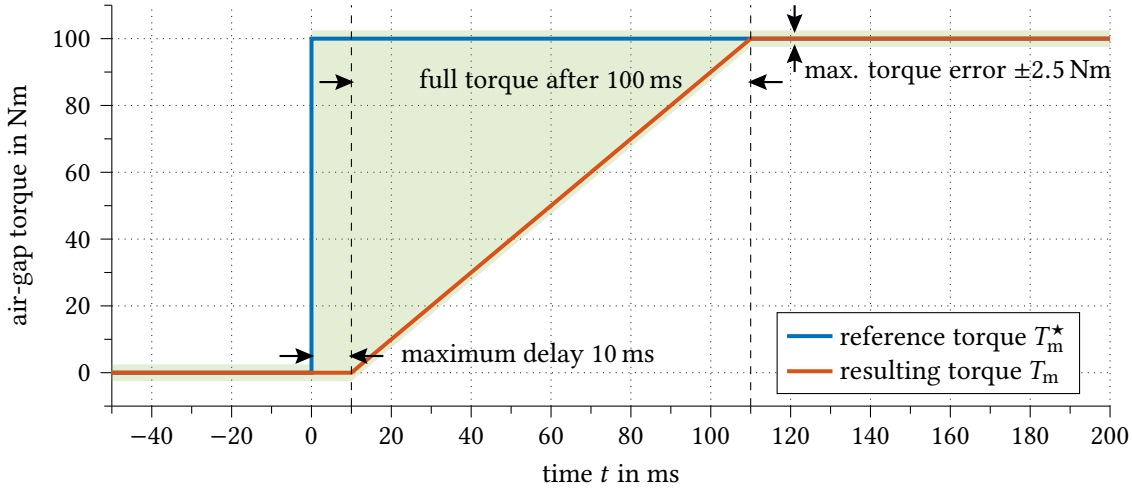

Fig. 1.5: Torque accuracy and dynamics requirement for the electrical traction drives.

to increase the regenerative braking force in curves, which notably decreases the overall power consumption [Kra+17].

Fig. 1.4 shows the top view of the C16 with the structural configuration of the drive components and the higher-level control units. The vehicle stability control is implemented on a dSPACE MicroAutoBox (MABX). It receives the acceleration request and the steering angle, set by the driver, via controller area network (CAN) from the vehicle control unit (VCU). Based on the driver request and the information collected from sensors for acceleration, yaw rate and orientation, the MABX calculates individual torque requests for the left and right traction drive. The task of *RWTH Aachen University*[(iv)], was to design the traction drives according to the torque accuracy and dynamics requirements defined by the outer stability control loop. While the *Institute of Electrical Machines* (IEM)[(v)] investigated the production influences of the electrical machine on the torque accuracy [PHH15], the focus at ISEA was on the development of a voltage-source inverter (VSI) and control algorithms for maximum torque accuracy and dynamics.

1.2 Objective and Outline of this Work

For sufficient dynamic performance of the outer vehicle-stability control loop, the requirements given in Fig. 1.5 were identified for both single-wheel drives:

- Maximum torque deviation of ±2.5 Nm in all operating points.
- Step response with full torque after 100 ms.
- Maximum additional propagation delay of 10 ms.

[(iv)] German name: Rheinisch-Westfälische Technische Hochschule (RWTH) Aachen
[(v)] German name: Institut für Elektrische Maschinen

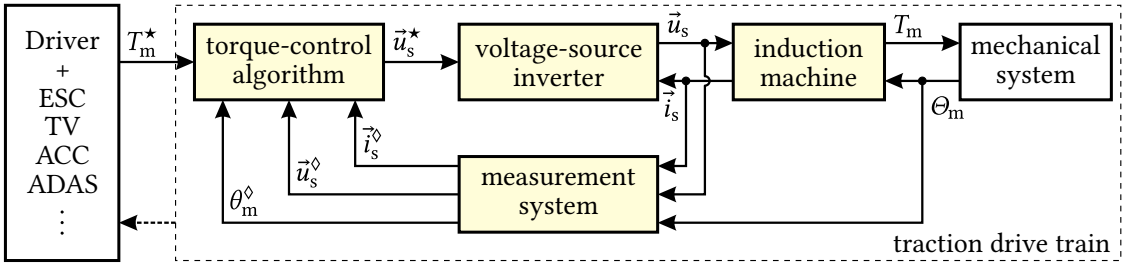

Fig. 1.6: System overview of an induction machine (IM) drive train with functional components.

The objective of this work is the development, implementation and experimental verification of a torque-control algorithm for induction machine (IM) drives that fulfills these requirements. To improve the torque accuracy, an analytical approach for the systematic minimization of the flux-linkage observer sensitivity to uncertain parameters and measurement error is proposed. The low-speed performance is enhanced by a gate-driver integrated voltage-sensing circuit, that not only allows instantaneous detection of the switching-period average value of the VSI output voltage, but also the implementation of new features for online sensor-offset calibration and VSI condition monitoring. A structural overview of the outline is given in Fig. 1.7.

Chapter 2: Modeling of Induction Machine Drives

Due to parameter drift and modeling error, precise torque control requires a deep insight into the modeling of IM drives and their components shown in Fig. 1.6. In this chapter, a detailed IM model considering nonlinear effects is introduced. The parameters are evaluated according to their degree of uncertainty. Furthermore, a brief overview of FOC with efficiency optimization and constraints handling is given. Based on a detailed metal–oxide–semiconductor field-effect transistor (MOSFET) model, an expression for the current-dependent voltage distortion caused by the six-pulse bridge (B6) VSI is derived.

Chapter 3: Stator Flux-Linkage Observers

To obtain a torque accuracy within the given limits, a flux-observer with minimal sensitivity to variations of uncertain parameters must be found. In this chapter, common open and closed-loop observers are presented, and analytical expressions for the sensitivity to parameter variations, voltage and current-sensor error are derived. Furthermore, details on the observer gain selection and the time-discrete implementation are given.

Chapter 4: The Torque Accuracy of the IM Drive – Analysis and Optimization

Based on the analytically expressions derived in Chapter 3, the influence of parameter variations, measurement error and inverter dead-time on the torque accuracy and controller detuning is analyzed. The results lead to the choice of an observer with low sensitivity

to measurement error and magnetic saturation. The remaining parameters – the stator and rotor resistance – are adapted using a spatially-resolved thermal model. Experimental results demonstrate the feasibility of this approach.

Chapter 5: Instantaneous Phase-Voltage Measurement

During low-speed operation, the precise detection of the IM stator voltage becomes increasingly important. In this chapter, estimation and sensing methods for the switching-period average value of the VSI output voltage are discussed. A gate-driver integrated voltage-sensing circuit is proposed, that is based on digital integration of the drain–source voltage across the bottom switch. To minimize the instantaneous measurement error, an analog low-pass filter (LPF) before digital integration is introduced and analytically optimized.

A novel online sensor-offset calibration method is proposed, that is based on the instantaneous sensing of the VSI distortion voltage. It allows fully decoupled offset compensation for all current and phase-voltage sensors, simultaneously. At the same time, the circuit is used for monitoring of the 'on'-state voltage drop of all switches. This way, individual junction-temperature and semiconductor failure detection is possible.

The performance of the sensing circuit is validated in extensive experiments. Stable torque control without dedicated speed transducer is demonstrated – even at standstill.

Chapter 6: Torque Dynamics of the Efficiency-Optimized IM Drive

Even though electrical drives are generally able to meet the torque dynamics requirements, for IM operated at maximum efficiency, this is quite challenging. As the flux-linkage is reduced during partial load, it must be increased before a higher torque can be produced. The dynamic response of this process is limited by the rotor time constant which is often in the range of 100 ms and more. In this chapter, an approach for the maximization of the dynamic torque response without violating the maximum current constraint is presented. Based on a model-predictive control (MPC) algorithm, a lookup-table-based trajectory planner for optimal dynamic current sharing is derived.

Chapter 7: Conclusions and Future Work

In the conclusions, the findings of the previous chapters are summarized, and the essential contributions are pointed out. Further steps and topics for future research are identified.

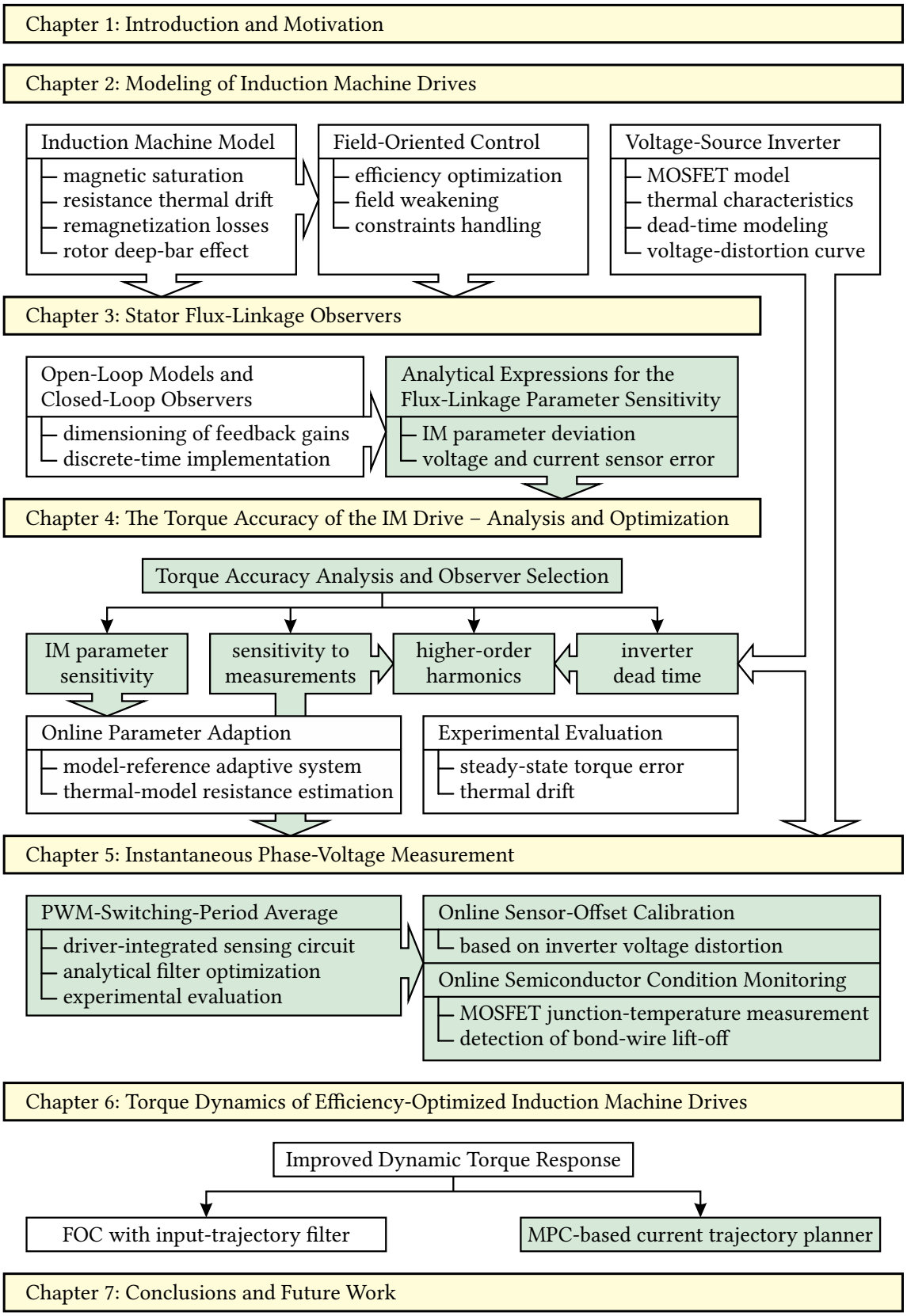

Fig. 1.7: Structure of the main contents of this work. Main contributions in light green.

2 Modeling of Induction Machine Drives

The performance of a speed-variable IM drive depends on many factors. Each component of the drive has an influence on the torque accuracy and the achievable dynamics. To analyze the system with respect to these criteria a deep understanding of each component and its impact is essential.

In this chapter, a detailed nonlinear model of the IM is derived, which is based on the fundamental IM equations. Special attention is given to the degree of uncertainty with that the model parameters are determined during initial parameterization measurements and during operation. This information serves as a basis for the choice and development of an appropriate torque-control algorithm. Therefore, a brief overview of state-of-the-art field-oriented controllers and their parameter dependency is given.

Furthermore, a detailed model of the VSI is introduced, which is fundamental for the linearization of the nonlinear inverter transfer function. This model is the basis for a novel online sensor-offset calibration scheme that is introduced in Chapter 5.3.

2.1 The Dynamic Model of the Induction Machine

The IM with squirrel-cage rotor is a rotating-field electrical machine with symmetrically-distributed stator windings. The cross-sectional view in Fig. 2.1 shows the common configuration with delta- or star-connected three-phase windings. The stator current $\vec{i}_\mathrm{s}$ in the windings produces a rotating magnetic field with the stator flux linkage $\vec{\psi}_\mathrm{s}$, which consists of a mutual component $\vec{\psi}_\mathrm{m}$ penetrating stator and rotor, and a leakage component $\vec{i}_\mathrm{s} L_{\sigma\mathrm{s}}$ only penetrating the stator. The field rotates at the stator angular frequency ω_s and induces a rotor current $\vec{i}_\mathrm{r}$ into the short-circuited rotor bars of the squirrel cage. The Lorenz force acting on the rotor bars then creates a mechanical air-gap torque, which is equal to

$$T_\mathrm{m} = \frac{3}{2} p \cdot \vec{\psi}_\mathrm{m} \,|\times|\, \vec{i}_\mathrm{r}, \quad \text{or} \quad T_\mathrm{m} = \frac{3}{2} p \cdot \vec{\psi}_\mathrm{m} \,|\times|\, \vec{i}_\mathrm{s} \tag{2.1}$$

with respect to the stator. The operator $|\times|$ is the cross-product of two-dimensional space vectors according to the mathematical conventions introduced in Appendix A.1. p is the number of pole pairs of the machine and the link between the mechanical quantities air-gap torque T_m, rotor angular frequency Ω_m and their electrically-related counterparts

$$T_\mathrm{e} = \frac{1}{p} \cdot T_\mathrm{m} \quad \text{and} \quad \omega_\mathrm{m} = p \cdot \Omega_\mathrm{m}. \tag{2.2}$$

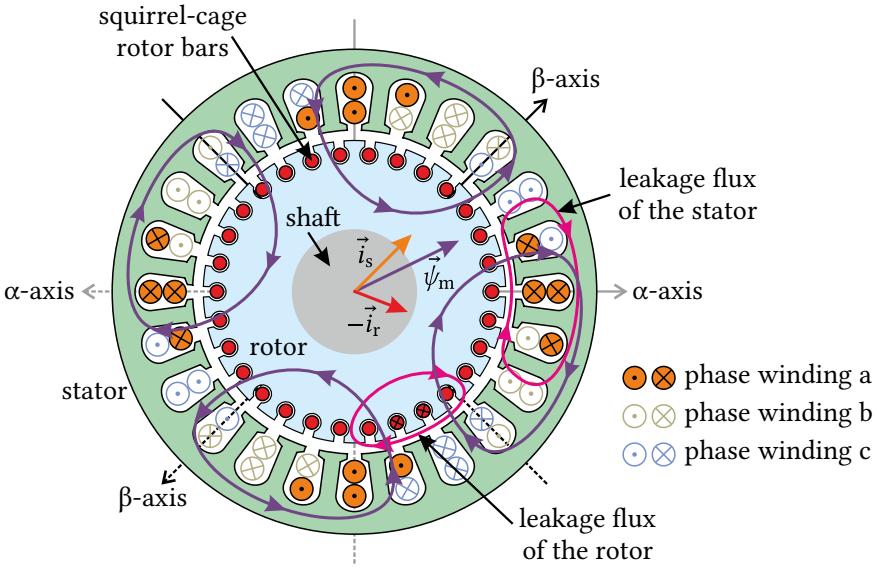

Fig. 2.1: Cross section of an IM with squirrel-cage rotor and two pole pairs $p = 2$ [DPV11].

To produce torque, rotor currents must be present in the machine. These are only induced if the magnetic field and the rotor rotate asynchronously to each other, with a non-zero slip frequency

$$\omega_{sl} = \omega_s - \omega_m \quad \text{and the slip} \quad s_{slip} = \frac{\omega_{sl}}{\omega_s}. \tag{2.3}$$

In the past, the IM has been studied extensively and a variety of modeling concepts exist. A very descriptive approach is the single-phase ideal rotating transformer (IRTF) representation, introduced by Veltman et al. in [Vv91], which is followed in this work. The IM is assumed to be perfectly symmetric, so that all quantities can be described as space vectors. Space vectors and reference frames are indicated corresponding to the notation conventions introduced in [DPV11]. Details about the notation and single-phase space-vector representation are summarized in Appendix A.1.

In the following, the fundamental IM models in IRTF and state-space representation are presented. They are essential for the synthesis of field-oriented controllers and flux-linkage observers. For torque accuracy and sensitivity analysis, a more realistic machine model is derived that takes into account nonlinear effects such as thermal parameter drift, iron losses and saturation.

2.1.1 The Ideal Rotating Transformer Model

The stator voltage equation of a rotating-field electrical machine is composed of a resistive term and the voltage induced into the stator windings as

$$\vec{u}_s = R_s \vec{i}_s + \frac{\mathrm{d}\vec{\psi}_s}{\mathrm{d}t} \tag{2.4}$$

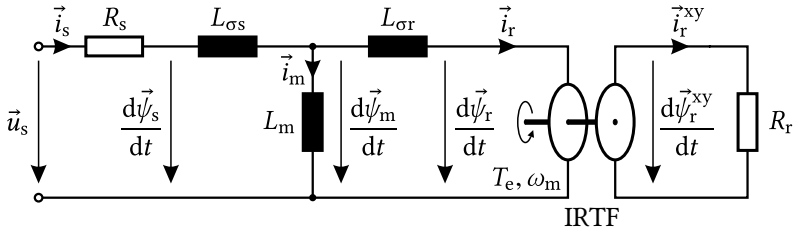

Fig. 2.2: Equivalent circuit of the induction machine with ideal rotating transformer (IRTF). The superscript 'xy' denotes the reference to the rotor-aligned coordinate system.

with the stator resistance R_s and the stator flux linkage $\vec{\psi}_\mathrm{s}$. Equation (2.4) is often referred to as the stator or voltage model of the IM.

Analogously to the stator, the voltage equation of the short-circuited rotor is given by

$$0 = -R_\mathrm{r}\vec{i}_\mathrm{r}^{\,\mathrm{xy}} + \frac{\mathrm{d}\vec{\psi}_\mathrm{r}^{\,\mathrm{xy}}}{\mathrm{d}t} \tag{2.5}$$

with the rotor resistance R_r and the rotor flux linkage $\vec{\psi}_\mathrm{r}$. The space-vector superscript 'xy' denotes the reference to the rotor-aligned coordinate system.

Stator and rotor are coupled by the mutual flux linkage $\vec{\psi}_\mathrm{m}$. With the stator and rotor leakage inductances $L_{\sigma\mathrm{s}}$, $L_{\sigma\mathrm{r}}$ and the mutual inductance L_m, the flux-linkage equations

$$\vec{\psi}_\mathrm{s} = \vec{\psi}_\mathrm{m} + L_{\sigma\mathrm{s}}\vec{i}_\mathrm{s}, \tag{2.6a}$$

$$\vec{\psi}_\mathrm{r} = \vec{\psi}_\mathrm{m} - L_{\sigma\mathrm{r}}\vec{i}_\mathrm{r}, \tag{2.6b}$$

$$\text{and} \quad \vec{\psi}_\mathrm{m} = L_\mathrm{m}\left(\vec{i}_\mathrm{s} - \vec{i}_\mathrm{r}\right) \tag{2.6c}$$

are obtained. (2.5) and (2.6) are often referred to as the rotor or current model of the IM.

The IM equations (2.4) to (2.6) can be expressed by the electrical equivalent circuit with IRTF depicted in Fig. 2.2. The IRTF is the electro-mechanical link between electrical and magnetic quantities of the stator and the rotor, and offers a descriptive representation of the electro-mechanical energy conversion within the circuit diagram [Vv91]. The IRTF is defined by the equations

$$\vec{i}_\mathrm{r}^{\,\mathrm{xy}} = \vec{i}_\mathrm{r}\mathrm{e}^{-\mathrm{j}\theta_\mathrm{m}}, \tag{2.7a}$$

$$\vec{\psi}_\mathrm{r}^{\,\mathrm{xy}} = \vec{\psi}_\mathrm{r}\mathrm{e}^{-\mathrm{j}\theta_\mathrm{m}}, \tag{2.7b}$$

$$\text{and} \quad T_\mathrm{e} = \frac{3}{2}\cdot\vec{\psi}_\mathrm{r}\,|\times|\,\vec{i}_\mathrm{r} = \frac{3}{2}\,\mathrm{Im}\left\{\vec{\psi}_\mathrm{r}^{\,*}\vec{i}_\mathrm{r}\right\}. \tag{2.7c}$$

θ_m is the mechanical rotor angle and serves as a mechanical input into the IRTF. T_e is the mechanical air-gap torque and the output to a mechanical system. Both are electrically related quantities and must be scaled by the number of pole pairs, according to (2.2), to determine the actual torque and rotor angle of the machine.

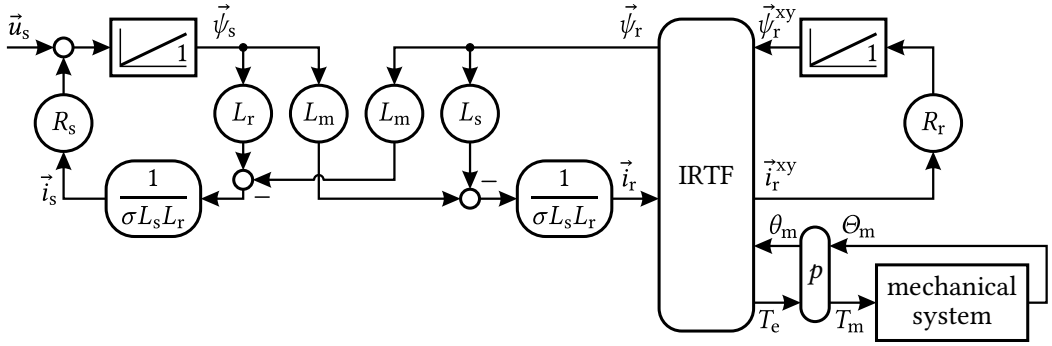

Fig. 2.3: Signal-flow diagram of the induction machine with ideal rotating transformer (IRTF).

The IM model equations (2.4) to (2.7) can be represented by the signal-flow diagram derived in Fig. 2.3. It is the basis for the MATLAB/SIMULINK model used in this work and will be extended by nonlinear effects, such as magnetic saturation, remagnetization losses, rotor deep-bar effect and thermal parameter drift in Section 2.1.3.

2.1.2 State-Space Representation of the Induction Machine Model

Just like any linear time-invariant system, the IM can be represented by a state-space model

$$\frac{\mathrm{d}}{\mathrm{d}t}\boldsymbol{x}_{\mathrm{im}} = \boldsymbol{A}_{\mathrm{im}}\boldsymbol{x}_{\mathrm{im}} + \boldsymbol{B}_{\mathrm{im}}\boldsymbol{u}_{\mathrm{im}} \tag{2.8a}$$

$$\text{and} \quad \boldsymbol{y}_{\mathrm{im}} = \boldsymbol{C}_{\mathrm{im}}\boldsymbol{x}_{\mathrm{im}} + \boldsymbol{D}_{\mathrm{im}}\boldsymbol{u}_{\mathrm{im}}. \tag{2.8b}$$

This general mathematical system representation allows the application of a wide range of control-theory tools, which will be advantageous for observer synthesis and analysis. The system is described by the system matrix $\boldsymbol{A}_{\mathrm{im}}$, the input matrix $\boldsymbol{B}_{\mathrm{im}}$, the output matrix $\boldsymbol{C}_{\mathrm{im}}$ and the feedthrough matrix $\boldsymbol{D}_{\mathrm{im}}$, according to the diagram given in Fig. 2.4. With the stator and rotor flux linkages $\vec{\psi}_s$ and $\vec{\psi}_r$ chosen as state variables, the input vector $\boldsymbol{u}_{\mathrm{im}}$, the state vector $\boldsymbol{x}_{\mathrm{im}}$ and the output vector $\boldsymbol{y}_{\mathrm{im}}$ are defined as

$$\boldsymbol{u}_{\mathrm{im}} = \vec{u}_s, \quad \boldsymbol{x}_{\mathrm{im}} = \begin{bmatrix} \vec{\psi}_s \\ \vec{\psi}_r \end{bmatrix} \quad \text{and} \quad \boldsymbol{y}_{\mathrm{im}} = \vec{i}_s. \tag{2.9}$$

With the help of (2.6), the stator current space vector $\vec{i}_s$ can be expressed as a function of the state variables, which yields

$$\vec{i}_s = \frac{1}{\sigma L_s L_r}\left(\vec{\psi}_s L_r - \vec{\psi}_r L_m\right). \tag{2.10}$$

The leakage inductances have been combined into the leakage factor $\sigma = 1 - L_m^2/L_s L_r$ with the stator inductance $L_s = L_m + L_{\sigma s}$ and the rotor inductance $L_r = L_m + L_{\sigma r}$. With (2.10)

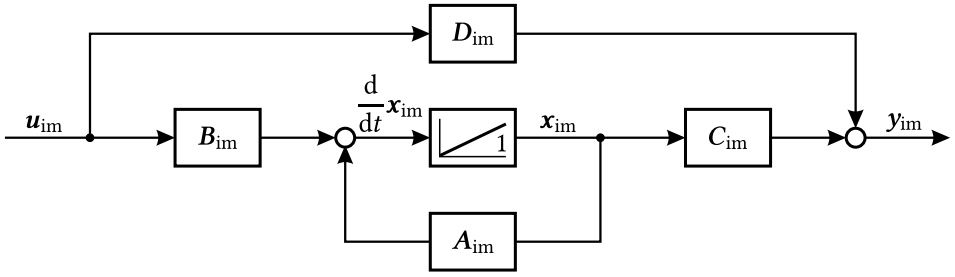

Fig. 2.4: Generel state-space representation of a linear time-invariant system.

inserted in (2.4), and (2.5) transformed to the stator side, the state equations for $\vec{\psi}_{\mathrm{s}}$ and $\vec{\psi}_{\mathrm{r}}$ are derived as

$$\frac{\mathrm{d}\vec{\psi}_{\mathrm{s}}}{\mathrm{d}t} = -\frac{R_{\mathrm{s}}}{\sigma L_{\mathrm{s}}}\vec{\psi}_{\mathrm{s}} + \frac{R_{\mathrm{s}}L_{\mathrm{m}}}{\sigma L_{\mathrm{s}}L_{\mathrm{r}}}\vec{\psi}_{\mathrm{r}} + \vec{u}_{\mathrm{s}} \tag{2.11a}$$

$$\text{and} \quad \frac{\mathrm{d}\vec{\psi}_{\mathrm{r}}}{\mathrm{d}t} = \frac{R_{\mathrm{r}}L_{\mathrm{m}}}{\sigma L_{\mathrm{s}}L_{\mathrm{r}}}\vec{\psi}_{\mathrm{s}} - \left(\frac{R_{\mathrm{r}}}{\sigma L_{\mathrm{r}}} - \mathrm{j}\omega_{\mathrm{m}}\right)\vec{\psi}_{\mathrm{r}}. \tag{2.11b}$$

To find the matrices of the state-space model, the state equations (2.11) are rewritten in matrix notation as

$$\frac{\mathrm{d}}{\mathrm{d}t}\begin{bmatrix}\vec{\psi}_{\mathrm{s}}\\ \vec{\psi}_{\mathrm{r}}\end{bmatrix} = \begin{bmatrix}-\frac{R_{\mathrm{s}}}{\sigma L_{\mathrm{s}}}\mathbf{I} & \frac{R_{\mathrm{s}}L_{\mathrm{m}}}{\sigma L_{\mathrm{r}}L_{\mathrm{s}}}\mathbf{I}\\ \frac{R_{\mathrm{r}}L_{\mathrm{m}}}{\sigma L_{\mathrm{s}}L_{\mathrm{r}}}\mathbf{I} & -\frac{R_{\mathrm{r}}}{\sigma L_{\mathrm{r}}}\mathbf{I} + \omega_{\mathrm{m}}\mathbf{J}\end{bmatrix}\begin{bmatrix}\vec{\psi}_{\mathrm{s}}\\ \vec{\psi}_{\mathrm{r}}\end{bmatrix} + \begin{bmatrix}\mathbf{I}\\ \mathbf{0}\end{bmatrix}\vec{u}_{\mathrm{s}} \tag{2.12a}$$

$$\text{and} \quad \vec{i}_{\mathrm{s}} = \begin{bmatrix}\frac{1}{\sigma L_{\mathrm{s}}}\mathbf{I} & -\frac{L_{\mathrm{m}}}{\sigma L_{\mathrm{s}}L_{\mathrm{r}}}\mathbf{I}\end{bmatrix}\begin{bmatrix}\vec{\psi}_{\mathrm{s}}\\ \vec{\psi}_{\mathrm{r}}\end{bmatrix} \quad \text{with} \quad \mathbf{I} = \begin{bmatrix}1 & 0\\ 0 & 1\end{bmatrix}, \mathbf{J} = \begin{bmatrix}0 & -1\\ 1 & 0\end{bmatrix}. \tag{2.12b}$$

$\mathbf{J}$ is the imaginary number in matrix notation, $\mathbf{I}$ the identity matrix and $\mathbf{0}$ the zero matrix. The system matrix, input matrix and output matrix are now found by comparison with (2.8) as

$$\begin{aligned}\boldsymbol{A}_{\mathrm{im}} &= \begin{bmatrix}-\frac{R_{\mathrm{s}}}{\sigma L_{\mathrm{s}}} & 0 & \frac{R_{\mathrm{s}}L_{\mathrm{m}}}{\sigma L_{\mathrm{s}}L_{\mathrm{r}}} & 0\\ 0 & -\frac{R_{\mathrm{s}}}{\sigma L_{\mathrm{s}}} & 0 & \frac{R_{\mathrm{s}}L_{\mathrm{m}}}{\sigma L_{\mathrm{s}}L_{\mathrm{r}}}\\ \frac{R_{\mathrm{r}}L_{\mathrm{m}}}{\sigma L_{\mathrm{s}}L_{\mathrm{r}}} & 0 & -\frac{R_{\mathrm{r}}}{\sigma L_{\mathrm{r}}} & -\omega_{\mathrm{m}}\\ 0 & \frac{R_{\mathrm{r}}L_{\mathrm{m}}}{\sigma L_{\mathrm{s}}L_{\mathrm{r}}} & \omega_{\mathrm{m}} & -\frac{R_{\mathrm{r}}}{\sigma L_{\mathrm{r}}}\end{bmatrix}, \qquad \boldsymbol{B}_{\mathrm{im}} = \begin{bmatrix}1 & 0\\ 0 & 1\\ 0 & 0\\ 0 & 0\end{bmatrix},\\ \boldsymbol{C}_{\mathrm{im}} &= \begin{bmatrix}\frac{1}{\sigma L_{\mathrm{s}}} & 0 & -\frac{L_{\mathrm{m}}}{\sigma L_{\mathrm{s}}L_{\mathrm{r}}} & 0\\ 0 & \frac{1}{\sigma L_{\mathrm{s}}} & 0 & -\frac{L_{\mathrm{m}}}{\sigma L_{\mathrm{s}}L_{\mathrm{r}}}\end{bmatrix} \quad \text{and} \quad \boldsymbol{D}_{\mathrm{im}} = \begin{bmatrix}0 & 0\\ 0 & 0\end{bmatrix}.\end{aligned} \tag{2.13}$$

To analyze the stability of the IM, the placement of the system poles $s_{\mathrm{p}n}$ in the complex s-plane can be derived. With the state-space model, the poles are conveniently found as

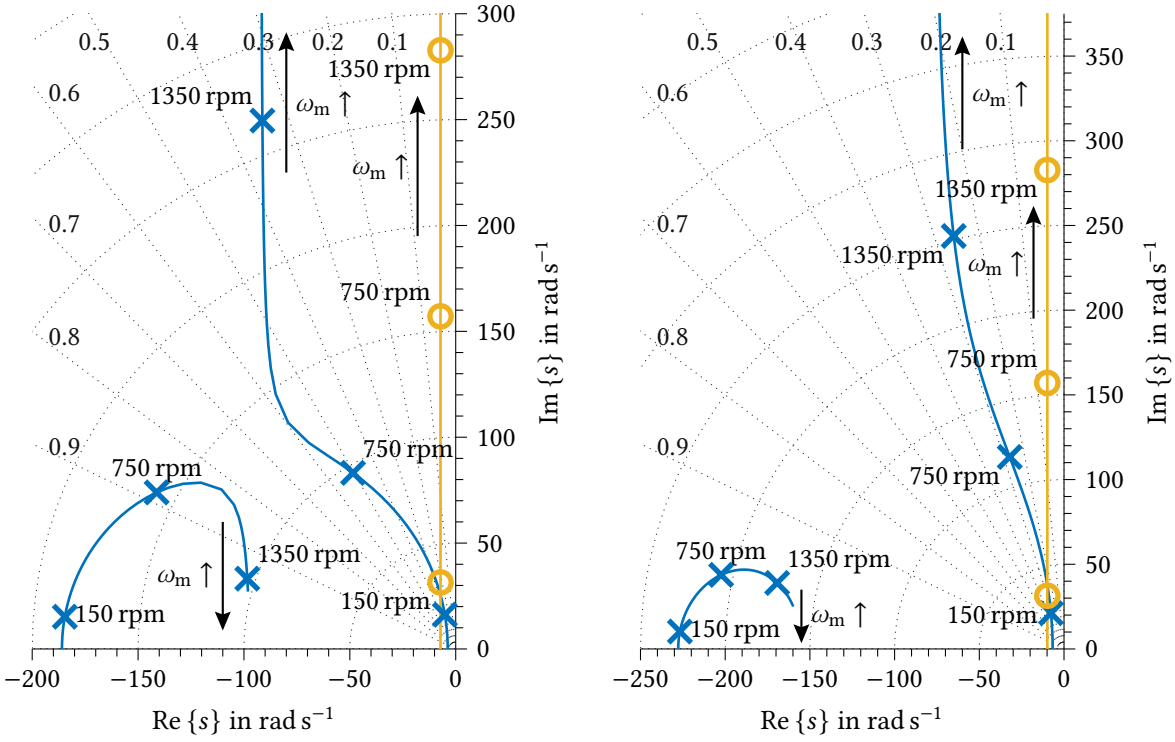

(a) IM26kA (b) IM750

Fig. 2.5: Root locus diagrams of the IM with two poles '×' and one zero '○', according to (2.15). Parameters of the 26 kW machine IM26kA and the 750 W machine IM750 are given in Appendix A.2.

the roots of the characteristic polynomial [DB11, pp. 386–442]

$$\det\left(s_{pn}\mathbf{I} - \boldsymbol{A}_{im}\right) \stackrel{!}{=} 0. \tag{2.14}$$

By solving (2.14), two complex poles s_{p1} and s_{p2} are identified which are a function of the mechanical rotor frequency. They can be calculated by

$$\begin{aligned} s_{p1} &= -\frac{R_s L_r + R_r L_s}{2\sigma L_s L_r} \pm \mathrm{j}\frac{1}{2}\omega_m + \sqrt{\frac{R_s R_r L_m^2}{\sigma^2 L_s^2 L_r^2} + \left(\frac{R_s L_r - R_r L_s}{2\sigma L_s L_r} \pm \mathrm{j}\frac{1}{2}\omega_m\right)^2} \\ \text{and} \quad s_{p2} &= -\frac{R_s L_r + R_r L_s}{2\sigma L_s L_r} \pm \mathrm{j}\frac{1}{2}\omega_m - \sqrt{\frac{R_s R_r L_m^2}{\sigma^2 L_s^2 L_r^2} + \left(\frac{R_s L_r - R_r L_s}{2\sigma L_s L_r} \pm \mathrm{j}\frac{1}{2}\omega_m\right)^2}. \end{aligned} \tag{2.15}$$

Another advantage of the state-space representation is that the IM model can directly be analyzed using the MATLAB Control System Toolbox. In Fig. 2.5, the characteristic root locus diagram of the IM is plotted for a 26 kW machine IM26kA and a 750 W machine IM750, using the `pzmap` command on the matrices in (2.13). It illustrates the position of the two poles (2.15) within the complex s-plane and their dependency on the mechanical rotor frequency ω_m. In addition to the poles, the IM has one zero which is located close to the

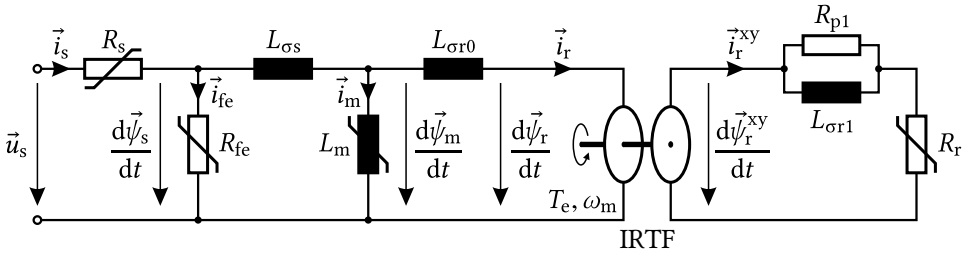

Fig. 2.6: Extended nonlinear induction machine model with IRTF.

imaginary axis. For increasing speed, s_{p1} and the zero travel in direction of the imaginary axis, whereas s_{p2} approaches the real axis. The root locus diagram will later be useful to define the flux-linkage observer gains.

2.1.3 Extended Nonlinear IM Model

The previously introduced IM model must be considered as an idealized model. In reality, additional effects exist that cause the IM parameters to vary during operation. The most relevant influences are magnetic saturation, temperature drift, iron losses and the rotor deep-bar effect. To analyze the torque accuracy and to investigate the robustness of the control algorithm and flux-linkage observers on parameter variations, a more realistic model must be used which takes these effects into account. To do so, the previous IM model is modified and an extended nonlinear model of the IM is introduced. Based on this model, a block diagram is derived and implemented in MATLAB/Simulink. It is used for dynamic simulations and steady-state calculations in this work. The resulting equivalent circuit is depicted in Fig. 2.6 and comprises additional components and nonlinear parameters, which will be explained in the following.

2.1.3.1 Magnetic Saturation

To optimize the power density and material consumption, the IM is generally designed to operate under magnetically saturated conditions. It causes the magnetic flux linkage to saturate with increasing magnetizing current. In the IM model, this is reflected by current-dependent parameter variations of the inductance values L_m, $L_{\sigma s}$ and $L_{\sigma r}$. However, precise identification of these parameters and their dependency on saturation is problematic because they are mutually coupled and not separately measurable.

A common approach is to only consider the saturation of the main flux path [LN90]. The dependency of the main inductance L_m is usually obtained by no-load tests. The rotor current then becomes zero and the inductance can be measured in conjunction with the stator leakage inductance. In Fig. 2.7a, this has been done for IM26kA with current magnitudes from 10 to 270 A in steps of 20 A, and with stator frequencies from 20 to 200 Hz in steps of 30 Hz. The stator inductance is plotted as a function of the stator flux linkage

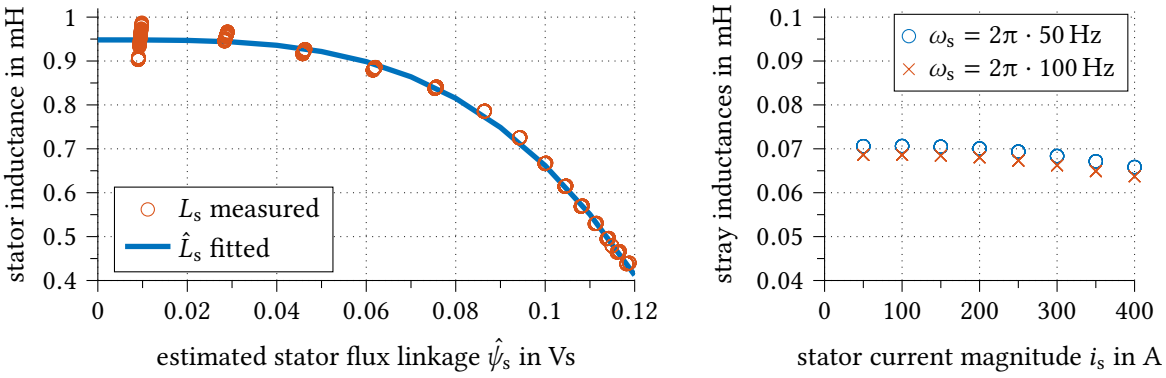

(a) stator inductance $L_s = L_m + L_{\sigma s}$

(b) stray inductances $L_{\sigma s} + L_{\sigma r}$

Fig. 2.7: The influence of magnetic saturation on the stator inductance, obtained for IM26kA through no-load tests and fitted using an exponential function. The dependency of the stray inductances on the current magnitude and the frequency was measured during locked-rotor tests.

which is calculated from voltage measurements using the voltage model according to (2.4). L_s is basically only dependent on the stator flux-linkage magnitude and decreases at rated flux linkage to half of its unsaturated value. The stator frequency has no noticeable influence on the inductance value.

The saturation dependent stator inductance can be described using the exponential function

$$L_s(\psi_s) = L_{s1} - l_{s2} \cdot \psi_s^{e_{s2}}, \tag{2.16}$$

which leads to a very close fit, as illustrated in Fig. 2.7a. In this work, the saturation of the main flux linkage is described using the stator quantities, because they are directly determinable from measurements. L_s can be obtained from the reactive power or the imaginary impedance component acquired during no-load tests without the influence of other model parameters. This makes (2.16) a reliable representation.

To identify the mutual inductance L_m, the stator leakage inductance $L_{\sigma s}$ must be subtracted from (2.16). However, explicit measurement of $L_{\sigma s}$ is not possible. It is usually determined by locked-rotor tests as the sum of both leakage inductances which are not clearly separable. Common practice is to assume both parameters to be equal. A better solution is to utilize the data generated by finite element method (FEM), if available. In this work, the ratio of both leakage inductances is taken from FEM data and is used to separate the stray inductance value obtained by locked-rotor tests. This leads to a more reasonable distribution, but is still a factor of uncertainty.

Another problem is the saturation of the leakage flux linkages. The locked rotor test implies almost zero magnetizing current. Thus, $L_{\sigma s}$ and $L_{\sigma r}$ are usually parameterized under unsaturated conditions. This is confirmed by the test results shown in Fig. 2.7b. For better comparison, in Fig. 2.7 the ordinates are proportionally scaled. Only slight saturation with an inductance reduction of only 7 % from zero to rated current is noticeable. It is almost negligible when compared to the stator inductance reduction of 50 % in Fig. 2.7a.

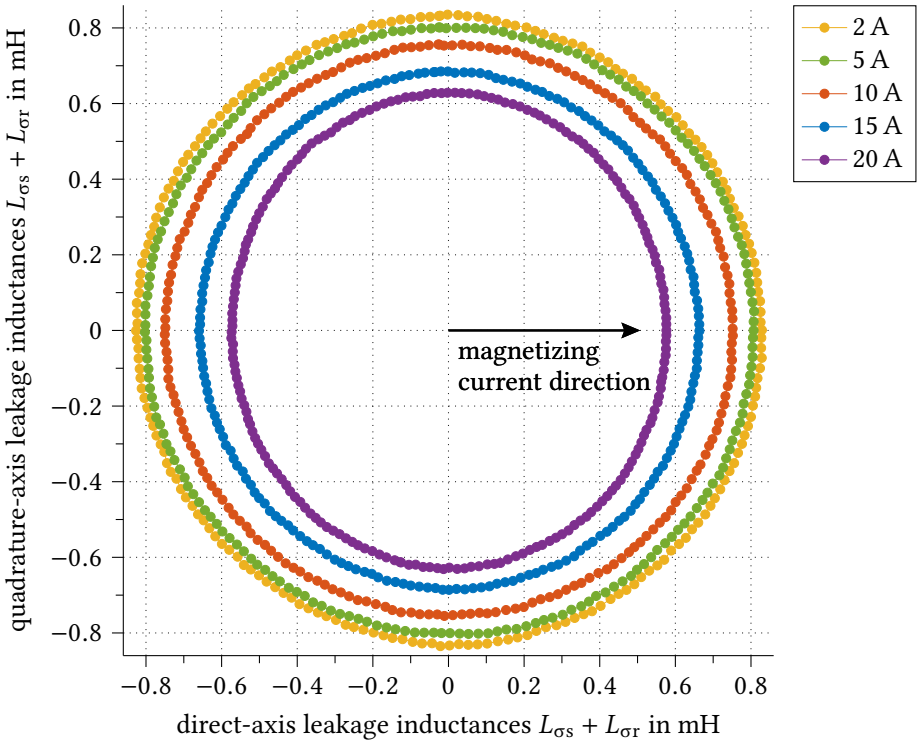

Fig. 2.8: Measured sum of leakage inductances as a function of the magnetizing current and field angle. Detected with IM750 by signal injection of an alternating voltage space vector with a sinusoidal magnitude of 2 V and 600 Hz, rotating at 1 Hz.

However, since the mutual and the leakage flux linkages share the same flux path, a saturation cross coupling exists which also decreases the leakage inductances in the presence of magnetizing current. In Fig. 2.8, this effect is experimentally investigated by injecting an alternating voltage at standstill using IM750. The direct current (DC) magnetizing current is varied from 10 % to 100 % of the rated current. At the same time, the sum of spatial leakage inductances is measured as a function of the angle to the magnetizing-current vector by superimposing a high-frequency voltage signal. The procedure can be understood as a spatial locked rotor test under saturated conditions. As expected, the leakage inductances are significantly reduced by about 20 %. Furthermore, the main flux linkage introduces a saliency which can be used for speed or flux angle estimation [JL96].

To include the impact of cross saturation, more complex models can be found in the references of [Lev97]. However, they introduce new uncertainties due to additional coupling parameters and have been subject of controversy. In [Ger+07], the cross saturation has been analyzed using a reluctance mesh modeling approach. Results show, that the effect of cross saturation is greatly enhanced by the skewing of the rotor.

One should note that the inductance values in Fig. 2.8 are much smaller than the parameters given in Table A.3. At 600 Hz, the overall leakage inductance is decreased to 65 % of its actual value. This and the frequency-dependent reduction of the leakage inductances in Fig. 2.7b are caused by the rotor deep-bar effect described in Section 2.1.3.4.

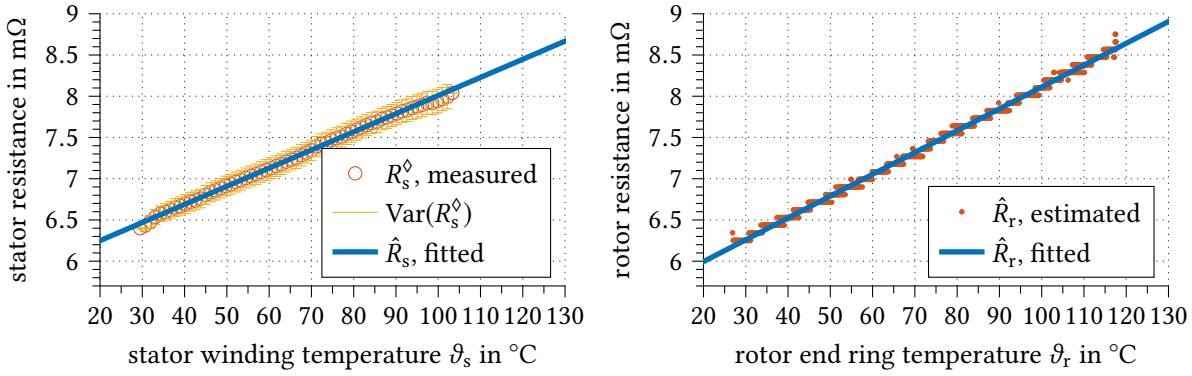

(a) stator resistance

(b) rotor resistance

Fig. 2.9: Temperature drift of the stator and rotor resistance for IM26kA. Stator temperature measured at the end winding and rotor temperature measured at the end ring using a rotor telemetry.

In this work, saturation is only considered in the main inductance L_m and is only defined for the stator inductance according to (2.16), because of the aforementioned parameterization uncertainties. $L_{\sigma s}$ and $L_{\sigma r}$ are assumed to be constant but may differ from the real values. Thus, the torque-control algorithm must be insensitive to leakage inductance variations and cross saturation to achieve precise torque production.

2.1.3.2 Thermal Drift of the Stator and Rotor Resistance

The major reason for stator and rotor resistance drift is temperature variation. For a limited temperature range, the electrical resistance of metals increases nearly linearly with the temperature [Gia14]. Thus, with changing temperature ϑ_s of the stator windings, the stator resistance may be described as

$$R_s(\vartheta_s) = R_s(\vartheta_s = 20\,^{\circ}\mathrm{C}) \cdot (1 + \alpha_{20} \cdot (\vartheta_s - 20\,^{\circ}\mathrm{C})). \tag{2.17}$$

$R_s(\vartheta_s = 20\,^{\circ}\mathrm{C})$ is the stator resistance at 20 °C and α_{20} is the corresponding temperature coefficient for copper. α_{20} is a material constant and only valid for a specific temperature.

The stator winding temperature usually changes with a time constant of several tens of minutes. Since this is very slow compared to all other dynamic processes of the IM drive, terms describing the dynamic change of stator resistance can be neglected and $R_s(\vartheta_s)$ can be considered as a steady-state quantity within all equations. Thus, no modification of the aforementioned model equations is necessary and R_s is simply updated as a function of the winding temperature.

The stator resistance and its dependency on the winding temperature can be determined by simple DC current measurements. In Fig. 2.9a this has been done during a cooling process from 104 to 30 °C. A current of 150 A has been applied to the stator windings while the voltage drop was captured along with the stator end-winding temperature. Since the temperature sensor is not equally coupled to each of the three phase-windings, and

TABLE 2.1
Stator and Rotor Resistance Temperature Coefficients

	unit	stator	rotor
measured resistances at 20 °C	mΩ	6.25	6
measured temperature coefficients α_{20}	$10^{-3}\,\mathrm{K}^{-1}$	3.5	4.4
literature values α_{20} [CD03]	$10^{-3}\,\mathrm{K}^{-1}$	3.95	4.2
material		copper	aluminum

since the sensing current introduces an unequally distributed temperature increase, the stator-current space vector was rotated slowly at 0.1 Hz. The results reflect the linear relationship according to (2.17). Fitting with a linear function leads to the temperature coefficient given in Table 2.1, which is similar to the literature value for pure copper.

The same relationship also applies to the rotor resistance. However, the parameterization is difficult because usually neither the resistance value nor the rotor temperature can be measured. In contrast to common setups, IM26kA is equipped with four thermal sensors of the type PT100 located at the end ring of the squirrel cage and a corresponding rotor telemetry. The rotor resistance can be indirectly determined using a flux-linkage observer and the IM model. From equations (2.5) and (2.6) an expression for the rotor resistance can be derived as

$$R_\mathrm{r} = \frac{\omega_\mathrm{sl}}{i_\mathrm{sq}}\left(\psi_\mathrm{s}\frac{L_\mathrm{r}}{L_\mathrm{s}} - i_\mathrm{sd}\left(L_\mathrm{r} - \frac{L_\mathrm{m}^2}{L_\mathrm{s}}\right)\right). \tag{2.18}$$

i_sd and i_sq are the direct and quadrature stator current components of the stator field oriented 'dq'-reference frame and are measured quantities. At sufficiently high speed, the stator flux linkage is accurately obtained from voltage measurements and the voltage equation (2.4) [SSD16]. However, since (2.18) is a function of the inductance values, small deviations might be introduced by the saturation related parameter uncertainties described in the previous section.

In Fig. 2.9b, R_r has been captured at an operating point of 60 Nm and 4000 rpm. The rotor was warmed-up from 26 to 118 °C. The results show the same linear relationship as in (2.17). With a least square fit, the corresponding coefficients of the rotor resistance can be found as given in Table 2.1. The temperature dependency of R_r is represented in the IM model analogously to the stator resistance. But since the characterization of R_r is more sensitive to errors and the rotor temperature is usually not measurable, the control algorithm should be rather insensitive to this parameter.

2.1.3.3 Remagnetization Losses in the Ferromagnetic Material

Remagnetization losses within the ferromagnetic material is a wide and active field of research itself. Many modeling concepts have been developed and discussed. Some of them try to emulate the physical mechanisms in detail, others are rather based on empirical studies. A common descriptive approach is to split the losses in magnetic hysteresis and

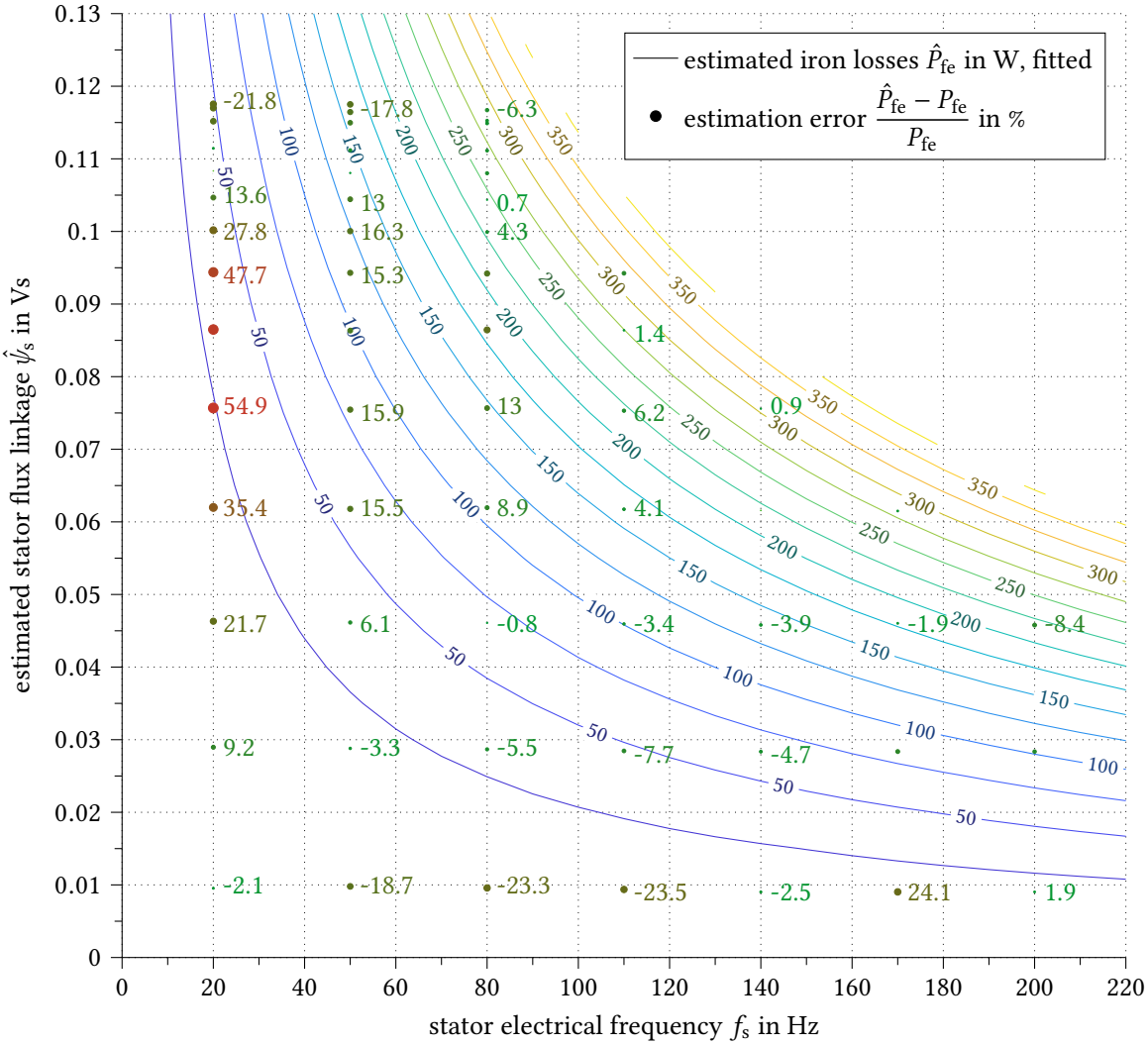

Fig. 2.10: Iron core losses of IM26kA measured by no-load tests and fitted using Steinmetz's equation.

eddy-currents losses. However, in material sciences and physics this conception is not accepted. A brief overview on the modeling of remagnetization losses and its physical origins can be found in [RBD01]. In the field of electrical drives, usually the alternative term *iron losses* is used when referring to these losses.

In this work, an empirical model for the iron losses is used. In the 19$^{\text{th}}$ century, Steinmetz conducted experimental studies and found an expression for the remagnetization losses. It is a function of the magnetic flux density and the frequency of a sinusoidal excitation voltage [Ste92]. Translated to the stator quantities of the IM, the Steinmetz equation

$$P_{\text{fe}} \overset{\text{steady state}}{=} \frac{3}{2} \cdot k_{\text{fe}} \cdot |\omega_{\text{s}}|^{a_{\text{fe}}} \cdot \psi_{\text{s}}^{b_{\text{fe}}} \tag{2.19}$$

is obtained with the material constants k_{fe}, a_{fe} and b_{fe}. Since the IM is a rotating-field machine with sinusoidal phase currents, (2.19) is applicable.

The iron losses are generally determined by measuring the active power consumption during no-load tests. After subtracting the stator copper losses, P_{fe} is obtained as a function of the estimated stator flux linkage $\hat{\psi}_{\mathrm{s}}$ and the stator angular frequency ω_{s}. To eliminate the influence of friction losses, the machine under test is driven by a second load machine.

Corresponding measurement results for IM26kA are given in Fig. 2.10. An estimate $\hat{P}_{\mathrm{fe}}$ for the iron losses is found by fitting the measured data points using the Steinmetz equation (2.19). The estimate $\hat{P}_{\mathrm{fe}}$ is in good agreement with the measurements. Only at low frequency when the signal-to-noise ratio is low, a notable relative error exists. The iron losses are then small compared to the stator copper losses which – due to temperature drift – cause a measurement error.

In the equivalent circuit of the IM, the iron losses are often represented by a frequency and flux-linkage dependent resistance R_{fe} in parallel to the mutual inductance. An approach for combined modeling of iron losses and saturation is given in [SL96]. However, the iron-loss resistor is not a physically precise representation and the positioning parallel to L_{m} is unfavorable because it interferes with other modeling concepts. Especially the transformation of the equivalent circuit to the stator-oriented Γ-model or the rotor-oriented inverse Γ-model becomes more complicated.

A better and not less accurate approach is the placement of R_{fe} parallel to the stator inductance L_{s}, as proposed in [Dit98]. The iron losses are then related to the stator quantities, according to Fig. 2.6. With (2.19), the steady-state iron-loss resistance can be calculated as

$$R_{\mathrm{fe}} \overset{\text{steady state}}{=} \frac{\omega_{\mathrm{s}}^2 \psi_{\mathrm{s}}^2}{P_{\mathrm{fe}}} = k_{\mathrm{fe}}^{-1} \cdot |\omega_{\mathrm{s}}|^{2-a_{\mathrm{fe}}} \cdot \psi_{\mathrm{s}}^{2-b_{\mathrm{fe}}}. \tag{2.20}$$

The additional stator current component through R_{fe} is orthogonal to the stator flux linkage and has therefore an influence on the torque production. It can be calculated by

$$\vec{i}_{\mathrm{fe}} = \frac{1}{R_{\mathrm{fe}}(\omega_{\mathrm{s}}, \psi_{\mathrm{s}})} \cdot \frac{\mathrm{d}\vec{\psi}_{\mathrm{s}}}{\mathrm{d}t} \overset{\text{steady state}}{=} \mathrm{j}\omega_{\mathrm{s}} \vec{\psi}_{\mathrm{s}} \cdot k_{\mathrm{fe}} \cdot |\omega_{\mathrm{s}}|^{a_{\mathrm{fe}}-2} \cdot \psi_{\mathrm{s}}^{b_{\mathrm{fe}}-2}. \tag{2.21}$$

One should note that the iron-loss model is an empirical model that has been parameterized by no-load tests under steady-state conditions. Thus, it does not include any information about transient processes and only describes losses occurring in the stator material. Although the magnetic field rotates slowly in relation to the rotor, notable additional iron losses can occur when torque is produced. In [vPSH17], the iron losses of IM26kA have been analyzed at IEM using FEM. The iron losses have been calculated for the entire operating range of the drive considering the application of an efficiency-optimized control strategy. Results in Fig. 2.11a show, that the calculated iron losses in the field-weakening region are notably higher than the measured data from no-load tests. Fig. 2.11b shows the discrepancy between the Steinmetz model and FEM. Equation (2.19) seems to be accurate for a wide operating range, but close to the maximum voltage limit in the field-weakening region the FEM results show a deviation of up to 800 W. As stated in [vPSH17], this is

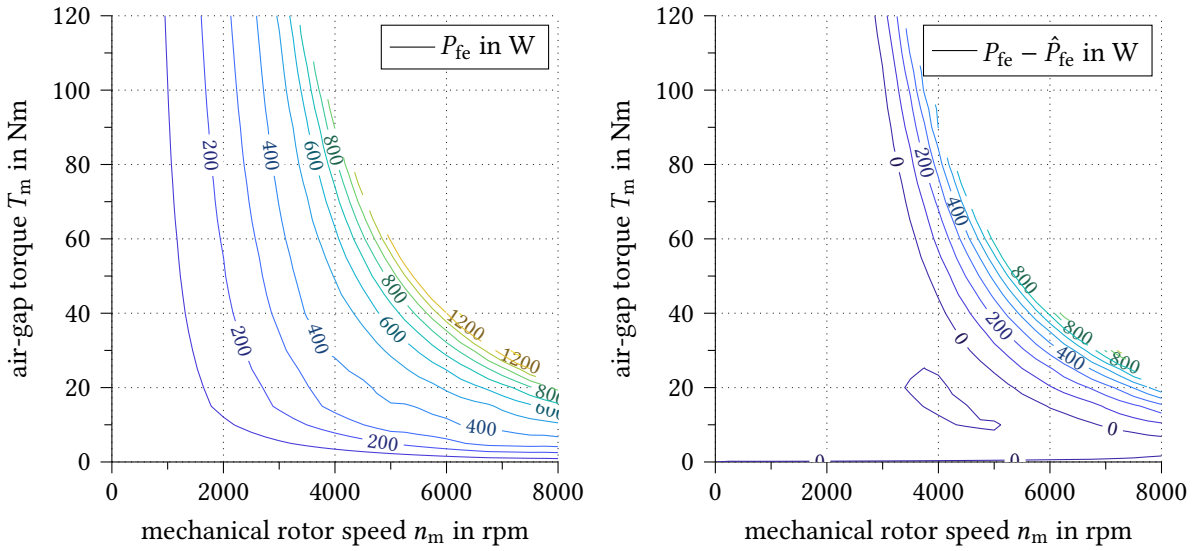

(a) FEM calculated data

(b) discrepancy between FEM and iron-loss model

Fig. 2.11: Comparison of calculated iron losses using FEM in [vPSH17], and iron-loss model using fitted data from no-load tests, according to Fig. 2.10. Results for the entire operating range of the efficiency-optimized drive using IM26kA.

caused by slot harmonics which are drastically increased at high slip frequencies. They introduce additional iron losses close to the air gap, especially on the rotor surface.

In this work, the additional slot-harmonics-related rotor iron losses are neglected. Basically, additional components in the rotor circuit could be introduced, but reliable information about the correlation to the electrical quantities of the fundamental frequency model in Fig. 2.6 is missing. Furthermore, the additional losses will not lead to wrong results when the model is used for efficiency optimization, since they only occur in the field-weakening region where the choice of flux linkage is no longer a degree of freedom. Additional rotor losses could be modeled as an additional resistive component in the rotor circuit on the right-hand side of the IRTF in the fundamental model. Thus, it can be assumed that they do not provoke torque deviation, in case a voltage-model observer based controller is used. The additional losses can then rather be seen as a distortion of the rotor-resistance value.

2.1.3.4 Rotor Deep-Bar Effect

At high slip frequency, the current in the rotor bars is no longer uniformly distributed across the rotor bar cross-sectional area. Due to the skin effect, the current is displaced in radial direction to the rotor surface. This leads to a higher effective rotor resistance and a reduced rotor leakage inductance. Consequently, both quantities alter with changing slip, especially during transients.

The rotor deep-bar effect is highly dependent on the shape of the rotor-bar cross section and is more pronounced for deeper rotor bars. It is often utilized to improve the starting torque of grid-connected IM. As illustrated in Fig. 2.12, the starting torque at $s_{slip} = 1$ is

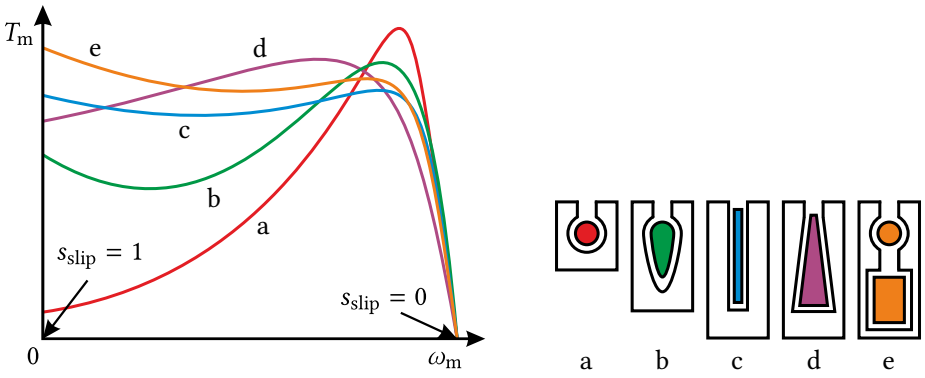

(a) torque–speed diagram (b) rotor-bar shape

Fig. 2.12: Influence of the rotor bar shape on the torque production [HVB99].

significantly increased by the deep rotor bars [HVB99]. However, in vector-controlled drives, the deep-bar effect is a parasitic effect that increases the rotor losses and can cause higher torque ripple.

A systematic approach to represent the rotor deep-bar effect in the IM model can be found in [DVG86a; De 92] and the supplementary of [DPV11]. An additional parallel network consisting of an inductance $L_{\sigma r1}$ and a resistance R_{p1} is added to the rotor circuit in Fig. 2.6. By matching the resulting complex rotor admittance to the admittance locus described by the skin-effect theory, a set of parameters for the rotor deep-bar effect can be found as

$$L_{\sigma r0} = 0.29 \cdot L_{\sigma r}, \quad L_{\sigma r1} = 0.71 \cdot L_{\sigma r} \quad \text{and} \quad R_{p1} = 2.53 \cdot R_r. \tag{2.22}$$

The so found parameters are a good representation of the rotor deep-bar effect. However, even better results can be achieved by matching the admittance to measured data. Since the IM in this work is only operated at moderate slip frequencies this step can be omitted without notable deviation of the model. Furthermore, the rotor deep-bar effect can often be considered as a parameter distortion of the rotor resistance and rotor leakage inductance. Therefore, no additional components are necessary.

2.1.3.5 Extended Nonlinear Simulation Model

The signal-flow diagram used for the implementation of the extended IM model in MATLAB/Simulink is given in Fig. 2.13. The magnetic saturation is modeled using a lookup table for the magnetization current in polar coordinates, as proposed in the supplementary chapter of [DPV11]. To find an expression for the stator and rotor current, with the stator and rotor flux linkage as inputs, (2.6) can be rewritten as

$$\vec{\psi}_m = \underbrace{\frac{L_{eq}}{L_{\sigma s}}\vec{\psi}_s + \frac{L_{eq}}{L_{\sigma r0}}\vec{\psi}_r}_{\psi_{mo}} - L_{eq}\vec{i}_m \quad \text{with} \quad L_{eq} = \frac{L_{\sigma s}L_{\sigma r0}}{L_{\sigma s} + L_{\sigma r0}} \quad \text{and} \quad \vec{i}_m = \vec{i}_s - \vec{i}_r. \tag{2.23}$$

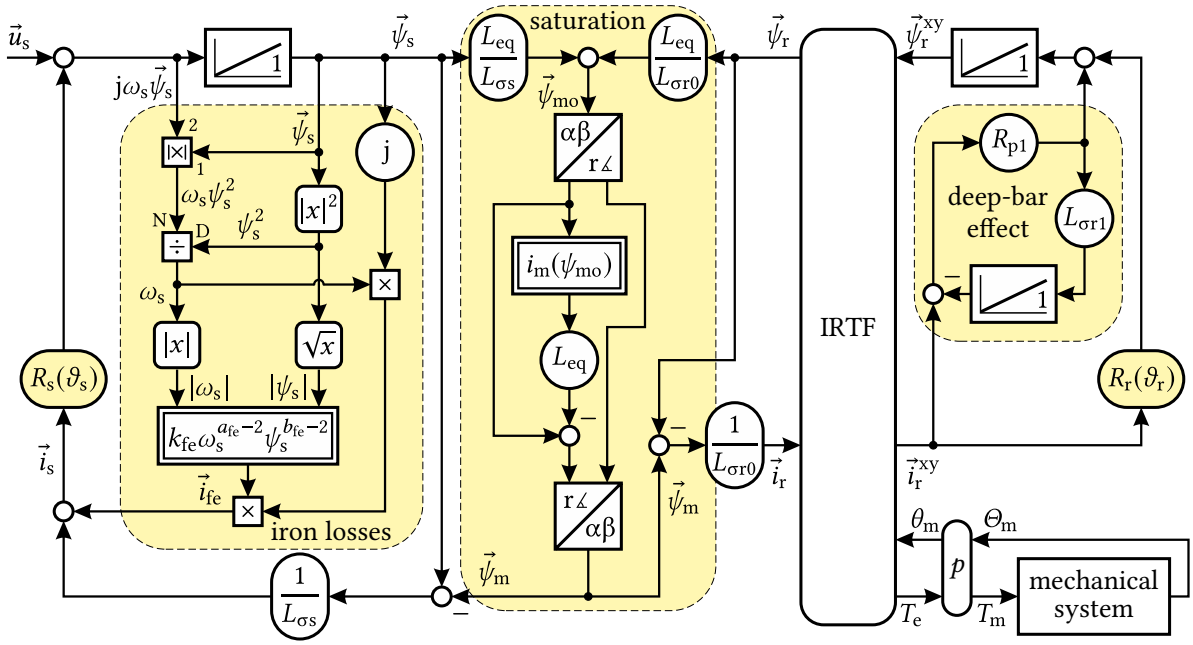

Fig. 2.13: Signal-flow diagram of the extended IM model with ideal rotating transformer (IRTF).

The magnetization current $\vec{i}_\mathrm{m}$ can now be determined using a lookup table with the auxiliary flux linkage ψ_mo as input. It is a fundamental component model without consideration of saturation or other higher-order harmonics caused by the rotor or stator slots and winding distribution. For the simulation model, the L_s saturation model in (2.16) needs to be transformed to the mutual inductance L_m by subtraction of the stator leakage inductance.

The thermal drift of the stator and rotor resistance is represented by time-varying resistance values. Since the dynamic temperature change is much slower than the other IM time constants, dynamic terms related to the temperature can be neglected and the resistance values can be considered as steady state.

Iron losses are included in the dynamic model by implementation of the current-related Steinmetz equation (2.21). Since the stator angular frequency is not a signal in the dynamic IM model, it must be extracted from the stator flux linkage. This can be done by calculation of the cross-product magnitude of $\vec{\psi}_\mathrm{s}$ with its derivative according to

$$\omega_\mathrm{s} = \frac{1}{\psi_\mathrm{s}^2}\left(\vec{\psi}_\mathrm{s}\,|\times|\,\mathrm{j}\omega_\mathrm{s}\vec{\psi}_\mathrm{s}\right). \tag{2.24}$$

To avoid problems in the case that $\vec{u}_\mathrm{s}$ is a switched voltage signal, the factors of (2.24) can be low-pass filtered before multiplication. Although it reduces the dynamic response, the overall quality of the iron-loss model is not affected, since it is an empirical steady-state model without proper representation of the dynamic behavior.

It should be noted that the model is built for a skewed rotor IM with open rotor slots. With closed rotor slots, leakage flux saturation is more pronounced and must be considered.

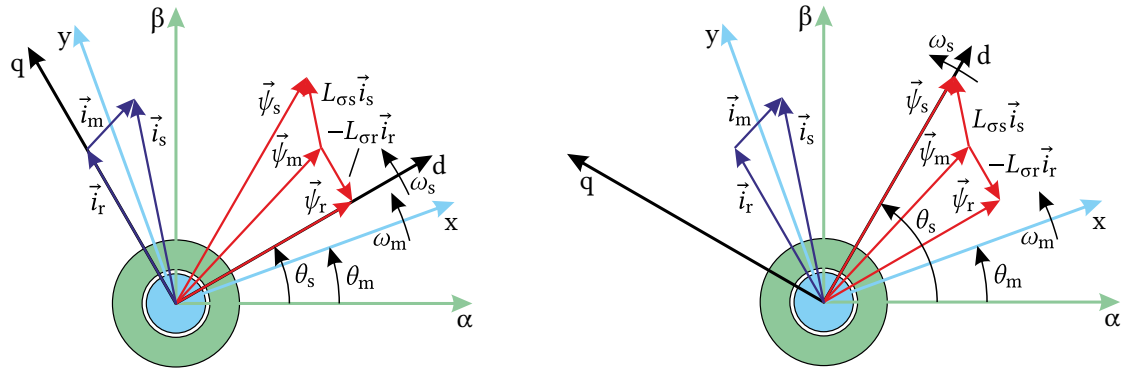

(a) rotor field orientation (RFO)

(b) stator field orientation (SFO)

Fig. 2.14: Space-vector diagram with stator (αβ), rotor (xy) and field-oriented (dq) reference frame.

2.2 Field-Oriented Torque Controllers

FOC, introduced by Blaschke in [Bla74], has become one of the major algorithms for dynamic torque control in IM drives. By orientation of a synchronously-rotating 'dq'-reference frame with the flux-linkage space vector, separate control of the flux linkage and the torque is achieved. Therefore, the electrical quantities are rotated by the field angle θ_s. Fig. 2.14 shows the resulting vector diagrams for the two most common cases – rotor field orientation (RFO) and stator field orientation (SFO). The torque produced by the IM is then only defined by the flux-linkage magnitude and the quadrature stator current component. Since in the field-oriented reference frame the flux linkage has only a real component, the torque equation (2.7c) can be expressed with the help of (2.6) as

$$T_e = \frac{3}{2} \cdot \frac{L_m}{L_r} \psi_r i_{sq} \quad \text{for RFO and} \quad T_e = \frac{3}{2} \cdot \psi_s i_{sq} \quad \text{for SFO, respectively.} \tag{2.25}$$

i_{sq} is also referred to as the *torque-producing* stator current component.

The relationship between the *flux-producing* stator current component i_{sd} and the flux linkage can be found using the current model of the IM. With (2.5) transformed to a 'dq'-reference frame rotating with the stator frequency ω_s, the current model of the IM is obtained as

$$\frac{\mathrm{d}\vec{\psi}_r^{\,dq}}{\mathrm{d}t} = R_r \vec{i}_r^{\,dq} - \mathrm{j}\omega_{sl} \vec{\psi}_r^{\,dq}. \tag{2.26}$$

With the help of the flux-linkage equations (2.6), the rotor flux linkage can be expressed as a function of the stator current and the rotor time constant τ_r as

$$\frac{\mathrm{d}\vec{\psi}_r^{\,dq}}{\mathrm{d}t} = \frac{L_m}{\tau_r} \vec{i}_s^{\,dq} - \left(\frac{1}{\tau_r} + \mathrm{j}\omega_{sl} \right) \vec{\psi}_r^{\,dq}, \quad \text{with} \quad \tau_r = \frac{L_r}{R_r}. \tag{2.27}$$

In RFO the reference frame is oriented to the rotor flux linkage and $\vec{\psi}_r^{\,dq}$ becomes real

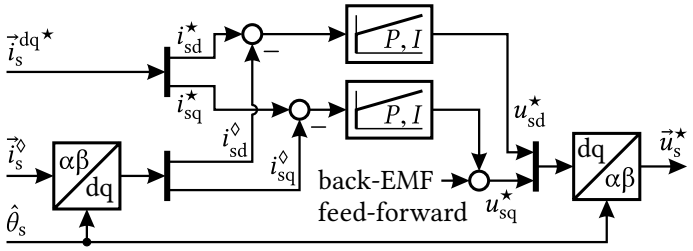

Fig. 2.15: Structure of field-oriented control (FOC) with current regulators and reference frame transformations. Superscripts and diacritical marks according to Appendix A.1.1.

with $\vec{\psi}_r^{\,dq} = \psi_r$. The current model (2.27) may then be rewritten as

$$\frac{d\psi_r}{dt} = -\frac{1}{\tau_r}\psi_r + \frac{L_m}{\tau_r} i_{sd} \quad \circ\!\!-\!\!\bullet^{\mathcal{L}} \quad \underset{\sim}{\psi}_r = \frac{L_m}{1+\tau_r s}\underset{\sim}{i}_{sd} \tag{2.28}$$

and can be expressed in the complex frequency domain using the Laplace transformation. It contains a first-order lag element with the rotor time constant τ_r, which limits the dynamic change of the flux linkage. This limitation determines the torque dynamics of the efficiency-optimized drive and will be analyzed in Chapter 6. In RFO, the torque and the rotor flux linkage are fully decoupled as long as the 'dq'-reference frame is accurately oriented with $\vec{\psi}_r$.

To find the relationship for SFO, the current model (2.27) must be expressed as a function of the stator flux linkage and the stator current. Substitution with (2.6) and some mathematics lead to

$$\frac{d\vec{\psi}_s^{\,dq}}{dt} + \left(\frac{1}{\tau_r} + j\omega_{sl}\right)\vec{\psi}_s^{\,dq} = \sigma L_s \frac{d\vec{i}_s^{\,dq}}{dt} + \left(\frac{L_s}{\tau_r} + j\omega_{sl}\sigma L_s\right)\vec{i}_s^{\,dq}. \tag{2.29}$$

After orientation with the stator flux linkage, (2.29) can be expressed as

$$\begin{aligned}\frac{d\psi_s}{dt} + \frac{\psi_s}{\tau_r} = \sigma L_s \frac{di_{sd}}{dt} + \frac{L_s}{\tau_r} i_{sd} - \omega_{sl}\sigma L_s i_{sq} \quad \circ\!\!-\!\!\bullet^{\mathcal{L}} \quad \underset{\sim}{\psi}_s &= \frac{L_s(1+\sigma\tau_r s)}{1+\tau_r s}\underset{\sim}{i}_{sd} \\ &\quad - \frac{\omega_{sl}\sigma L_s \tau_r}{1+\tau_r s}\underset{\sim}{i}_{sq}.\end{aligned} \tag{2.30}$$

In SFO, a cross coupling with the torque-producing current component i_{sq} exists in the flux-linkage term. A universal field-orientation approach that covers both cases can be found in [DN88; DN94; DPV11]. However, for better illustration this work focuses on RFO and SFO, only.

The FOC controller is basically a current regulator that allows independent control of the flux-producing and the torque-producing current as shown in Fig. 2.15. Both current components are DC quantities in the field-oriented reference frame. Therefore, the measured stator current $\vec{i}_s^{\,\Diamond}$ and the resulting reference voltage vector $\vec{u}_s^{\,\star}$ must be rotated by

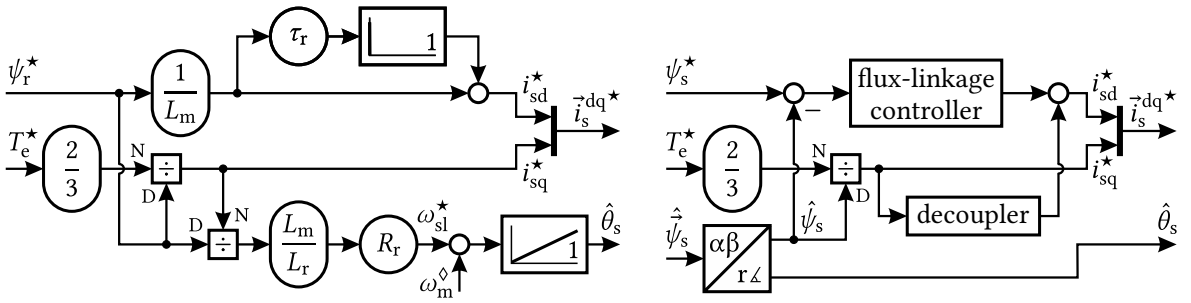

(a) indirect RFO (b) direct SFO

Fig. 2.16: Structure of the indirect RFO and direct SFO decoupling networks.

the field angle $\hat{\theta}_\mathrm{s}$. There are two major methods to obtain the stator current reference $\vec{i}_\mathrm{s}^{\,\mathrm{dq}\star}$ and the field-angle estimate $\hat{\theta}_\mathrm{s}$:

Indirect FOC is an open-loop solution where $i_\mathrm{sd}^\star$ and $i_\mathrm{sq}^\star$ are calculated from the IM current model. For RFO this is done by inverting (2.28). The field angle is obtained by solving the imaginary component of (2.27) for the slip angular frequency. With the help of the measured rotor angular frequency $\omega_\mathrm{m}^\Diamond$ the estimated field angle is defined by

$$\hat{\theta}_\mathrm{s} = \int \left(\omega_\mathrm{sl}^\star + \omega_\mathrm{m}^\Diamond\right) \mathrm{d}t \quad \text{with} \quad \omega_\mathrm{sl}^\star = \frac{L_\mathrm{m} i_\mathrm{sq}^\star}{\tau_\mathrm{r} \psi_\mathrm{r}^\star}. \tag{2.31}$$

The resulting signal-flow diagram of the decoupling network for indirect RFO is given in Fig. 2.16a. It includes a derivative in the flux-producing current reference, which compensates the first-order lag element. To limit the output of the derivative, a trajectory filter – e.g. a rate limiter – can be applied to the flux-linkage reference.

Direct FOC uses an estimate or measurement of the flux linkage as a closed-loop feedback. A controller is used to regulate the flux linkage with $i_\mathrm{sd}^\star$ as the manipulated variable. For SFO a decoupling term can be included to improve the dynamic performance as given in Fig. 2.16b. The field angle is directly taken from the feedback flux-linkage.

Table 2.2 gives a brief overview of the parameter dependencies of the basic FOC controllers. The open-loop nature of the indirect FOC makes it sensitive to parameter variations of the IM current model. For example magnetic saturation causes a significant flux-linkage error in indirect RFO and SFO [De 91]. Parameter-adaption schemes, such as (2.16), or improved decoupling equations, as proposed in [De 92], which take the rotor deep-bar effect into account, improve the torque control performance. However, according to Section 2.1.3.2, especially the rotor resistance is not certainly detectable and causes controller detuning and torque error.

The sensitivity of the direct FOC to parameter variations is directly dependent on the method used to determine the feedback flux linkage. Direct flux-linkage measurement

TABLE 2.2
Parameter Dependencies of Basic Field Oriented IM Controllers

	indirect FOC based on the IM current model	direct FOC with voltage-model observer
rotor field orientation (RFO)	The rotor flux linkage magnitude is highly dependent on magnetic saturation: $\psi_\mathrm{r} = L_\mathrm{r}(\psi_\mathrm{r}) \cdot \frac{1}{1+\tau_\mathrm{r} s} i_\mathrm{sd}$ and the flux angle is highly dependent on rotor temperature: $\measuredangle \vec{\psi}_\mathrm{r} = \int \left(R_\mathrm{r}(\vartheta_\mathrm{r}) \cdot \frac{L_\mathrm{m} i_\mathrm{sq}}{L_\mathrm{r} \psi_\mathrm{r}} + \omega_\mathrm{m} \right) \mathrm{d}t.$ *The controller tuning and the produced torque are very sensitive to temperature drift of the rotor resistance and magnetic saturation.*	The rotor flux linkage magnitude and angle are estimated using the stator voltage equation and are mainly a function of the stator resistance but additional inductance related terms exist: $\vec{\psi}_\mathrm{r} = \frac{L_\mathrm{r}}{L_\mathrm{m}} \left(\int \left(\vec{u}_\mathrm{s} - R_\mathrm{s}(\vartheta_\mathrm{s}) \cdot \vec{i}_\mathrm{s} \right) \mathrm{d}t - \overbrace{\sigma L_\mathrm{s} \vec{i}_\mathrm{s}}^{f(\psi_\mathrm{s})} \right).$ However, the observer becomes unstable at very low speed and has an offset integration problem. *The controller tuning and the produced torque are mainly sensitive to temperature drift of the stator resistance. A minor dependency on magnetic saturation is present.*
stator field orientation (SFO)	The stator flux linkage magnitude shows the same dependency as the indirect RFO, but includes an additional cross-coupling term: $\psi_\mathrm{s} = L_\mathrm{s}(\psi_\mathrm{s}) \cdot \frac{1+\sigma\tau_\mathrm{r} s}{1+\tau_\mathrm{r} s} i_\mathrm{sd} - \overbrace{L_\mathrm{s} \frac{\omega_\mathrm{sl} \sigma \tau_\mathrm{r}}{1+\tau_\mathrm{r} s} i_\mathrm{sq}}^{f(\psi_\mathrm{s}, \vartheta_\mathrm{r})}.$ The same applies to the stator flux angle: $\measuredangle \vec{\psi}_\mathrm{s} = \int \left(\frac{R_\mathrm{r}(\vartheta_\mathrm{r}) \cdot L_\mathrm{s} i_\mathrm{sq} + \sigma L_\mathrm{s} L_\mathrm{r} \frac{\mathrm{d}i_\mathrm{sq}}{\mathrm{d}t}}{L_\mathrm{r}(\psi_\mathrm{s} - \sigma L_\mathrm{s} i_\mathrm{sd})} + \omega_\mathrm{m} \right) \mathrm{d}t.$ *The controller tuning and the produced torque are very sensitive to temperature drift of the rotor resistance and magnetic saturation.*	The stator flux linkage magnitude and angle are determined by estimation using the stator voltage model and are only dependent on the stator resistance: $\vec{\psi}_\mathrm{s} = \int \left(\vec{u}_\mathrm{s} - R_\mathrm{s}(\vartheta_\mathrm{s}) \cdot \vec{i}_\mathrm{s} \right) \mathrm{d}t.$ However, the observer becomes unstable at very low speed and has an offset integration problem. *The produced torque is only sensitive to stator resistance temperature drift but requires additional measures at low speeds.*

involves considerable effort and is usually not applied to drive systems that are taken into consideration in this work. Instead, observers are used to determine the flux-linkage from the electrical terminal quantities of the IM. While a direct FOC with current-model-based observer would produce results similar to those of the indirect FOC, the parameter sensitivity can be significantly reduced by using a voltage-model observer [JLN94]. The direct SFO controller then only depends on the stator resistance [XDN88a] which – according to Section 2.1.3.2 – can be easily determined. This fact makes the direct SFO the controller of choice in this work. However, the voltage-model observer becomes unstable at very low speed since the induced stator-voltage magnitude decreases linearly with the stator frequency and the stator flux linkage. At standstill the flux linkage is not observable. Be-

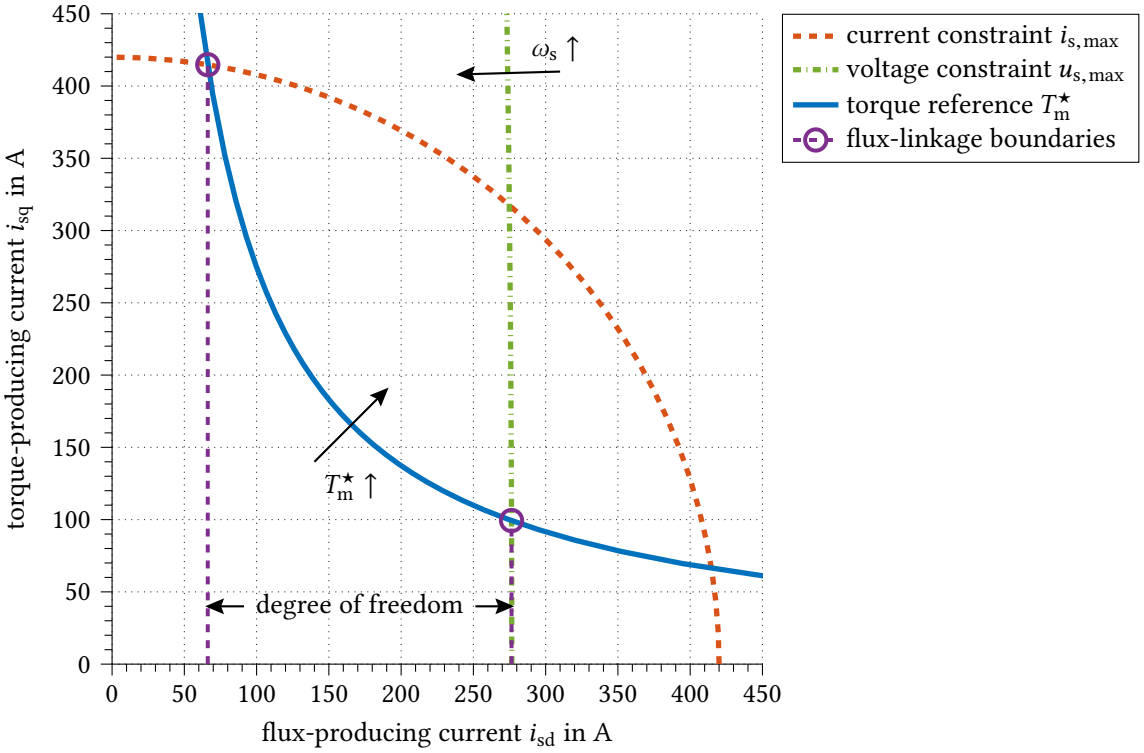

Fig. 2.17: Steady-state current locus diagram in RFO with current and voltage constraints for IM26kA at $f_s = 60\,\text{Hz}$ stator frequency and $T_m^\star = 50\,\text{Nm}$ torque reference.

sides this signal-to-noise ratio problem at low speed, the observer also has a sensor-offset integration problem, which requires additional measures. Approaches to compensate these disadvantages and alternative stator flux-linkage observers will be introduced in Chapter 3, followed by a detailed parameter sensitivity and torque accuracy analysis in Chapter 4.

2.2.1 Efficiency Optimization – Field Weakening at Light Loads

The torque reference $T_m^\star$ is usually defined by the user or an outer control loop, according to the application – for example adaptive cruise control (ACC). The flux-linkage magnitude, however, offers a control degree of freedom. It can be freely chosen within the boundaries defined by the torque reference and the machine or inverter operating constraints. The available operating points can be illustrated by the steady-state current-locus diagram in RFO, as given in Fig. 2.17. With (2.28) substituted in Equation (2.25), the torque reference can be represented by a hyperbola in the current diagram. Any operating point on this hyperbola produces the requested torque. However, the operating range is limited by the maximum current $i_{s,max}$ that can be delivered by the inverter and the maximum inverter voltage $u_{s,max}$ defined by the DC-link voltage. The current constraint $i_{s,max}$ is a circle in the current diagram and the latter boundary is an ellipse that shrinks with increasing stator frequency or decreasing DC-link voltage.

In efficiency-optimized IM drives, this degree of freedom – the choice of the flux-linkage magnitude – is utilized to choose the operating point with minimum system losses. Methods to achieve this can be divided into three general categories [Abr02]:

Simple state control is an approach where a single quantity is controlled in a simple way, for example by keeping the slip frequency or the power factor constant. The method is usually not applied to FOC. It offers poor dynamic performance and does not lead to the proper efficiency-optimal solution [VL03b].

Search control is a closed-loop method which continuously adjusts the flux-linkage to track the efficiency-optimal point of operation. For example in [KNL85; KNL87] the measured electrical power is used as a feedback which is minimized by the algorithm. It requires accurate torque control to keep the mechanical power constant. This is not trivial and makes the algorithm sensitive to IM parameter variations. Fast convergence can be obtained using fuzzy logic [SBC95] or artificial neuronal networks [CJR97].

Loss-model-based control utilizes a loss model of the IM or of the overall drive system, as the one described in [Sou+92], to find the optimal flux-linkage magnitude. Optimization can be performed online using an analytical model [SK11; RT97], or based on a lookup table [FO93] which is calculated offline. The latter allows efficiency optimization on low-cost microcontrollers using a high-complexity loss model which takes nonlinear effects into account [SKD13].

A hybrid solution which combines the advantages of search control and loss-model-based methods has been proposed in [VL03b]. However, for this work an offline efficiency-optimization approach based on that in [SKD13] is sufficient. Using the extended nonlinear IM model given in Section 2.1.3, a lookup table for the optimal stator flux-linkage can be calculated as a function of the stator angular frequency and the torque reference. The problem is solved numerically to take into account nonlinear effects such as rotor deep-bar effect, iron losses and magnetic saturation.

In the first step, the stator inductance is determined using Equation (2.16). Then, the slip-frequency dependent rotor impedance is calculated based on the rotor deep-bar model introduced in Section 2.1.3.4. Therefore, an expression for the slip angular frequency must be found. With the SFO current model (2.29) separated to real and imaginary parts, the two steady-state equations

$$\frac{\psi_\mathrm{s}}{\tau_\mathrm{r}} \overset{\text{steady state}}{=} \frac{L_\mathrm{s}}{\tau_\mathrm{r}} i_\mathrm{sd} + \omega_\mathrm{sl} \sigma L_\mathrm{s} i_\mathrm{sq} \tag{2.32}$$

$$\text{and} \quad \omega_\mathrm{sl} \psi_\mathrm{s} \overset{\text{steady state}}{=} \frac{L_\mathrm{s}}{\tau_\mathrm{r}} i_\mathrm{sq} + \omega_\mathrm{sl} \sigma L_\mathrm{s} i_\mathrm{sd} \tag{2.33}$$

are obtained. Eliminating i_sd by inserting (2.33) in (2.32) and substitution of i_sq with (2.25)

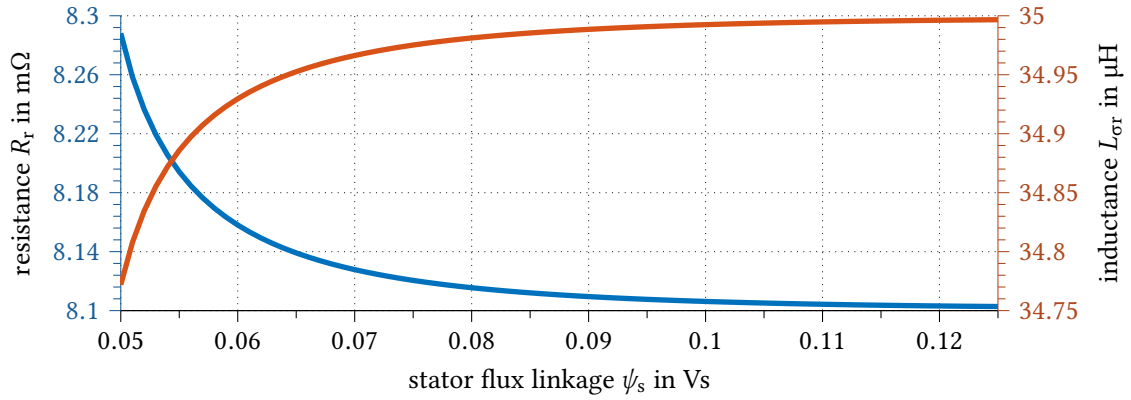

Fig. 2.18: Equivalent slip-frequency-dependent rotor parameters due to rotor deep-bar effect for IM26kA at $f_s = 60\,\text{Hz}$ stator frequency and $T_m^\star = 50\,\text{Nm}$ torque reference as a function of the stator flux-linkage.

leads to the quadratic expression

$$0 \overset{\text{steady state}}{=} \omega_{sl}^2 - \omega_{sl} \underbrace{\frac{\psi_s^2}{\frac{2}{3} T_e \tau_r L_s} \cdot \frac{1-\sigma}{\sigma^2}}_{-p} + \underbrace{\frac{1}{\sigma^2 \tau_r^2}}_{q}. \tag{2.34}$$

The slip angular frequency can now be found using the 'pq'-formula as

$$\omega_{sl} = -\frac{p}{2} - \sqrt{\left(\frac{p}{2}\right)^2 - q}. \tag{2.35}$$

The resulting equivalent rotor quantities can now be calculated based on the rotor deep-bar model with

$$R_r^{\text{new}} \overset{\text{steady state}}{=} R_r + \frac{\omega_{sl}^2 L_{\sigma r1}^2 R_{p1}}{\omega_{sl}^2 L_{\sigma r1}^2 + R_{p1}^2} \tag{2.36}$$

$$\text{and} \quad L_{\sigma r}^{\text{new}} \overset{\text{steady state}}{=} L_{\sigma r0} + \frac{L_{\sigma r1} R_{p1}^2}{\omega_{sl}^2 L_{\sigma r1}^2 + R_{p1}^2}. \tag{2.37}$$

Since ω_{sl} has been previously calculated without considering the rotor deep-bar effect, ω_{sl}, R_r^{new} and $L_{\sigma r}^{\text{new}}$ are inaccurate. It can be proven, that an iterative process repeating (2.34) to (2.37) with updated rotor parameters converges to the correct solution. As termination criterion, $\Delta\omega_{sl} < 10^{-6}$ is used, which is typically fulfilled after less than 10 iterations.

Taking into account the rotor deep-bar effect is recommendable as the rotor parameters vary significantly with the stator flux-linkage magnitude. In Fig. 2.18, R_r and $L_{\sigma r}$ have been calculated for the operating point at $f_s = 60\,\text{Hz}$ and $T_m^\star = 50\,\text{Nm}$. The rotor resistance increases by up to 20 %. Consequently, the rotor deep-bar effect causes increased rotor losses in addition to the increased rotor current at low stator flux-linkage magnitude.

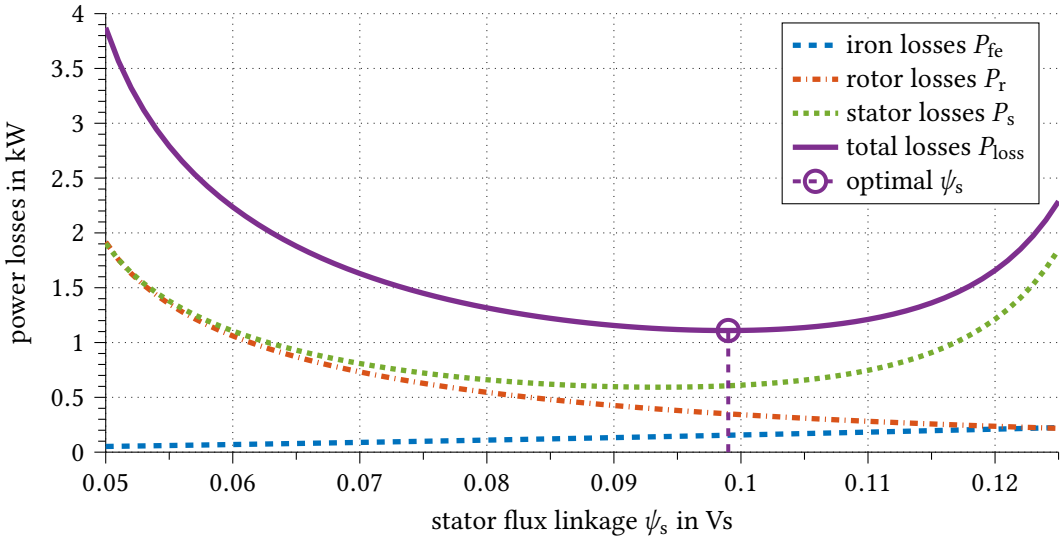

Fig. 2.19: Electromagnetic losses as a function of the stator flux-linkage. Calculated for IM26kA at $f_s = 60\,\text{Hz}$ stator frequency and $T_m^\star = 50\,\text{Nm}$ torque reference.

The flux-linkage dependent steady-state rotor losses P_r, iron losses P_{fe} and stator losses P_s are found using

$$P_r = R_r|\vec{i}_r|^2 \quad \text{with} \quad \vec{i}_r \overset{\text{steady state}}{=} \frac{L_m}{L_s} \cdot \frac{j\omega_{sl}\vec{\psi}_s}{R_r + j\omega_{sl}\sigma L_r}, \tag{2.38}$$

$$P_{fe} = R_{fe}|\vec{i}_{fe}|^2 \quad \text{with (2.21)} \tag{2.39}$$

$$\text{and} \quad P_s = R_s|\vec{i}_s|^2 \quad \text{with} \quad \vec{i}_s \overset{\text{steady state}}{=} \frac{L_m}{L_s}\left(\vec{i}_{fe} + \vec{i}_r + \frac{\vec{\psi}_s}{L_m}\right). \tag{2.40}$$

The losses have been calculated for IM26kA at $f_s = 60\,\text{Hz}$ and $T_m^\star = 50\,\text{Nm}$ and are given in Fig. 2.19. As expected, the iron losses increase with increasing stator flux-linkage, whereas the rotor losses decrease due to the reduced slip and rotor current. The ohmic stator losses and the total losses $P_{loss} = P_s + P_r + P_{fe}$ are convex functions.

The minimum of P_{loss} defines the efficiency-optimal stator flux linkage ψ_s^{opt} which can be found for each operating point using numerical optimization. The resulting stator flux-linkage lookup table is given in Fig. 2.20. The efficiency optimization requires continuous adaption of the stator flux linkage during changes of the operating point. Due to the rotor time constant, this causes limitations in the dynamic performance of the drive system – especially if a torque step from zero to rated torque is required. The area of the orthogonal contour lines indicate the field-weakening region where the degree of freedom is lost and the flux-linkage is defined by the maximum inverter voltage. A comparison with Fig. 2.11b proves, that the iron-loss model deviation described in Section 2.1.3.3 does not affect the efficiency optimization because the error only occurs in the field-weakening region where no optimization is possible.

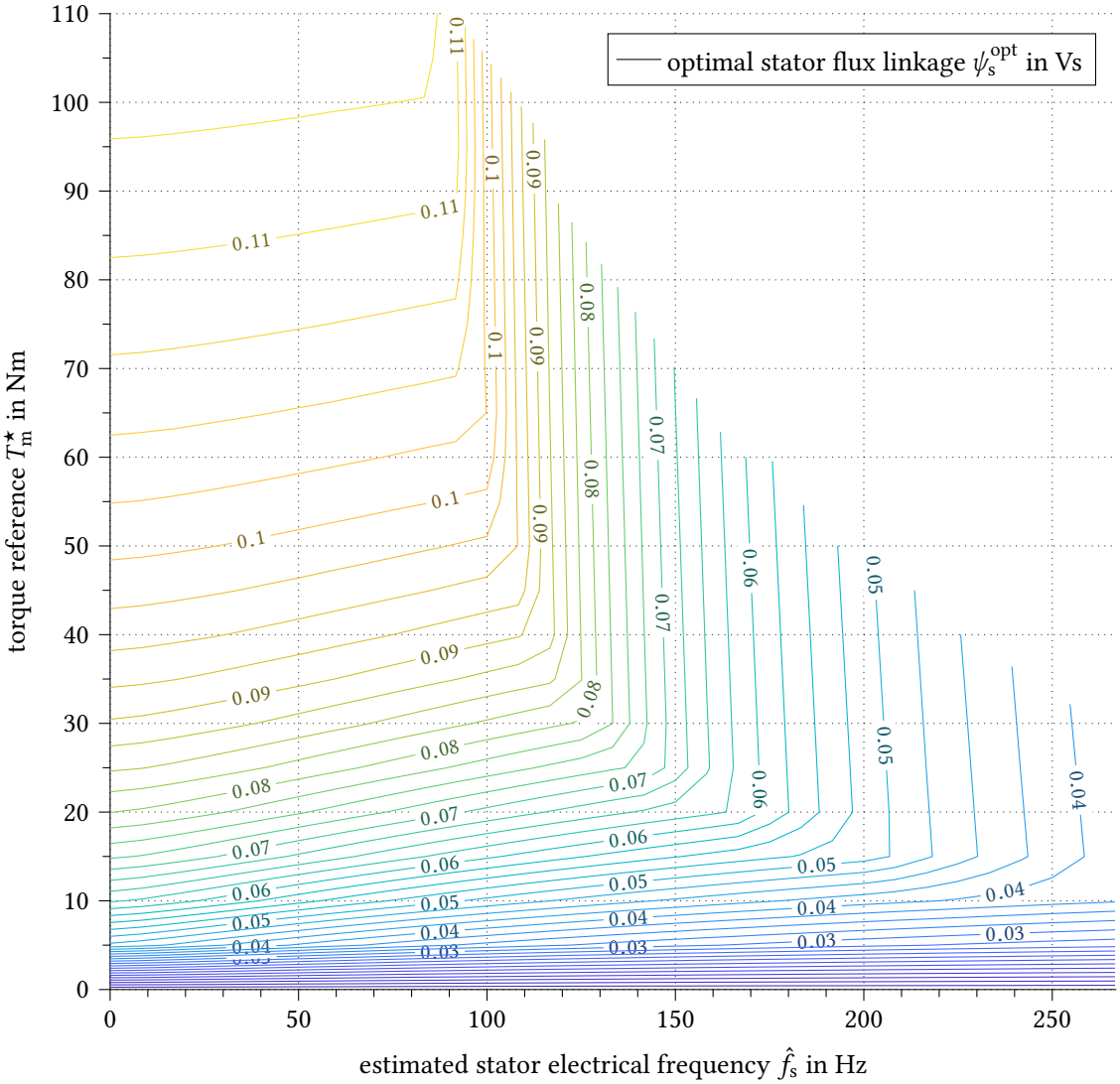

Fig. 2.20: Efficiency optimal stator flux linkage as a function of stator frequency and torque reference. Lookup table calculated offline for IM26kA using the extended nonlinear IM model.

2.2.2 The Direct Stator Field-Oriented Torque Controller

The structure of the SFO controller used in this work is given in Fig. 2.21a. The current PI-controller gains have been chosen to obtain a bandwidth of 500 Hz. Regulation of the flux-linkage is achieved using a PI controller with a bandwidth of 10 Hz. The decoupling of the stator flux linkage requires a derivative of the torque-producing current to obtain the slip frequency, according to the model given in Fig. 2.21b. To avoid problematic behavior due to differentiation of measured quantities, the slip frequency is calculated using an estimate of the stator frequency $\hat{\omega}_s$ according to (2.24), and the measured rotor frequency $\omega_m^\Diamond$. Another advantage of this approach is the reduced parameter sensitivity of the decoupler.

To compensate the torque error caused by the iron-losses, the controller is extended by

the steady-state iron-loss model introduced in Section 2.1.3.3. According to (2.21), in SFO, the equivalent iron-loss current $\vec{i}_{\mathrm{fe}}$ has only a quadrature component and can be added to the torque-producing current. The resulting controller structure is given in Fig. 2.22. Since the stator current is a measured and regulated quantity, the SFO torque controller produces zero torque error if the iron loss model and the estimated flux linkage are correct.

2.2.3 Operational Constraints and the Field-Weakening Region

In the field-weakening region the maximum stator voltage constraint is satisfied by limiting the stator flux-linkage magnitude. Neglecting the stator resistance voltage drop the maximum stator flux linkage is given by

$$\psi_{\mathrm{s}}^{\star} \leq \frac{u_{\mathrm{s,max}}}{\hat{\omega}_{\mathrm{s}}} \quad \text{with} \quad u_{\mathrm{s,max}} = \frac{u_{\mathrm{dc}}}{\sqrt{3}}. \tag{2.41}$$

To ensure safe operation under this constraint an additional voltage margin should be reserved to take account for the stator resistance voltage drop and the inverter voltage distortion. The latter is caused by the semiconductor voltage drop and the dead-time effect, as described in Section 2.3.

During operation of the drive, the maximum current limit with $i_{\mathrm{s}} \leq i_{\mathrm{s,max}}$ must be satisfied at all times. With priority given to the flux-producing current, this is achieved by limiting the torque-producing current according to

$$i_{\mathrm{sq}}^{\star} \leq \sqrt{i_{\mathrm{s,max}}^2 - i_{\mathrm{sd}}^{\star 2}}. \tag{2.42}$$

In SFO another constraint is defined by the pull-out torque [XDN88a; XDN88b]. The slip frequency in (2.34) only has a real solution if

$$T_{\mathrm{e}} \leq \frac{3}{4}\hat{\psi}_{\mathrm{s}}^2 \frac{1-\sigma}{\sigma L_{\mathrm{s}}} \quad \text{with} \quad |\omega_{\mathrm{sl}}| \leq \frac{1}{\sigma \tau_{\mathrm{r}}} \tag{2.43}$$

being the stability limit for the SFO controller. Substituting (2.25) leads to the second constraint for the torque-producing current, which is proportional to the present stator flux-linkage magnitude with

$$i_{\mathrm{sq}}^{\star} \leq \frac{1}{2}\hat{\psi}_{\mathrm{s}} \frac{1-\sigma}{\sigma L_{\mathrm{s}}}. \tag{2.44}$$

By applying both current constraints to the torque-producing current, field-weakening is fully implemented. The constraint (2.42) limits the torque within the constant power region, whereas (2.44) is equivalent to maximum torque per flux linkage (MTPF) conditions. Fig. 2.23 shows the resulting SFO controller structure with implemented constraints handling and the calculation of the flux-linkage reference. $\psi_{\mathrm{s}}^{\star}$ is obtained from the efficiency optimization lookup table in Fig. 2.20 as a function of the estimated stator frequency $\hat{\omega}_{\mathrm{s}}$ and

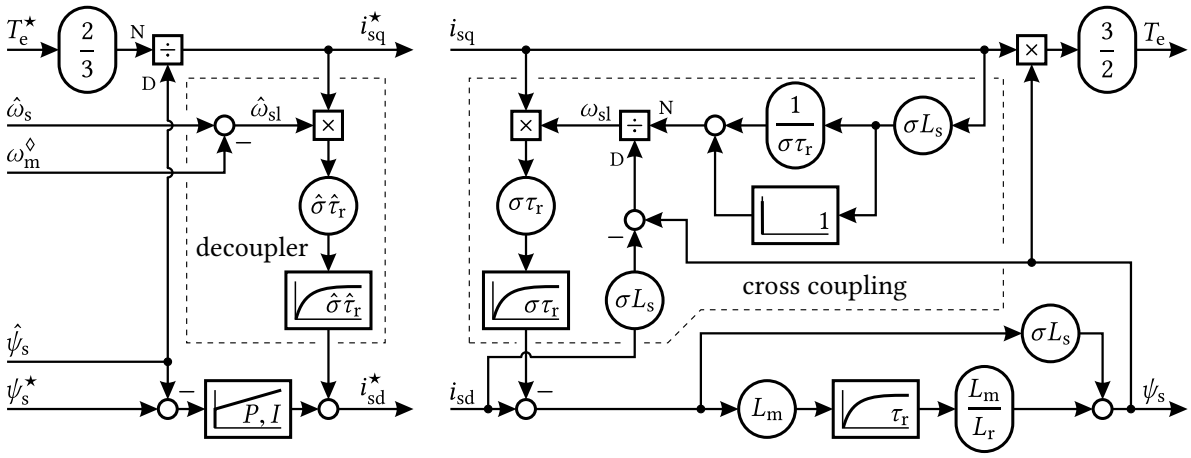

(a) direct SFO controller (b) IM model in stator field orientation

Fig. 2.21: Implementation of the direct SFO controller with decoupling using the estimated stator frequency.

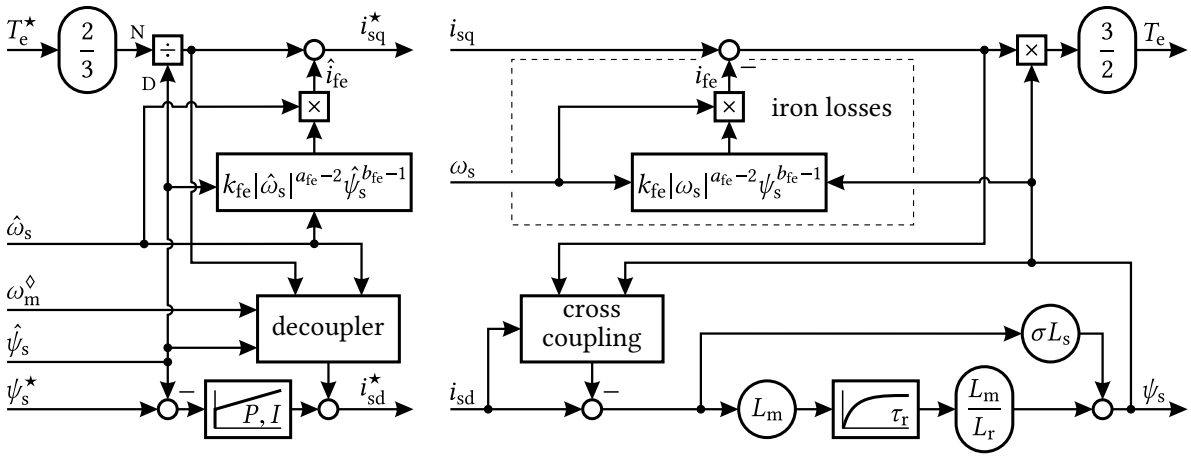

(a) FOC with iron-loss compensation (b) IM model in stator field orientation with iron losses

Fig. 2.22: Signal-flow diagram of the steady-state iron-loss compensation implementation within the direct SFO controller.

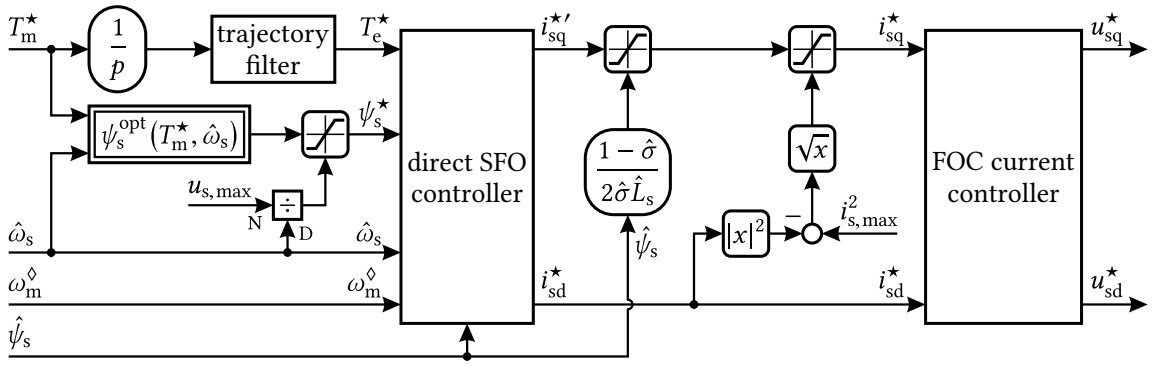

Fig. 2.23: Constraints handling of the direct SFO controller with input trajectory filter.

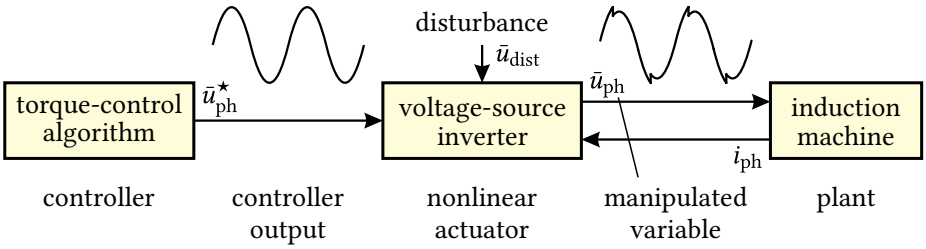

Fig. 2.24: The inverter as nonlinear actuator within the drive control loop according to Fig. 1.6 with disturbance caused by dead time and semiconductor voltage drop. Feedback not shown.

the reference torque $T^{\star}_{\mathrm{m}}$. The limited dynamics of the flux linkage must be considered when calculating $i^{\star}_{\mathrm{sq}}$ to obtain sufficient dynamic current sharing between $i^{\star}_{\mathrm{sd}}$ and $i^{\star}_{\mathrm{sq}}$. The current sharing can be influenced by an input trajectory filter applied to the torque reference. For IM26kA, a rate limiter is used, which only limits the rising torque magnitude to $2\,\mathrm{Nm\,ms^{-1}}$. A deeper insight and a novel approach for further optimization of the dynamic response is given in Chapter 6.

2.3 Output Voltage Distortion of Voltage-Source Inverters

In the control loop of the drive system, the VSI acts as an actuator that applies the reference phase voltage $\bar{u}^{\star}_{\mathrm{ph}}$ – which is determined by the controller – to the electrical machine, as illustrated in Fig. 2.24. The phase output u_{ph} of the VSI is a rectangular-shaped voltage wave generated by pulse-width modulation (PWM). However, in terms of the control algorithm, the major quantities of interest are the PWM-period average values $\bar{u}_{\mathrm{ph}}$ and $\bar{u}^{\star}_{\mathrm{ph}}$ which are denoted by the 'bar'-diacritic. Due to the inverter dead-time that prevents the system from a half-bridge short circuit and the voltage drop across the semiconductor, the VSI introduces a nonlinear voltage disturbance $\bar{u}_{\mathrm{dist}}$ which degrades the control performance, introduces a torque ripple, and can reduce the torque accuracy of the drive system.

In the following, a model of the inverter half-bridge is derived, that is used as feed-forward to linearize the actuator within the control loop of the drive system. The inverter used in this work is based on MOSFET switches. Consequently, a detailed MOSFET model is derived, which takes into account parasitic capacitances to obtain the resulting distortion voltage as a function of the phase current for each half bridge, individually.

2.3.1 Dead Time and Inverter Voltage-Drop Model

In order to derive the model for the inverter half-bridges, the MOSFET switch and its structure is analyzed in detail. Fig. 2.25a shows the cross section of a common power MOSFET. The doped silicon chip is covered by the drain metalization at the bottom surface and by the source metalization at the top surface, which also covers the gate. This layered structure introduces the parasitic capacitances C_{ds} between drain and source, C_{gs}

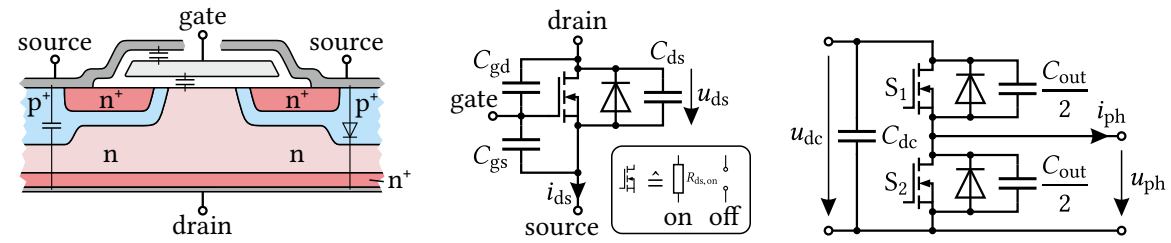

(a) cross section of a power MOSFET (b) MOSFET model (c) inverter half-bridge model

Fig. 2.25: Parasitic capacitances of a power metal–oxide–semiconductor field-effect transistor (MOSFET) and simplified inverter half-bridge model with parasitic drain-source capacitance.

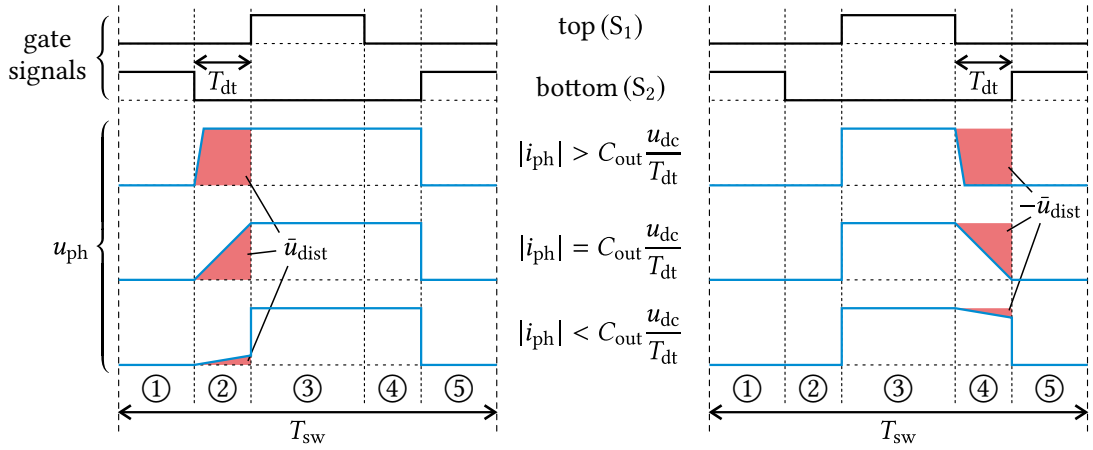

(a) $i_{ph} < 0$ (b) $i_{ph} > 0$

Fig. 2.26: Simplified waveforms of the inverter half bridge output voltage with dead time and parasitic capacitor effect. $R_{ds,on}$ and body diode voltage drop are neglected.

from gate to source and C_{gd} from gate to drain. Furthermore, an inherent body diode is formed between source and drain. This leads to the equivalent-circuit shown in Fig. 2.25b. The switch can be modeled as a resistance $R_{ds,on}$ for the 'on'-state and as open terminals for the 'off'-state, respectively. Each inverter phase leg consists of two MOSFETs which are connected in series to form an inverter half bridge, as depicted in Fig. 2.25c. The equivalent drain–source capacitance measurable across the MOSFET is a combination of C_{ds}, C_{gs} and C_{gd}, and is defined as $C_{out}/2$. The total half-bridge output capacitance considered in the following is then equal to C_{out}.

To derive the voltage distortion caused by the dead time, the switches and diodes are assumed to be ideal with $R_{ds,on} = 0$ and zero diode forward voltage. In the following, the PWM switching pattern of a single half bridge is analyzed. In Fig. 2.26a ①, the phase current is negative, the top switch S_1 is open, and the bottom switch S_2 is closed. Consequently, the phase voltage u_{ph} is zero. During the dead time T_{dt} ②, both switches are opened and the phase voltage is mainly defined by the phase current i_{ph} and the output capacitance C_{out}. Due to the relatively high IM inductance, i_{ph} can be considered to be constant during the dead time. As illustrated in Fig. 2.26, C_{out} must be recharged

TABLE 2.3
MOSFET Voltage Drop Datasheet Values

Values @ 25 °C	Inverter 1	Inverter 2
MOSFET type	Semikron SKAI 120V	2× IRFP4668 (parallel)
'on'-state resistance $R_{ds,on}$	2.4 mΩ	4 mΩ
MOSFET voltage drop	0.58 V @ 240 A	0.32 V @ 81 A
body-diode voltage drop	0.88 V @ 240 A	1.3 V @ 81 A
maximum system phase current	410 A	21 A

before the phase current commutates to the free-wheeling diode of the top-switch. If the current magnitude $|i_{ph}|$ exceeds $C_{out}u_{dc}/T_{dt}$, the commutation process is completed before the dead time is over and before the top switch S_1 is closed. For low current magnitudes $|i_{ph}| < C_{out}u_{dc}/T_{dt}$, C_{out} is not fully recharged before S_1 is closed. Then, the phase voltage nearly instantly changes to the DC-link voltage u_{dc} after the dead time. During ③, the top switch S_1 is closed and the phase voltage is forced to u_{dc}. At the falling edge of the phase voltage ④, S_1 is opened again and the current commutates to the diode of the top-switch. The phase voltage remains equal to u_{dc} for the entire dead time. In step ⑤, the bottom switch is closed and C_{out} is recharged instantaneously. The conditions are identical to ①. If the phase current is positive (Fig. 2.26b), the phase voltage remains zero during ②, and the recharge process only occurs at the falling-edge ④.

The dead-time related PWM-period average value of the distortion voltage $\bar{u}_{dist}$ is equal to the red-shaded area highlighted in Fig. 2.26. It is positive for negative phase current and negative for positive phase current.

The semiconductor voltage drop is superimposed on the dead-time voltage distortion. It depends on the current magnitude, the current direction, and the switching state of the conducting device. Fig. 2.27 shows the measured voltage drop u_{ds} across a single power MOSFET of the type Infineon IRFP4668 which is used in Inverter 2. In regions ①, ③ and ⑤, the conducting switch is always in the 'on'-state. If the drain–source current i_{ds} is positive, the MOSFET behaves like a resistor $R_{ds,on}$ with a positive temperature coefficient and can be modeled analogously to (2.17). In negative current direction an alternative current path through the body diode exists that becomes relevant once the voltage drop across $R_{ds,on}$ exceeds the diode voltage drop. During the dead time in regions ② and ④, the body diode conducts after the recharging process of C_{out} is completed.

The behavior of the inverter half bridge can efficiently be modeled by the signal-flow diagram developed in Fig. 2.28. It has been implemented in MATLAB/Simulink and is used for dynamic simulations in this work. The dead time is dependent on the turn-on and turn-off delays of the drivers, and the switches and have been parameterized by experiments at a high positive and negative current magnitude. C_{out} can be determined by manipulating i_{ph} until the recharging process occupies the entire dead time according to the case $|i_{ph}| = C_{out}\dfrac{u_{dc}}{T_{dt}}$ in Fig. 2.26, where C_{out} is uniquely defined.

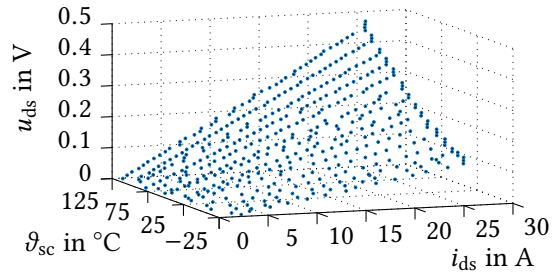

(a) 'on'-state forward voltage-drop measurement

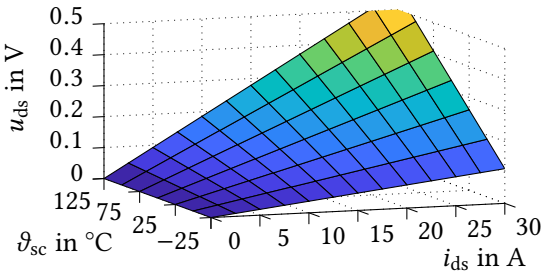

(b) 'on'-state forward voltage-drop fit

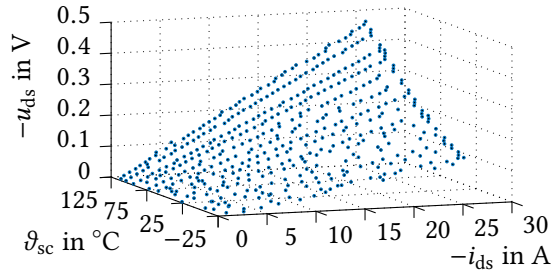

(c) 'on'-state reverse voltage-drop measurement

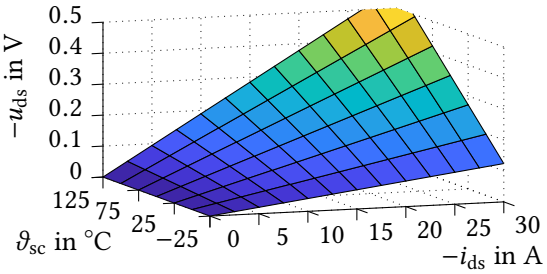

(d) 'on'-state reverse voltage-drop fit

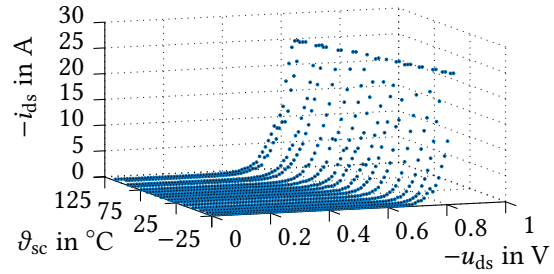

(e) 'off'-state body diode voltage-drop measurement

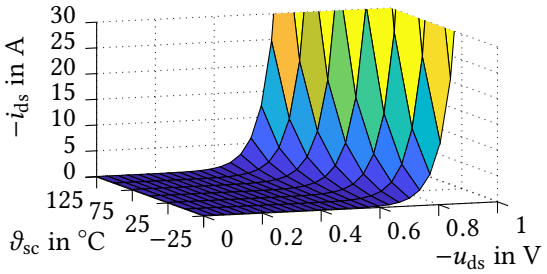

(f) 'off'-state body diode voltage-drop fit

Fig. 2.27: Power MOSFET and body diode voltage drop as a function of the current i_{ds} and the semiconductor temperature ϑ_{sc}. Measured with a single device, type: Infineon IRFP4668 in TO-247.

2.3.2 The Inverter Voltage Distortion Curve

To linearize the VSI transfer function, a dead-time compensation scheme is developed in the following. Therefore, an expression for the PWM-period average distortion voltage $\bar{u}_{dist}$ as a function of the phase current i_{ph} must be found.

As long as the voltage drop remains lower than the forward voltage of the body diode in reverse current direction, the diode is blocking and the 'on'-state semiconductor voltage drop is symmetrical. According to the datasheet values given in Table 2.3, this is the case for a large current range [Int08; Sem13]. For Inverter 2, it applies to the entire system operating range – even at high semiconductor temperatures ϑ_{sc}, as illustrated in Fig. 2.29. Because of the positive temperature coefficient of $R_{ds,on}$ and the negative temperature coefficient of the diode voltage drop, the margin between both voltages increases at lower temperatures. Thus, the body diode only conducts during the dead time. The measurements in Section 5.4

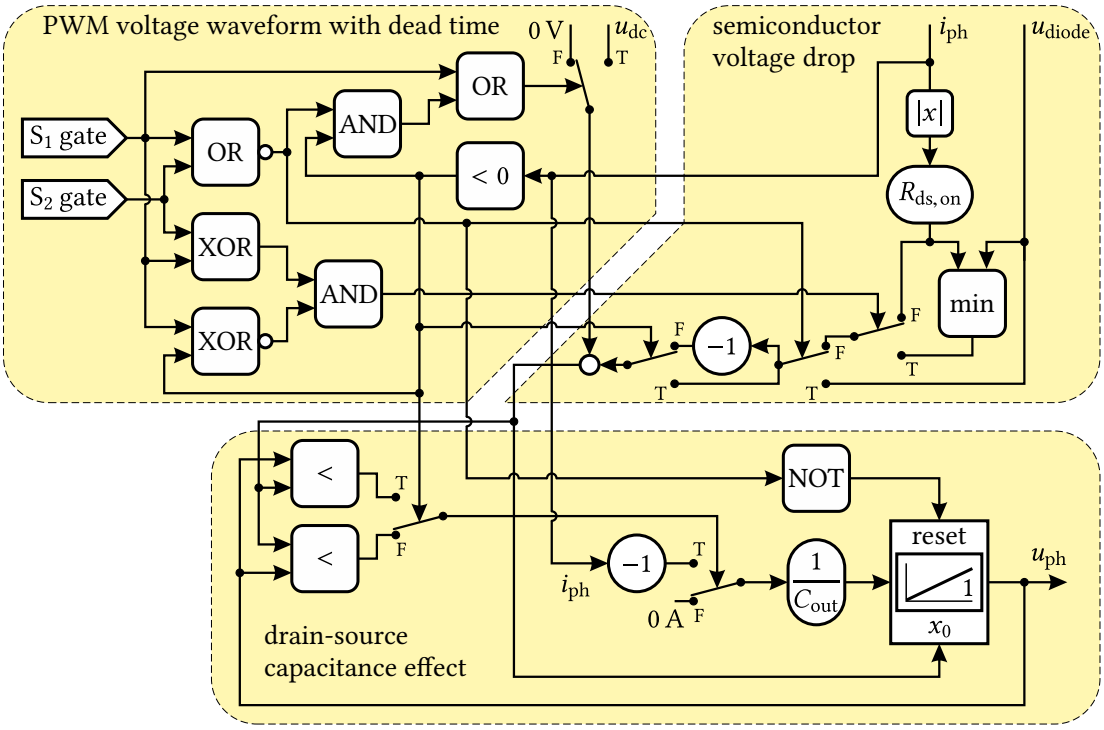

Fig. 2.28: Signal-flow diagram of the inverter half-bridge model with semiconductor voltage drop and dead-time effect implemented in MATLAB/SIMULINK.

show, that this also applies to Inverter 1.

Since the dead time T_{dt} is small compared to the PWM period-time T_{sw}, and since the body diode voltage drop is small compared to the dead-time related voltage distortion, the diode can be neglected in $\bar{u}_{dist}$. Instead, the voltage drop is simplified by assuming resistive behavior at all times. $\bar{u}_{dist}$ is then derived according to the consideration in Fig. 2.26 as

$$\bar{u}_{dist} \approx \begin{cases} -i_{ph} \cdot \dfrac{T_{dt}^2}{2C_{out}T_{sw}} - R_{ds,on} i_{ph}, & \text{if } |i_{ph}| < C_{out}\dfrac{u_{dc}}{T_{dt}}, \\ u_{dc} \cdot \left(\dfrac{C_{out}u_{dc}}{2i_{ph}T_{sw}} - \operatorname{sgn}(i_{ph})\dfrac{T_{dt}}{T_{sw}} \right) - R_{ds,on} i_{ph}, & \text{otherwise.} \end{cases} \tag{2.45}$$

An analog modeling approach for insulated-gate bipolar transistor (IGBT) inverter systems can be found in [BCP14].

The distortion voltage $\bar{u}_{dist}$ has been plotted in Fig. 2.30. At high current magnitude it is nearly linear with the gradient $-R_{ds,on}$. In the region of the current zero crossing, the gradient is dominated by the parasitic drain–source capacitance. Due to the recharge process of C_{out}, the distortion voltage changes continuously with a finite slope. This is advantageous if (2.45) is used for open-loop dead-time compensation. Taking C_{out} into account not only increases the accuracy of the model, it also makes the algorithm less sensitive to current-sensor noise in the region of the current zero crossing.

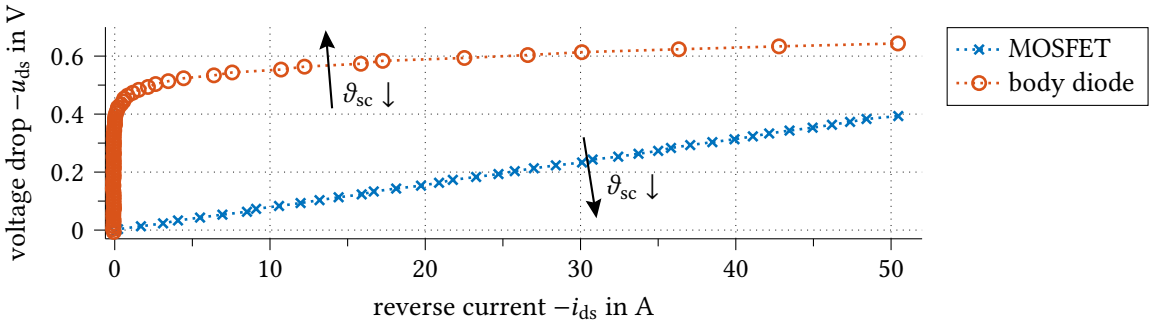

Fig. 2.29: Measured reverse voltage drop of two parallel 'on'-state MOSFETs and the body diode at $\vartheta_{sc} = 95\,°C$, type IRFP4668. The body diode is only conducting during the dead time.

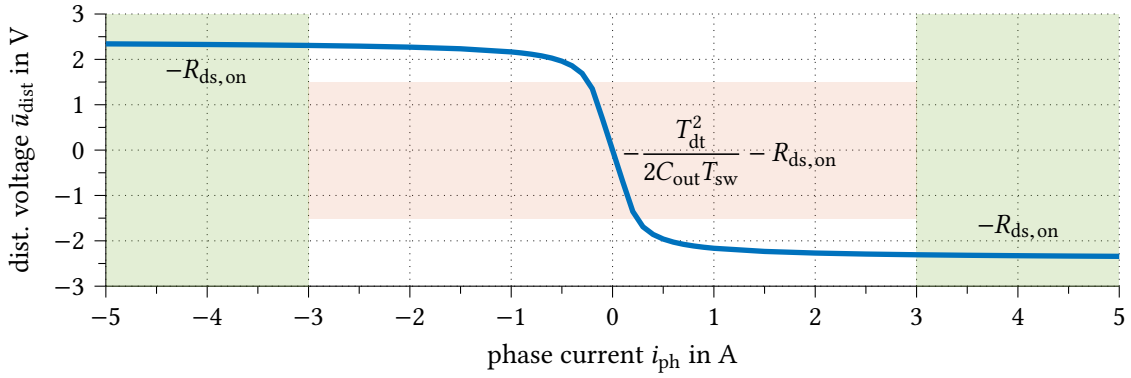

Fig. 2.30: Distortion voltage $\bar{u}_{dist}$ as a function of the phase current i_{ph} with three linear regions.

2.4 Summary

In this chapter, the primary components of variable-speed IM drive systems have been introduced. Mathematical models of the components were derived, focusing on their contribution to FOC detuning and torque deviation.

Each parameter of the fundamental IM model was analyzed with respect to its dependency on nonlinear external influences and its accessibility for parameterization and adaption during operation. Generally, none of the IM model parameters remains constant during operation. However, some of them are sufficiently determinable by measurements and can be adapted online, such as the stator resistance or the stator inductance. The others can only be obtained with rather high uncertainty, which applies to the rotor resistance and leakage inductances. Furthermore, additional effects exist, that are not holistically represented by the model, such as cross saturation or slip-related iron losses.

Table 2.4 gives a summarized overview of the IM model parameter uncertainties described in this chapter. Each of them affects the torque accuracy of the IM drive and must be considered when designing a precise torque control algorithm. Preferably, the controller should be insensitive to uncertain model parameters. It has been pointed out, that the direct SFO controller with voltage-model flux-linkage observer satisfies this requirement,

TABLE 2.4
Overview of the IM Model Parameter Uncertainties

parameter	uncertainty	description
R_s	initially low, high during operation	The stator resistance can accurately be measured at standstill. However, thermal drift causes up to 50 % parameter deviation during operation. Precise parameter adaption can be achieved using signal injection [MVZ15].
R_fe	low at base speed	The Steinmetz equation model is a good representation of the iron losses in the base speed region. During field weakening at high slip frequency, additional losses are introduced by slot harmonics which are not represented by the fundamental frequency model [vPSH17].
L_m	medium	The magnetic saturation of the mutual flux linkage can accurately be determined during no-load tests. However, the model does not consider cross saturation caused by the torque-producing current component through the leakage inductances. It cannot be measured by no-load tests.
$L_{\sigma\mathrm{s}}$ and $L_{\sigma\mathrm{r}0}$	very high	The leakage inductances are measured during locked rotor tests at low flux magnitude. They cannot accurately be separated and are subject to cross saturation.
$L_{\sigma\mathrm{r}1}$ and R_p1	low	Rotor deep-bar effect becomes notable only during transients and in the field-weakening region. At base speed, it can be neglected for the steady-state analysis, otherwise it is considered as a deviation of the rotor resistance. The influence on the rotor leakage inductance is negligible.
R_r	very high	Detection of the rotor resistance is associated with high uncertainty since no direct measurement of this parameter is possible. Furthermore, thermal drift causes a deviation of up to 50 %. Adaption schemes are usually sensitive to other parameter variations.

since the produced torque is only dependent on the stator resistance. However, the voltage model observer is based on open-loop integration of the back electromotive force (EMF), which comes along with a low signal-to-noise ratio at standstill and carries the risk of open integration of sensor offsets. Both causes instability and make the observer not applicable in non-ideal conditions. Besides the IM parameters, the torque accuracy also depends on the measured current and voltage feedback signals. Measured quantities are subject to offset and gain errors and can be distorted by nonlinearity or hysteresis.

Another common source of torque deviation is the voltage distortion caused by the nonlinear VSI transfer function. A precise physical model of the VSI was derived and implemented in MATLAB/Simulink. It includes the resistive voltage drop of the MOSFET switches and considers the recharge process of the parasitic drain–source capacitance during the dead time. The VSI transfer function, derived in this chapter, allows precise open-loop feed-forward compensation of the nonlinear inverter distortion.

Improved voltage-model-based closed-loop observers without zero-speed instability or offset-integration problem are introduced in Chapter 3. Their sensitivity to IM parameter deviation and sensor feedback distortion is evaluated using analytical expressions for the FOC detuning and torque deviation, derived from the fundamental IM equations.

3 Stator Flux-Linkage Observers

The stator flux-linkage observer is the most critical component of the direct SFO controlled IM drive in terms of parameter dependency of the produced torque and the sensitivity to sensor errors. In this chapter, the basic open-loop and three promising closed-loop observers are discussed. Based on the observer transfer functions, expressions for the relative steady-state stator flux-linkage deviation

$$\underline{F}(\mathrm{j}\omega_\mathrm{s}) = \frac{\hat{\underline{\psi}}_\mathrm{s}}{\underline{\psi}_\mathrm{s}}, \tag{3.1}$$

caused by given parameter estimation errors, are derived. Therefore, the analytical approach used in [JL94] is applied to another group of observers and is extended to take into account the stator iron losses. Furthermore, corresponding expressions are derived which allow to also apply this method to balanced sensor-gain errors. The resulting frequency-response functions are the basis for the analysis of the steady-state torque error caused by parameter deviation and balanced sensor-gain errors in Chapter 4.

3.1 Open-Loop Observers

The two fundamental open-loop stator flux-linkage observers can be derived directly from the current and the voltage model of the IM and are the basis for the development of closed-loop observers in the following.

3.1.1 Current Model

The transfer function of the open-loop current-model observer can be found by transforming (2.29) to the stator-aligned reference frame and then to the frequency domain with

$$\frac{\mathrm{d}\hat{\vec{\psi}}_\mathrm{s}}{\mathrm{d}t} + \left(\frac{1}{\hat{\tau}_\mathrm{r}} - \mathrm{j}\omega_\mathrm{m}\right)\hat{\vec{\psi}}_\mathrm{s} = \hat{\sigma}\hat{L}_\mathrm{s}\left(\frac{\mathrm{d}\vec{i}_\mathrm{s}^{\,\lozenge}}{\mathrm{d}t} + \left(\frac{1}{\hat{\sigma}\hat{\tau}_\mathrm{r}} - \mathrm{j}\omega_\mathrm{m}\right)\vec{i}_\mathrm{s}^{\,\lozenge}\right) \quad \circ\!\!-\!\!\bullet^{\,\mathcal{F}} \quad \hat{\underline{\psi}}_\mathrm{s} = \hat{L}_\mathrm{s}\frac{1 + \mathrm{j}\omega_\mathrm{sl}\hat{\sigma}\hat{\tau}_\mathrm{r}}{1 + \mathrm{j}\omega_\mathrm{sl}\hat{\tau}_\mathrm{r}}\underline{i}_\mathrm{s}^{\lozenge}. \tag{3.2}$$

The parameters of the observer are estimated quantities and are denoted with the 'hat'-diacritic. $\underline{i}_\mathrm{s}^{\lozenge}$ is the measured value of the stator current, which is the observer input. The current model is implemented as a low-pass filter (LPF) in the rotor reference frame with

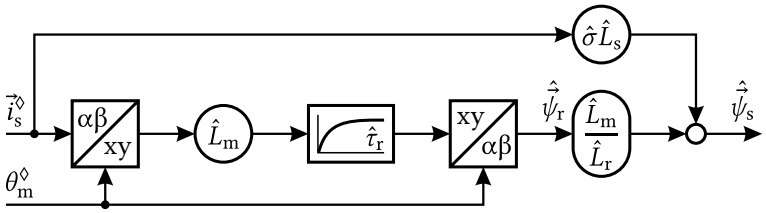

Fig. 3.1: Structure of the open-loop current-model stator flux-linkage observer.

the rotor time constant $\hat{\tau}_\mathrm{r}$, as illustrated in Fig. 3.1. Therefore, the quantities need to be rotated by the measured rotor angle $\theta_\mathrm{m}^{\Diamond}$ which is considered to be ideal. Since the current-model observer only compromises an LPF, it is inherently stable.

The iron-loss model introduced in Section 2.1.3.3 is only valid in the steady state. Thus, iron losses are neglected in the dynamic observer models. However, to calculate the actual flux linkage for the parameter sensitivity analysis, they must be taken into account. Therefore, (3.2) is extended by substituting $\underline{i}_\mathrm{s}^{\Diamond} = \underline{i}_\mathrm{s} - \mathrm{j}\omega_\mathrm{s}\underline{\psi}_\mathrm{s}/R_\mathrm{fe}$, which gives

$$\underline{\psi}_\mathrm{s} = L_\mathrm{s}\frac{1+\mathrm{j}\omega_\mathrm{sl}\sigma\tau_\mathrm{r}}{1+\mathrm{j}\omega_\mathrm{sl}\tau_\mathrm{r}+\mathrm{j}\omega_\mathrm{s}\dfrac{L_\mathrm{s}}{R_\mathrm{fe}}(1+\mathrm{j}\omega_\mathrm{sl}\sigma\tau_\mathrm{r})}\underline{i}_\mathrm{s}. \tag{3.3}$$

The relative error caused by parameter deviation is then found with the division of (3.2) by (3.3) and assuming an ideal current measurement as

$$\underline{F}_\mathrm{C}(\mathrm{j}\omega_\mathrm{s}) = \frac{\hat{L}_\mathrm{s}}{L_\mathrm{s}}\cdot\frac{1+\mathrm{j}\omega_\mathrm{sl}\hat{\sigma}\hat{\tau}_\mathrm{r}}{1+\mathrm{j}\omega_\mathrm{sl}\sigma\tau_\mathrm{r}}\cdot\left(\frac{1+\mathrm{j}\omega_\mathrm{sl}\tau_\mathrm{r}}{1+\mathrm{j}\omega_\mathrm{sl}\hat{\tau}_\mathrm{r}}+\mathrm{j}\omega_\mathrm{s}\frac{L_\mathrm{s}}{R_\mathrm{fe}}\cdot\frac{1+\mathrm{j}\omega_\mathrm{sl}\sigma\tau_\mathrm{r}}{1+\mathrm{j}\omega_\mathrm{sl}\hat{\tau}_\mathrm{r}}\right). \tag{3.4}$$

It includes the deviation resulting from the fact that iron losses are not taken into account.

The sensitivity to balanced current-sensor-gain error is calculated in the same way assuming ideal parameters, which gives

$$\underline{F}_\mathrm{C}^{\Delta\mathrm{i}}(\mathrm{j}\omega_\mathrm{s}) = \frac{\underline{i}_\mathrm{s}^{\Diamond}}{\underline{i}_\mathrm{s}}\left(1+\mathrm{j}\omega_\mathrm{s}\frac{L_\mathrm{s}}{R_\mathrm{fe}}\cdot\frac{1+\mathrm{j}\omega_\mathrm{sl}\sigma\tau_\mathrm{r}}{1+\mathrm{j}\omega_\mathrm{sl}\tau_\mathrm{r}}\right). \tag{3.5}$$

Since the current model is not a function of the stator voltage, voltage-sensor error has no impact on the estimated stator flux linkage.

3.1.2 Voltage Model

The transfer function of the open-loop voltage-model observer can be found by transforming Equation (2.4) to the frequency domain with

$$\frac{\mathrm{d}\hat{\vec{\psi}}_\mathrm{s}}{\mathrm{d}t} = \vec{u}_\mathrm{s}^{\Diamond} - \hat{R}_\mathrm{s}\vec{i}_\mathrm{s}^{\Diamond} \quad \circ\!\!-\!\!\bullet^{\mathcal{F}} \quad \underline{\hat{\psi}}_\mathrm{s} = \frac{1}{\mathrm{j}\omega_\mathrm{s}}\left(\underline{u}_\mathrm{s}^{\Diamond} - \hat{R}_\mathrm{s}\underline{i}_\mathrm{s}^{\Diamond}\right), \tag{3.6}$$

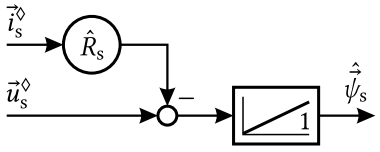

Fig. 3.2: Structure of the open-loop voltage-model stator flux-linkage observer with open integration.

where $\vec{u}_s^{\,\Diamond}$ is the measured voltage input. The resulting observer structure is given in Fig. 3.2, with $\hat{R}_s$ being the only IM model parameter. To calculate the parameter sensitivity, $\underline{u}_s^{\Diamond}$ is considered to be ideal and can be substituted by Equation (2.4), which gives

$$\underline{\hat{\psi}}_s = \underline{\psi}_s + \frac{1}{\mathrm{j}\omega_s}\left(R_s\underline{i}_s - \hat{R}_s\underline{i}_s^{\Diamond}\right). \tag{3.7}$$

With ideal current measurement and substituting $\underline{i}_s$ with (3.3), the relative stator flux-linkage error caused by stator-resistance drift is obtained as

$$\underline{F}_V(\mathrm{j}\omega_s) = 1 + \left(\frac{R_s}{\mathrm{j}\omega_s L_s}\cdot\frac{1+\mathrm{j}\omega_{sl}\tau_r}{1+\mathrm{j}\omega_{sl}\sigma\tau_r} + \frac{R_s}{R_{fe}}\right)\left(1-\frac{\hat{R}_s}{R_s}\right). \tag{3.8}$$

The sensitivity to current-sensor error is determined assuming $\hat{R}_s = R_s$ and substituting (3.3) in Equation (3.7) as

$$\underline{F}_V^{\Delta i}(\mathrm{j}\omega_s) = 1 + \left(\frac{R_s}{\mathrm{j}\omega_s L_s}\cdot\frac{1+\mathrm{j}\omega_{sl}\tau_r}{1+\mathrm{j}\omega_{sl}\sigma\tau_r} + \frac{R_s}{R_{fe}}\right)\left(1-\frac{\underline{i}_s^{\Diamond}}{\underline{i}_s}\right). \tag{3.9}$$

The sensitivity to voltage-sensor error is derived from Equation (3.6) using

$$\underline{F}_V^{\Delta u}(\mathrm{j}\omega_s) = \frac{\underline{u}_s^{\Diamond} - R_s\underline{i}_s}{\underline{u}_s - R_s\underline{i}_s} = 1 + \frac{\underline{u}_s^{\Diamond} - \underline{u}_s}{\underline{u}_s - R_s\underline{i}_s} \overset{(3.6)}{=} 1 + \left(1-\frac{\underline{u}_s^{\Diamond}}{\underline{u}_s}\right)\frac{\mathrm{j}\omega_s\underline{\psi}_s + R_s\underline{i}_s}{\mathrm{j}\omega_s\underline{\psi}_s}. \tag{3.10}$$

With substituting (3.3), the frequency-response function is analogously obtained as

$$\underline{F}_V^{\Delta u}(\mathrm{j}\omega_s) = 1 - \left(1 + \frac{R_s}{\mathrm{j}\omega_s L_s}\cdot\frac{1+\mathrm{j}\omega_{sl}\tau_r}{1+\mathrm{j}\omega_{sl}\sigma\tau_r} + \frac{R_s}{R_{fe}}\right)\left(1-\frac{\underline{u}_s^{\Diamond}}{\underline{u}_s}\right). \tag{3.11}$$

Even though the voltage-model stator flux-linkage observer seems to have a very low parameter sensitivity, it is not a feasible solution, because zero back EMF at standstill and the open integration make the observer unstable.

3.2 Closed-Loop Observers

The low parameter sensitivity of the voltage-model observer and the stability of the current model can be combined by a closed-loop observer. An error feedback is generated from

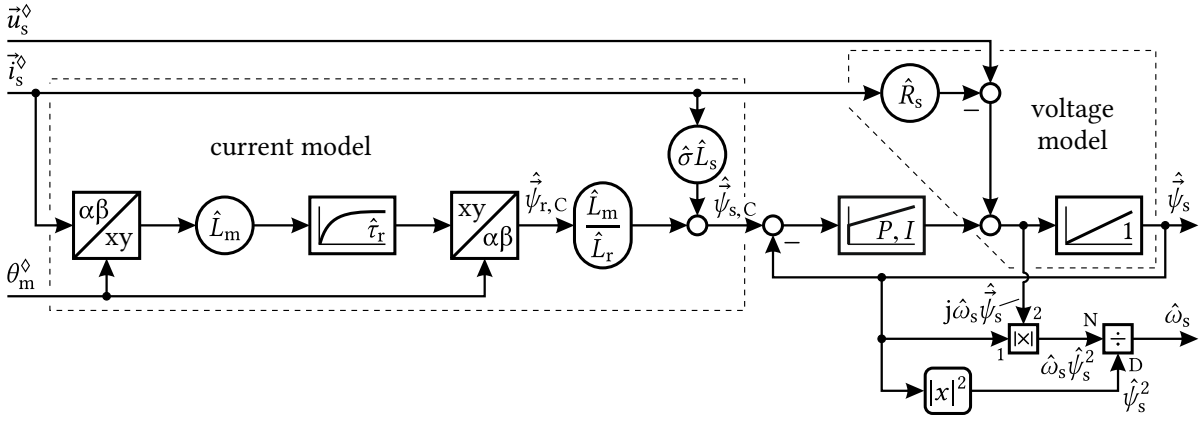

Fig. 3.3: Structure of the closed-loop voltage-model observer with open-loop current-model corrective feedback [JLN94].

both models to correct the estimation errors and ensure the stability of the flux-linkage observer. A reduced-order and a full-order closed-loop stator flux-linkage observer are presented below. Both were implemented in this work and evaluated during measurements.

3.2.1 Voltage-Model Observer with Current-Model Feedback

A simple closed-loop observer can be constructed in the stationary reference frame based on both open-loop observers. The difference of the observer outputs is used as corrective feedback and is applied to the voltage-model integrator input using a PI-controller, as shown in Fig. 3.3. The observer has been proposed in [JLN94] and is loosely based on Gopinath's minimal-order observer theory [Gop71]. It is also referred to as the *Gopinath-style* stator flux-linkage observer [JL94].

Since the observer is implemented in the stationary reference frame, the input and output of the PI-controller are sinusoidal quantities. At a stator frequency below the controller bandwidth, the open-loop current-model observer overwrites the voltage-model output and eliminates its stability problem. At a frequency above the controller bandwidth, the current-model output is suppressed by the PI-controller and the observer becomes equal to the voltage model. The feedback loop then only eliminates the DC offset, which solves the open-integration problem. This way, the PI-controller offers a smooth transition between the current and the voltage model with the transition frequency equal to its bandwidth.

The observer has been extended by an estimator for the stator angular frequency, which is based on Equation (2.24). $\hat{\omega}_\mathrm{s}$ is required for the decoupling of the flux-producing current and the iron losses, the calculation of the efficiency-optimal flux-linkage magnitude and the implementation of field-weakening.

The stator flux-linkage observer is described by the differential equation

$$\hat{\vec{\psi}}_\mathrm{s} = \int \left(\vec{u}_\mathrm{s}^{\,\lozenge} - \hat{R}_\mathrm{s} \vec{i}_\mathrm{s}^{\,\lozenge} + K_\mathrm{P} \left(\hat{\vec{\psi}}_\mathrm{s,C} - \hat{\vec{\psi}}_\mathrm{s} \right) + K_\mathrm{I} \int \left(\hat{\vec{\psi}}_\mathrm{s,C} - \hat{\vec{\psi}}_\mathrm{s} \right) \mathrm{d}t \right) \mathrm{d}t. \tag{3.12}$$

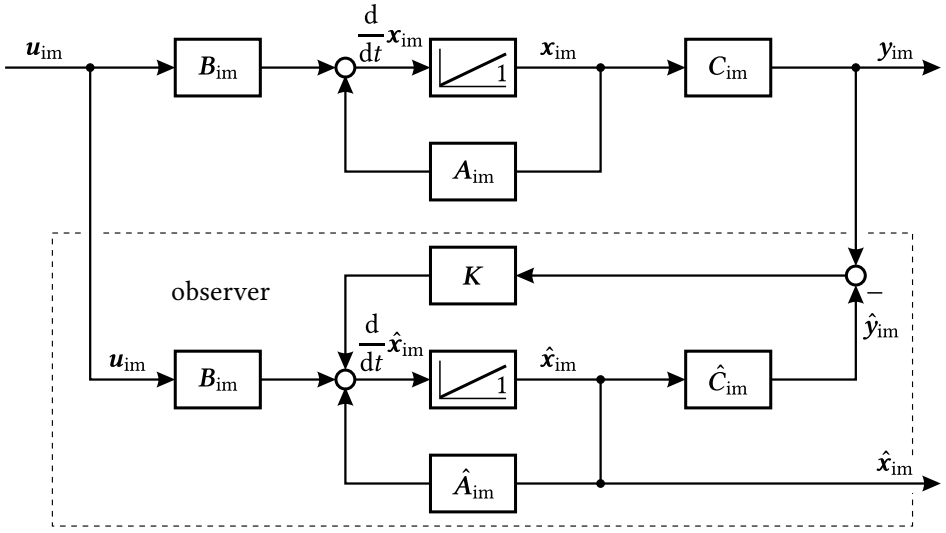

Fig. 3.4: General structure of a Luenberger observer in state-space representation with feedback gain matrix $\boldsymbol{K}$ [Lue64].

After transformation to the frequency domain, the estimated flux linkage is obtained as

$$\underline{\hat{\psi}}_{\mathrm{s}} = \frac{\underline{u}_{\mathrm{s}}^{\Diamond} - \hat{R}_{\mathrm{s}}\underline{i}_{\mathrm{s}}^{\Diamond} + \underline{G}_{\mathrm{PI}}(\mathrm{j}\omega_{\mathrm{s}}) \cdot \hat{\underline{\psi}}_{\mathrm{s,C}}}{\mathrm{j}\omega_{\mathrm{s}} + \underline{G}_{\mathrm{PI}}(\mathrm{j}\omega_{\mathrm{s}})} \quad \text{with} \quad \underline{G}_{\mathrm{PI}}(\mathrm{j}\omega_{\mathrm{s}}) = K_{\mathrm{P}} + \frac{K_{\mathrm{I}}}{\mathrm{j}\omega_{\mathrm{s}}}. \tag{3.13}$$

By substituting the voltage-model term using (3.6) and division by $\underline{\psi}_{\mathrm{s}}$, the relative stator flux-linkage error can be described as a function of the open-loop observer expressions as

$$\underline{F}_{\mathrm{G}}(\mathrm{j}\omega_{\mathrm{s}}) = \frac{\mathrm{j}\omega_{\mathrm{s}} \cdot \underline{F}_{\mathrm{V}}(\mathrm{j}\omega_{\mathrm{s}}) + \underline{G}_{\mathrm{PI}}(\mathrm{j}\omega_{\mathrm{s}}) \cdot \underline{F}_{\mathrm{C}}(\mathrm{j}\omega_{\mathrm{s}})}{\mathrm{j}\omega_{\mathrm{s}} + \underline{G}_{\mathrm{PI}}(\mathrm{j}\omega_{\mathrm{s}})}. \tag{3.14}$$

The expression for the sensitivity to current- or voltage-sensor deviation is determined the same way using Equation (3.14) with the corresponding open-loop model functions.

In this work, the observer transition bandwidth has been chosen to 2.5 Hz. It can be optimized based on the parameter sensitivity analysis in Chapter 4 and Equation (3.14).

3.2.2 Full-Order Luenberger-Type Observer

A full-order observer can be constructed based on the state observer introduced by Luenberger in [Lue64]. The general structure of the observer in state-space representation is shown in Fig. 3.4, with the feedback-gain matrix

$$\boldsymbol{K} = \begin{bmatrix} k_1\mathbf{I} + k_2\mathbf{J} \\ k_3\mathbf{I} + k_4\mathbf{J} \end{bmatrix}. \tag{3.15}$$

According to the state-space representation of the IM introduced in Section 2.1.2, the

state equations of the Luenberger observer in space-vector notation are given by

$$\frac{\mathrm{d}\hat{\vec{\psi}}_\mathrm{s}}{\mathrm{d}t} = -\frac{\hat{R}_\mathrm{s}}{\hat{\sigma}\hat{L}_\mathrm{s}}\hat{\vec{\psi}}_\mathrm{s} + \frac{\hat{R}_\mathrm{s}\hat{L}_\mathrm{m}}{\hat{\sigma}\hat{L}_\mathrm{s}\hat{L}_\mathrm{r}}\hat{\vec{\psi}}_\mathrm{r} + \vec{u}_\mathrm{s}^{\,\lozenge} + \underline{K}_\mathrm{s}\left(\vec{i}_\mathrm{s}^{\,\lozenge} - \hat{\vec{i}}_\mathrm{s}\right) \quad \text{with} \quad \underline{K}_\mathrm{s} = k_1 + \mathrm{j}k_2 \tag{3.16a}$$

$$\text{and} \quad \frac{\mathrm{d}\hat{\vec{\psi}}_\mathrm{r}}{\mathrm{d}t} = \frac{\hat{L}_\mathrm{m}}{\hat{\sigma}\hat{L}_\mathrm{s}\hat{\tau}_\mathrm{r}}\hat{\vec{\psi}}_\mathrm{s} - \left(\frac{1}{\hat{\sigma}\hat{\tau}_\mathrm{r}} - \mathrm{j}\omega_\mathrm{m}\right)\hat{\vec{\psi}}_\mathrm{r} + \underline{K}_\mathrm{r}\left(\vec{i}_\mathrm{s}^{\,\lozenge} - \hat{\vec{i}}_\mathrm{s}\right) \quad \text{with} \quad \underline{K}_\mathrm{r} = k_3 + \mathrm{j}k_4. \tag{3.16b}$$

$\hat{\vec{\psi}}_\mathrm{s}$ and $\hat{\vec{\psi}}_\mathrm{r}$ have been chosen as state variables with the estimated stator current

$$\hat{\vec{i}}_\mathrm{s} = \frac{1}{\hat{\sigma}\hat{L}_\mathrm{s}\hat{L}_\mathrm{r}}\left(\hat{\vec{\psi}}_\mathrm{s}\hat{L}_\mathrm{r} - \hat{\vec{\psi}}_\mathrm{r}\hat{L}_\mathrm{m}\right) = \frac{1}{\hat{\sigma}\hat{L}_\mathrm{s}}\hat{\vec{\psi}}_\mathrm{s} - \frac{\hat{L}_\mathrm{m}}{\hat{\sigma}\hat{L}_\mathrm{s}\hat{L}_\mathrm{r}}\hat{\vec{\psi}}_\mathrm{r} \tag{3.17}$$

as output, according to (2.10). Comparison with the measured current gives the error feedback $\vec{\varepsilon}_\mathrm{i} = \vec{i}_\mathrm{s}^{\,\lozenge} - \hat{\vec{i}}_\mathrm{s}$.

3.2.2.1 Observer Feedback-Gain Selection

The feedback-gain matrix $\boldsymbol{K}$ must be selected so that the observer converges faster than the IM dynamics. This is achieved by placing the observer poles in the complex s-plane to the left of those of the IM. The observer poles are found by solving the characteristic polynomial [DB11, pp. 847–856]

$$\det\left(s_{\mathrm{p}n}\mathbf{I} - \left(\hat{\boldsymbol{A}}_\mathrm{im} - \boldsymbol{K}\hat{\boldsymbol{C}}_\mathrm{im}\right)\right) \stackrel{!}{=} 0. \tag{3.18}$$

The solution can be simplified using the substitutions

$$\underline{K}_\mathrm{Rs} = \hat{R}_\mathrm{s} + \underline{K}_\mathrm{s} \quad \text{and} \quad \underline{K}_\mathrm{Rr} = \hat{R}_\mathrm{r} - \frac{\hat{L}_\mathrm{m}}{\hat{L}_\mathrm{s}}\underline{K}_\mathrm{r}. \tag{3.19}$$

After some mathematical operations, the poles are obtained as

$$\begin{aligned}
\hat{s}_\mathrm{p1} &= -\frac{\underline{K}_\mathrm{Rs}\hat{L}_\mathrm{r} + \underline{K}_\mathrm{Rr}\hat{L}_\mathrm{s}}{2\hat{\sigma}\hat{L}_\mathrm{s}\hat{L}_\mathrm{r}} \pm \mathrm{j}\frac{1}{2}\omega_\mathrm{m} + \sqrt{\frac{\underline{K}_\mathrm{Rs}\left(\underline{K}_\mathrm{Rr} - \hat{R}_\mathrm{r}\hat{\sigma}\right)}{\hat{\sigma}^2\hat{L}_\mathrm{s}\hat{L}_\mathrm{r}} + \left(\frac{\underline{K}_\mathrm{Rs}\hat{L}_\mathrm{r} - \underline{K}_\mathrm{Rr}\hat{L}_\mathrm{s}}{2\hat{\sigma}\hat{L}_\mathrm{s}\hat{L}_\mathrm{r}} \pm \mathrm{j}\frac{1}{2}\omega_\mathrm{m}\right)^2}, \\
\hat{s}_\mathrm{p2} &= -\frac{\underline{K}_\mathrm{Rs}\hat{L}_\mathrm{r} + \underline{K}_\mathrm{Rr}\hat{L}_\mathrm{s}}{2\hat{\sigma}\hat{L}_\mathrm{s}\hat{L}_\mathrm{r}} \pm \mathrm{j}\frac{1}{2}\omega_\mathrm{m} - \sqrt{\frac{\underline{K}_\mathrm{Rs}\left(\underline{K}_\mathrm{Rr} - \hat{R}_\mathrm{r}\hat{\sigma}\right)}{\hat{\sigma}^2\hat{L}_\mathrm{s}\hat{L}_\mathrm{r}} + \left(\frac{\underline{K}_\mathrm{Rs}\hat{L}_\mathrm{r} - \underline{K}_\mathrm{Rr}\hat{L}_\mathrm{s}}{2\hat{\sigma}\hat{L}_\mathrm{s}\hat{L}_\mathrm{r}} \pm \mathrm{j}\frac{1}{2}\omega_\mathrm{m}\right)^2}.
\end{aligned} \tag{3.20}$$

The common approach is to place the observer poles proportional to the poles of the IM [KMN93]. As derived in Appendix A.5.1, k_1, k_3 are then constant coefficients and k_2, k_4 are proportional to ω_m. At high angular speed this leads to poles with large imaginary

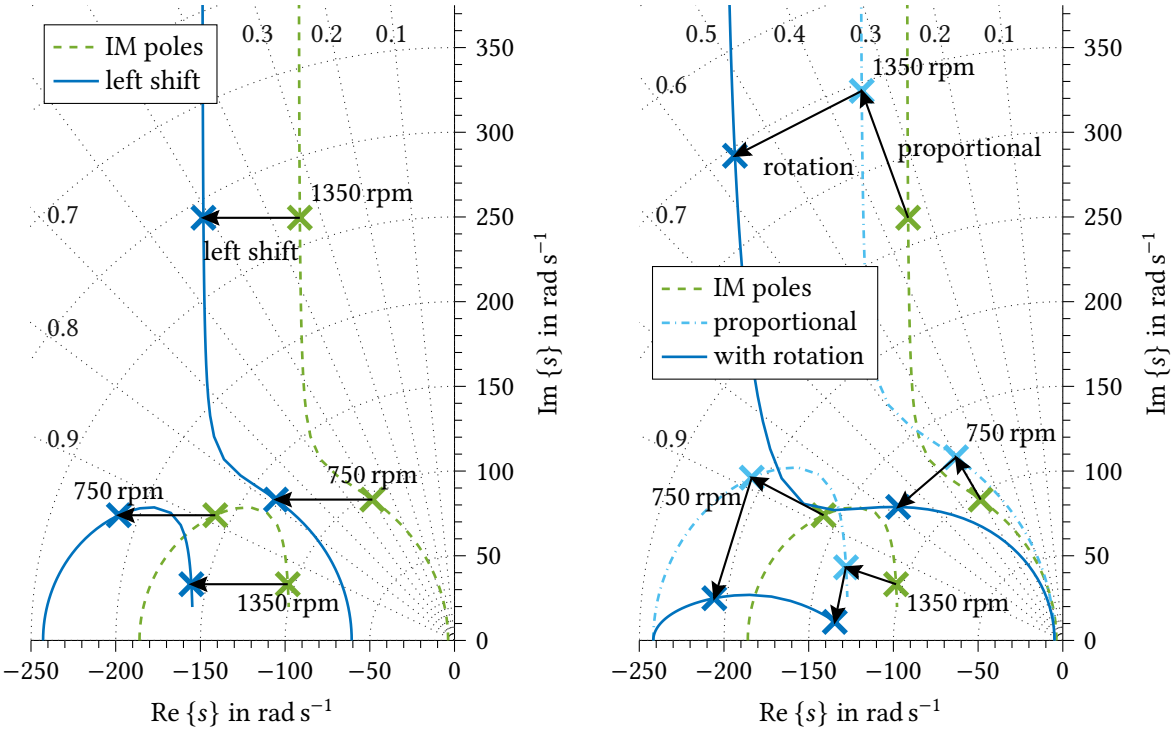

(a) left-shifted poles with $g = 0.3$

(b) proportional poles with rotation, $|g| = 1.3$

Fig. 3.5: Root-locus diagrams of the full-order observer poles for IM26kA, using different pole placement methods. Calculated using the equations derived in Appendix A.5.

part, which can cause instability in digital implementation. In [MM00] this problem is solved by shifting the observer poles to the left in the s-plane, according to Fig. 3.5a. The resulting rotor-speed-dependent coefficients are given in Appendix A.5.2. Alternatively, in [Gri+01], the proportional poles are additionally rotated to improve the high-speed behaviour. However, this leads to undesired poles at low frequencies, which can be avoided using a speed-dependent rotation angle [GŽ10]. The pole placement for the latter two is derived in Appendix A.5.3. In Fig. 3.5b, the rotation angle has been chosen to be 75 % of the angle between the real axis and its closest pole. But this requires additional computational effort for the original pole angle and leads to a negligible rotation angle at high speed.

An optimal solution can be derived based on the theory of robust design by $\mathcal{H}_\infty$ optimization [GKP05]. The approach optimizes the feedback-gain matrix $\boldsymbol{K}$, taking into account system parameter uncertainties. However, the solution for the flux-linkage observer is rotor-speed dependent [Dav+12] and requires offline calculation and storage in a lookup table. Furthermore, the optimization aims at the stability of the observer and does not necessarily lead to a minimized estimation error of the observed system states.

In this work, the proportional placement without rotation and the left-shift pole placements are examined more closely. In Chapter 4, the torque accuracy of the full-order observer is analyzed for both placement methods. The degree of left or proportional shift is chosen based on the resulting sensitivity of the estimation error to parameter variations.

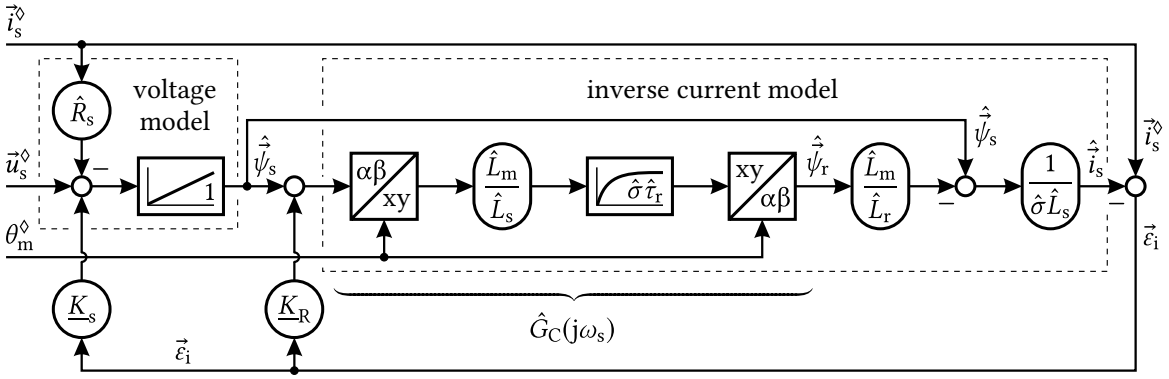

Fig. 3.6: Structure of the closed-loop Luenberger-type stator flux-linkage observer with modified voltage model. Instead of the current estimate, the measured current is used for calculating the stator-resistance voltage drop.

3.2.2.2 Voltage-Model Modification

A comparison of (3.17) with (3.16a) indicates that (3.16a) is equal to the voltage model with the estimated stator current $\hat{\vec{i}}_\mathrm{s}$ used to calculate the stator resistance voltage drop. In this work, the measured current $\vec{i}_\mathrm{s}^\,\lozenge$ is used instead, which leads to the modified state equations

$$\frac{\mathrm{d}\hat{\vec{\psi}}_\mathrm{s}}{\mathrm{d}t} = \vec{u}_\mathrm{s}^\,\lozenge - \hat{R}_\mathrm{s}\vec{i}_\mathrm{s}^\,\lozenge + \underline{K}_\mathrm{s}\left(\vec{i}_\mathrm{s}^\,\lozenge - \hat{\vec{i}}_\mathrm{s}\right) \tag{3.21a}$$

$$\text{and} \quad \frac{\mathrm{d}\hat{\vec{\psi}}_\mathrm{r}}{\mathrm{d}t} = \frac{\hat{L}_\mathrm{m}}{\hat{\sigma}\hat{L}_\mathrm{s}\hat{\tau}_\mathrm{r}}\hat{\vec{\psi}}_\mathrm{s} - \left(\frac{1}{\hat{\sigma}\hat{\tau}_\mathrm{r}} - \mathrm{j}\omega_\mathrm{m}\right)\hat{\vec{\psi}}_\mathrm{r} + \underline{K}_\mathrm{r}\left(\vec{i}_\mathrm{s}^\,\lozenge - \hat{\vec{i}}_\mathrm{s}\right). \tag{3.21b}$$

The resulting observer structure is given in Fig. 3.6 and consists of the voltage model to calculate the estimated stator flux linkage from the measured quantities. An inverse current model is applied in the rotor reference frame to calculate a stator-current estimate from the estimated flux linkage. The current estimate is then compared to the measured current and used as a corrective feedback to the inputs of both models.

To derive the steady-state stator flux-linkage error, (3.21) is transformed to the frequency domain as

$$\underline{\hat{\psi}}_\mathrm{s} = \frac{1}{\mathrm{j}\omega_\mathrm{s}}\left(\underline{u}_\mathrm{s}^\lozenge - \hat{R}_\mathrm{s}\underline{i}_\mathrm{s}^\lozenge + \underline{K}_\mathrm{s}\underline{\varepsilon}_\mathrm{i}\right) \tag{3.22a}$$

$$\text{and} \quad \underline{\hat{\psi}}_\mathrm{r} = \underbrace{\frac{\hat{L}_\mathrm{m}}{\hat{L}_\mathrm{s}} \cdot \frac{1}{1 + \mathrm{j}\omega_\mathrm{sl}\hat{\sigma}\hat{\tau}_\mathrm{r}}}_{\underline{\hat{G}}_\mathrm{C}(\mathrm{j}\omega_\mathrm{s})}\left(\underline{\hat{\psi}}_\mathrm{s} + \underline{K}_\mathrm{R}\underline{\varepsilon}_\mathrm{i}\right) \quad \text{with} \quad \underline{K}_\mathrm{R} = \frac{\hat{\sigma}\hat{L}_\mathrm{s}\hat{\tau}_\mathrm{r}}{\hat{L}_\mathrm{m}}\underline{K}_\mathrm{r}. \tag{3.22b}$$

With the help of Fig. 3.6 or substituting the estimated current in $\vec{\varepsilon}_\mathrm{i} = \vec{i}_\mathrm{s}^\,\lozenge - \hat{\vec{i}}_\mathrm{s}$ with Equa-

tion (3.17) and replacing $\underline{\hat{\psi}}_\mathrm{r}$ by (3.22b), an expression for the current error feedback is found with

$$\underline{\varepsilon}_\mathrm{i} = \underline{i}_\mathrm{s}^{\lozenge} - \frac{1}{\hat{\sigma}\hat{L}_\mathrm{s}}\left(\underline{\hat{\psi}}_\mathrm{s} - \frac{\hat{L}_\mathrm{m}}{\hat{L}_\mathrm{r}} \cdot \underline{\hat{G}}_\mathrm{C}(\mathrm{j}\omega_\mathrm{s}) \cdot \left(\underline{K}_\mathrm{R}\underline{\varepsilon}_\mathrm{i} + \underline{\hat{\psi}}_\mathrm{s}\right)\right). \tag{3.23}$$

Solving for $\underline{\varepsilon}_\mathrm{i}$ leads to

$$\underline{\varepsilon}_\mathrm{i} = \frac{\hat{R}_\mathrm{r}}{\hat{R}_\mathrm{r} - \underline{K}_\mathrm{r}\underline{\hat{G}}_\mathrm{C}(\mathrm{j}\omega_\mathrm{s})}\underline{i}_\mathrm{s}^{\lozenge} + \frac{\hat{R}_\mathrm{r}}{\hat{\sigma}\hat{L}_\mathrm{s}\hat{L}_\mathrm{r}} \cdot \frac{\hat{L}_\mathrm{m}\underline{\hat{G}}_\mathrm{C}(\mathrm{j}\omega_\mathrm{s}) - \hat{L}_\mathrm{r}}{\hat{R}_\mathrm{r} - \underline{K}_\mathrm{r}\underline{\hat{G}}_\mathrm{C}(\mathrm{j}\omega_\mathrm{s})}\underline{\hat{\psi}}_\mathrm{s}. \tag{3.24}$$

Inserted in (3.22a) and substituting the voltage-model term with the results of the open-loop voltage-model observer in Section 3.1.2, an expression for the relative steady-state flux-linkage error is obtained as

$$\begin{aligned}\underline{F}_\mathrm{F}(\mathrm{j}\omega_\mathrm{s}) &= \underline{F}_\mathrm{V}(\mathrm{j}\omega_\mathrm{s}) + \underline{K}_\mathrm{s}\frac{\underline{\varepsilon}_\mathrm{i}}{\mathrm{j}\omega_\mathrm{s}\underline{\psi}_\mathrm{s}} \\ &= \underline{F}_\mathrm{V}(\mathrm{j}\omega_\mathrm{s}) + \frac{\underline{K}_\mathrm{s}}{\mathrm{j}\omega_\mathrm{s}}\left(\frac{\hat{R}_\mathrm{r}}{\hat{R}_\mathrm{r} - \underline{K}_\mathrm{r}\underline{\hat{G}}_\mathrm{C}(\mathrm{j}\omega_\mathrm{s})} \cdot \frac{\underline{i}_\mathrm{s}^{\lozenge}}{\underline{\psi}_\mathrm{s}} + \frac{\hat{R}_\mathrm{r}}{\hat{\sigma}\hat{L}_\mathrm{s}\hat{L}_\mathrm{r}} \cdot \frac{\hat{L}_\mathrm{m}\underline{\hat{G}}_\mathrm{C}(\mathrm{j}\omega_\mathrm{s}) - \hat{L}_\mathrm{r}}{\hat{R}_\mathrm{r} - \underline{K}_\mathrm{r}\underline{\hat{G}}_\mathrm{C}(\mathrm{j}\omega_\mathrm{s})}\underline{F}_\mathrm{F}(\mathrm{j}\omega_\mathrm{s})\right).\end{aligned} \tag{3.25}$$

With the solutions of Section 3.1.1 and with (3.2), the steady-state flux-linkage error of the modified full-order Luenberger-type stator flux-linkage observer can be calculated as a function of the corresponding open-loop observer expressions with

$$\underline{F}_\mathrm{F}(\mathrm{j}\omega_\mathrm{s}) = \frac{\underline{F}_\mathrm{V}(\mathrm{j}\omega_\mathrm{s}) \cdot \left(\hat{R}_\mathrm{r} - \underline{K}_\mathrm{r}\underline{\hat{G}}_\mathrm{C}(\mathrm{j}\omega_\mathrm{s})\right) + \underline{F}_\mathrm{C}(\mathrm{j}\omega_\mathrm{s}) \cdot \dfrac{\hat{R}_\mathrm{r} + \mathrm{j}\omega_\mathrm{sl}\hat{L}_\mathrm{r}}{\mathrm{j}\omega_\mathrm{s}\hat{L}_\mathrm{m}}\underline{K}_\mathrm{s}\underline{\hat{G}}_\mathrm{C}(\mathrm{j}\omega_\mathrm{s})}{\hat{R}_\mathrm{r} - \underline{K}_\mathrm{r}\underline{\hat{G}}_\mathrm{C}(\mathrm{j}\omega_\mathrm{s}) + \dfrac{\hat{L}_\mathrm{r} - \hat{L}_\mathrm{m}\underline{\hat{G}}_\mathrm{C}(\mathrm{j}\omega_\mathrm{s})}{\mathrm{j}\omega_\mathrm{s}\hat{\tau}_\mathrm{r}\hat{\sigma}\hat{L}_\mathrm{s}}\underline{K}_\mathrm{s}}. \tag{3.26}$$

Equation (3.26) is also used to calculate the balanced current- and voltage-sensor-gain-dependent flux-linkage error. Therefore, the corresponding open-loop model functions must be inserted.

3.2.2.3 Sliding-Mode Inherently Speed-Sensorless Observer

With a further modification of the full-order observer, the current model can be made independent from the measured rotor angular frequency. Instead of the rotor angle, Lascu et al. proposed to use the angle of the rotor flux linkage for the reference frame transformation within the current model [LBB05]. The differential equation for the rotor flux linkage (3.21b) in the RFO reference frame then becomes equal to

$$\frac{\mathrm{d}\hat{\vec{\psi}}_\mathrm{r}}{\mathrm{d}t} = \frac{\hat{L}_\mathrm{m}}{\hat{\sigma}\hat{L}_\mathrm{s}\hat{\tau}_\mathrm{r}}\hat{\vec{\psi}}_\mathrm{s}\mathrm{e}^{-\mathrm{j}\theta_\mathrm{s}} - \left(\frac{1}{\hat{\sigma}\hat{\tau}_\mathrm{r}} + \mathrm{j}\omega_\mathrm{sl}\right)\hat{\vec{\psi}}_\mathrm{r} + \underline{K}_\mathrm{r}\underline{\varepsilon}_\mathrm{i}\mathrm{e}^{-\mathrm{j}\theta_\mathrm{s}}. \tag{3.27}$$

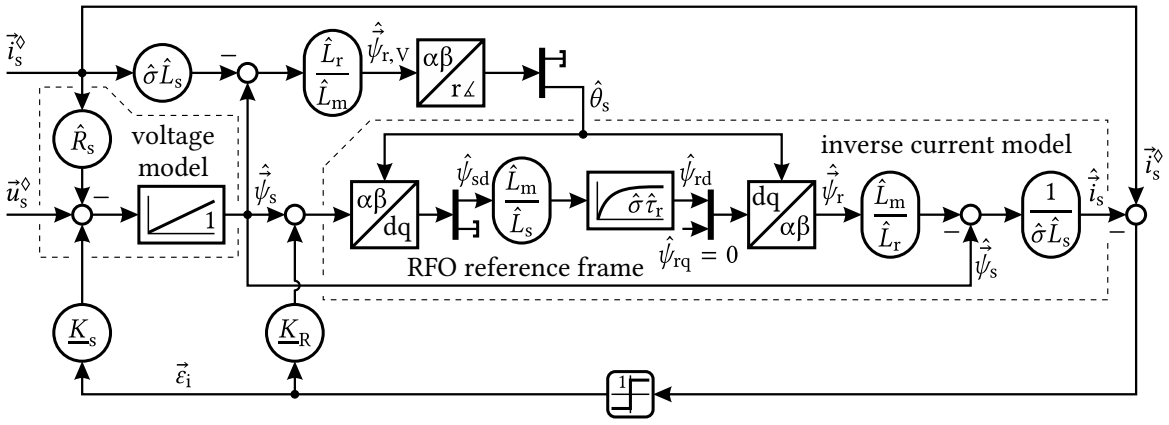

Fig. 3.7: Structure of the sliding-mode inherently speed-sensorless flux-linkage observer with modified voltage and current models.

Since in RFO the rotor flux linkage only has a real part ($\hat{\psi}_{\mathrm{rq}} = 0$), the differential equation can be simplified and the slip-angular-frequency term disappears with

$$\frac{\mathrm{d}\hat{\psi}_{\mathrm{rd}}}{\mathrm{d}t} = \frac{\hat{L}_{\mathrm{m}}}{\hat{\sigma}\hat{L}_{\mathrm{s}}\hat{\tau}_{\mathrm{r}}}\hat{\psi}_{\mathrm{sd}} - \left(\frac{1}{\hat{\sigma}\hat{\tau}_{\mathrm{r}}}\right)\hat{\psi}_{\mathrm{rd}} + \mathrm{Re}\left\{\underline{K}_{\mathrm{r}}\underline{\varepsilon}_{\mathrm{i}}\mathrm{e}^{-\mathrm{j}\theta_{\mathrm{s}}}\right\} \quad \circ\!\!-\!\!\bullet^{\mathcal{F}} \quad \hat{\psi}_{\mathrm{rd}} = \frac{\frac{\hat{L}_{\mathrm{m}}}{\hat{L}_{\mathrm{s}}}\hat{\psi}_{\mathrm{sd}} + \mathrm{Re}\left\{\underline{K}_{\mathrm{r}}\underline{\varepsilon}_{\mathrm{i}}\mathrm{e}^{-\mathrm{j}\theta_{\mathrm{s}}}\right\}}{1 + \mathrm{j}\omega_{\mathrm{sl}}\hat{\sigma}\hat{\tau}_{\mathrm{r}}}. \tag{3.28}$$

The angle of the RFO reference frame is determined using a second estimate for the rotor flux-linkage space vector from the voltage model and the measured current with (2.10) as

$$\hat{\vec{\psi}}_{\mathrm{r,V}} = \frac{\hat{L}_{\mathrm{r}}}{\hat{L}_{\mathrm{m}}}\left(\hat{\vec{\psi}}_{\mathrm{s}} - \hat{\sigma}\hat{L}_{\mathrm{s}}\vec{i}_{\mathrm{s}}^{\,\diamondsuit}\right). \tag{3.29}$$

The rotor speed can be obtained from the estimated stator angular frequency and a slip frequency estimate according to (2.31) with

$$\hat{\omega}_{\mathrm{m}} = \hat{\omega}_{\mathrm{s}} - \frac{\frac{2}{3}\hat{T}_{\mathrm{e}}\hat{R}_{\mathrm{r}}}{\hat{\tau}_{\mathrm{r}}\hat{\psi}_{\mathrm{r}}^2}. \tag{3.30}$$

It should be noted, that the low-speed stability is affected by this modification. Especially at zero speed, offsets or parameter mismatch can cause improper alignment of the RFO reference frame, which leads to similar problems as the model-reference adaptive system (MRAS) with adaptive mechanism to determine the rotor speed [Sch92] or the corresponding full-order sensorless observer in [MM00].

In [LBB05], an additional modification concerns the feedback loop. In case of parameter uncertainty, the Luenberger observer with linear feedback is generally not able to force the output estimation error to zero and the observer states cannot converge to the system states [Sht+14]. By using $\mathrm{sgn}(\vec{\varepsilon}_{\mathrm{i}})$ as feedback, a sliding-mode observer is obtained [Utk77; DU95],

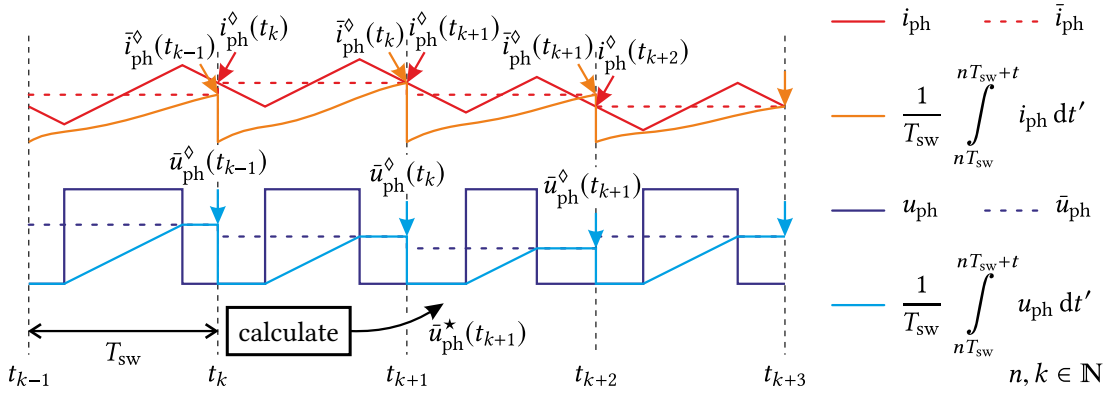

Fig. 3.8: Discrete-time representation of measured currents and voltages in the inverter system with sampled and switching-period average quantities.

which resolves that issue. The resulting structure of the sliding-mode inherently speed-sensorless observer is shown in Fig. 3.7. The pole placement is determined analogously to Section 3.2.2.1. A comparison of this modification to the full-order observer with adaptive rotor-speed estimator has been reported to show superior performance in speed-sensorless applications [LBB06].

With the sliding-mode feedback, the voltage-model feedback gain $\underline{K}_{\mathrm{s}}$ must be chosen higher than the worst-case sensor offset to avoid the offset-integration problem. In [LA06] and [LBB09], an additional PI-controller in parallel to $\underline{K}_{\mathrm{s}}$ is suggested to compensate these sensor offsets. However, this workaround adds another state variable to the system, which can cause undesired effects, such as integration of parameter errors during standstill.

3.3 Discrete-Time Implementation

The control algorithm and the flux-linkage observers have been implemented on a digital signal processor (DSP) in C++. As described in Appendix A.2.2, the system operates at a constant switching frequency of $f_{\mathrm{sw}} = 10\,\mathrm{kHz}$ and performs sequential calculations at discrete time instants nT_{sw} with $T_{\mathrm{sw}} = 100\,\mu\mathrm{s}$. Since the flux-linkage observer is crucial for the stability and accuracy of the torque controller, this section pays special attention to the discrete-time implementation of the aforementioned observers.

For optimal performance, the measurement-data acquisition within the inverter system must be considered. The DSP used in this work is not equipped with integrated analog-to-digital (A/D) converters. Instead, separate A/D converters are used which are attached to a field-programmable gate array (FPGA) via serial peripheral interface (SPI). The FPGA processes all measured quantities of the inverter system and includes the PWM unit. It communicates with the DSP via an asynchronous memory interface (AMI) bus and has been programmed using very high speed integrated hardware description language (VHDL). This configuration with FPGA processed A/D conversion allows operation at a sampling

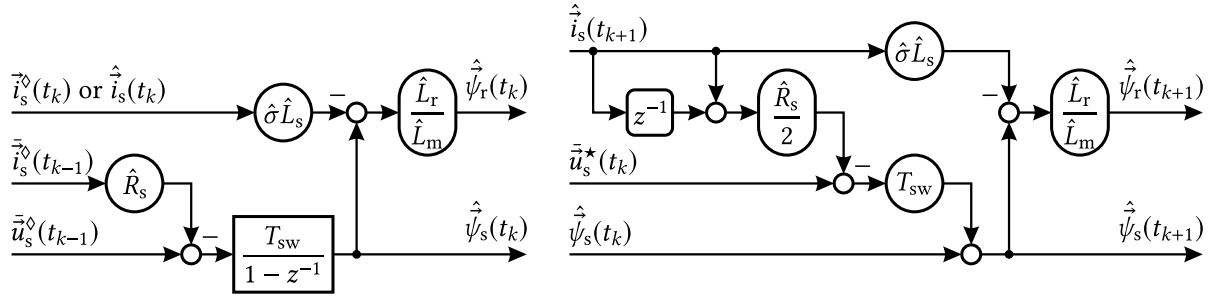

(a) voltage model (b) single-step flux-linkage prediction

Fig. 3.9: Optimal discrete-time voltage model of the IM using the backward-Euler method on switching-period average quantities and prediction of the next flux-linkage sample based on the reference voltage. The future stator-current switching-period average is obtained from a current predictor and first-order approximation.

rate much higher than the switching frequency. In this work, current and voltages are sampled at $f_s = 1\,\mathrm{MHz}$ and are digitally integrated to obtain the *switching-period average* signal, as illustrated in Fig. 3.8.

Since the sampling frequency is much higher than the controller update frequency, the switching-period average stator current can be approximated with negligible error by the continuous-time integral

$$\bar{\vec{i}}_s^{\,\diamond}(t_{k-1}) = \frac{1}{T_{sw}} \int_{t_{k-1}}^{t_k} \vec{i}_s^{\,\diamond}\, \mathrm{d}t. \tag{3.31}$$

The same approximation is applied to the voltage measurement in this section. However, due to the switching nature of the PWM voltage signal, some additional considerations are required to ensure accurate voltage measurement. The optimization of the voltage measurement is adressed in Chapter 5.

3.3.1 Discrete-Time Voltage and Current Model of the IM

With the switching-period average measurements, the ideal integral of the voltage model can be formed using

$$\hat{\vec{\psi}}_s(t_k) = \int_{t_{k-1}}^{t_k} \left(\vec{u}_s^{\,\diamond} - \hat{R}_s \vec{i}_s^{\,\diamond}\right) \mathrm{d}t + \hat{\vec{\psi}}_s(t_{k-1}) = T_{sw}\left(\bar{\vec{u}}_s^{\,\diamond}(t_{k-1}) - \hat{R}_s \bar{\vec{i}}_s^{\,\diamond}(t_{k-1})\right) + \hat{\vec{\psi}}_s(t_{k-1}), \tag{3.32}$$

which leads to the structure of the discrete voltage model with backward-Euler integration, given in Fig. 3.9a. $\hat{\vec{\psi}}_s(t_k)$ is the stator flux linkage at the time instant of the last sample before the actual calculation step. However, for optimal dynamic control the quantities at time instant t_{k+1} are desired. They can be determined based on the reference voltage

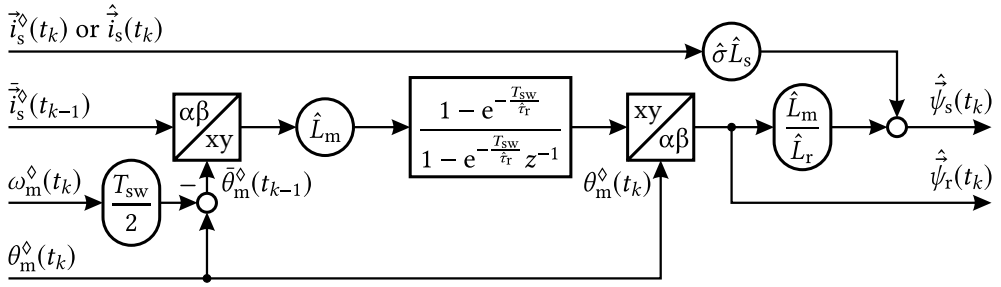

Fig. 3.10: Optimal discrete-time current model of the IM using the zero-order hold (ZOH) method for switching-period average input quantities.

$\bar{\vec{u}}_s^{\star}(t_k)$ calculated during the previous time step. With the result of (3.32) it is obtained as

$$\hat{\vec{\psi}}_s(t_{k+1}) = T_{sw}\left(\bar{\vec{u}}_s^{\star}(t_k) - \hat{R}_s\bar{\hat{\vec{i}}}_s(t_k)\right) + \hat{\vec{\psi}}_s(t_k), \quad \text{with} \quad \bar{\hat{\vec{i}}}_s(t_k) = \frac{\hat{\vec{i}}_s(t_k) + \hat{\vec{i}}_s(t_{k+1})}{2} \tag{3.33}$$

being the first-order approximate of the future stator-current switching-period average. The resulting block diagram is given in Fig. 3.9b. To obtain the future stator-current estimate, a current predictor as described in Section 3.3.2 is required.

The current model in Section 3.1.1 contains an LPF with the rotor time constant, which needs to be discretized. According to the dashed line in Fig. 3.8, the measured current is a staircase input signal. An exact match from the continuous to the discrete-time system for such an input signal is provided by the zero-order hold (ZOH) discretization method [FPW02, pp. 187–210]. The ZOH equivalent of the LPF is given by

$$\left(1 - z^{-1}\right) \cdot \mathcal{Z}\left\{\frac{1}{s} \cdot \frac{1}{1 + \hat{\tau}_r s}\right\} = \frac{1 - e^{\frac{T_{sw}}{\hat{\tau}_r}}}{1 - e^{\frac{T_{sw}}{\hat{\tau}_r}} z^{-1}} z^{-1}. \tag{3.34}$$

It leads to the block diagram in Fig. 3.10. By omitting the one-step delay in the transfer function, the flux linkage at the time instant t_k is obtained from the switching-period average quantities at t_{k-1}. Another important detail are the rotor angles used for the reference frame transformations. The switching-period average signals on the left side of the LPF must be rotated by the corresponding switching-period average angle which is obtained by first-order approximation, analogously to the current in (3.33), whereas right of the LPF the sampled angle must be used. This leads to slightly different angles for both rotation transformations and avoids misalignment, especially at high rotational speed.

When the current-model observer is used for the error feedback of the Gopinath-style observer in Fig. 3.3, the rotor or stator flux-linkage at the time instant t_k is compared to the corresponding signal of the voltage model in Fig. 3.9a. Prediction of the current-model flux linkage at t_{k+1} is not necessary, since the desired PI-controller bandwidth is much lower than the switching frequency. The PI-controller can be discretized using the backward-Euler method.

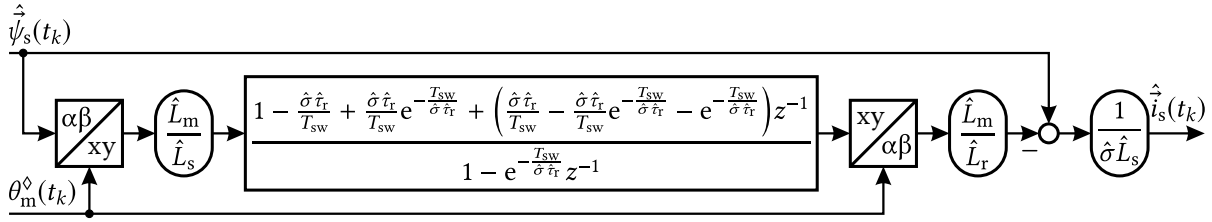

Fig. 3.11: Discrete-time inverse current model of the full-order observer using the first-order hold (FOH) method.

The full-order observer is implemented using the discrete-time voltage model in Fig. 3.9 and an inverse current model, which includes another LPF with the time constant $\hat{\sigma}\hat{\tau}_\mathrm{r}$. The input of the LPF is now equivalent to a sampled continuous signal. It can be considered as a piecewise linear input, which is a good first-order approximation. An exact discrete-time equivalent to the continuous LPF is then found using the first-order hold (FOH) method [FPW02, pp. 187–210] as

$$\frac{(z-1)^2}{T_\mathrm{sw} z} \cdot \mathcal{Z}\left\{\frac{1}{s^2} \cdot \frac{1}{1+\hat{\tau}_\mathrm{r} s}\right\} = \frac{1 - \frac{\hat{\sigma}\hat{\tau}_\mathrm{r}}{T_\mathrm{sw}} + \frac{\hat{\sigma}\hat{\tau}_\mathrm{r}}{T_\mathrm{sw}} e^{-\frac{T_\mathrm{sw}}{\hat{\sigma}\hat{\tau}_\mathrm{r}}} + \left(\frac{\hat{\sigma}\hat{\tau}_\mathrm{r}}{T_\mathrm{sw}} - \frac{\hat{\sigma}\hat{\tau}_\mathrm{r}}{T_\mathrm{sw}} e^{-\frac{T_\mathrm{sw}}{\hat{\sigma}\hat{\tau}_\mathrm{r}}} - e^{-\frac{T_\mathrm{sw}}{\hat{\sigma}\hat{\tau}_\mathrm{r}}}\right) z^{-1}}{1 - e^{-\frac{T_\mathrm{sw}}{\hat{\sigma}\hat{\tau}_\mathrm{r}}} z^{-1}}. \tag{3.35}$$

The resulting structure of the discrete-time inverse current model is shown in Fig. 3.11.

3.3.2 Stator-Current Predictor

To obtain the future estimate of the flux linkage in Fig. 3.9b, a future estimate of the stator current at time instant t_{k+1} is required. It can be determined using a stator-current predictor, that utilizes the stator-voltage reference value calculated in the previous step. Such a predictor has been proposed in [WL09] and has been implemented in this work.

Starting from Equation (3.2) with substitution of $\hat{\vec{\psi}}_\mathrm{s}$ using (2.10) and replacing $\mathrm{d}\hat{\vec{\psi}}_\mathrm{s}/\mathrm{d}t$ by (2.4), a differential equation for the estimated stator current is derived as

$$\frac{\mathrm{d}\hat{\vec{i}}_\mathrm{s}}{\mathrm{d}t} = \frac{1}{\hat{\sigma}\hat{L}_\mathrm{s}} \cdot \left(\vec{u}^{\star}_\mathrm{s} - \underbrace{\left(\hat{R}_\mathrm{s} + \hat{R}_\mathrm{r}\frac{\hat{L}^2_\mathrm{m}}{\hat{L}^2_\mathrm{r}}\right)}_{\hat{R}_\mathrm{eq}} \hat{\vec{i}}_\mathrm{s} + \frac{\hat{L}_\mathrm{m}}{\hat{L}_\mathrm{r}}\left(\frac{1}{\hat{\tau}_\mathrm{r}} - \mathrm{j}\omega^{\Diamond}_\mathrm{m}\right)\hat{\vec{\psi}}_\mathrm{r}\right). \tag{3.36}$$

After substituting the resistive term by an equivalent resistance $\hat{R}_\mathrm{eq}$, and with the equivalent time constant $\hat{\tau}_\mathrm{eq}$, the differential equation can be expressed in the complex frequency domain with

$$\hat{\underset{\sim}{i}}_\mathrm{s} = \frac{1}{\hat{R}_\mathrm{eq}} \cdot \frac{1}{1+\hat{\tau}_\mathrm{eq} s} \cdot \left(\underset{\sim}{u}^{\star}_\mathrm{s} + \frac{\hat{L}_\mathrm{m}}{\hat{L}_\mathrm{r}}\left(\frac{1}{\hat{\tau}_\mathrm{r}} - \mathrm{j}\omega^{\Diamond}_\mathrm{m}\right)\hat{\underset{\sim}{\psi}}_\mathrm{r}\right) \quad \text{and} \quad \hat{\tau}_\mathrm{eq} = \frac{\hat{\sigma}\hat{L}_\mathrm{s}}{\hat{R}_\mathrm{eq}}. \tag{3.37}$$

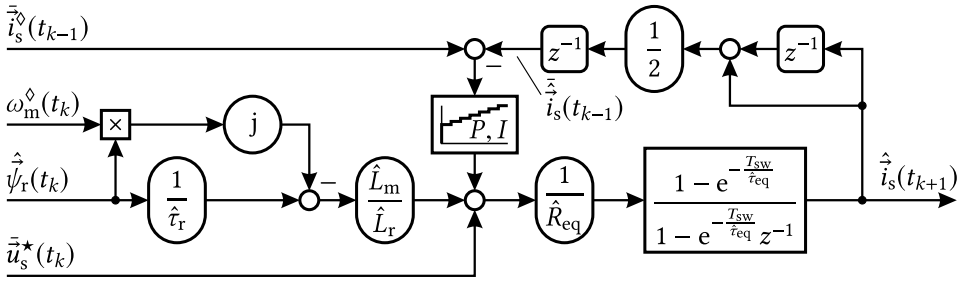

Fig. 3.12: Discrete-time single-step current predictor using the stator voltage reference [WL09].

The transfer function of the LPF can be discretized analogously to the current model in Fig. 3.10 using the ZOH equivalent. The resulting block diagram of the current predictor is given in Fig. 3.12.

The structure is comparable to that of a Smith predictor, but has a PI-controller in its feedback loop. The inputs of the LPF should ideally be switching-period average quantities like the stator-voltage reference. However, for the back EMF feed-forward term $\omega_m^{\Diamond}(t_k)$ and $\hat{\vec{\psi}}_r(t_k)$ are used, because more recent data is not available. The distortion caused by these unsynchronized inputs and parameter deviation can effectively be compensated by the PI-controller feedback, which has been chosen at a bandwidth between 0.5 and 2 kHz, in this work.

3.4 Summary

Starting from the fundamental open-loop current and voltage model of the IM, three closed-loop observers for the stator flux linkage have been presented. Inspired by the approach of Jansen et al. in [JL94], frequency-response functions for the relative steady-state estimation error were derived. They are the basis for an analytical parameter-sensitivity analysis in Chapter 4.

Beyond the state-of-the-art, the calculated frequency-response functions for the flux-linkage estimation error take into account the distortion of the measured current and voltage feedback and consider iron losses. Furthermore, the method has been applied to a class of full-order Luenberger-type observers.

Another contribution is the discrete-time implementation using switching-period average input signals. With the oversampling current- and voltage-sensing method, introduced in Chapter 5 and with proper selection of the hold equivalents, nearly zero discretization error is achieved. Using switching-period average quantities not only reduces measurement noise but also allows nearly ideal integration inside the voltage model and the LPF of the current model. Thus, no linear first-order approximation is required, except for the full-order observer current-model section.

4 The Torque Accuracy of the IM Drive – Analysis and Optimization

The torque generated by the IM drive relies on the functional interaction of its components presented in the previous chapters. The key requirements for precise torque production of the FOC-controlled IM drive are:

- Precise control of the stator current in the FOC reference frame and compensation of the stator iron losses.
- Accurate estimation of the stator flux-linkage magnitude and angle.
- Precise sensing of the stator current and determination of the stator terminal voltage.

The first has already been discussed in Chapter 2. By using a direct SFO controller, the parameter sensitivity of the torque controller is minimized. Stator iron losses are compensated by an additional quadrature current obtained by the steady-state model introduced in Section 2.1.3.3. Assuming ideal current measurement and an ideal estimation of the stator flux linkage, the stationary torque error is driven to zero by the current controller. Consequently, the torque accuracy can be analyzed based on the estimation error of the flux-linkage observer and the distortion of the measurement feedback.

With the analytical expressions for the stationary flux-linkage error derived in Chapter 3, the torque accuracy is analyzed for each parameter and balanced sensor-gain error, individually. The results are the basis for selecting the stator flux-linkage observer and suitable feedback gains. This approach was published in the course of this work under [SSD16] and is further developed in the following. Additionally, the effect of imbalanced sensor gains and offsets, and the influence of inverter voltage distortion is discussed.

Different methods for adaptive compensation of parameter faults and sensor offsets are presented and evaluated in dynamic simulations. The steady-state torque accuracy of the IM drive with and without parameter adaption is experimentally evaluated on the test bench.

4.1 Sensitivity of the Controller to Nonlinear Effects

The steady-state error expressions derived in Chapter 3 allow the calculation of the flux-linkage error as a function of the stator angular frequency ω_s for a given parameter deviation, e.g. $\hat{R}_\mathrm{s} \neq R_\mathrm{s}$, at a given slip angular frequency ω_sl. For the following considerations,

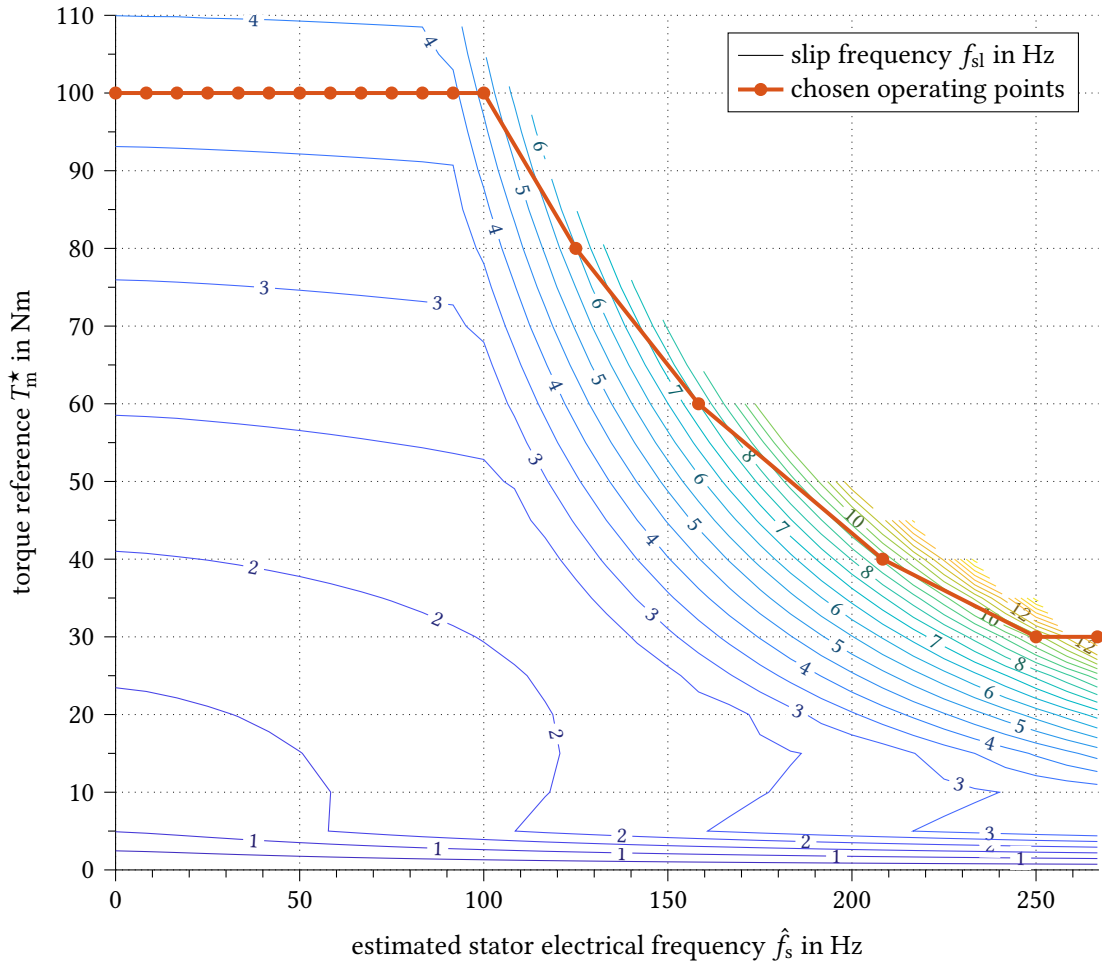

Fig. 4.1: Slip frequency as a function of the operating point of the efficiency-optimized IM drive with the operating points used for the worst-case torque accuracy analysis. Numerically calculated for IM26kA using the nonlinear extended IM model.

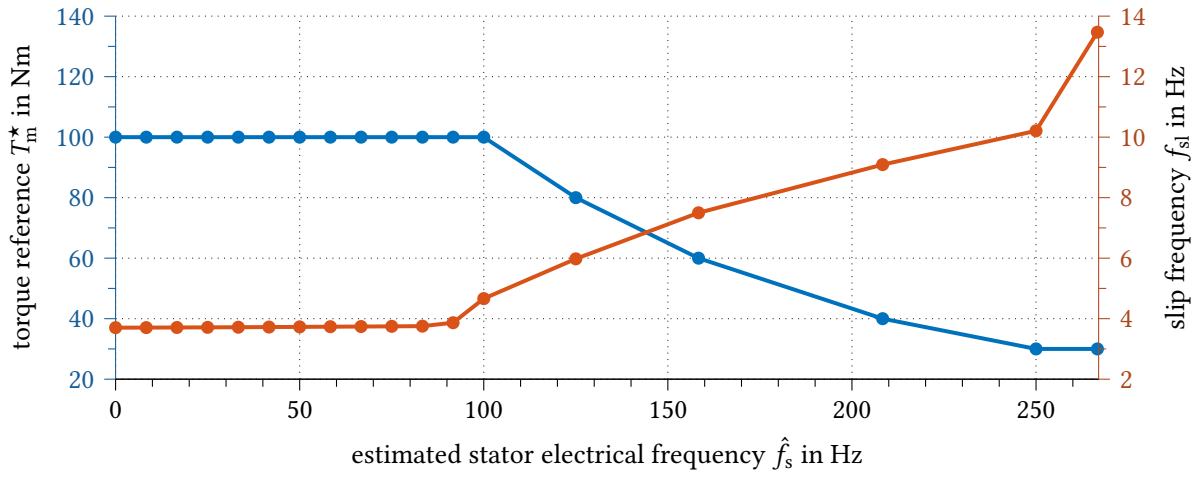

Fig. 4.2: Chosen slip frequency used for the worst-case torque accuracy analysis and the corresponding torque as a function of the stator electrical frequency for IM26kA.

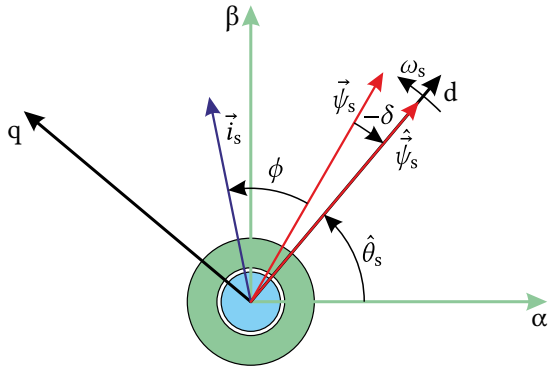

Fig. 4.3: Definition of the flux-linkage estimation error angle δ.

only a single parameter or sensor is assumed to be distorted at a time. The resulting flux-linkage magnitude and angle deviation are plotted as a function of the rotor rotational speed $n_m = 60 \cdot (\omega_s - \omega_{sl})/2\pi p$. This allows better comparability to the measurements.

The slip frequency is chosen according to the operating points of maximum power, highlighted in Fig. 4.1. It has been calculated for the efficiency-optimized IM drive using the extended nonlinear IM model introduced in Section 2.1.3 and using Equation (2.34) on page 31 with the values given in Table A.3. The resulting slip frequency profile is plotted in Fig. 4.2 as a function of the stator electrical frequency along with the reference air-gap torque. It is about 3.75 Hz in the base-speed region and rises up to 13.5 Hz in the field-weakening region above 2460 rpm.

To calculate the torque deviation resulting from the flux-linkage estimation error, the FOC current controller is assumed to be ideal and may be considered as an ideal current source. With the torque equation (2.1) rewritten as

$$T_m = \frac{3}{2} \cdot p \cdot \psi_s \cdot i_s \cdot \sin\phi, \tag{4.1}$$

an expression for the steady-state torque error can be derived as

$$\underline{F}_T(j\omega_s) = \frac{\hat{T}_m}{T_m} = \frac{\hat{\psi}_s}{\psi_s} \cdot \frac{i_s^\Diamond}{i_s} \cdot \frac{\sin(\phi - \delta)}{\sin\phi} = \frac{\hat{\psi}_s}{\psi_s} \cdot \frac{i_s^\Diamond}{i_s} \cdot (\cos\delta - \sin\delta \cot\phi). \tag{4.2}$$

$i_s^\Diamond/i_s$ represents the balanced current-sensor-gain error contributed by the current controller. δ is the angle from the stator flux-linkage space vector to its estimated value, according to the definition in Fig. 4.3. The angle between the flux linkage and the stator-current space vector ϕ can by calculated with the help of Equation (3.3) as

$$\phi = \arctan \frac{\mathrm{Im}\left\{\underline{i}_s/\underline{\psi}_s\right\}}{\mathrm{Re}\left\{\underline{i}_s/\underline{\psi}_s\right\}} = \arctan \frac{\omega_{sl}\tau_r(1-\sigma) + \omega_s \dfrac{L_s}{R_{fe}}\left(1 + \omega_{sl}^2\sigma^2\tau_r^2\right)}{1 + \omega_{sl}^2\sigma\tau_r^2}. \tag{4.3}$$

TABLE 4.1
Assumed Worst-Case Parameter Deviation

parameter	R_s	R_r	L_m	$L_{\sigma\mathrm{s}}$	$L_{\sigma\mathrm{r}}$
uncertainty	low to medium	very high	medium	very high	very high
max. deviation ratio	1.2	1.5	1.2	1.5	1.5

(4.3) inserted in (4.2) gives the frequency-response function of the resulting torque error

$$\underline{F}_\mathrm{T}(\mathrm{j}\omega_\mathrm{s}) = \frac{\hat{\psi}_\mathrm{s}}{\psi_\mathrm{s}} \cdot \frac{i_\mathrm{s}^{\diamondsuit}}{i_\mathrm{s}} \cdot \left(\cos\delta - \sin\delta \cdot \frac{1 + \omega_\mathrm{sl}^2 \sigma \tau_\mathrm{r}^2}{\omega_\mathrm{sl}\tau_\mathrm{r}(1-\sigma) + \omega_\mathrm{s}\dfrac{L_\mathrm{s}}{R_\mathrm{fe}}\left(1 + \omega_\mathrm{sl}^2\sigma^2\tau_\mathrm{r}^2\right)} \right). \tag{4.4}$$

4.1.1 Induction Machine Parameter Deviation

Due to magnetic saturation, thermal drift and the frequency-dependent rotor deep-bar effect, the machine parameters of the fundamental IM model used for the FOC vary with operating point and time. The worst-case torque error caused by a particular parameter is calculated based on its assumed maximum deviation.

In this work, the parameter deviation is defined as the ratio of the estimated to the actual parameter. Based on the parameter-uncertainty considerations summarized in Table 2.4, the maximum parameter deviation has been defined according to Table 4.1. Since the stator resistance and the main inductance can be determined with sufficient accuracy during parameterization, they are classified as rather certain with a maximum error ratio of 1.2. Even though both vary significantly during operation, they can be easily adapted based on temperature sensing at the end winding and using the saturation model given in Section 2.1.3.1. However, the rotor resistance and leakage inductances are difficult to parameterize, and reliable adaption algorithms do not exist. Therefore, they are classified as rather uncertain with a maximum error ratio of 1.5.

4.1.1.1 Open-Loop Observers

Fig. 4.4 shows the resulting estimation error of the open-loop flux-linkage observers. The stator-resistance curve in blue belongs to the voltage model (3.8) and the others to the current model (3.4). The results are specific for a particular machine which is IM26kA in this case. The flux-linkage observers do not take into account the iron losses. However, the torque deviation caused by the stator iron losses is very small for this machine. R_fe causes only 0.3 % torque deviation and 0.3° angle error at its maximum point in the field-weakening region and will therefore not be plotted for the following cases.

Since the current model in Equation (3.4) is independent from the mechanical rotor frequency and the slip frequency is nearly constant, the resulting curves in Fig. 4.4 are

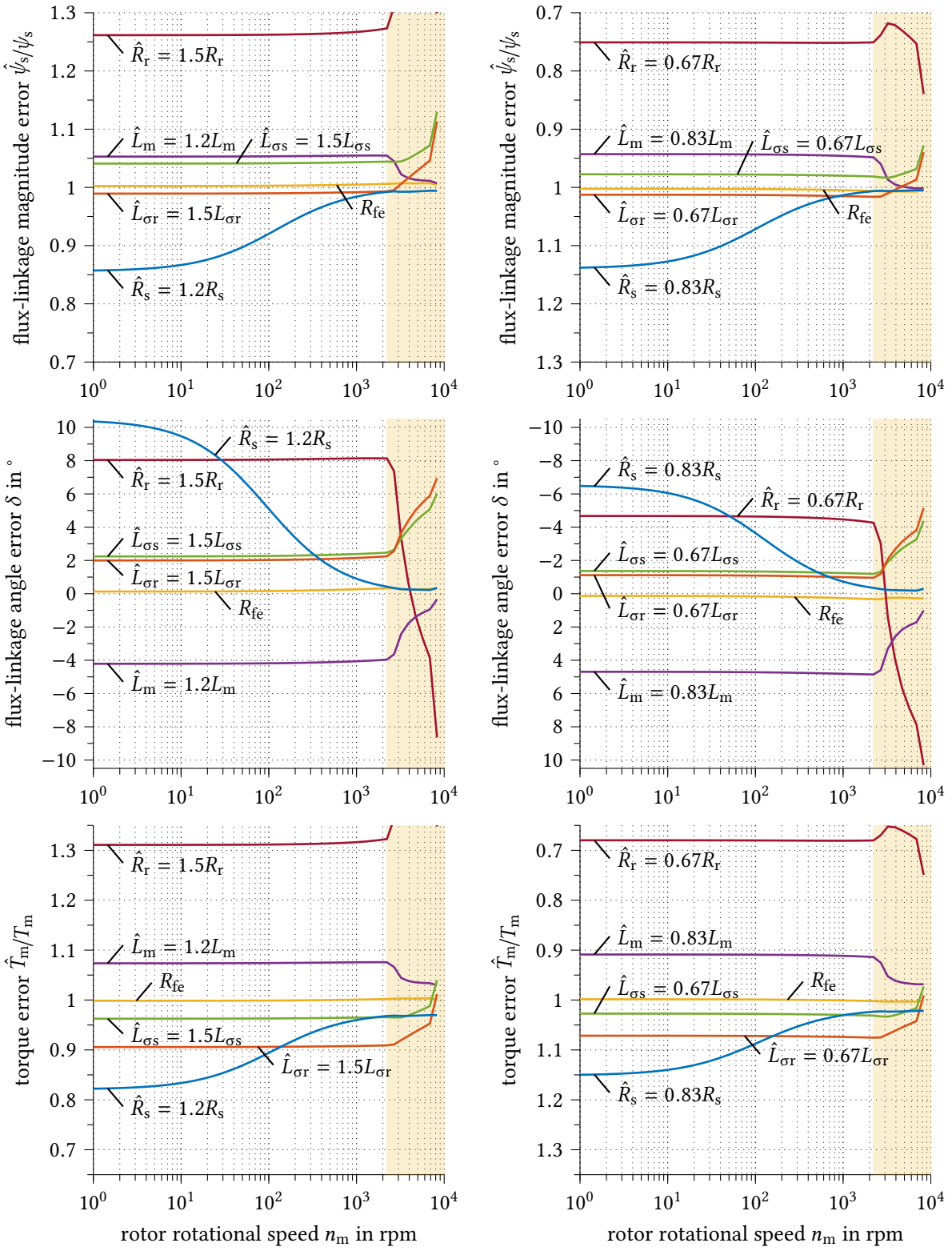

(a) $\hat{X} > X$ (b) $\hat{X} < X$

Fig. 4.4: Steady-state error of the open-loop flux-linkage observers and resulting torque error as a function of the IM parameter for IM26kA with $X = R_s, R_r, L_m, \ldots$.

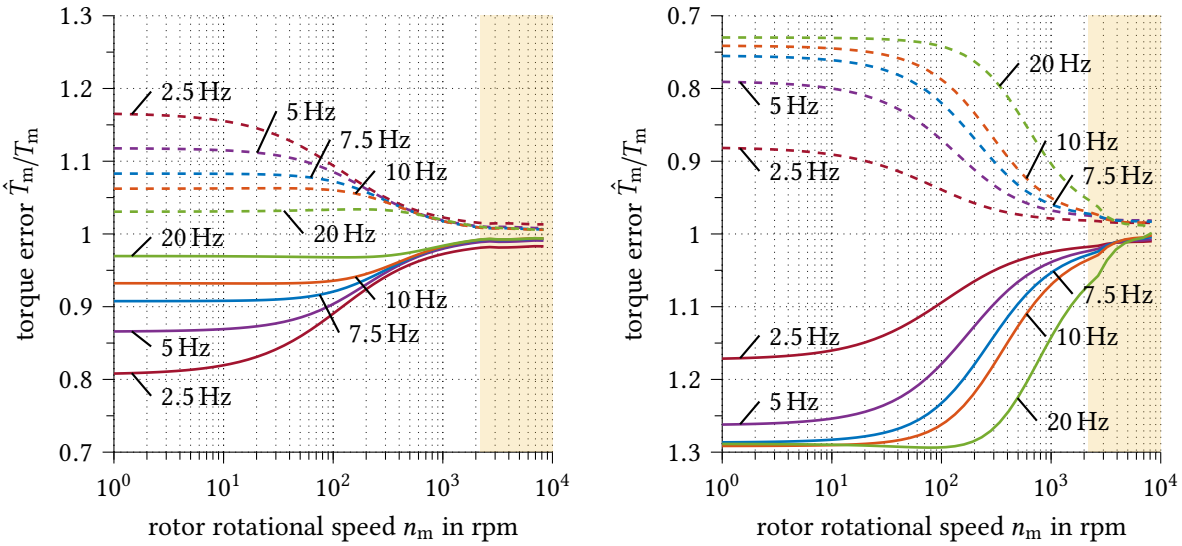

(a) solid: $\hat{R}_s = 1.2R_s$, dashed: $\hat{R}_s = 0.83R_s$

(b) solid: $\hat{R}_r = 1.5R_r$, dashed: $\hat{R}_r = 0.67R_r$

Fig. 4.5: Steady-state torque error caused by stator- and rotor-resistance drift as a function of the observer PI controller bandwidth for IM26kA.

almost straight lines, except for the field-weakening region indicated by the shaded area. The current model is very sensitive to rotor-resistance deviation which causes up to 32 % torque error at base speed and even more during field weakening. The sensitivity to the main inductance and the rotor leakage inductance is also notable with up to 10 % torque error. Even though the flux-linkage magnitude error caused by $L_{\sigma s}$ is similar to that caused by L_m, the resulting torque error is lower because it is partially compensated by the angle error. For the other parameters, the angle error leads to higher torque deviation.

The voltage model is only sensitive to the stator resistance. Due to the stator frequency in the denominator of Equation (3.8), the influence of R_s decreases significantly with increasing rotational speed. However, at very low speed it causes up to 18 % torque error and an angular detuning of more than 10°.

4.1.1.2 Closed-Loop Voltage-Model Observer with Current-Model Feedback

According to the results of the open-loop models, it is advantageous to combine the low-frequency characteristics of the current model with the characteristics of the voltage model at high speeds. This can be achieved using the Gopinath-style observer introduced in [JLN94] and described in Section 3.2.1. The PI-controller in the stationary reference frame offers a smooth transition between both models and eliminates the open-integration problem of the voltage model.

The transition frequency is equal to the bandwidth of the PI-controller and is chosen based on the torque deviation caused by stator- and rotor-resistance drift in Fig. 4.5. Above 200 rpm, the influence of the bandwidth on the sensitivity to R_s in Fig. 4.5a is very limited,

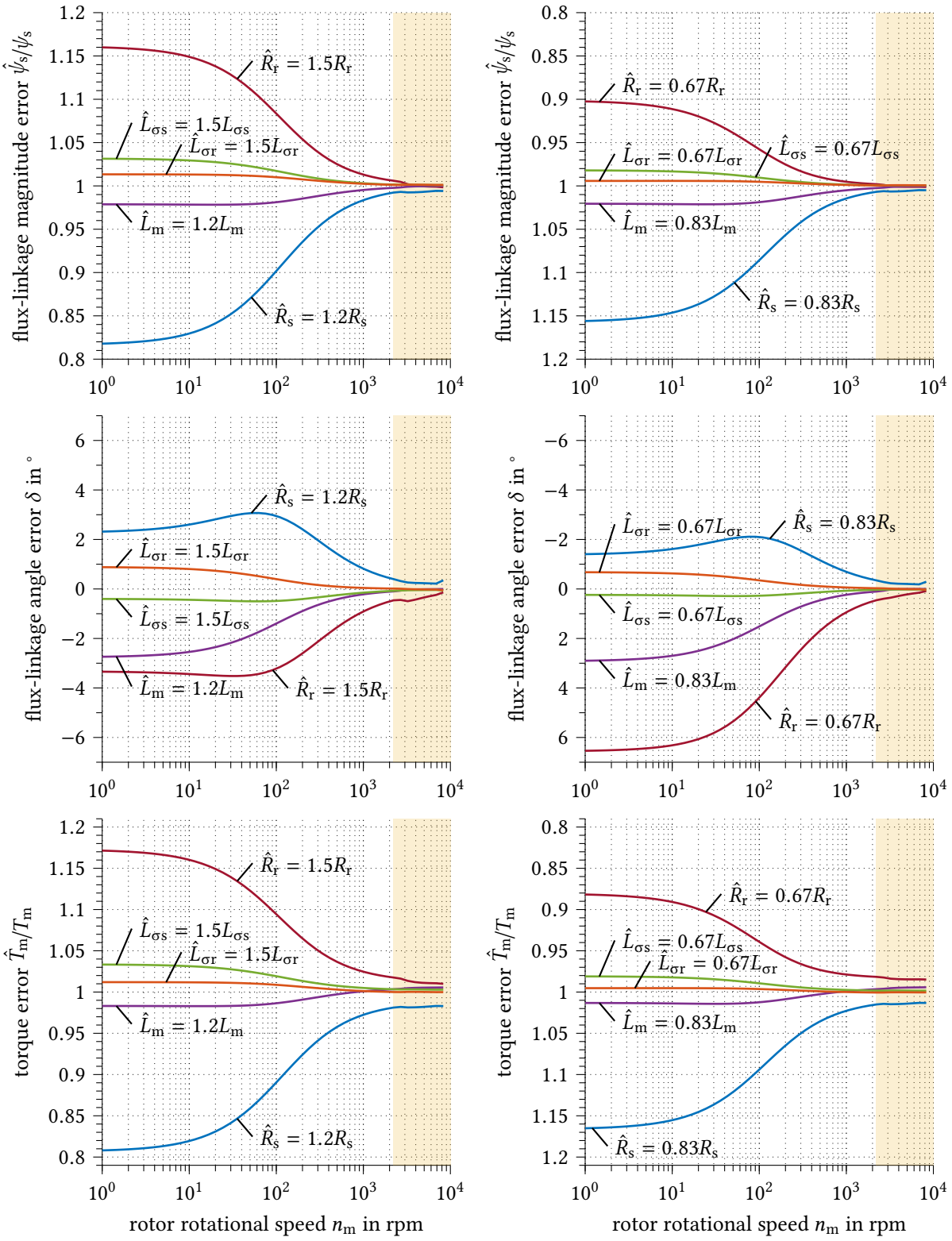

(a) $\hat{X} > X$ (b) $\hat{X} < X$

Fig. 4.6: Steady-state error of the Gopinath-style flux-linkage observer and resulting torque error as a function of the IM parameter for IM26kA.

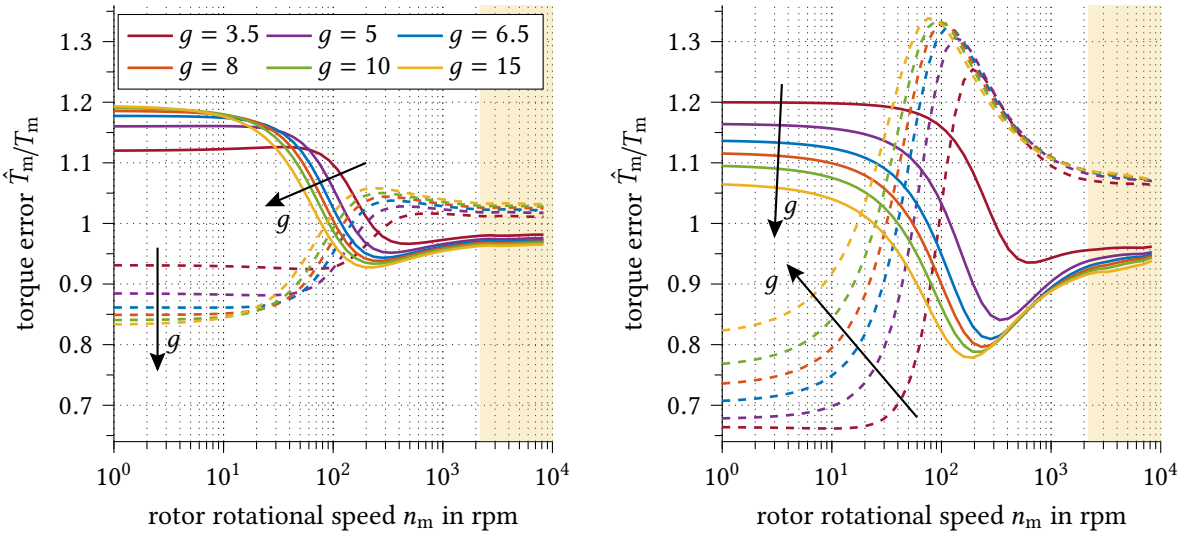

(a) solid: $\hat{R}_s = 1.2R_s$, dashed: $\hat{R}_s = 0.83R_s$

(b) solid: $\hat{R}_r = 1.5R_r$, dashed: $\hat{R}_r = 0.67R_r$

Fig. 4.7: Steady-state torque error caused by stator- and rotor-resistance drift as a function of the observer proportional pole-placement design factor g for IM26kA.

whereas a lower bandwidth significantly reduces the sensitivity to R_r in Fig. 4.5b. Thus, above 200 rpm a low bandwidth is desirable. At lower speeds, a low bandwidth suppresses the rotor-resistance-induced error but increases the sensitivity to stator-resistance drift. The PI-controller bandwidth also defines the dynamic response to sensor offsets. In this work, the bandwidth is chosen at 2.5 Hz which is a good compromise and ensures sufficient dynamics for the compensation of offsets.

The resulting steady-state parameter sensitivity is analyzed using Equation (3.14) and leads to the curves plotted in Fig. 4.6. Because the PI-controller bandwidth is lower than the slip frequency, the stator-resistance-induced torque error is nearly unchanged compared to the open-loop voltage model. However, the angular detuning is improved by more than 70 % at low speed. The sensitivity to the current-model parameters is significantly reduced, especially above 100 rpm.

4.1.1.3 Full-Order Luenberger-Type Closed-Loop Observer

The parameter sensitivity of the full-order Luenberger-type flux-linkage observer is investigated using Equation (3.26) with (3.8) and (3.4). The feedback gains are again chosen based on the stator- and rotor-resistance-induced torque error for the proportional pole placement method in Fig. 4.7, and the left-shift method in Fig. 4.8.

The influence of the proportional design factor g in Equation (A.10) on the stator-resistance induced torque error in Fig. 4.7a is limited. Above $g = 5$ the resulting maximum error below 100 rpm stays relatively constant, but higher values shift the error curve towards lower speeds, which increases the region of low error at higher speeds. The sensitivity to rotor-resistance deviation in Fig. 4.7b decreases with increasing design factor

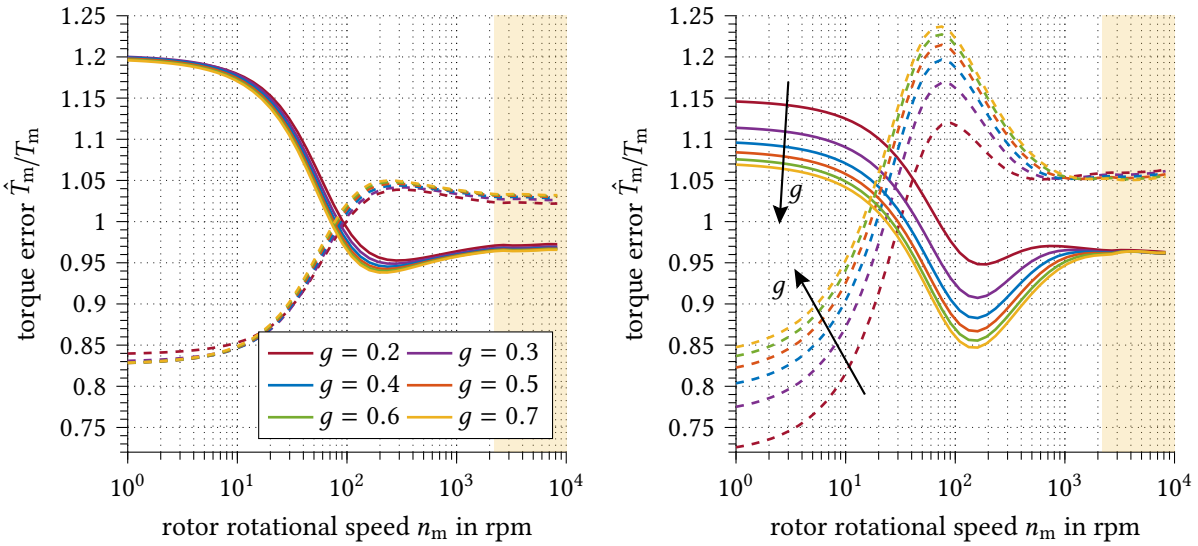

(a) solid: $\hat{R}_s = 1.2R_s$, dashed: $\hat{R}_s = 0.83R_s$

(b) solid: $\hat{R}_r = 1.5R_r$, dashed: $\hat{R}_r = 0.67R_r$

Fig. 4.8: Steady-state torque error caused by stator- and rotor-resistance drift as a function of the observer left-shift pole-placement design factor g for IM26kA.

g, except for the area of a local maximum between 50 and 500 rpm. In the following, $g = 10$ is chosen for the proportional design factor.

In the case of left-shift pole placement, the design factor g in Equation (A.12) has no significant influence on the sensitivity to stator-resistance drift, as shown in Fig. 4.8a. The torque error caused by rotor-resistance deviation is given in Fig. 4.8b and has a local maximum at around 100 rpm, which is similar to the proportional case. The local maximum reduces with decreasing design factor at the cost of a higher torque error below 20 rpm. With $g = 0.3$ a relatively low value is chosen for the following considerations.

A major difference of both placement methods is the dynamic behavior at different rotational speeds. Due to the proportional placement, at low speed in Fig. 3.5, the poles of the first method are very close to the IM poles, which leads to a comparably slow convergence rate. Thus, a rather high design factor must be chosen to ensure sufficient convergence at very low speed. With increasing rotor speed, the observer with proportional poles converges increasingly fast, which can cause stability issues. In contrast, the left-shift pole placement offers a rather constant convergence rate at all speeds. Both characteristics can be beneficial depending on the design goals.

The steady-state flux-linkage magnitude error, the angle deviation and the resulting torque error are given in Fig. 4.9 for the proportional poles and in Fig. 4.10 for the left-shifted poles, respectively. Both lead to qualitatively similar results with a high sensitivity to rotor-resistance mismatch and a considerable angular misalignment which is about five times higher than with the Gopinath-style observer. In the low-speed region, the full-order observer is also more sensitive to main-inductance and leakage-inductance deviation but performs slightly better in terms of stator-resistance drift. Above 1000 rpm, the full-order

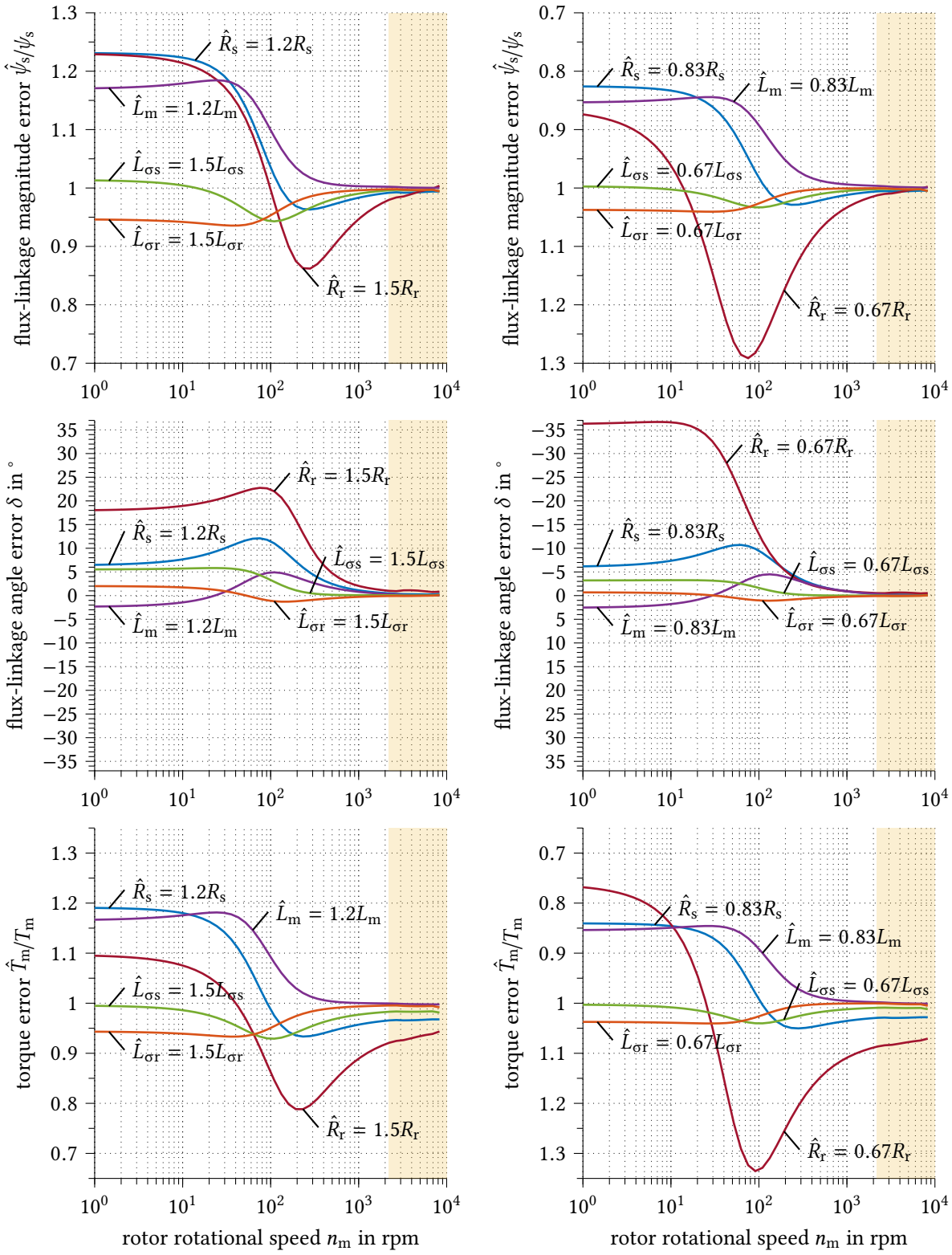

(a) $\hat{X} > X$ (b) $\hat{X} < X$

Fig. 4.9: Steady-state error of the full-order flux-linkage observer with proportional pole placement ($g = 10$) and resulting torque error as a function of the IM parameter for IM26kA.

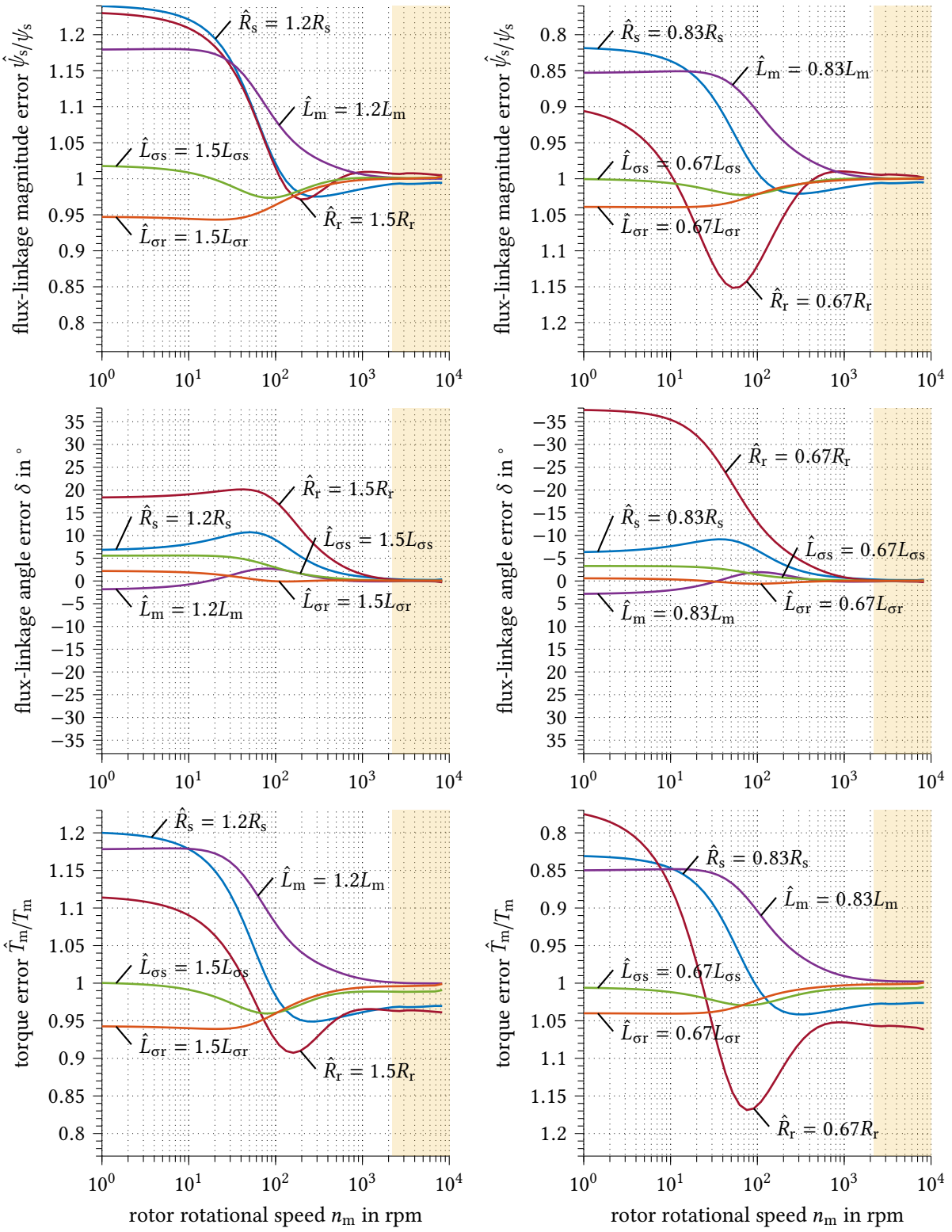

(a) $\hat{X} > X$ (b) $\hat{X} < X$

Fig. 4.10: Steady-state error of the full-order flux-linkage observer with left-shift pole placement ($g = 0.3$) and resulting torque error as a function of the IM parameter for IM26kA.

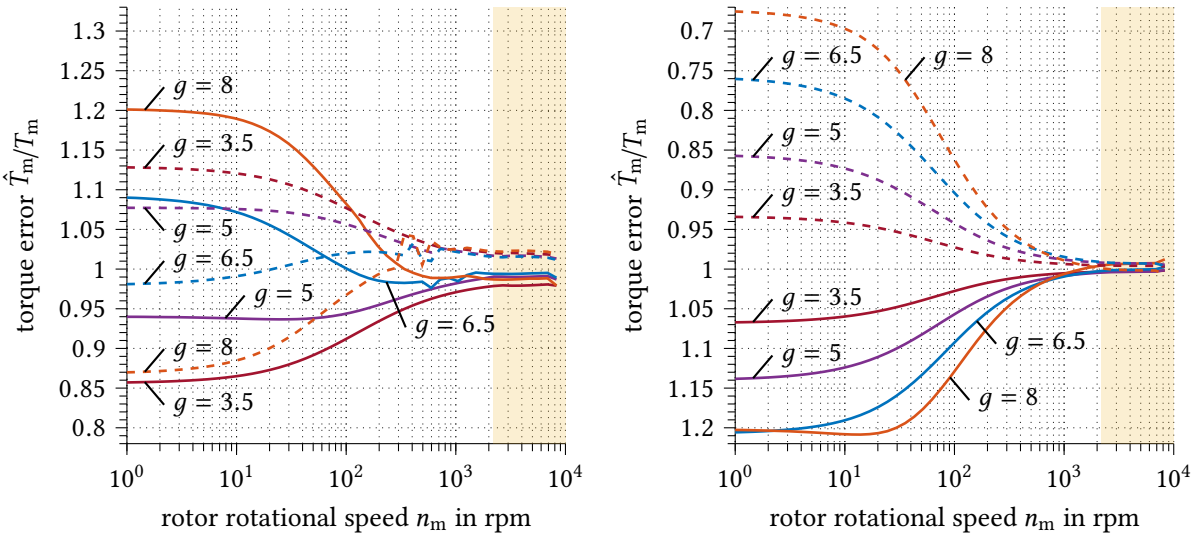

(a) solid: $\hat{R}_s = 1.2R_s$, dashed: $\hat{R}_s = 0.83R_s$

(b) solid: $\hat{R}_r = 1.5R_r$, dashed: $\hat{R}_r = 0.67R_r$

Fig. 4.11: Steady-state torque error caused by stator- and rotor-resistance drift as a function of the sliding-mode observer proportional pole-placement design factor g for IM26kA.

observer is not able to suppress the rotor-resistance induced torque error to a value below 5 %, which is about three times more when compared to the Gopinath-style observer. The sensitivity to inductance and stator resistance deviation is similar, though. Compared to the proportional-pole approach, the left-shift pole placement method leads to slightly better results in the whole operating range.

4.1.1.4 Full-Order Closed-Loop Observer with Sliding-Mode Feedback

Due to the nonlinear feedback, the sliding-mode observer cannot be analyzed analytically. Instead, the observer is implemented in discrete time, according to Section 3.3, and is analyzed in simulation using MATLAB/SIMULINK with the simulation model described in Appendix A.4. Each curve consists of 50 simulation runs at different rotational speed for a given distorted parameter and observer-gain design factor g. To obtain steady-state results, the model is simulated for 10 s at a given stator and rotor frequency. The result is taken from the mean value of the last simulated second.

For the sliding-mode observer, the same pole-placement methods as in the previous cases are used. The torque error resulting from stator- and rotor-resistance deviation with different proportional poles is shown in Fig. 4.11. Compared to the linear case, a lower design factor is advantageous. The influence of R_s is minimal between $g = 5$ and $g = 6.5$. Since the sensitivity to R_r reduces with decreasing design factor, $g = 5$ is selected. The left-shifted poles are chosen to the benefit of a reduced sensitivity to rotor-resistance drift with $g = 0.3$, according to Fig. 4.12. Therefore, a higher sensitivity to stator-resistance drift must be accepted.

The sensitivity plots for all observer parameters are given in Fig. 4.13 for the proportional

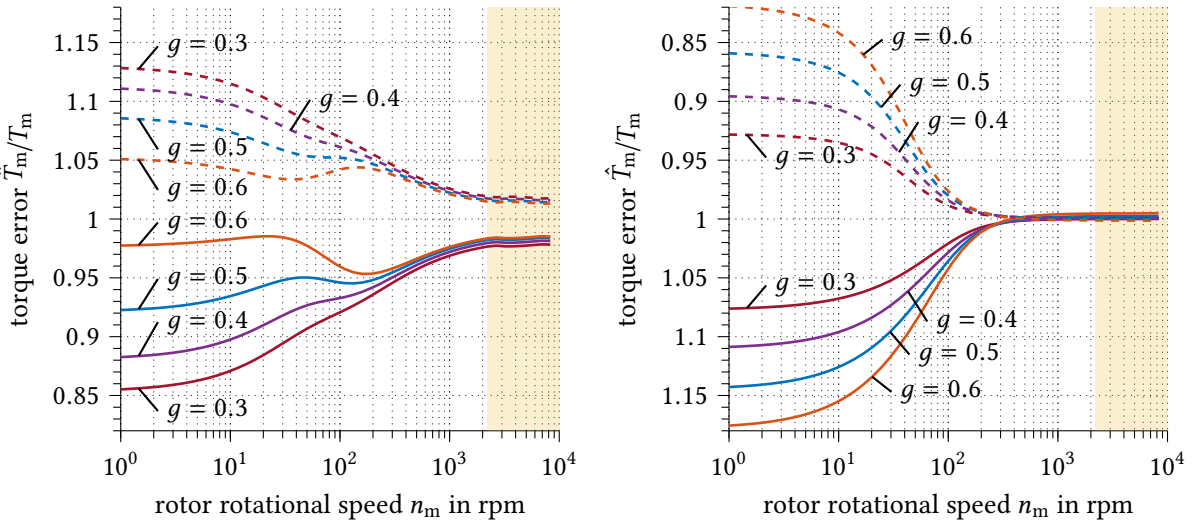

(a) solid: $\hat{R}_s = 1.2R_s$, dashed: $\hat{R}_s = 0.83R_s$

(b) solid: $\hat{R}_r = 1.5R_r$, dashed: $\hat{R}_r = 0.67R_r$

Fig. 4.12: Steady-state torque error caused by stator- and rotor-resistance drift as a function of the sliding-mode observer left-shift pole-placement design factor g for IM26kA.

poles and in Fig. 4.14 for the left-shifted poles. The first is more sensitive to the current-model parameters, whereas the latter is more sensitive to the stator resistance of the voltage model. Compared to the linear-feedback Luenberger-type observer, the overall sensitivity is significantly reduced by the switching-function feedback. Especially the angular deviation is improved by a factor of seven. The local maximum for R_r at around 100 rpm is fully eliminated.

At very low speed, the torque deviation caused by thermal drift of the resistances is below 14 %, which is about four percentage points lower than with the Gopinath-style observer in Fig. 4.6. However, the sliding-mode observer is more sensitive to deviations in the inductance values, especially in case of the main inductance which causes a four times higher torque deviation of up to 11 % with proportional poles and 4 % with left-shifted poles. With up to 5 %, the sensitivity to the rotor leakage inductance is five times higher than with the Gopinath-style observer.

Above 1000 rpm, the stator resistance still causes a torque error of up to 2 % which is equal to the Gopinath-style observer. The sensitivity to the other parameters is very low, but higher than with the Gopinath-style observer, especially in the case of proportional pole placement.

Even though the sensitivity to the stator resistance is higher, the left-shifted observer poles are preferable because adaption of R_s is simpler than for the highly uncertain current-model parameters. With left-shifted poles, the influence of the current-model parameters – including the rotor resistance – is effectively suppressed above 200 rpm, which is a notable improvement over the Gopinath-style observer. However, in the presence of a sufficient adaption algorithm for both resistances, the Gopinath-style observer is preferable due to its insensitivity to main- and leakage-inductance saturation.

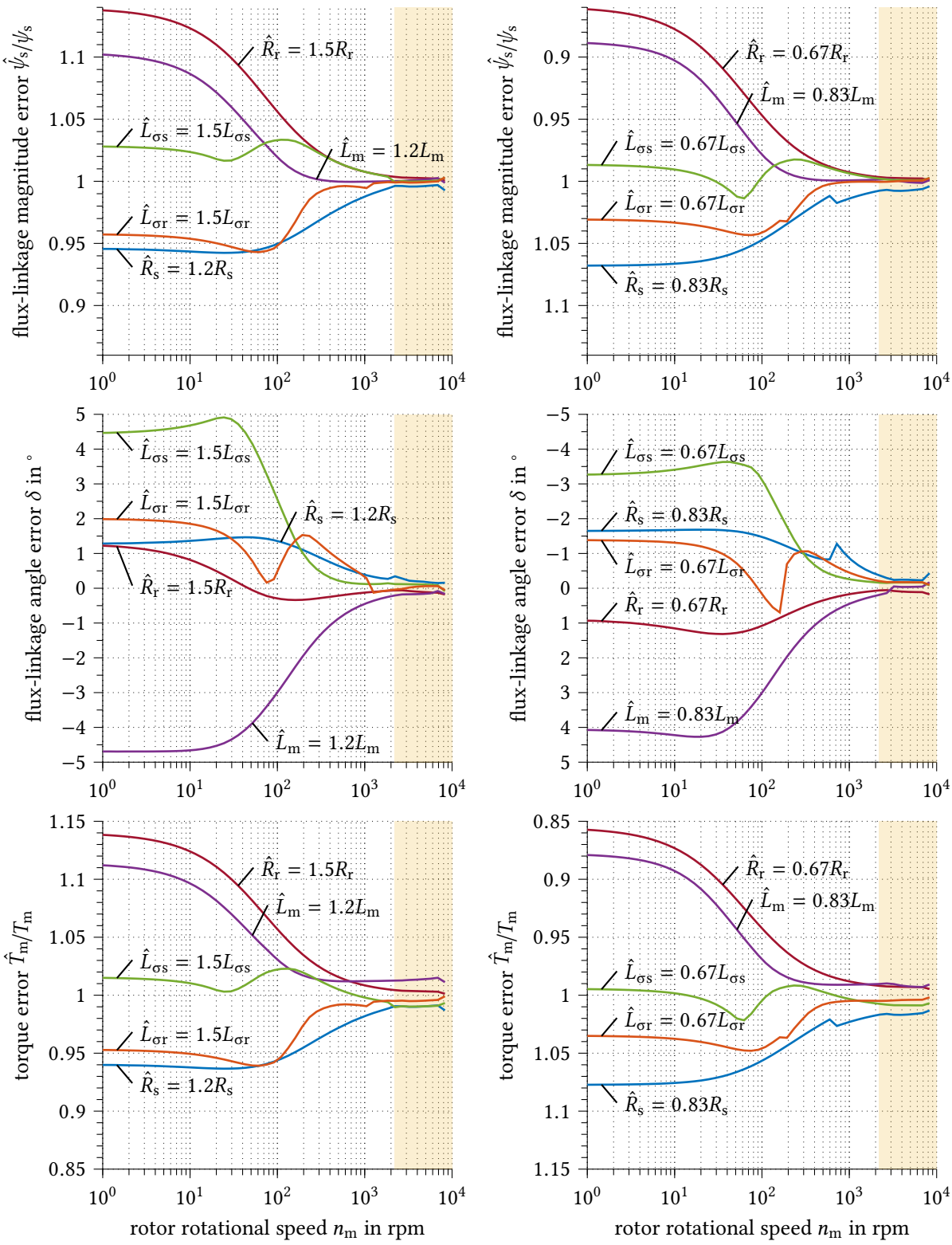

(a) $\hat{X} > X$ (b) $\hat{X} < X$

Fig. 4.13: Steady-state error of the sliding-mode flux-linkage observer with proportional pole placement ($g = 5$) and resulting torque error as a function of the IM parameter for IM26kA.

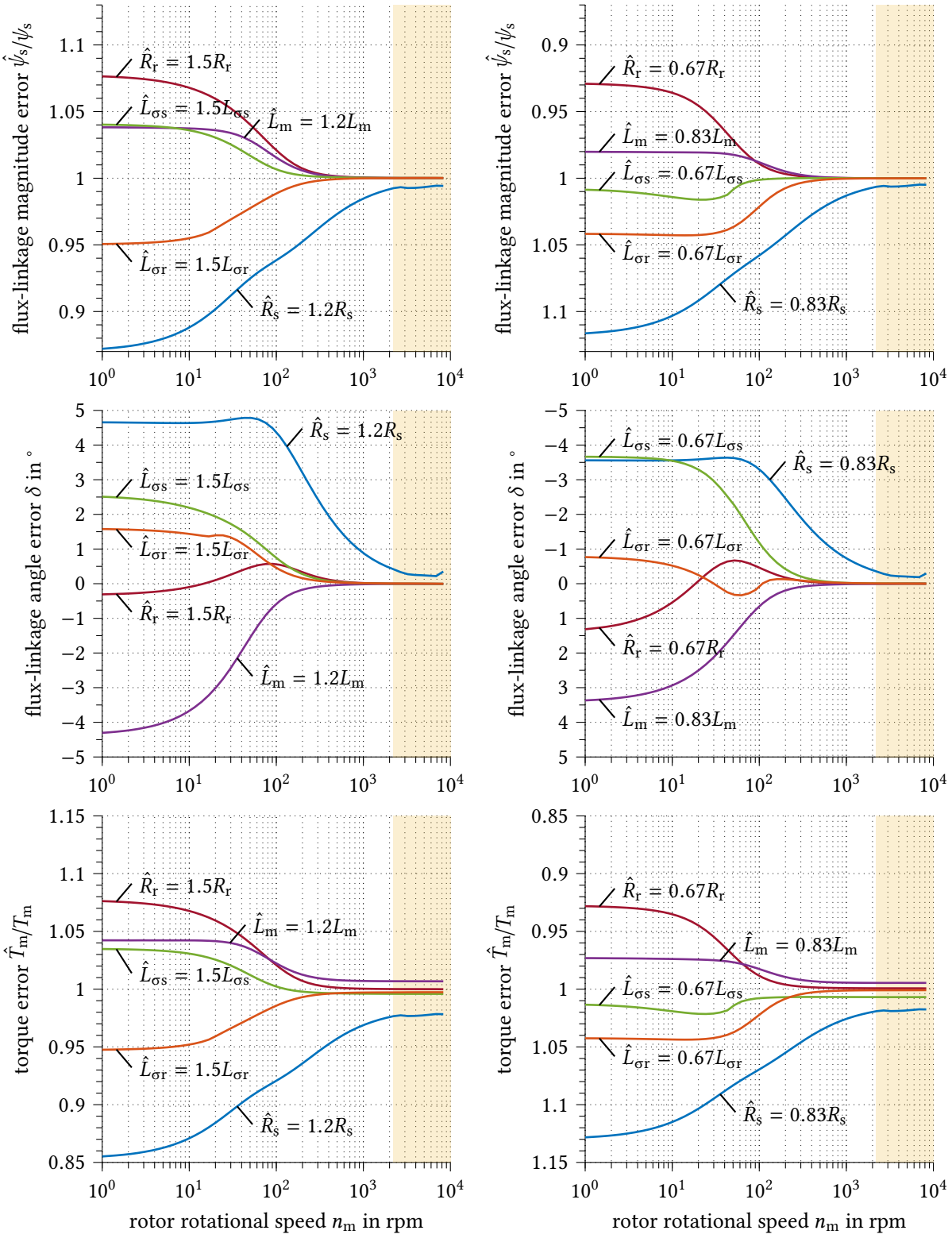

(a) $\hat{X} > X$ (b) $\hat{X} < X$

Fig. 4.14: Steady-state error of the sliding-mode flux-linkage observer with left-shift pole placement ($g = 0.3$) and resulting torque error as a function of the IM parameter for IM26kA.

4.1.2 Measurement-Feedback Distortion

Besides the model parameter sensitivity, the robustness of the observer against deviations in the current- and voltage-sensor signals is important to achieve an optimal torque accuracy of the drive system. The inverter used in this work is equipped with three current and three output-terminal voltage sensors. Due to parasitic effects, such as temperature dependency of analog-circuit components, each sensor is subject to individual offset $i_{\mathrm{ph,off}}$ and gain errors $g_{\mathrm{ph}} \neq 1$, which are analyzed in the following. The sensors are assumed to be perfectly linear and without hysteresis. The latter will be addressed later in Chapter 5. The considerations below are valid for using three sensors. However, the common special case with only two current sensors leads to analogous results, as shown in Appendix A.6.

Assuming sinusoidal currents during steady-state with $\measuredangle \vec{i}_{\mathrm{s}}(t=0) = 0$, the three measured phase currents can be described as

$$i^{\Diamond}_{\mathrm{ph1}} = g_{\mathrm{ph1}} \cdot i_{\mathrm{s}} \cos(\omega_{\mathrm{s}} t) + i_{\mathrm{ph1,off}}, \tag{4.5a}$$

$$i^{\Diamond}_{\mathrm{ph2}} = g_{\mathrm{ph2}} \cdot i_{\mathrm{s}} \cos\left(\omega_{\mathrm{s}} t - \frac{2\pi}{3}\right) + i_{\mathrm{ph2,off}} \tag{4.5b}$$

$$\text{and} \quad i^{\Diamond}_{\mathrm{ph3}} = g_{\mathrm{ph3}} \cdot i_{\mathrm{s}} \cos\left(\omega_{\mathrm{s}} t + \frac{2\pi}{3}\right) + i_{\mathrm{ph3,off}}. \tag{4.5c}$$

Using the Clarke transformation (A.1) and with the help of the addition theorems for trigonometric functions, the real and imaginary parts of the measured stator-current space vector are found as

$$\begin{aligned} i^{\Diamond}_{\mathrm{s}\alpha} &= \frac{4g_{\mathrm{ph1}} + g_{\mathrm{ph2}} + g_{\mathrm{ph3}}}{6} i_{\mathrm{s}} \cos(\omega_{\mathrm{s}} t) - \frac{g_{\mathrm{ph2}} - g_{\mathrm{ph3}}}{2\sqrt{3}} i_{\mathrm{s}} \sin(\omega_{\mathrm{s}} t) \\ &\quad + \frac{2i_{\mathrm{ph1,off}} - i_{\mathrm{ph2,off}} - i_{\mathrm{ph3,off}}}{3} \\ \text{and} \quad i^{\Diamond}_{\mathrm{s}\beta} &= \frac{g_{\mathrm{ph2}} + g_{\mathrm{ph3}}}{2} i_{\mathrm{s}} \sin(\omega_{\mathrm{s}} t) - \frac{g_{\mathrm{ph2}} - g_{\mathrm{ph3}}}{2\sqrt{3}} i_{\mathrm{s}} \cos(\omega_{\mathrm{s}} t) + \frac{i_{\mathrm{ph2,off}} - i_{\mathrm{ph3,off}}}{\sqrt{3}}. \end{aligned} \tag{4.6}$$

By expanding the trigonometric terms and after some rearrangements, the measured current can be written in polar form as

$$\begin{aligned} \vec{i}^{\,\Diamond}_{\mathrm{s}} = &\underbrace{\frac{g_{\mathrm{ph1}} + g_{\mathrm{ph2}} + g_{\mathrm{ph3}}}{3}}_{\text{balanced error } \vec{i}^{\,\Diamond}_{\mathrm{s,pos}}/\vec{i}_{\mathrm{s}}} \underbrace{i_{\mathrm{s}} \mathrm{e}^{\mathrm{j}\omega_{\mathrm{s}} t}}_{\vec{i}_{\mathrm{s}}} + \underbrace{\left(\frac{2g_{\mathrm{ph1}} - g_{\mathrm{ph2}} - g_{\mathrm{ph3}}}{6} - \mathrm{j}\frac{g_{\mathrm{ph2}} - g_{\mathrm{ph3}}}{2\sqrt{3}}\right) i_{\mathrm{s}} \mathrm{e}^{-\mathrm{j}\omega_{\mathrm{s}} t}}_{\text{imbalanced sensor-gain error } \vec{i}^{\,\Diamond}_{\mathrm{s,neg}}} \\ &+ \underbrace{\frac{2i_{\mathrm{ph1,off}} - i_{\mathrm{ph2,off}} - i_{\mathrm{ph3,off}}}{3} + \mathrm{j}\frac{i_{\mathrm{ph2,off}} - i_{\mathrm{ph3,off}}}{\sqrt{3}}}_{\text{sensor-offset error } \vec{i}^{\,\Diamond}_{\mathrm{s,off}}}. \end{aligned} \tag{4.7}$$

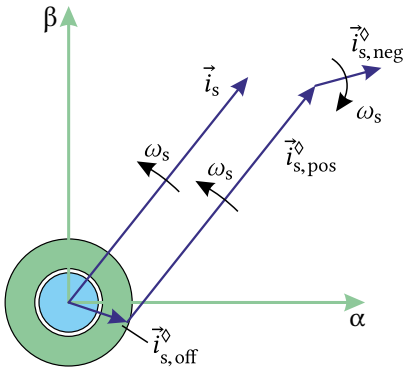

Fig. 4.15: Offset, positive and negative-sequence components of the measured stator-current space vector, caused by sensor offset and imbalanced sensor-gain errors. The resulting measured current space vector follows an ellipse at steady-state, shifted by the offset error.

Consequently, the measured current can be represented by a constant offset component $\vec{i}_{s,off}^{\lozenge}$, a positive-sequence component $\vec{i}_{s,pos}^{\lozenge}$ and a negative-sequence component $\vec{i}_{s,neg}^{\lozenge}$, as illustrated in Fig. 4.15. The error caused by the voltage sensors can be derived analogously by repeating (4.5) to (4.7) using the stator voltage in place of the stator current.

4.1.2.1 Balanced Sensor-Gain Error

The positive-sequence component compromises the original signal which is scaled by a real factor of balanced sensor-gain errors with $g_{ph1} = g_{ph2} = g_{ph3} \neq 1$. Therefore, this signal component does not experience any phase shift. When transformed to the field-oriented reference frame, it appears as a stationary current or voltage-sensor error in the steady-state. The resulting stationary flux-linkage and torque error can be calculated using the same approach applied to the model parameter deviation in the previous section. Both are dependent on the IM parameters and the flux-linkage observer used for the direct FOC. Fig. 4.16 shows the results for the Gopinath-style, Fig. 4.17 for the full-order Luenberger-type and Fig. 4.18 for the sliding-mode observer. The latter has been obtained from simulations and the other two from Equation (3.14) and (3.26), respectively. The required expressions for the open-loop current model (3.5) and the voltage model (3.9) and (3.11) have been derived in Section 3.1.

According to Fig. 4.16a, above 1000 rpm, the Gopinath-style observer is insensitive to balanced current-sensor errors. The torque error is only caused by the current controller with a magnitude equal to the sensor error. At lower speeds, the influence of the current model increases and causes a flux-linkage estimation error with comparably low angular detuning. The error magnitude is lower and inverted compared to the current-sensor error. This leads to a reduction of the superimposed torque error at low speeds.

The flux-linkage estimation error caused by voltage-sensor error is given in Fig. 4.16b. Above 1000 rpm, the estimation error is equal to the sensor deviation with zero angle error. At lower speeds, the error increases to up to 1.75 times the sensor deviation. Due to the

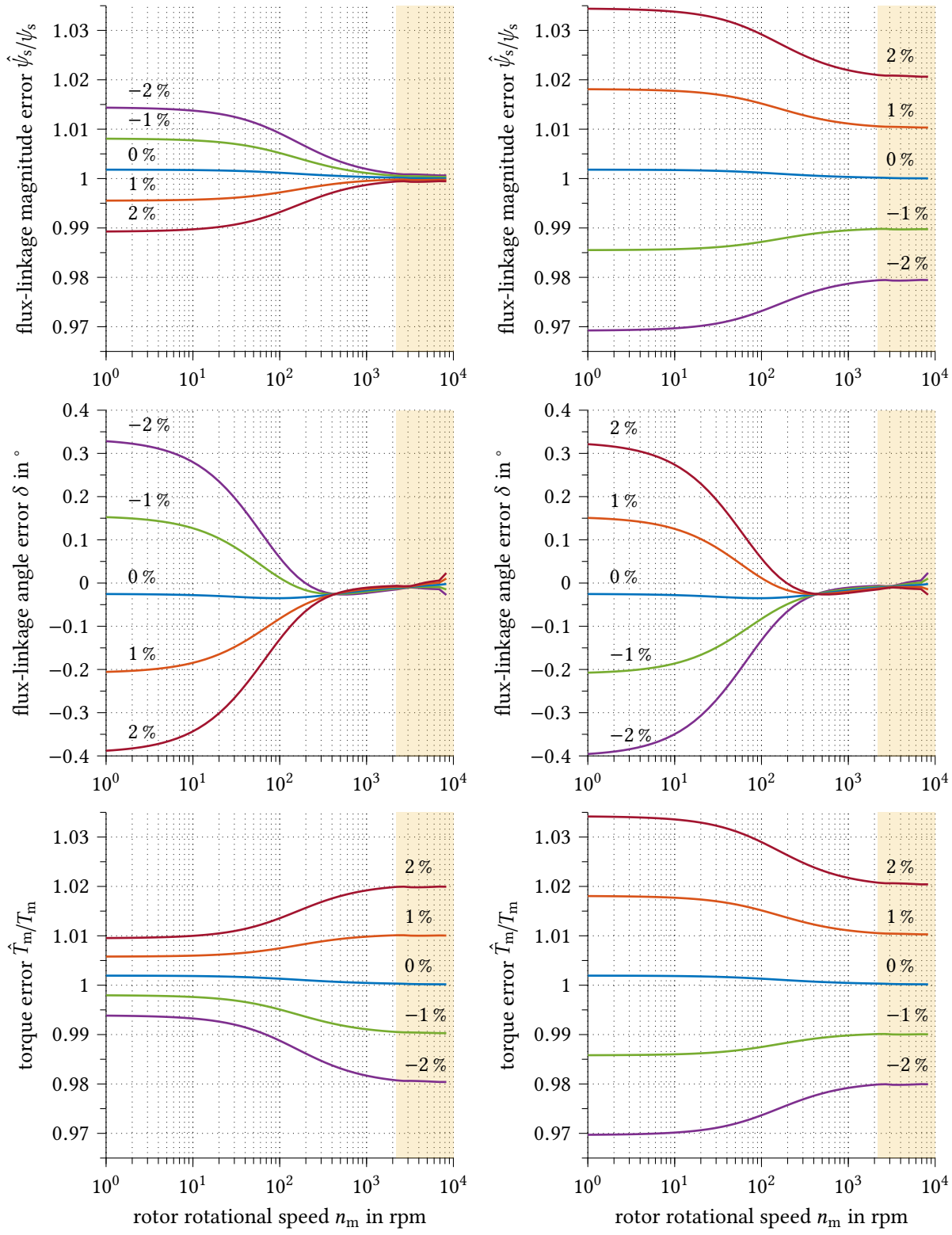

(a) current-sensor error

(b) voltage-sensor error

Fig. 4.16: Steady-state error of the Gopinath-style flux-linkage observer and the resulting torque deviation caused by balanced current- and voltage-sensor deviation. Results for IM26kA with PI-controller bandwidth of 2.5 Hz.

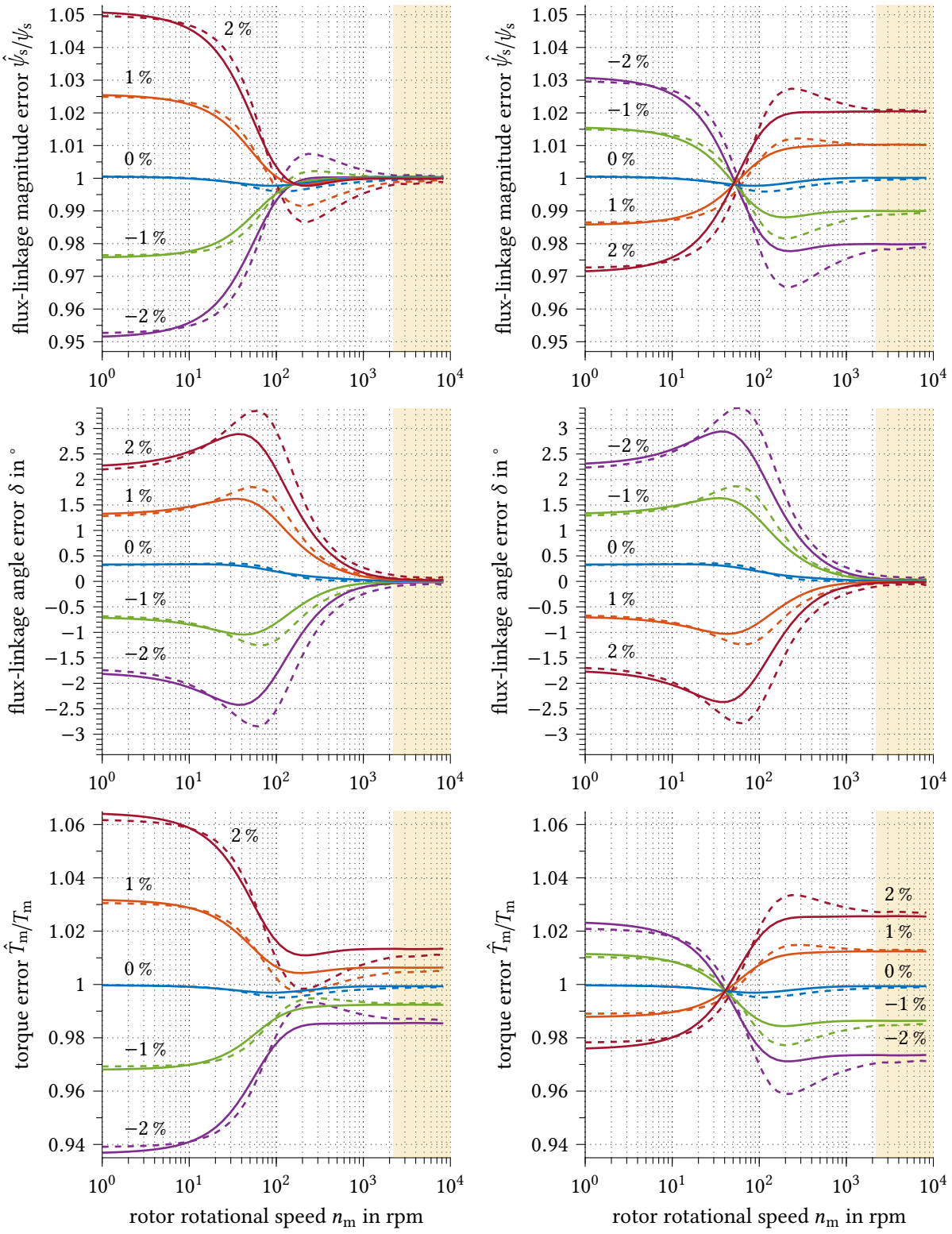

(a) current-sensor error

(b) voltage-sensor error

Fig. 4.17: Steady-state error of the full-order flux-linkage observer and the resulting torque deviation caused by balanced current- and voltage-sensor deviation. Results for IM26kA with proportional pole placement (solid, $g = 10$) and left-shift pole placement (dashed, $g = 0.3$).

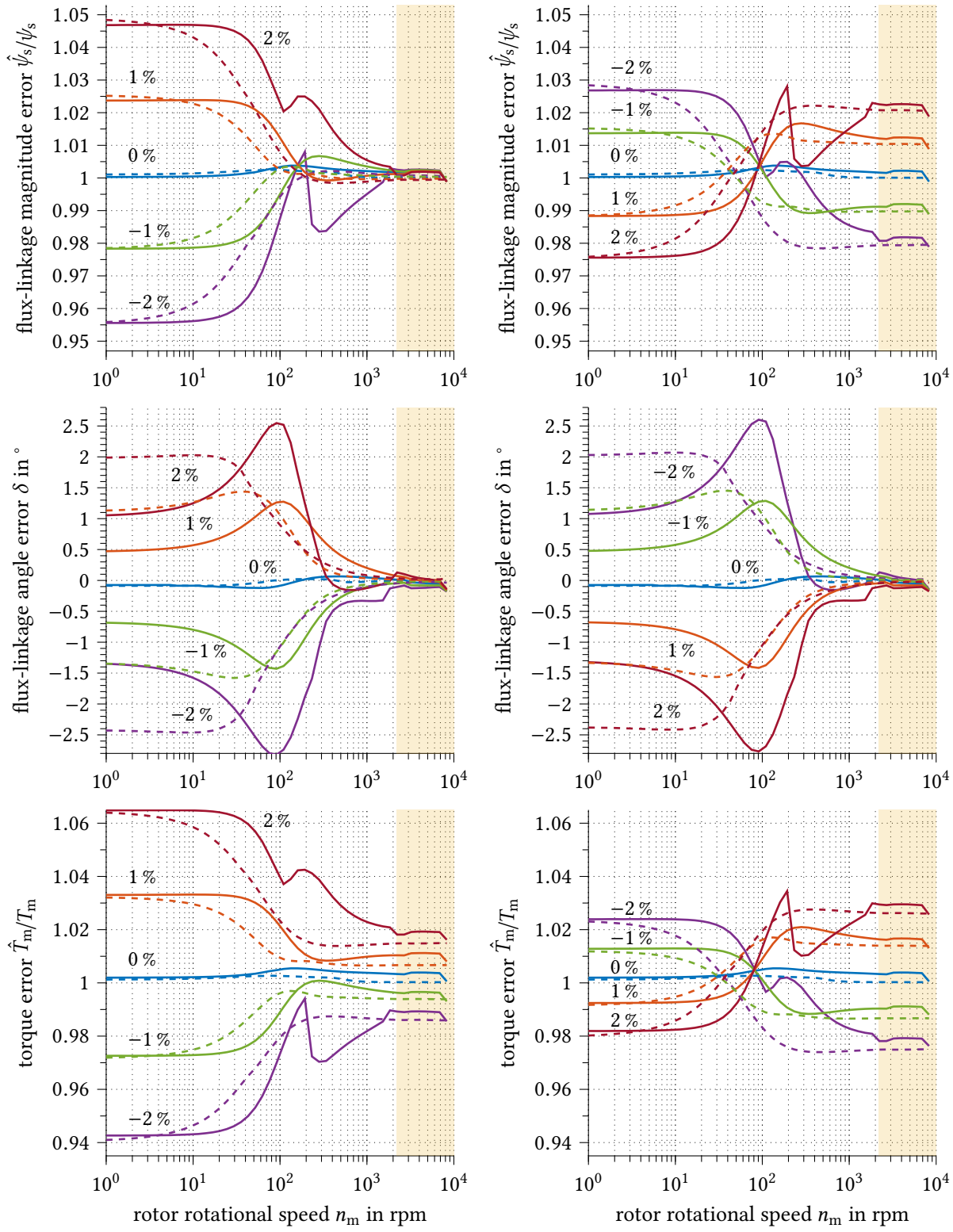

(a) current-sensor error

(b) voltage-sensor error

Fig. 4.18: Steady-state error of the sliding-mode flux-linkage observer and the resulting torque deviation caused by balanced current- and voltage-sensor deviation. Results for IM26kA with proportional pole placement (solid, $g = 5$) and left-shift pole placement (dashed, $g = 0.3$).

negligible angular detuning, the torque error remains equal to the flux-linkage magnitude error. The deviation at 0 % sensor error is caused by the stator iron losses, which are not considered in the flux-linkage observer.

The full-order Luenberger-type observer is more sensitive to current-sensor deviation. Above 1000 rpm, the results in Fig. 4.17a are comparable to those of the Gopinath-style observer. But at lower speeds, the torque error is up to six times higher with notable angular detuning. The dependency on voltage-sensor deviation is plotted in Fig. 4.17b. At high speeds, it is similar to that of the Gopinath-style observer. With decreasing speed, the error changes sign and remains slightly lower. However, the angle error is still up to 3.5°, which is ten times higher than with the Gopinath-style observer. The choice of the observer pole-placement method shows only minor influence.

The simulation results for the sliding-mode observer are plotted in Fig. 4.18 and show similar sensitivity to sensor errors as the previous case with linear observer feedback. The angle deviation is reduced but still significant. With proportional observer poles, the error is slightly increased and shows discontinuities above 100 rpm, which are caused by the nonlinear feedback. The left-shifted poles lead to a similar torque error as the linear feedback case with continuous results.

In terms of the sensitivity to balanced sensor-gain errors, the Gopinath-style observer is advantageous. It generally produces a significantly lower angle error and a lower dependency on current-sensor faults compared to the full-order observers. Only the torque error caused by voltage-sensor deviation in the low-speed region is increased by up to one percentage point.

4.1.2.2 Imbalanced Sensor-Gain Error

The negative-sequence component $\vec{i}^{\,\Diamond}_{\mathrm{s,neg}}$ is rotating at the stator frequency in reverse direction and is caused by unequal gains of the three current sensors. Together with $\vec{i}^{\,\Diamond}_{\mathrm{s,pos}}$, it forms an ellipse in the stationary reference frame. Its influence on the torque production becomes clear after transformation to the field-oriented reference frame. The negative-sequence component is then rotating at twice the stator frequency, which superimposes a ripple onto the estimated flux-linkage and torque. Since the estimated flux-linkage is regulated and used to calculate the torque-producing current reference, the imbalanced voltage- or current-sensor gains superimpose a ripple of twice the stator frequency onto the actual torque. For imbalanced current-sensor gains, a second feedback loop exists through the current controller, which also superimposes a torque ripple.

The magnitude of the torque ripple depends on the filtering characteristics of the observer and the bandwidths of the flux-linkage and the current controllers. Especially at low speeds when the ripple is not filtered off, it introduces undesired effects, such as low frequency speed ripple [CS98], or degrades the low-speed performance of speed-sensorless drives. To overcome these problems, differential-gain compensation algorithms have been proposed. A simple approach is the spectral separation of the negative-sequence com-

ponent, for example by filtering in a synchronous reference frame. However, for this method a minimum stator electrical frequency is required, which limits its applicability to higher speeds. To deploy this method at low speeds, signal injection is required [Har+08]. In [CS98] a ripple compensator is proposed that is based on a mechanical model and the feed-forward of the speed ripple. A similar approach is presented in [CS08], where a voltage-model-based measurement-disturbance observer is utilized to compensate the gain imbalance. However, both methods require additional information about the mechanical or IM model parameters and do not adapt the sensor gains.

Parameter independent methods are usually based on the elimination of harmonic content present in the voltage reference. In [Jun+06], an error feedback is generated by piece-wise integration of the direct-axis current-regulator integral output. The algorithm introduced in [HL08] is based on the isolation of the positive-sequence component and the imbalanced distortion, which are then used for the decoupling and adaption of the sensor gains through a regulator.

The compensation algorithms found in literature are mostly related and limited to the current sensors, as stator-voltage sensing is not very common in drive systems. A simple approach for the adaption of imbalanced voltage-sensor gains is the comparison of the measured negative-sequence component to that of the reference-voltage signal. However, it requires accurate separation of the inverter dead-time effect and can be influenced by imbalanced semiconductor voltage drop, as caused by inhomogeneous temperature distribution. Alternatively, an adaption algorithm as the one in [HL08] can be used, which is applicable to current and voltage sensors.

Since the negative-sequence component does not contribute to the average stationary torque error, compensation algorithms for imbalanced sensor gains are not further discussed. Instead, reference is made to the existing methods. In Section 4.1.4, the damping characteristics of the flux-linkage observers for the higher harmonics are investigated.

4.1.2.3 Sensor-Offset Error

In the field-oriented reference frame, the offset component $\vec{i}^{\,\diamondsuit}_{\mathrm{s,neg}}$ is rotating at the stator electrical frequency. Analogously to the negative-sequence component, it superimposes a ripple onto the estimated flux-linkage and the produced torque. Due to the pure integrator in the IM voltage model, sensor offsets can have a significant influence on the flux-linkage observer and can even cause instability. With the Gopinath-style flux-linkage observer, this issue is eliminated by the integral component of the feedback PI-controller. However, the Luenberger-type observer is sensitive to offset integration. Especially with sliding-mode feedback, the offset compensation capabilities are reduced, as the magnitude of the voltage-model feedback is limited by the feedback gain $\underline{K}_{\mathrm{s}}$. Consequently, the offset error at the integrator input must remain lower than $|\underline{K}_{\mathrm{s}}|$ to avoid open offset integration.

According to Fig. 4.19, $|\underline{K}_{\mathrm{s}}|$ decreases by more than 90 % with increasing rotational speed when the left-shifted pole-placement is used, whereas it remains constant with

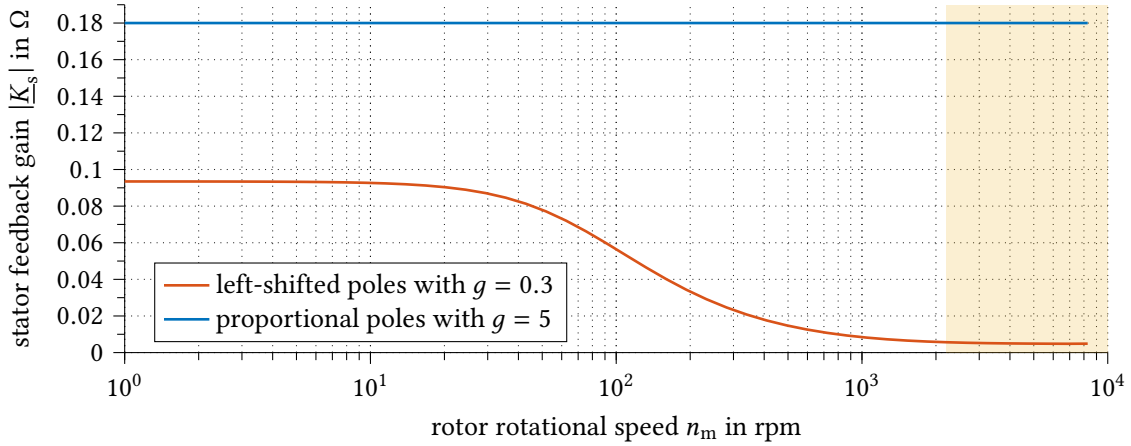

Fig. 4.19: Absolute value of the voltage-model feedback gain $\underline{K}_s$ for proportional ($g = 5$) and left-shifted ($g = 0.3$) pole placement as a function of the rotor rotational speed.

proportional poles. That makes the proportional pole-placement method more attractive for the sliding-mode observer. The problem can be eliminated by adding an integrator to the feedback loop [LA06]. But, the integrator introduces an additional state variable and also integrates errors caused by parameter deviations, which is problematic at low speeds.

Sensor offsets are usually recalibrated during the initialization of the drive system. The offsets are determined by measurement of the currents and voltages when no current is present, with additional filtering using an LPF. However, temperature drift of the analog circuit components can cause offset variations during operation, which can require additional compensation. In [CS08; USO10] this is achieved using a measurement disturbance observer and offset estimator. Both methods require knowledge of the load parameters. In [TAN13; Tam+14; TIN15] the DC component is extracted from the voltage reference using a discrete Fourier-transformation approach. In [KSL14] the current offset is separated from a positive- and negative-sequence component present in the voltage reference of a permanent-magnet synchronous machine (PMSM) drive. All these compensation methods are sensitive to model parameters, interference with the control algorithm, phase coupling or harmonics caused by load ripple, machine saliencies or other external influences.

In Section 5.3, a novel online offset-calibration method is introduced, which utilizes the inverter voltage distortion curve described in Section 2.3.2. The algorithm is applied to each phase, individually, and is completely decoupled from the control algorithm and disturbances caused by torque ripple or machine saliencies.

4.1.3 Nonlinear Inverter Voltage Distortion

In this work, the inverter voltage distortion caused by the dead-time effect and the semiconductor voltage drop is compensated using the open-loop nonlinear inverter model introduced in Section 2.3.1. However, because of temperature drift or parameterization error, a fractional voltage error remains and superimposes additional harmonic content to

the currents and voltages. This causes additional torque ripple and can disturb compensation schemes as those mentioned previously. Thus, the harmonic content induced by the MOSFET inverter voltage distortion is of considerable importance, especially if the reference voltage is used instead of a voltage measurement.

The VSI voltage error is derived using Equation (2.45). Since the drain–source resistance is in series with the stator resistance of the IM, thermal drift of $R_{\mathrm{ds,on}}$ may be considered as an estimation error in $\hat{R}_\mathrm{s}$. By neglecting the inverter output capacitance C_out, the simplified voltage error of a single phase is then rectangular with

$$\Delta u_\mathrm{ph} = -u_\mathrm{dc} \cdot \frac{\Delta T_\mathrm{dt}}{T_\mathrm{sw}} \operatorname{sgn}\left(i_\mathrm{ph}\right), \tag{4.8}$$

where ΔT_dt is the dead-time estimation error. With $\measuredangle \vec{i}_\mathrm{s}(t=0) = 0$, the resulting voltage errors for the three phases can be described by the Fourier series

$$\Delta u_\mathrm{ph1} = -\frac{4u_\mathrm{dc}}{\pi} \cdot \frac{\Delta T_\mathrm{dt}}{T_\mathrm{sw}} \cdot \sum_{n=1}^{\infty} \frac{\cos((2n-1)\cdot\omega_\mathrm{s}t)}{2n-1}, \tag{4.9a}$$

$$\Delta u_\mathrm{ph2} = -\frac{4u_\mathrm{dc}}{\pi} \cdot \frac{\Delta T_\mathrm{dt}}{T_\mathrm{sw}} \cdot \sum_{n=1}^{\infty} \frac{\cos\left((2n-1)\cdot\left(\omega_\mathrm{s}t - \frac{2\pi}{3}\right)\right)}{2n-1} \tag{4.9b}$$

$$\text{and} \quad \Delta u_\mathrm{ph3} = -\frac{4u_\mathrm{dc}}{\pi} \cdot \frac{\Delta T_\mathrm{dt}}{T_\mathrm{sw}} \cdot \sum_{n=1}^{\infty} \frac{\cos\left((2n-1)\cdot\left(\omega_\mathrm{s}t + \frac{2\pi}{3}\right)\right)}{2n-1} \quad \text{with} \quad n \in \mathbb{N}. \tag{4.9c}$$

They only consist of odd frequency components. With the Clarke transformation (A.1) and the addition theorems, third-order harmonics get cancelled out and the voltage error can be expressed as a space vector in the stationary reference frame with

$$\begin{aligned} \vec{u}_\mathrm{s,dist} &= -\frac{4u_\mathrm{dc}}{\pi} \cdot \frac{\Delta T_\mathrm{dt}}{T_\mathrm{sw}} \cdot \sum_{n=1}^{\infty} \left(\frac{\mathrm{e}^{\mathrm{j}(6n-5)\omega_\mathrm{s}t}}{6n-5} + \frac{\mathrm{e}^{-\mathrm{j}(6n-1)\omega_\mathrm{s}t}}{6n-1} \right) \quad \text{with} \quad n \in \mathbb{N} \\ &= -\frac{4u_\mathrm{dc}}{\pi} \cdot \frac{\Delta T_\mathrm{dt}}{T_\mathrm{sw}} \cdot \left(\mathrm{e}^{\mathrm{j}\omega_\mathrm{s}t} + \frac{1}{5} \cdot \mathrm{e}^{-\mathrm{j}5\omega_\mathrm{s}t} + \frac{1}{7} \cdot \mathrm{e}^{\mathrm{j}7\omega_\mathrm{s}t} + \frac{1}{11} \cdot \mathrm{e}^{-\mathrm{j}11\omega_\mathrm{s}t} + \ldots \right). \end{aligned} \tag{4.10}$$

Consequently, in the field-oriented reference frame, the dead-time effect creates a stationary voltage error and higher-order harmonics with a multiple of the sixfold stator frequency, which also get superimposed on the torque.

4.1.4 Rejection of Higher-Order Harmonics by the Flux Observer

The impact of higher-order harmonics on the estimated flux-linkage can be analyzed by modifying the observer transfer functions derived in Chapter 3. The current and the stator

flux-linkage are normalized with respect to the condition $\omega_\mathrm{s} = \omega_\mathrm{m}$, which leads to

$$\underline{\psi}_\mathrm{s} = L_\mathrm{s}\underline{i}_\mathrm{s}. \tag{4.11}$$

The frequency-response function of the open-loop current model is derived by dividing Equation (3.2) by (4.11), and replacing ω_sl by the k^{th}-order harmonic term, according to

$$\underline{F}^{\Delta\mathrm{i}}_{\mathrm{C,h}}(\mathrm{j}k\omega_\mathrm{s}) = \frac{1 + \mathrm{j}(k\omega_\mathrm{s} - \omega_\mathrm{m})\hat{\sigma}\hat{\tau}_\mathrm{r}}{1 + \mathrm{j}(k\omega_\mathrm{s} - \omega_\mathrm{m})\hat{\tau}_\mathrm{r}}. \tag{4.12}$$

It describes the relative damping of harmonic content in the stator current by the current model low-pass filtering characteristics. Since the current model is not a function of the stator voltage, the corresponding expression for the voltage harmonics is equal to zero.

The frequency-response functions of the open-loop voltage model are adapted from Equation (3.6). For the current and voltage harmonics, the expressions are obtained as

$$\underline{F}^{\Delta\mathrm{i}}_{\mathrm{V,h}}(\mathrm{j}k\omega_\mathrm{s}) = -\frac{\hat{R}_\mathrm{s}}{\mathrm{j}k\omega_\mathrm{s}L_\mathrm{s}} \quad \text{and} \quad \underline{F}^{\Delta\mathrm{u}}_{\mathrm{V,h}}(\mathrm{j}k\omega_\mathrm{s}) = \frac{\mathrm{j}\omega_\mathrm{m}L_\mathrm{s} + R_\mathrm{s}}{\mathrm{j}k\omega_\mathrm{s}L_\mathrm{s}}. \tag{4.13}$$

The latter is normalized using the voltage model at the condition $\omega_\mathrm{s} = \omega_\mathrm{m}$ and substituting $\underline{i}_\mathrm{s}$ using (4.11) with

$$\underline{\psi}_\mathrm{s} = \frac{\underline{u}_\mathrm{s}}{\mathrm{j}\omega_\mathrm{m}L_\mathrm{s} + R_\mathrm{s}}. \tag{4.14}$$

The damping characteristics of the Gopinath-style observer can be obtained using Equation (3.14) with the frequency-response functions of the open-loop models (4.12) and (4.13). Therefore, ω_s is replaced by $k\omega_\mathrm{s}$ in (3.14) and in $\underline{G}_\mathrm{PI}(\mathrm{j}\omega_\mathrm{s})$. The damping characteristic of the Luenberger-type observer is found analogously by modifying Equation (3.26).

Fig. 4.20 shows the resulting frequency response of the Gopinath-style and Luenberger-type observers for harmonics present in the current and voltage input signals. As per Fig. 4.20a, current offsets are damped by the Gopinath-style observer above 20 rpm. At high speeds the offset harmonic is reduced to about 10 %. The Luenberger-type observer behaves similarly, however at low speeds, the current offset harmonic appears magnified in the flux-linkage signal.

Because of the integrator of the PI-controller, the voltage offset in Fig. 4.20b gets completely filtered off using the Gopinath-style observer. The Luenberger-type observer damps the voltage offset by 20 % below 100 rpm and magnifies it at higher speeds. However, since the offset-to-signal ratio decreases linearly with increasing stator frequency, the actual influence of the voltage offset converges to zero at higher speeds.

The negative sequence first-order harmonic caused by imbalanced current-sensor gains is damped by the flux-linkage observers similarly to the current offsets, as illustrated in Fig. 4.20c. But at low speeds, the Gopinath-style observer already reduces the harmonic by 60 %. This is about four times lower than with the full-order observers. Above 1000 rpm, the

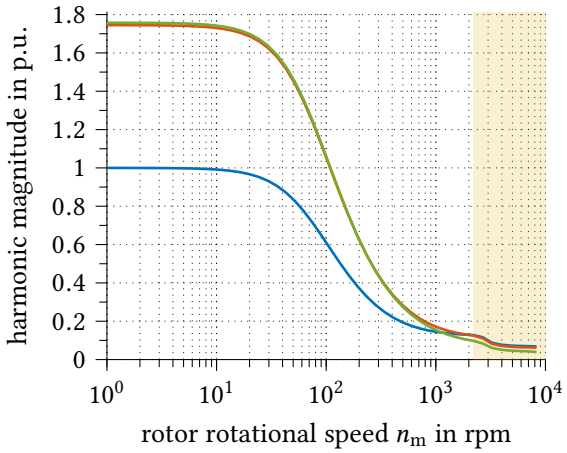

(a) current offset harmonic, $k = 0$

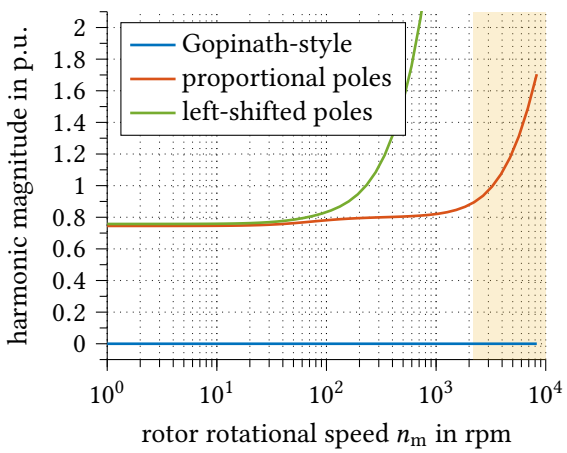

(b) voltage offset harmonic, $k = 0$

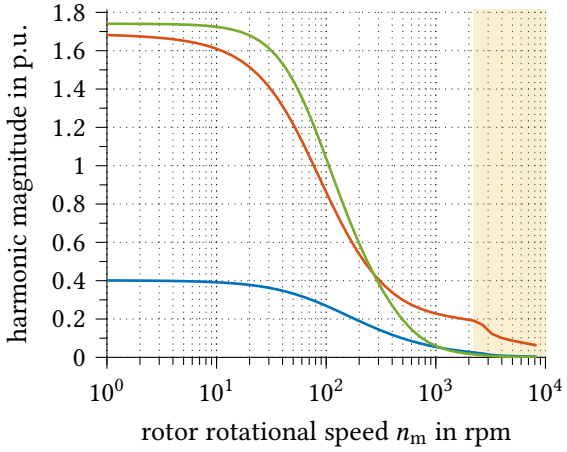

(c) current differential gain harmonic, $k = -1$

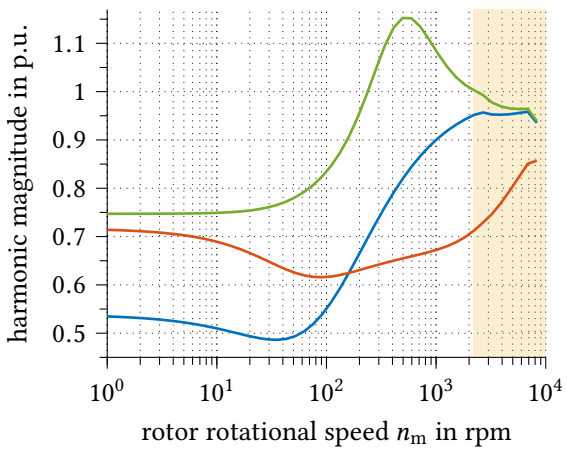

(d) voltage differential gain harmonic, $k = -1$

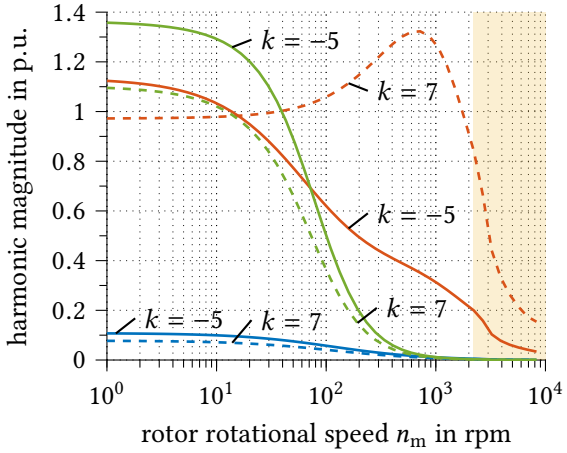

(e) current dead-time harmonics

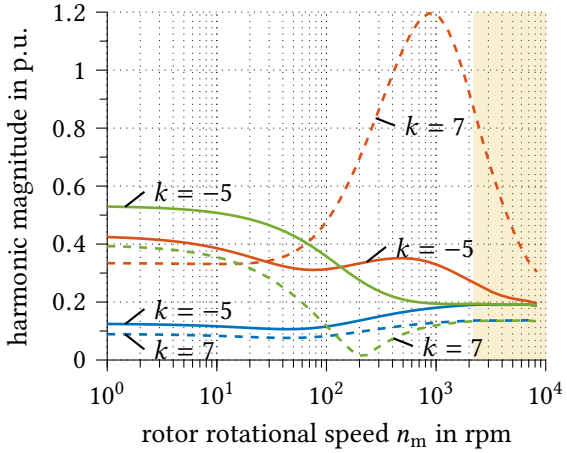

(f) voltage dead-time harmonics

Fig. 4.20: Normalized flux-linkage frequency response of the Gopinath-style and Luenberger-type observers with proportional and left-shifted poles for harmonics in the voltage and current signal caused by offset, differential gain error and dead-time effect.

proportional pole placement full-order observer offers less damping compared to the other observers. As shown in Fig. 4.20d, the first-order negative sequence harmonic caused by differential voltage-sensor gains is damped by up to 50 %. At very low speed, the Gopinath-style observer is advantageous, but above 100 rpm the proportional-pole Luenberger-type observer performs best.

The frequency response function for the first two higher-order current harmonics caused by inverter dead time is plotted in Fig. 4.20e. Both are significantly damped by the Gopinath-style observer to less than 11 %. The full-order observer with left-shifted poles offers good damping above 100 rpm. However, it is still poorer than with the Gopinath-style observer. The proportional-pole solution shows significant influence of the harmonics above 1000 rpm. For improved readability, higher-order harmonics with $k > 7$ have not been plotted, as they are generally damped sufficiently.

In Fig. 4.20f, the frequency response shows similar behavior for the dead-time harmonics present in the voltage signal. The Gopinath-style observer leads to a damping of more than 80 % at all speeds. It should be noted, that again the dead-time induced harmonic magnitude does not scale with the stator frequency, which drives the relative harmonic magnitude to zero at higher speeds.

Taken as a whole, out of the three observers considered in this work, the Gopinath-style stator flux-linkage observer offers the best rejection of higher-order current- or voltage-signal harmonics for IM26kA. Only in the case of differential voltage-sensor gains, the Luenberger-type observer with proportional pole placement performs slightly better.

4.2 Adaptive Compensation of Parameter Faults

As proven is the previous section, the accuracy of the estimated flux-linkage is crucial for accurate torque control. The analysis of the flux-linkage observers has shown, that for the system used in this work, the Gopinath-style observer is advantageous over conventional open-loop and full-order closed-loop observers in terms of the sensitivity to parameter and sensor errors, as well as the rejection of higher harmonics. The Gopinath-style observer leads to comparably low flux-linkage magnitude error and low angular detuning. However, full suppression of parameter and sensor faults is not possible, particularly in the low-speed region. An improvement can be achieved by estimating the faulty parameters, offsets and differential gains in combination with online adaption of the observer and sensor parameters. The problem is closely related to that of stable low-speed operation in speed-sensorless drives. Thus, various parameter adaption algorithms have been studied related to that topic. An overview can be found in [Hol06] and [BM07].

As seen in Fig. 4.6, the Gopinath-style observer effectively suppresses estimation errors of the main-inductance and the leakage-inductance values. Along with the open-loop compensation schemes for stator flux-linkage saturation in (2.16) and stator iron losses according to Section 2.2.2, the controller can be considered as sufficiently insensitive to

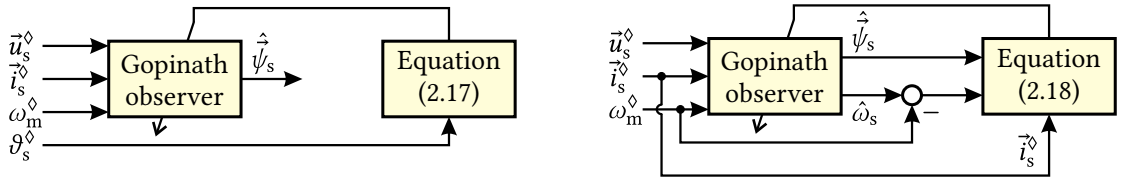

(a) temperature-measurement-based $\hat{R}_\mathrm{s}$ adaption (b) current-model-based $\hat{R}_\mathrm{r}$ adaption

Fig. 4.21: Model-based open-loop resistance estimation and adaption using the measured stator-winding temperature and the measured slip frequency.

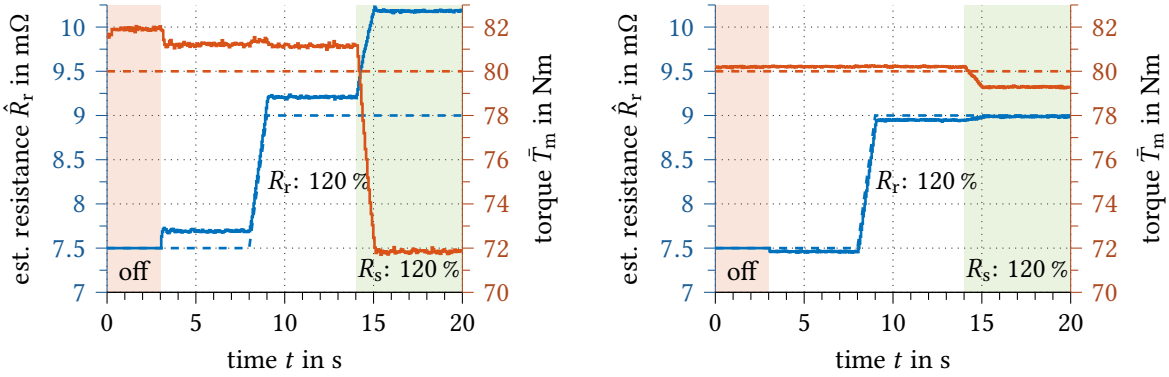

(a) 80 Nm, 100 rpm (b) 80 Nm, 2000 rpm

Fig. 4.22: Simulation results of the model-based open-loop rotor-resistance estimation using Equation (2.18) without stator-resistance adaption. Simulated using the software-in-the-loop simulation model in Appendix A.4 for IM26kA.

saturation and iron losses. However, Fig. 4.6 reveals a strong dependency on the stator and rotor resistances, which can lead to an unacceptable torque deviation that violates the objectives of the MAs:Stab project. Thus, adaption of both resistances is recommendable to further improve the torque accuracy of the drive system.

4.2.1 Stator- and Rotor-Resistance Estimation Methods

Online resistance-estimation and adaption schemes can be divided into four categories:

- Model-based open-loop estimation
- Model-reference adaptive system (MRAS) using IM voltage and current model
- Signal-injection-based resistance measurement
- Thermal-model-based resistance estimation with IM loss model

Similar to the stator-inductance adaption using (2.16), the stator resistance can be obtained by model-based open-loop estimation. Since the IM is equipped with a temperature sensor at the stator end-winding, the resistance can be adapted using its thermal relationship

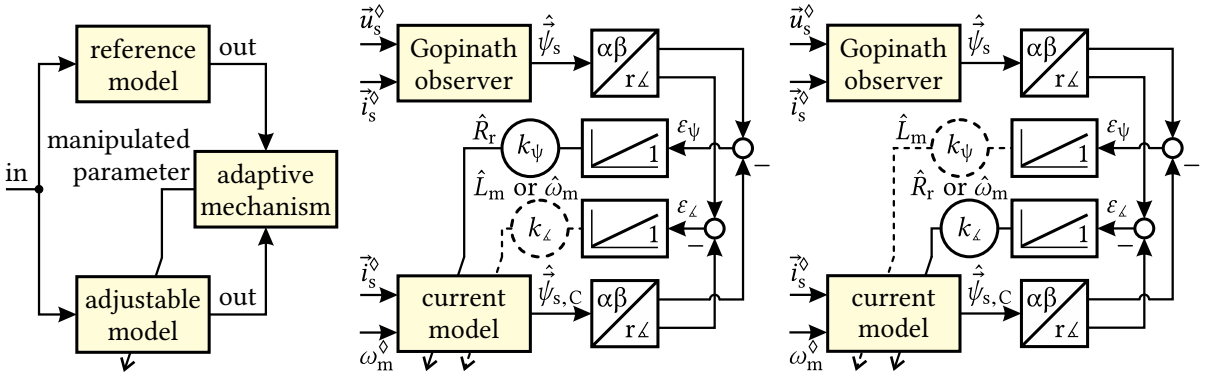

(a) general MRAS structure (b) flux-based resistance adaption (c) angle-based resistance adaption

Fig. 4.23: MRAS-based parameter adaption. The two-dimensional stator flux linkage offers two linear-independent feedback signals, which can be used for simultaneous adaption of two parameters.

(2.17), as shown in Fig. 4.21a. One should note, that the thermal sensor is located at the end-winding to monitor the winding hot-spot temperature, which is the most critical temperature due to the poor thermal coupling to the cooling system. Consequently, the measured temperature does not necessarily represent the average winding temperature in the stator slots, which leads to an incorrect stator-resistance estimate, especially at high currents and during transients.

As the rotor temperature is not measured in common drive systems, online estimation of the rotor resistance is generally more problematic. However, even though thermal rotor-resistance estimation is not directly possible, the resistance can be estimated from the measured slip frequency in a model-based open-loop manner by using (2.18), as illustrated in Fig. 4.21b. Fig. 4.22 shows simulation results of the rotor-resistance estimation at low and high speed. First, the estimator is switched off. After 3 s, the estimation is activated and at 8 s, the rotor resistance of the IM model is increased to 120 % of its initial value to evaluate the adaption process. After 14 s, also the stator resistance is increased by 20 % to analyze the sensitivity to the stator resistance. It can be seen in Fig. 4.22b, that during high-speed operation the rotor resistance is precisely estimated and the torque deviation remains below 1 Nm. The slight deviation is caused by small deviations in the stator inductance, as – according to Chapter 2 – the magnetic saturation in the controller is differently modeled from the simulation model. At low speed, the estimation and the torque error are acceptable before the deviation of the stator resistance is introduced at 14 s. This indicates, that the adaption scheme is very sensitive to stator-resistance drift, which makes this approach only applicable in the high-speed region.

In general, rotor-resistance estimation based on electrical quantities can only be applied when current is present in the rotor, and thus, torque is produced. Another limitation of the scheme described above is, that it requires a speed sensor to obtain the slip frequency. Adaption schemes suitable for sensorless drives are often based on MRAS where the output of an adjustable model is compared to a reference model and the error is driven

to zero by parameter adaption, as illustrated in Fig. 4.23a. In the case of IM drives, the MRAS is usually constructed using the voltage model as the reference model and the current model as adjustable model, and vice versa. Since the flux-linkage estimate is a two-dimensional quantity, two linear-independent error feedbacks can be obtained which allow simultaneous adaption of two parameters. For example in [VVL03], the IM voltage model serves as the reference model for the adaption of the rotor speed in the current model, using the angular difference of both observer outputs as error feedback. At the same time, the current model is used as the reference model to adapt the stator resistance in the voltage model. In this case, the models exchange their roles and the deviation of the flux-linkage magnitude is used as error feedback.

To estimate the rotor resistance with the Gopinath-style observer, an MRAS can be formed using the current-model submodel as the adjustable model. Either the flux-linkage magnitude error or the angular error can be used as adaptive feedback. The simplified adaption schemes are given in Fig. 4.23b and Fig. 4.23c. In Fig. 4.24, the flux-linkage magnitude error of both models has been calculated for different operating points, based on the equations derived in Chapter 3. The rotor resistance is the dominant parameter, especially at higher speeds. To be suitable for parameter adaption, the error must be of equal sign in all operating points, which is the case. Furthermore, the influence of other parameters should be sufficiently low as the cross-coupling can cause adaption of the rotor resistance to a wrong value. For example, from Equation (3.3) it can be deduced, that at zero slip the flux-linkage is no longer a function of the rotor resistance and adaption must be suspended. If not, even a small stator-inductance deviation causes a misleading adaption of the rotor resistance and thus, even worse controller detuning and torque error.

In Fig. 4.26a and Fig. 4.26b the simulation in Fig. 4.22 has been repeated using the magnitude-error-based MRAS approach. The error is effectively driven to zero. But the cross-coupling to the inductances leads to a wrong estimate and a torque error, worse than without adaption. At higher speeds, the accuracy is better, but an offset of 0.5 mΩ remains.

Rotor-resistance adaption based on the angular flux-linkage deviation, according to Fig. 4.23c, can become unstable, as the error in Fig. 4.25d changes sign in the field-weakening region. Other than that, in Fig. 4.25, the influence of other parameters seems to be higher compared to the previous case. However, at partial load, the rotor resistance becomes more dominant, which implies a more accurate parameter estimation. The simulation results in Fig. 4.26c are considerably better than in the previous case. The estimation error is much smaller and the torque error is within the acceptable range of 2.5 Nm even though the estimated rotor resistance is notably distorted by the stator-resistance error. At higher speeds, the accuracy is similar to the magnitude-error-based approach. However, the estimation error is of inverse sign, which according to Fig. 4.24 and Fig. 4.25 confirms that a small deviation is present in the main-inductance value.

The main inductance can be simultaneously adapted using the flux-linkage magnitude error. The corresponding simulation results have also been plotted in Fig. 4.26. The rotor-resistance estimation is now significantly improved. At low speeds, however, the stator

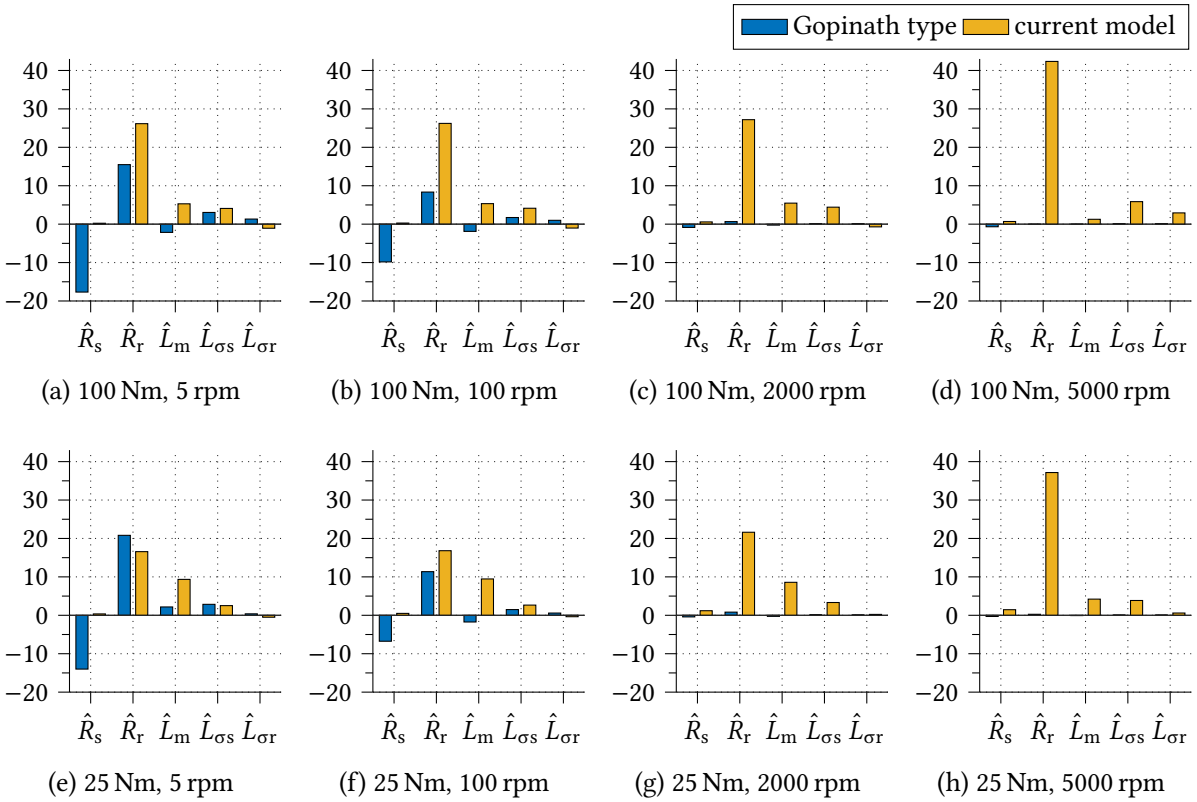

(a) 100 Nm, 5 rpm (b) 100 Nm, 100 rpm (c) 100 Nm, 2000 rpm (d) 100 Nm, 5000 rpm

(e) 25 Nm, 5 rpm (f) 25 Nm, 100 rpm (g) 25 Nm, 2000 rpm (h) 25 Nm, 5000 rpm

Fig. 4.24: Parameter sensitivity of the stator flux-linkage magnitude $\hat{\psi}_s/\psi_s - 1$ in %.

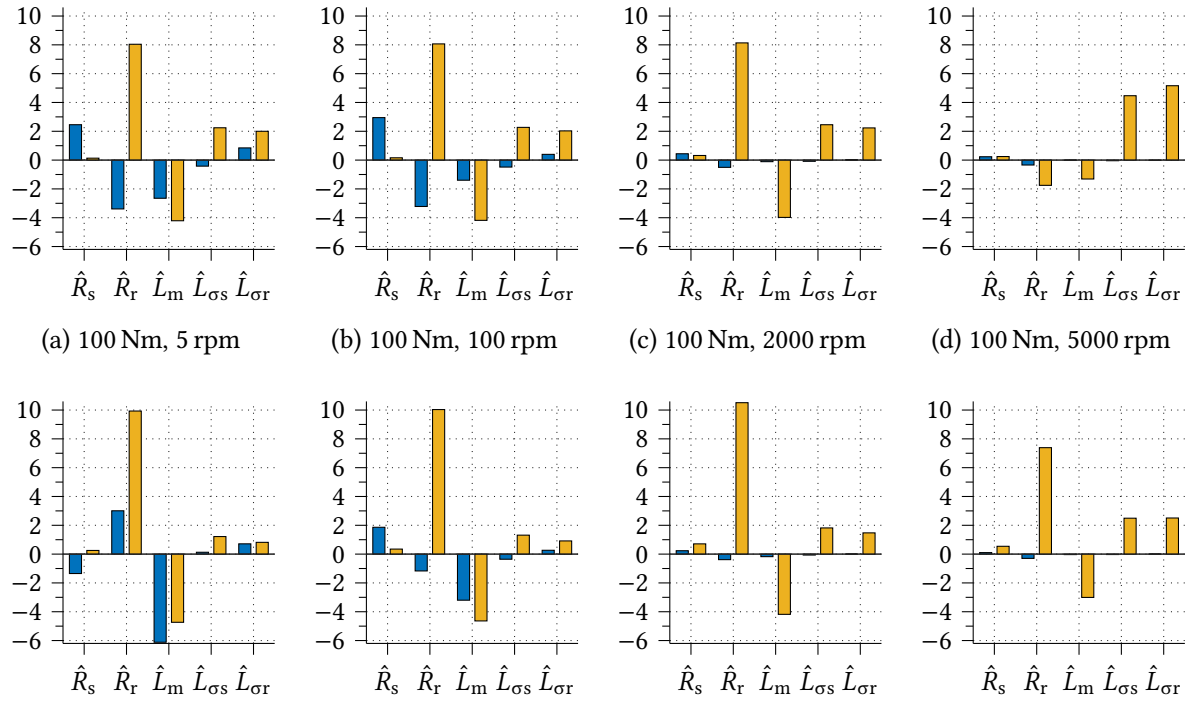

(a) 100 Nm, 5 rpm (b) 100 Nm, 100 rpm (c) 100 Nm, 2000 rpm (d) 100 Nm, 5000 rpm

(e) 25 Nm, 5 rpm (f) 25 Nm, 100 rpm (g) 25 Nm, 2000 rpm (h) 25 Nm, 5000 rpm

Fig. 4.25: Parameter sensitivity of the stator flux-linkage angle δ in electrical degrees (°).

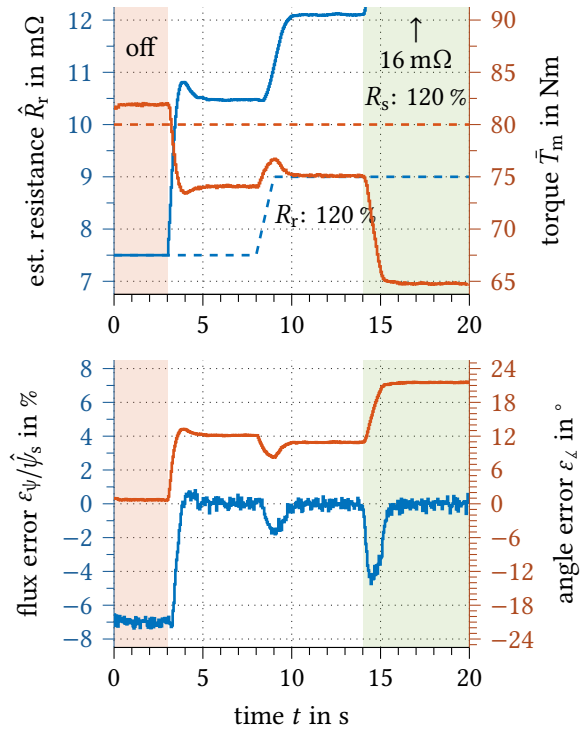

(a) flux-linkage error, 100 rpm

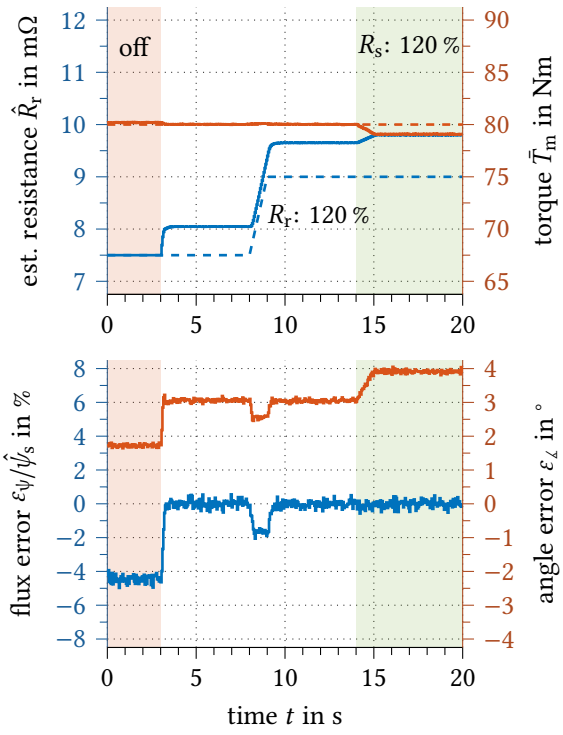

(b) flux-linkage error, 2000 rpm

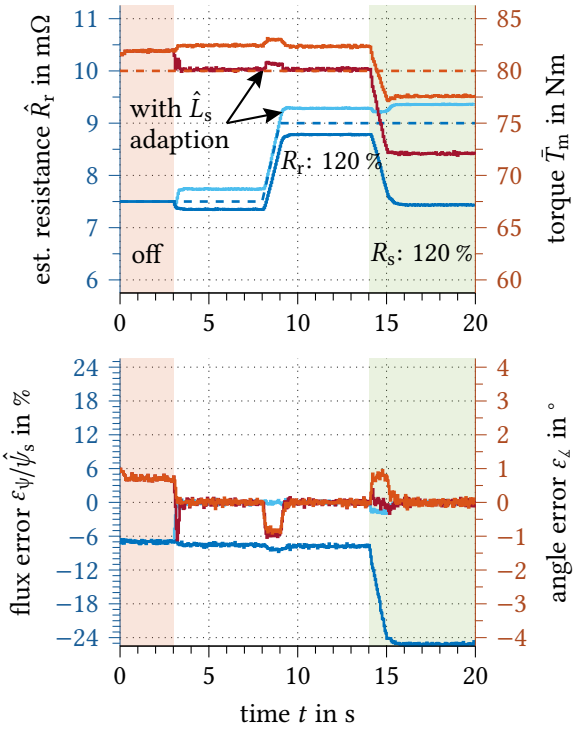

(c) flux-linkage angle error, 100 rpm

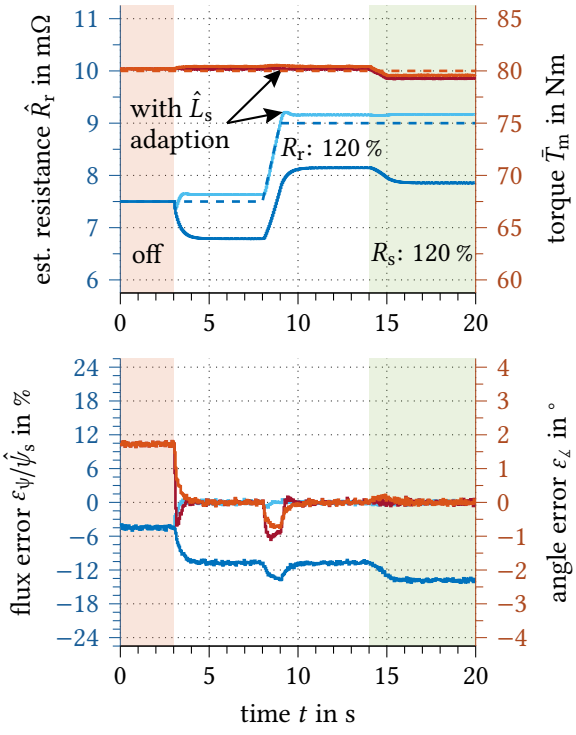

(d) flux-linkage angle error, 2000 rpm

Fig. 4.26: Simulation results of the MRAS-based rotor-resistance adaption as a function of the error feedback and speed. Simulated using the simulation model in Appendix A.4 for IM26kA.

resistance error is now compensated by incorrect adaption of the main inductance, which causes increased torque error. At higher speeds, the influence of the stator resistance is almost negligible, and the estimation is accurate.

It can be concluded, that the MRAS rotor-resistance adaption with the Gopinath-style observer is very sensitive to parameter mismatch of the other model parameters. This is why at higher speed, the model-based open-loop approach in Fig. 4.22b leads to more accurate results. Even though the angular-deviation-based MRAS shows acceptable torque error, the method comes along with numerous limitations:

- In the field-weakening region the estimator can become unstable.
- Decoupling from other parameter errors is not sufficiently possible.
- Rotor-resistance estimation is not possible at zero slip frequency.
- Simultaneous stator-resistance adaption is not or only possible at low speed [KLM15].

Direct measurement of the resistance value can only be applied to the stator resistance during standstill. To measure the resistance during operation, an additional test signal can be injected. Whereas for PMSMs the frequency of the injected signal can be chosen freely [MVZ15], the stator resistance of the IM can only be separated from the other parameters by injecting a DC current. This leads to additional losses and an undesirable low-frequency torque ripple at low speeds [KLM16]. An isolated measurement of the rotor resistance is not possible.

4.2.2 Thermal Model Feedback Approach

Since the major cause for stator- and rotor-resistance drift is the thermal dependency of the electric conductivity of copper and aluminum, knowledge about the temperature distribution within the IM is the key for decoupled and simultaneous estimation of the stator and rotor resistances [DBG85; DVG86b]. This is why in the following, a 3D spatially-resolved thermal model is used for the adaption of the resistance values. The work presented in this section was conducted in collaboration with Fang Qi, whose doctoral research on thermal modeling of electrical machines at ISEA was completed at the same time this work was written. The results have been partially published under [Qi+17].

The thermal model consists of a multitude of spatial units with a single thermal capacity, which are thermally interconnected. To do so, the IM is divided into multiple cylindrical volume elements which reflect its structural assembly, as shown in Fig. 4.27. Due to symmetry, only a small arc segment needs to be modeled. To obtain accurate results, the geometric resolution of the thermal model must be sufficiently high to also represent local temperature differences. This especially applies to the stator winding and the end winding. The resulting model geometry is described by Fig. 4.27b. For better illustration, air segments – which are modeled similarly – are not shown. The structural segments can

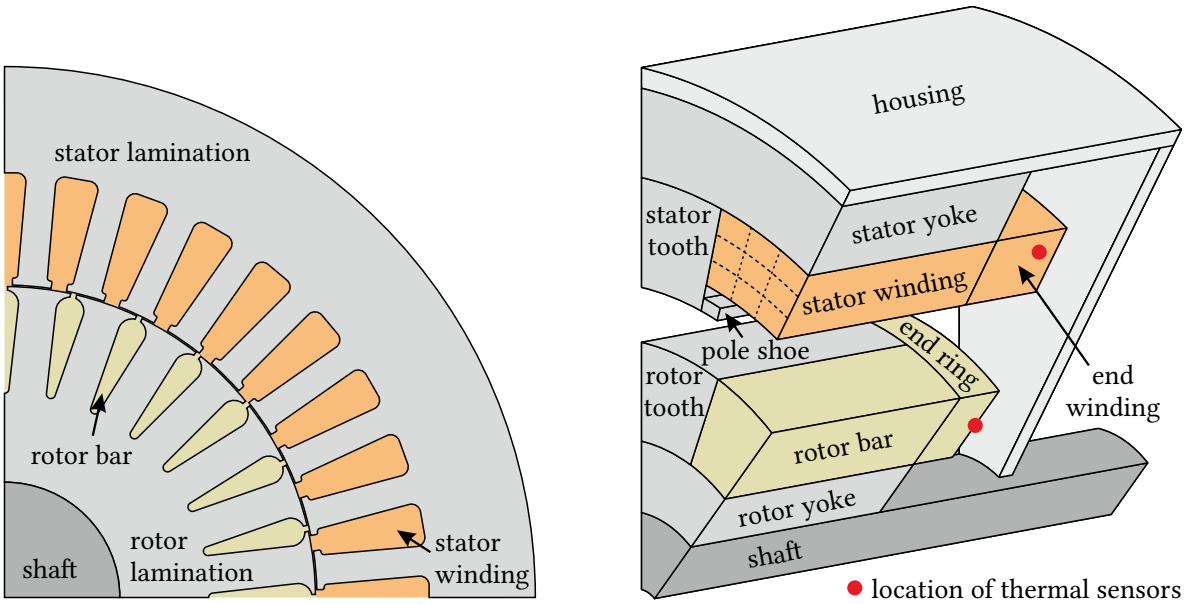

(a) cross section of IM26kA and IM26kB (b) 3D spatially-segmented IM

Fig. 4.27: Geometric structure of the lumped-parameter thermal network (LPTN). The IM is described by the smallest unit of symmetry which is approximated by cylindrical volume elements. The resolution can be increased by subdivision of the elements into smaller units [Qi+17].

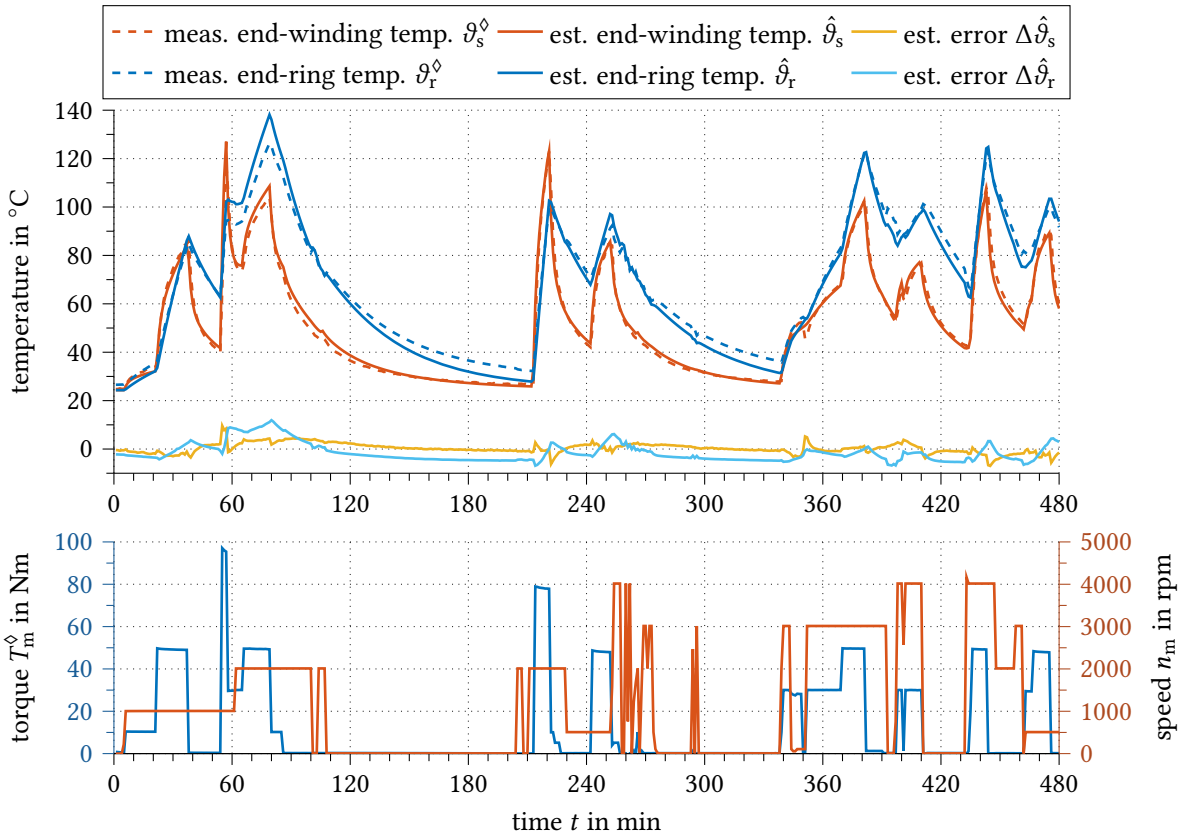

Fig. 4.28: Comparison between measured and simulated stator and rotor temperatures using the LPTN.

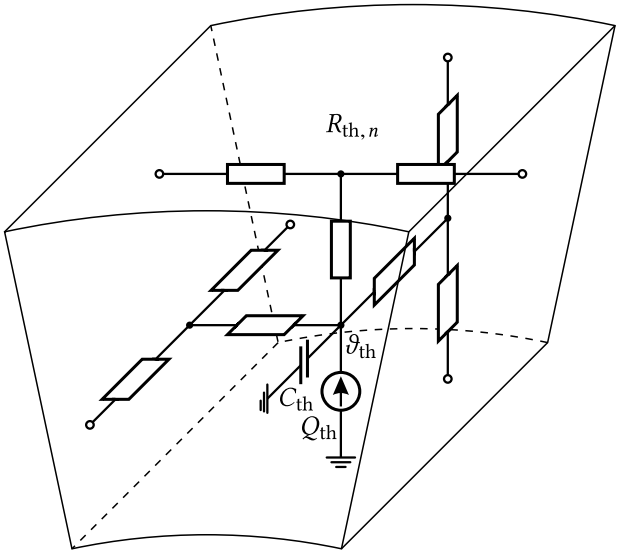

Fig. 4.29: LPTN unit with heat input, consisting of thermal lumped parameters [Qi+17].

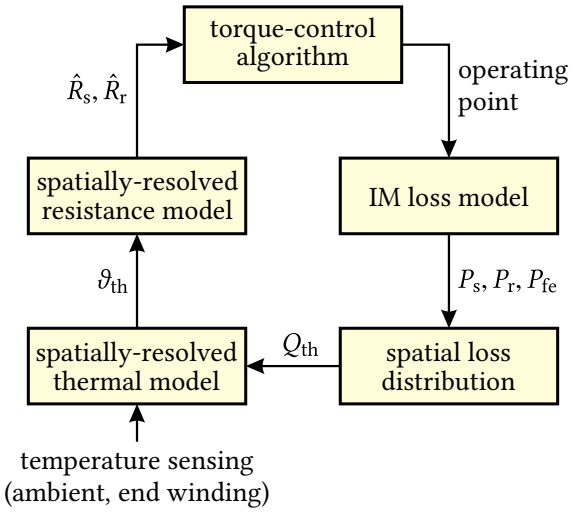

Fig. 4.30: Structure of the LPTN thermal-model-based resistance-adaption scheme.

be further divided into smaller subunits as indicated for the stator winding. For the model used in this work a total of 46 units – including the air gap – are used.

Each unit is represented by lumped-parameter thermal elements as illustrated in Fig. 4.29. Therefore, the analogy to electrical lumped-parameter models is used, with C_{th} being the thermal capacitance, R_{th} the thermal resistance and Q_{th} the thermal power dissipated within the volume element. This way, a 3D spatially-resolved LPTN is constructed [QSD14; Qi+14]. Compared to FEM analysis, the LPTN requires significantly lower computational effort, ehich makes it suitable for real-time online estimation [Qi+16a]. For efficient implementation on a microcontroller, the model complexity can be further reduced by the model-order-reduction approach presented in [BS10; Qi+16b].

The LPTN is experimentally parameterized by a series of alternating heating and cooling cycles, as given in Fig. 4.28. The model parameters are fitted so that the temperatures measured at various locations match those calculated by the thermal model. Here, a deviation in the range of ±5 °C could be achieved with overshoots of up to ±10 °C during transients. Since a higher temperature leads to an increased heat transfer to the ambient, the temperature model consisting of thermal resistances, capacitances and heat sources is generally stable. However, the open-loop model can drift to incorrect temperatures, due to model or parameter errors in the LPTN or in the loss-distribution model. Thus, using the end-winding temperature sensor and an ambient or housing sensor as corrective feedback is generally recommendable. It should be noted, that for precise parameterization and corrective feedback, the spatial resolution at the sensor locations must be sufficiently high. If this requirement is fulfilled at the potential locations of temperature hot-spots, the LPTN can simultaneously be used for adaptive overload control, which leads to an improved performance and higher thermal utilization [Qi+15].

The general structure of the resistance-adaption scheme is given in Fig. 4.30. Before the temperature distribution is calculated, the heat Q_{th} dissipated into the thermal model must be determined. In a first step, the ohmic losses in the stator and rotor are obtained from the FOC controller using

$$P_{\mathrm{s}} = \hat{R}_{\mathrm{s}}\left(i_{\mathrm{sd}}^{\Diamond 2} + i_{\mathrm{sq}}^{\Diamond 2}\right) \quad \text{and} \quad P_{\mathrm{r}} = \hat{R}_{\mathrm{r}}\frac{\hat{L}_{\mathrm{s}}^2}{\hat{L}_{\mathrm{m}}^2}\left(\left(i_{\mathrm{sd}}^{\Diamond} - \frac{\hat{\psi}_{\mathrm{s}}}{\hat{L}_{\mathrm{s}}}\right)^2 + \left(i_{\mathrm{sq}}^{\Diamond} - \hat{i}_{\mathrm{fe}}\right)^2\right). \tag{4.15}$$

The losses are distributed between stator slots and end winding or rotor bars and end ring, based on the relative resistance share which is a function of the stator and rotor geometry. The iron losses are obtained from the Steinmetz equation (2.19) and are distributed across the stator lamination and the rotor surface. For high-speed machines, also the friction losses in the air gap and the bearings should be considered.

With the temperature distribution resulting from the LPTN, the stator and rotor resistances can now be calculated using the same geometric relationship. Since the thermal time constants of the LPTN are generally higher by several orders of magnitude, the resistances can be considered as constant quantities within the dynamic equations of the FOC.

4.3 Measurement Results and Conclusions

To verify the torque accuracy of the IM drive, the torque deviation was measured over the entire torque and speed range. Fig. 4.31 shows the torque-deviation maps of the first-generation series drive of the StreetScooter along with the direct SFO controller using the Gopinath-style observer without rotor-resistance adaption and with spatially-resolved LPTN-based resistance adaption.

The initial series drive in Fig. 4.31a had a torque deviation in the range of −5 Nm in the base-speed region and up to 5 Nm during field weakening. The shaded areas indicate the operating points where the ±2.5 Nm requirement is not fulfilled. This almost applies to the entire base-speed region.

The direct SFO controller is inherently less parameter sensitive. Especially above 1500 rpm where the voltage model is dominant and the stator-resistance voltage drop is small compared to the back EMF, the torque accuracy is significantly improved. In this operating region, the absolute error remains below 2 Nm and the requirement is fulfilled. Only at high torque and low speeds, the torque deviation exceeds the desired limit. This is caused by the increasing influence of the current model in the stator flux-linkage observer. Since the rotor resistance is not adapted, significant estimation error occurs.

In Fig. 4.31c the LPTN-based adaption of the stator and rotor resistances was activated. The LPTN is executed with low priority in the main loop of the DSP. Together with the Gopinath-style stator flux-linkage observer, the absolute torque error remains below 1 Nm for the entire operating range.

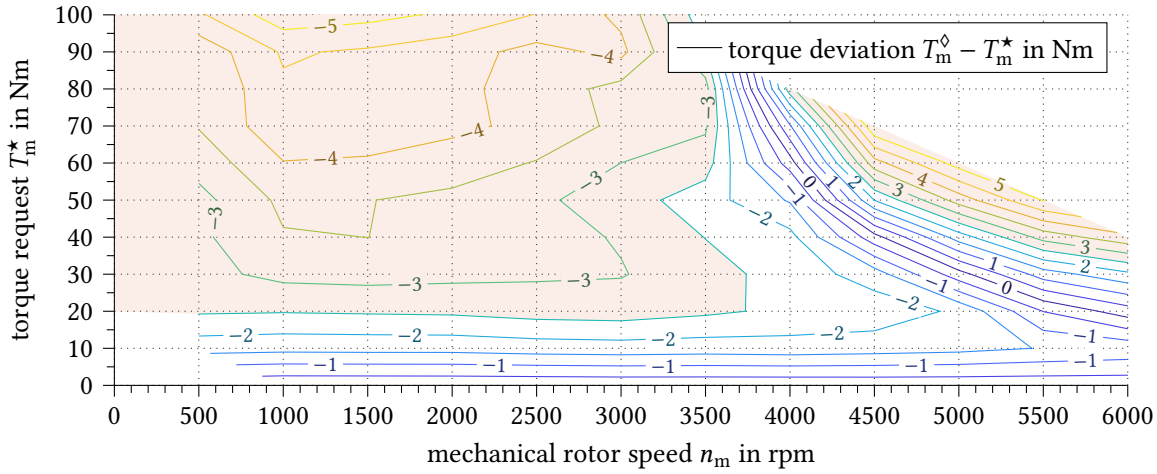

(a) first-generation series IM drive of the StreetScooter

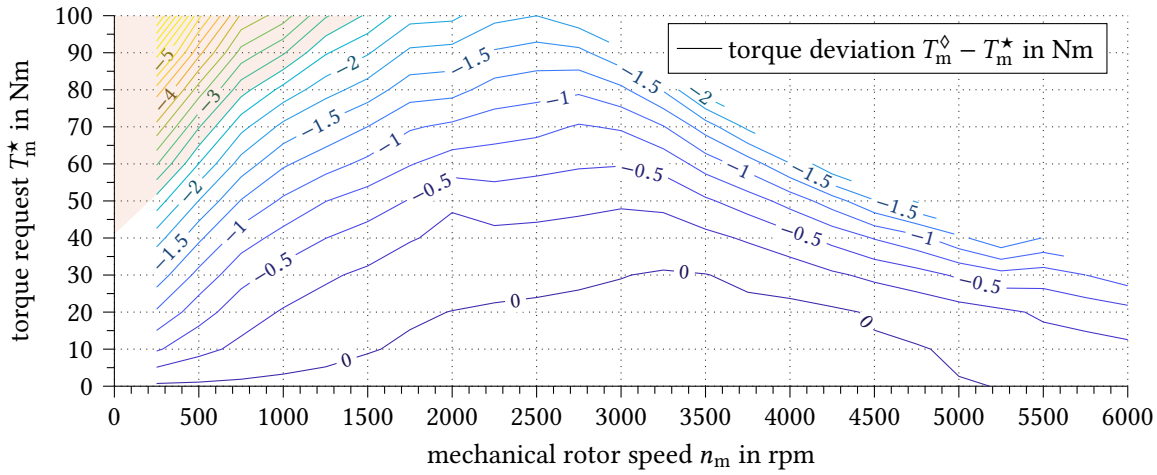

(b) direct SFO with Gopinath-style observer and without rotor-resistance adaption

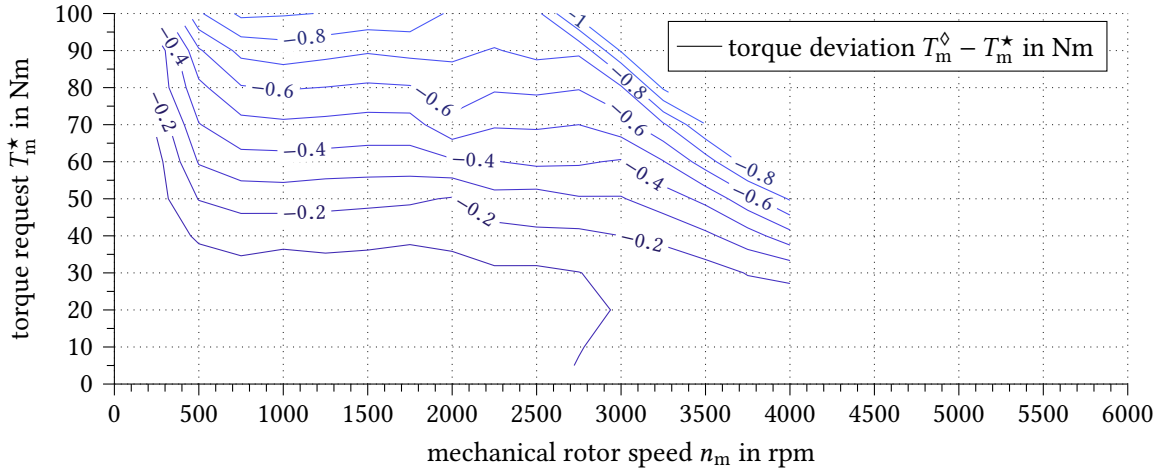

(c) with spatially/resolved LPTN thermal-model-based resistance adaption

Fig. 4.31: Measured absolute torque deviation of the IM drive with IM26kA.

4.4 Summary

Based on the frequency-response functions of the stator flux-linkage observers derived in Chapter 3, in Chapter 4, the open-loop and closed-loop observers were analyzed in terms of IM model parameter sensitivity, measurement distortion and inverter dead-time distortion. The introduced method allows a systematic analytical assessment of the resulting torque error and controller detuning caused by parameter deviations or balanced sensor-gain errors over the whole speed range. It is also supportive during dimensioning of the observer feedback gains with respect to parameter sensitivity. Furthermore, analytical expressions for the rejection of higher-order harmonics caused by imbalanced sensor gains, sensor offsets and inverter dead-time effect were derived.

The comparison between the Gopinath-style and Luenberger-type closed-loop observers revealed, that the Gopinath-style observer is generally less parameter sensitive. Torque deviation is mainly caused by thermal drift of the stator and rotor resistances. The influence of the inductances is relatively low. Especially the angular detuning using the Luenberger-type observer is much higher. Even though its parameter sensitivity could be significantly reduced using a sliding-mode feedback, the Gopinath-style observer still performs better – especially in terms of the inductance values. The same applies to the sensitivity to sensor errors and the rejection of higher harmonics, which makes the Gopinath-style observer the preferable option to achieve a high torque accuracy.

Experimental results show that the torque error using the Gopinath-style observer remains below 2 % of the nominal torque for a large operating range. Only at low speed and high torque, the deviation exceeds the target value of 2.5 %. This is a drastic improvement over the standard drive used in the first-generation StreetScooter.

For further improvement, adaptive compensation of parameter faults becomes necessary. As the torque error – with the Gopinath-style observer – is mainly caused by thermal resistance drift, only the stator and the rotor resistances need to be focused on. In this chapter, a spatially-resolved LPTN-based thermal model is proposed to determine the temperature distribution of the conductors, and thus estimate the resistance values. The thermal model approach has several advantages compared to MRAS and other electromagnetic-model-based methods. It is sufficiently decoupled from deviating inductance values, which – with MRAS – can lead to wrong estimation of the resistances and thus considerably increases the parameter sensitivity to inductance deviations. It allows simultaneous adaption of both resistances under all operating conditions, even during standstill. Since it describes the actual cause of the resistance drift, it inherently leads to physically reasonable values, and the thermal model can simultaneously be used for the monitoring of hot spots and dynamic overload control to increase the thermal utilization of the IM. Experimental results show a maximum torque deviation of 1 % of the maximum torque for the entire operating range.

5 Instantaneous Phase-Voltage Measurement

As discussed in the previous chapters, flux-linkage estimation using the IM voltage model requires precise information about the instantaneous stator voltage. This is especially critical at low speeds when the induced back EMF and thus the resulting signal-to-noise ratio are very low. Conventional stator flux-estimators which use the reference voltage $\vec{u}_\mathrm{s}^\star$ may then fail or produce a high estimation error. This leads to considerable torque error and causes speed-sensorless control algorithms to malfunction at low speeds.

The main reason for voltage disturbances are the dead-time effect and the semiconductor voltage drop of the VSI, as described in Section 2.3 and illustrated in Fig. 5.1. At low speed, they can become significant in relation to the back EMF. Direct voltage measurement at the converter outputs can reduce or solve this problem and enables additional features, which makes it a main aspect of this work. In the following, an improved instantaneous stator-voltage sensing circuit is proposed, which is closely integrated with the gate-driver circuit. The method is applicable to PWM based VSI systems with constant switching frequency, which is the most common setup in speed-variable electrical drives today. The components of the measurement circuit are dimensioned based on an analytical worst-case error assessment. The proposed voltage-sensing method is the prerequisite for a novel current- and voltage-sensor-offset calibration technique, which is independent from the control algorithm and the load of the VSI. Furthermore, an approach for online semiconductor condition monitoring, such as temperature detection, using the voltage-sensing circuit is presented. All features are implemented and experimentally evaluated. Partial contents of this chapter were published in the course of this work in [SJD16; SD18; Sch+17].

Instantaneous measurement of the VSI output voltages is not a trivial exercise. As illustrated in Fig. 5.1, in addition to the dead-time effect and semiconductor voltage drop,

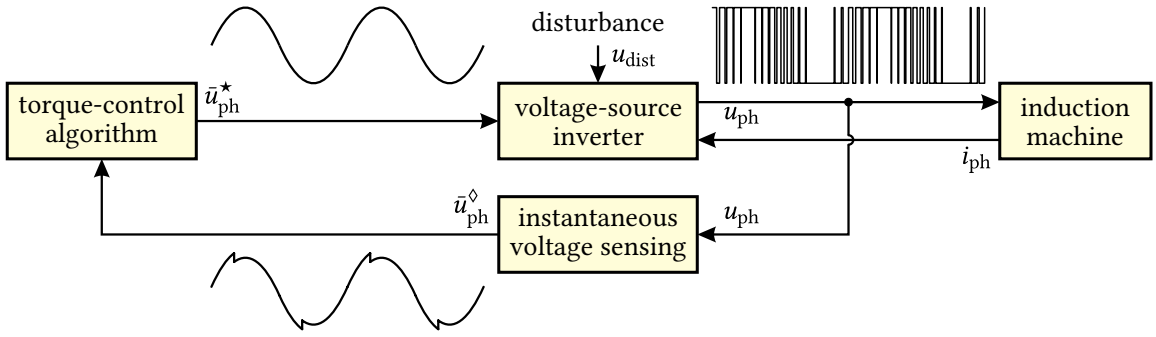

Fig. 5.1: Scheme of the drive system with instantaneous voltage sensing. Measurement of the switched PWM output voltage of the voltage-source inverter (VSI) requires additional effort.

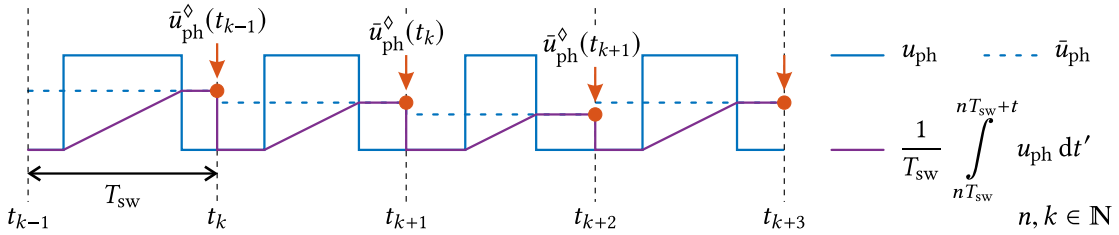

Fig. 5.2: Definition of the switching-period average voltage and notation of the voltage quantities.

the disturbances introduced by the inverter include higher-order switching harmonics. Due to the switching nature of this PWM modulated voltage, simple sampling – once per PWM switching period T_{sw} – is not sufficient. Instead, the switching-period average voltage must be obtained, which requires additional preconditioning of the voltage to be measured. It is defined by the integral

$$\bar{u}_{\mathrm{ph}}(t_k) = \frac{1}{T_{\mathrm{sw}}} \int_{t_k}^{t_{k+1}} u_{\mathrm{ph}}\,\mathrm{d}t, \tag{5.1}$$

as illustrated in Fig. 5.2. Equation (5.1) is considered as the ideal solution. However, implementation in a real VSI system which operates at switching frequencies of a few kHz to some MHz, accurate detection is challenging.

5.1 State-of-the-Art Methods for Stator Voltage Detection

In the past, only few publications have been written on the problem of instantaneous PWM inverter output voltage measurement. The most important ones and the common alternative solution are briefly described below. For consistent illustration, the voltage is considered to be detected from the VSI phase output to the DC-link ground potential.

5.1.1 Reference Voltage with Feed-Forward Disturbance Compensator

Since voltage sensing requires additional hardware circuitry and signal processing, dedicated measurement of the stator voltage has not been very attractive in the past. The improved low-speed performance – compared to using reference quantity available in the controller – did not justify the extra cost which comes along with the measuring circuit. As a result, the reference voltage $\vec{u}^{\star}_{\mathrm{s}}$ is usually used as the observer input.

To improve the accuracy and the low-speed performance, a feed-forward disturbance compensator as shown in Fig. 5.3 can be used. After inverse Clarke transformation and superposition of a zero-sequence voltage defined by the modulation strategy, the reference phase voltage $\bar{u}^{\star}_{\mathrm{ph}}$ is equal to the product of the PWM duty cycle and the DC-link

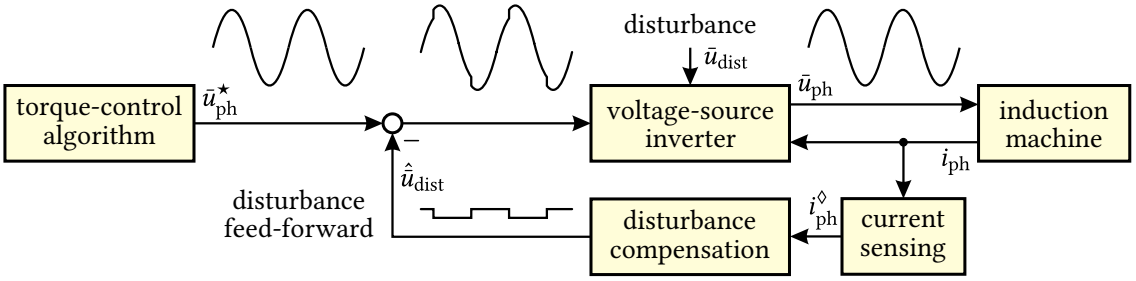

Fig. 5.3: Feed-forward dead time and semiconductor voltage drop compensation scheme by open-loop linearization of the inverter transfer function.

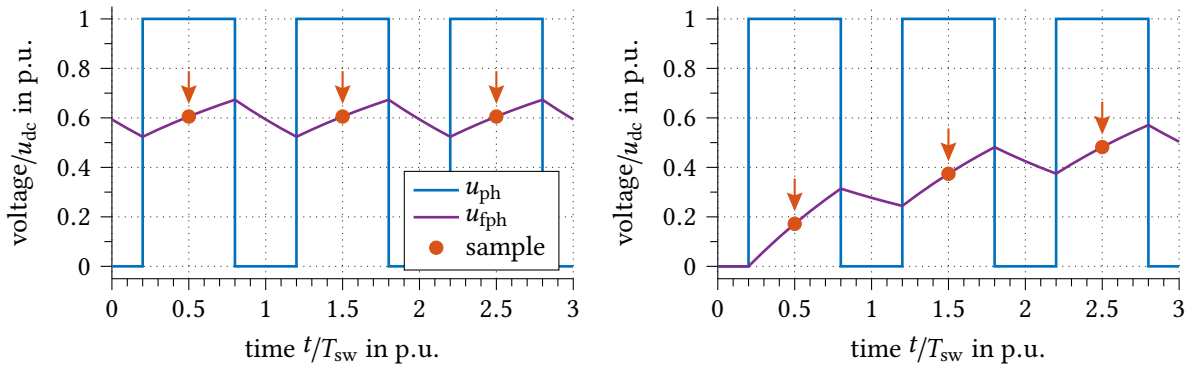

(a) steady state

(b) step response

Fig. 5.4: Voltage measurement using the integrating behavior of a low-cutoff-frequency low-pass filter (LPF) and center-aligned sampling.

voltage u_{dc}. Its only difference from the IM terminal phase-to-ground voltage $\bar{u}_{\mathrm{ph}}$ is the inverter distortion voltage $\bar{u}_{\mathrm{dist}}$ which has been derived in Section 2.3. With the measured phase current $\bar{i}^{\Diamond}_{\mathrm{ph}}$ and the DC-link voltage it can be calculated using (2.45) on page 40.

The distortion voltage calculated this way is subtracted from the reference voltage and compensates the VSI distortion voltage in a feed-forward manner. $\bar{\hat{u}}^{\star}_{\mathrm{s}}$ is then decoupled from the disturbance and can be used for flux-linkage estimation. However, (2.45) is an open-loop model and thus sensitive to parameter drift which causes a compensation error. Furthermore, the measured current is delayed by two switching periods, which is why in this work the current reference is used instead. Even though the remaining absolute error is low, the relative error at low speed becomes significant and has a considerable effect on the flux-linkage estimation, according to Section 4.1.2.

5.1.2 Phase Voltage Measurement Techniques

With the availability and cost reduction of powerful electronic components, the use of additional components for output-voltage sensing becomes more and more attractive. A common solution found in commercial products utilizes the integrating behavior of a low-cutoff-frequency LPF which suppresses the switching harmonic content [Tex13]. The

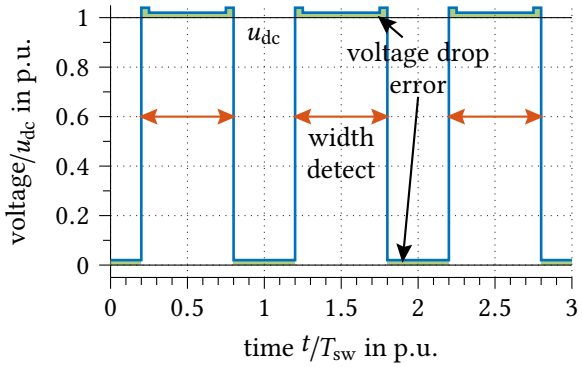

Fig. 5.5: Pulse-width detection and calculation using the measured DC-link voltage.

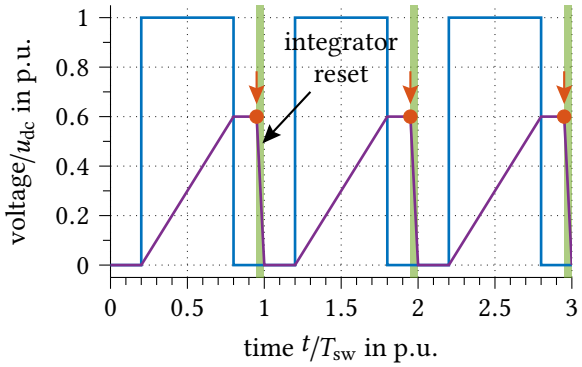

Fig. 5.6: Switching-period average voltage measurement using an analog integrator.

switching-period average voltage can then be determined by center-aligned sampling of the filtered phase voltage u_{fph}, as shown in Fig. 5.4a. The method allows accurate measurement in DC conditions. For AC signals, it leads to a constant magnitude error and phase-shift

$$\bar{u}_s^{\diamond} = \bar{u}_s \cdot \frac{1}{\sqrt{1 + \omega_s^2 \tau_f^2}} \tag{5.2a}$$

$$\text{and} \quad \varphi_f = -\arctan(\omega_s \tau_f) \tag{5.2b}$$

in steady-state conditions. Equation (5.2) can be used for compensation, however, the dynamic performance is drastically degraded by the LPF, as illustrated in Fig. 5.4b. Consequently, this solution may not be considered as *instantaneous* voltage sensing.

In [YC90], only the PWM pulse width and the DC-link voltage are measured. The switching-period average is then determined by multiplication of both and division by the switching period time T_{sw}. As illustrated in Fig. 5.5, this approach ignores the semiconductor voltage drop, which has been reported to cause an error of several tens of percent at low speeds [CNH97].

The most promising approaches are based on periodical integration over the switching period, according to Fig. 5.2. The problem with analog integration in a real system is, that it requires a nonzero settling time for proper reset, as shown in Fig. 5.6. The resulting error can be minimized when the integrator is reset during the low output state. In [CNH97] this problem is omitted by using two alternating integrators. However, this solution requires considerable effort, since eight switches must be controlled for signal routing and reset triggering per phase. In [SBS02] and [BC07], only a single integrator is used. The latter utilizes a storage capacitor to continue integration during A/D conversion and reset. Experimental results in [SBS02] show stable sensorless operation of a PMSM drive at 1 % of the rated speed.

With newer publications, the method of digital integration is gaining in importance. It promises a fixed accuracy, excellent linearity and less sensitivity to component tolerances

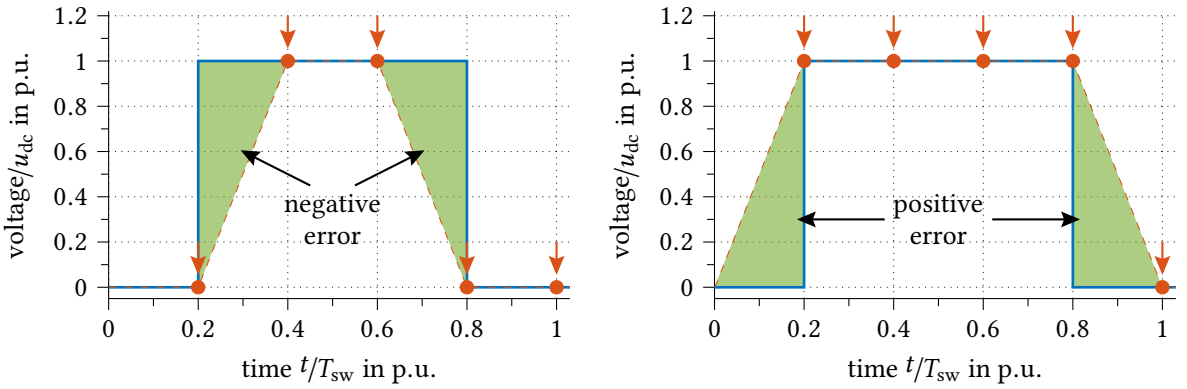

(a) duty cycle: $0.6 - \varepsilon$

(b) duty cycle: $0.6 + \varepsilon$

Fig. 5.7: Detection of the switching-period average by oversampling and digital integration. Worst-case situation of the duty-cycle dependent error with slightly different duty cycle $0 < \varepsilon \ll 1$.

and aging when compared to the analog method [PZ10]. However, a comparably high sampling frequency f_a is required to obtain sufficient accuracy. As demonstrated in Fig. 5.7, the measurement error depends on the location of the voltage edges between two adjacent sampling points. In the worst-case, a slightly different duty cycle can cause the sampling points next to the edges to be located on the low or high voltage potential, which causes maximum negative or positive error. The integration error is equal to the shaded area in the figure. The maximum error magnitude is defined by number of samples per PWM period $m_a = f_a/f_{sw}$ as

$$\max\left(\Delta\bar{u}_{ph}^{\Diamond}\right) = \frac{u_{dc}}{m_a}. \tag{5.3}$$

In [PZ10] a measurement error below 2 % of the peak voltage was achieved using a sampling frequency of 1.28 MHz at 10 kHz switching frequency. With $f_a = 20$ MHz the maximum error was reduced to 0.5 %. The values differ from the theoretical maximum in (5.3) because the voltage in [PZ10] is measured from phase to phase and due to the presence of a superimposed first-harmonic error, which is probably caused by improper gains in relation to the reference measurement. The digital integration error typically manifests itself in a high-frequency noise with a magnitude defined by (5.3), which in [PZ10] meets the theoretical maximum.

The digital integration method is commonly used for example in high precision voltage and power meters which use high resolution A/D converters with sampling rates above some MHz [ZES12]. Oscilloscopes even achieve sampling rates above 10 GHz. However, very high sampling rate A/D converters usually come along with a reduced resolution, or they are very expensive and thus not suitable for low-cost inverter systems [SD18].

An alternative low-cost solution, that does not require dedicated A/D converters is proposed in [WL16; Wan+17]. The switching-period average voltage is obtained by counting the number of pulses produced by a voltage-controlled oscillator (VCO) that is applied to the VSI terminals. This way, only one digital signal per measurement is required. Experi-

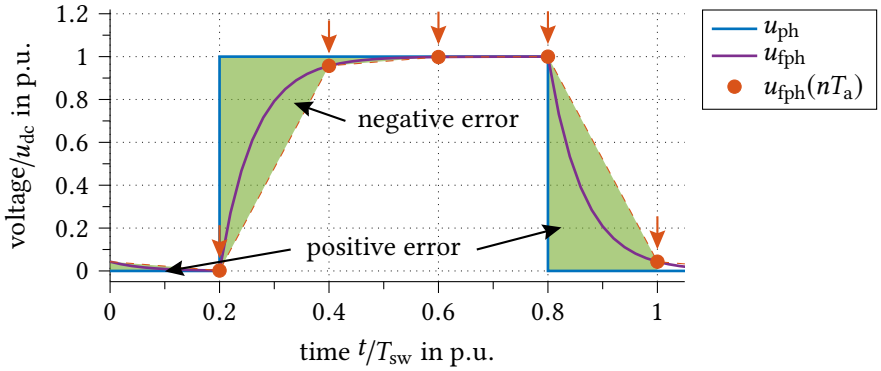

Fig. 5.8: Significant reduction of the digital integration error using a first-order high-cutoff-frequency LPF. Error at rising and falling edge are canceled out.

ments show precise voltage sensing at a switching frequency of 1.5 kHz using a 4.16 MHz VCO. However, the resolution is limited. In order to achieve results comparable to the solution presented below, a linear VCO with a minimum frequency range of 0 to 170 MHz is required, which implies corresponding demands on the evaluation logic.

5.2 Instantaneous Measurement of the PWM Switching-Period Average Voltage

In this work, the digital integration method is followed and improved by an analog first-order LPF. With a cutoff-frequency higher than the switching frequency f_{sw} and lower than the sampling frequency f_a, the worst-case sampling error in (5.3) can be significantly reduced. In contrast to the low-cutoff-frequency LPF solution in Section 5.1.2, this approach does not utilize the integrating behavior, but the rate-limiting characteristics of the LPF. This way the slope of the rectangular PWM voltage is reduced and the position of the voltage edge contributes to the measurement. As shown in Fig. 5.8, the problem present in Fig. 5.7 without LPF is reduced. Due to the high cutoff frequency, only a minimal distortion occurs, whereas the area under the filtered voltage remains the same. In other words, the filter suppresses higher harmonic content above the Nyquist frequency but allows the fundamental frequency to pass without notable distortion.

This approach promises an accuracy comparable to that of the high-sampling-rate digital method using a low-cost lower-sampling-rate A/D converter, less sensitivity to noise and all other advantages of the digital integration method. A similar approach was also followed and patented by Tallam et al. at the same time as this work was created [Tal+16].

As the digital integration error reduces with decreasing LPF cutoff frequency and the filter distortion increases, there is an optimum filter time constant which minimizes the total measurement error. To derive the error optimal filter time constant, the worst-case measurement error is analyzed analytically in the following.

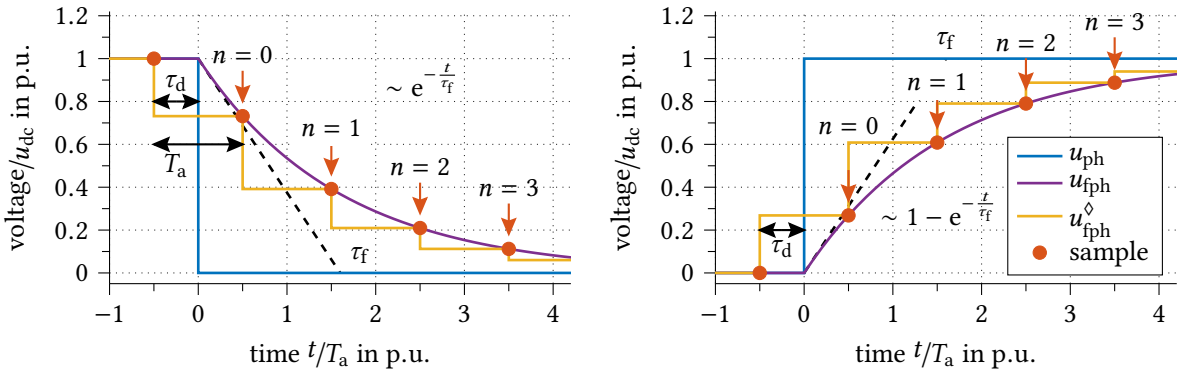

(a) falling edge

(b) rising edge

Fig. 5.9: Digital integration error at the rising and falling PWM voltage edge using the backward Euler method.

5.2.1 Theoretical Worst-Case Measurement Error Analysis

The worst-case measurement error can be understood as the superposition of the maximum remaining digital integration error after filtering and the LPF induced distortion caused by (5.2) at the maximum stator electrical frequency f_s with

$$\max\left(\Delta\bar{u}^{\Diamond}_{ph}\right) = \underbrace{\max\left(\Delta\bar{u}^{\Diamond}_{fph}\right)}_{\text{dig. integration}} + \underbrace{\max\left(\Delta\bar{u}_{fph}\right)}_{\text{LPF distortion}} . \tag{5.4}$$

Both can be analyzed individually and form a convex function when superimposed and described as a function of the LPF time constant τ_f.

5.2.1.1 Digital Integration Error with LPF

The following assumptions are beneficial for the calculation of the sampling-related error.

- The VSI output voltage is assumed to be perfectly rectangular. Then, only the edges of the voltage signal contribute to the measurement error.
- The LPF time constant τ_f is assumed to be much smaller than the switching period T_{sw} and the PWM pulse width. The error contribution of the rising and falling edge may then be analyzed separately with an infinite bound of integration.

The general validity of these assumptions is proven by experimental and numerical verification in Section 5.2.4.1.

The digital integration error at the falling edge is calculated according to the illustration in Fig. 5.9a. The dashed line shows the maximum voltage slope which is limited by the LPF to $\pm u_{dc}/\tau_f$. The yellow curve represents the sampled signal of the filtered phase voltage

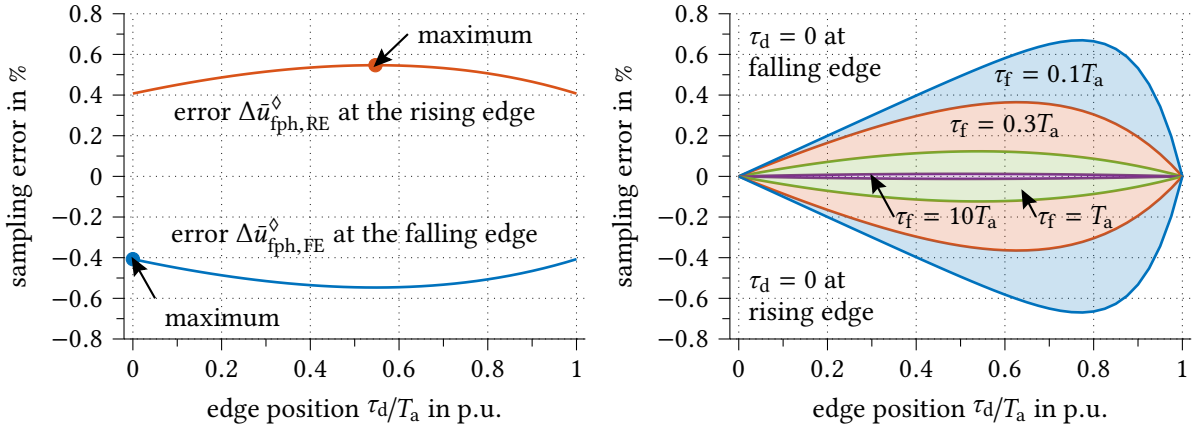

(a) integration error at the edges (b) total integration error

Fig. 5.10: Digital integration error at the rising and falling edge as a function of the edge position τ_d (a) and total integration error as a function of τ_d and τ_f (b). The number of samples per switching period is set to $m_\mathrm{a} = 100$.

$u^{\diamond}_{\mathrm{fph}}$, which is integrated using the backward Euler method. The digital integration error is then equal to the area between $u^{\diamond}_{\mathrm{fph}}$ and u_{fph} and can be calculated using

$$\begin{aligned}\Delta\bar{u}^{\diamond}_{\mathrm{fph,FE}} &= \underbrace{\frac{u_\mathrm{dc}}{T_\mathrm{sw}} \cdot \sum_{n=0}^{\infty} T_\mathrm{a} \mathrm{e}^{-\frac{(n+1)T_\mathrm{a}-\tau_\mathrm{d}}{\tau_\mathrm{f}}}}_{\text{area below } u^{\diamond}_{\mathrm{fph}}} - \underbrace{\frac{u_\mathrm{dc}}{T_\mathrm{sw}} \cdot \int_0^{\infty} \mathrm{e}^{-\frac{t}{\tau_\mathrm{f}}}\,\mathrm{d}t}_{\text{area below } u_{\mathrm{fph}}} - \frac{\tau_\mathrm{d}}{T_\mathrm{sw}} u_\mathrm{dc} \\ &= \frac{T_\mathrm{a}}{T_\mathrm{sw}} u_\mathrm{dc} \mathrm{e}^{-\frac{T_\mathrm{a}-\tau_\mathrm{d}}{\tau_\mathrm{f}}} \cdot \underbrace{\sum_{n=0}^{\infty} \left(\mathrm{e}^{-\frac{T_\mathrm{a}}{\tau_\mathrm{f}}}\right)^n}_{\text{geometric series}} - \frac{T_\mathrm{a}+\tau_\mathrm{f}}{T_\mathrm{sw}} u_\mathrm{dc} \quad \text{with} \quad n \in \mathbb{N}.\end{aligned} \tag{5.5}$$

With the help of the geometric series, a compact expression is found as

$$\Delta\bar{u}^{\diamond}_{\mathrm{fph,FE}} = \frac{T_\mathrm{a}}{T_\mathrm{sw}} u_\mathrm{dc} \cdot \frac{\mathrm{e}^{-\frac{T_\mathrm{a}}{\tau_\mathrm{f}}}}{1-\mathrm{e}^{-\frac{T_\mathrm{a}}{\tau_\mathrm{f}}}} \mathrm{e}^{\frac{\tau_\mathrm{d}}{\tau_\mathrm{f}}} - \frac{T_\mathrm{a}+\tau_\mathrm{f}}{T_\mathrm{sw}} u_\mathrm{dc} \quad \text{with} \quad 0 \le \tau_\mathrm{d} < T_\mathrm{a}. \tag{5.6}$$

The digital integration error at the rising edge can be calculated using the same approach, which leads to

$$\Delta\bar{u}^{\diamond}_{\mathrm{fph,RE}} = -\frac{T_\mathrm{a}}{T_\mathrm{sw}} u_\mathrm{dc} \cdot \frac{\mathrm{e}^{-\frac{T_\mathrm{a}}{\tau_\mathrm{f}}}}{1-\mathrm{e}^{-\frac{T_\mathrm{a}}{\tau_\mathrm{f}}}} \mathrm{e}^{\frac{\tau_\mathrm{d}}{\tau_\mathrm{f}}} + \frac{T_\mathrm{a}+\tau_\mathrm{f}}{T_\mathrm{sw}} u_\mathrm{dc} \quad \text{with} \quad 0 \le \tau_\mathrm{d} < T_\mathrm{a}. \tag{5.7}$$

The resulting integration error at both edges is plotted in Fig. 5.10a as a function of τ_d for $m_\mathrm{a} = 100$ and $\tau_\mathrm{f} = 0.88T_\mathrm{a}$. The error at the rising edge is partially compensated at the

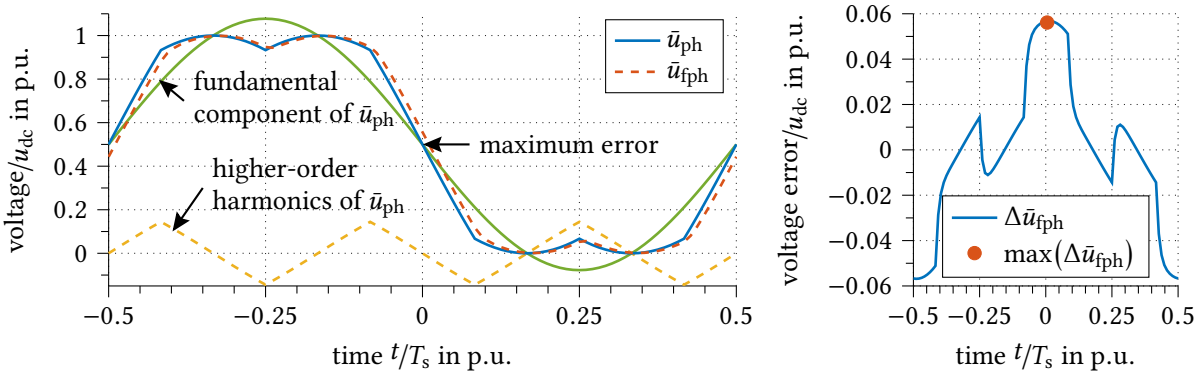

(a) SVM voltage and LPF filtered signal

(b) phase delay induced error

Fig. 5.11: Switching period average of the original and the filtered voltage signal (a). The LPF phase delay causes an angle dependent error (b). Simulation result with $f_s = 250\,\text{Hz}$ and $\tau_f = 42\,\mu\text{s}$.

falling edge. However, since τ_d – induced by dead-time effects, unequal propagation delays and other nonlinearities – varies independently for both edges, a small error according to the shaded area in Fig. 5.10b remains. The worst-case positive error is found by choosing $\tau_d = 0$ at the falling edge, as marked in Fig. 5.10a. The maximum error at the rising edge is then obtained by finding the root of the derivative of (5.7) as

$$\tau_d = T_a + \tau_f \ln\left(\frac{\tau_f}{T_a}\left(1 - e^{-\frac{T_a}{\tau_f}}\right)\right). \tag{5.8}$$

With $\tau_d = 0$ in (5.6) and (5.8) in (5.7), the worst-case digital integration error is derived as

$$\max\left(\Delta\bar{u}^{\Diamond}_{fph}\right) = \frac{\tau_f}{T_{sw}} u_{dc} \cdot \left(\ln\left(\frac{\tau_f}{T_a}\left(1 - e^{-\frac{T_a}{\tau_f}}\right)\right) - 1\right) + \frac{T_a}{T_{sw}} \cdot \frac{u_{dc}}{1 - e^{-\frac{T_a}{\tau_f}}}. \tag{5.9}$$

5.2.1.2 Measurement Error caused by LPF distortion

The LPF cutoff frequency is chosen higher than the switching frequency and lower than the sampling frequency. If the value is at least $2 \cdot f_{sw}$, and assuming that the fundamental frequency is 20 times lower than f_{sw}, the relative magnitude error (5.2a) introduced by the LPF is as low as 0.03 % and may therefore be neglected.

However, the phase shift (5.2b) of the filter produces an instantaneous error in the filtered switching-period average voltage, which has a maximum in the region of the voltage first harmonic zero crossing, as illustrated in Fig. 5.11. Since the relevant frequency components of $\bar{u}_{ph}$ – which are the first and the third harmonic – are much lower than the LPF cutoff frequency the group delay can be simplified as

$$-\frac{d\varphi_f(\omega_s)}{d\omega_s} = \frac{d}{d\omega_s}\arctan(\omega_s\tau_f) = \frac{\tau_f}{1 + \omega_s^2\tau_f^2} \approx \tau_f. \tag{5.10}$$

In the case of space-vector modulation (SVM), $\bar{u}_{\mathrm{ph}}$ consists of a sinusoidal component with a maximum magnitude of $u_{\mathrm{dc}}/\sqrt{3}$, which is shifted by half the DC-link voltage, and a superimposed triangular component of three times the fundamental frequency, as given in Fig. 5.11a [vSS88; Rei96]. The magnitude of the latter is typically a fourth of the fundamental wave. With $\sin(x) \approx x$ at the first harmonic zero crossing, the worst-case LPF distortion error can be calculated from the slopes of both voltage components multiplied by the group delay as

$$\max\left(\Delta\bar{u}_{\mathrm{fph}}\right) = \frac{2\pi + 3}{\sqrt{3}} u_{\mathrm{dc}} f_{\mathrm{s}} \cdot \tau_{\mathrm{f}} \tag{5.11}$$

According to Fig. 5.11b, the analytical calculation matches the simulation result very well, even for the relatively low filter cutoff frequency of only $15 \cdot f_{\mathrm{s}}$, chosen for better illustration.

It should be noted, that the rate-limiting nature of the LPF is of major interest to reduce the digital integration error. It is sufficient to use an easy-to-implement first-order LPF, since higher-order filters, such as bessel filters, have very similar rate-limiting characteristics. Higher-order filters even have negative effect on the accuracy as they generally cause a higher group delay.

5.2.2 Dimensioning of the Filter Time Constant

The resulting filter-dependent worst-case error components (5.9) and (5.11) are plotted along with the total error (5.4) in Fig. 5.12a. As expected, the digital integration error decreases strictly monotonously with increasing LPF time constant, whereas the LPF distortion increases linearly. Consequently, a filter time constant exists, which minimizes the maximum instantaneous measurement error. For the VSI configuration used in this work – which is $f_{\mathrm{sw}} = 10\,\mathrm{kHz}$ and $f_{\mathrm{a}} = 1\,\mathrm{MHz}$ as given in Appendix A.2.2 – the optimal filter cutoff frequency is equal to 169 kHz. It is calculated for a maximum fundamental frequency of $f_{\mathrm{s}} = 250\,\mathrm{Hz}$. Designing the filter for a lower stator frequency can be advantageous, as it leads to an improved low-speed accuracy. However, a higher error at frequencies above the design frequency must be tolerated, which can be compensated in steady-state conditions.

It should be emphasized, that the resulting measurement error – here 0.26 % of u_{dc} – is a worst-case error magnitude. The actual measurement error alternates quickly as a function of the duty-cycle and the slope of the fundamental signal and must rather be seen as a high-frequency noise within this error limit.

Since the derivative of Equation (5.9) contains terms with nested logarithms, a numerical solution for determining the error-optimal LPF time constant is preferred. Fig. 5.12b shows the resulting cutoff frequency and error as a function of the sampling rate. To limit the measurement error to 1 % of u_{dc}, a minimum of $m_{\mathrm{a}} = 25$ samples must be taken per switching period.

With the filter time constant expressed as a ratio with the sampling time $\tau_{\mathrm{f}}/T_{\mathrm{a}}$ and the fundamental frequency as a ratio with the switching frequency $f_{\mathrm{s}}/f_{\mathrm{sw}}$, a general configuration-

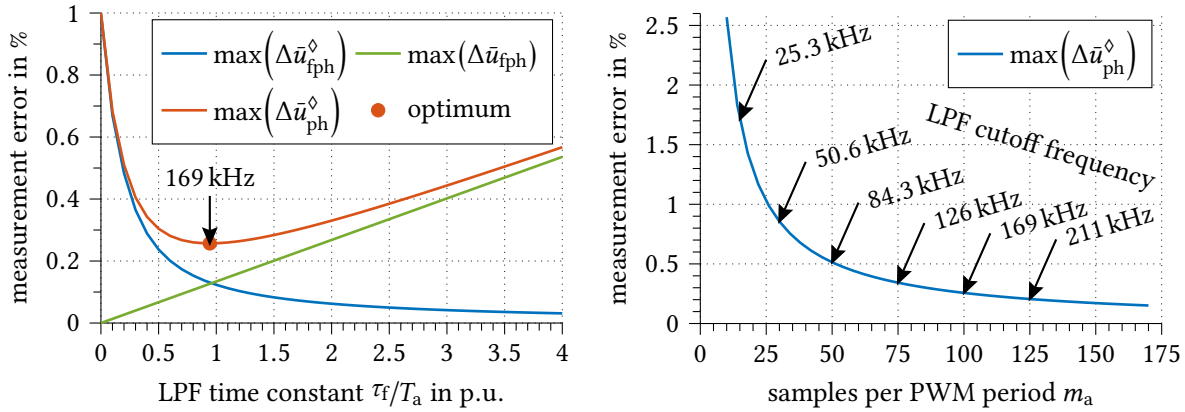

(a) worst-case error components with $m_a = 100$

(b) minimum worst-case error

Fig. 5.12: Worst-case integration, phase-shift and resulting total error as a function of the LPF time constant with a global minimum at 169 kHz and optimal LPF cutoff-frequency with resulting worst-case measurement error as a function of m_a for $f_{sw} = 10\,\text{kHz}$ and $f_s = 250\,\text{Hz}$.

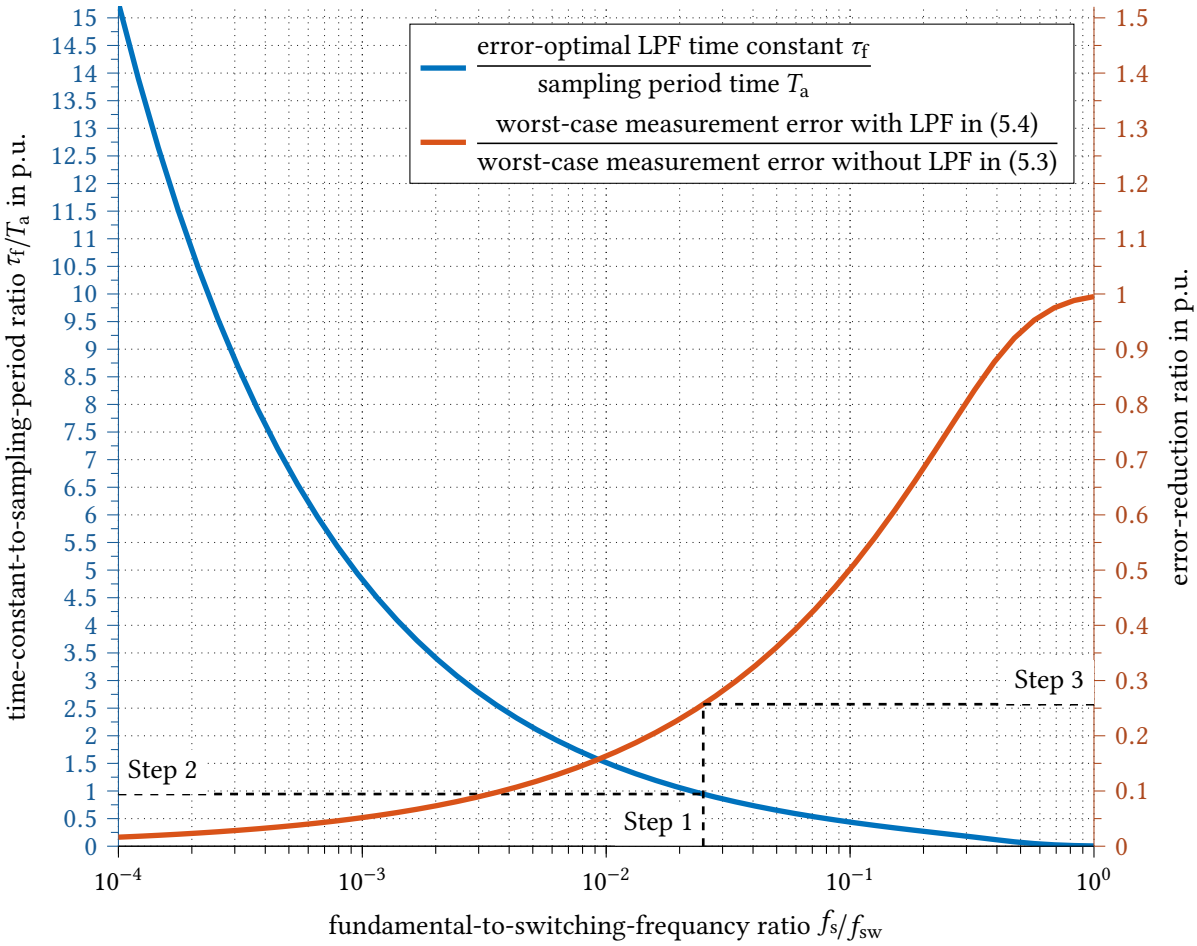

Fig. 5.13: General solution for the optimal LPF time-constant ratio τ_f/T_a as a function of the fundamental-to-switching-frequency ratio f_s/f_{sw} and the resulting reduction of the measurement error compared to digital integration without filter. The optimal time-constant ratio and the error reduction are independent from m_a and may be used as lookup table for LPF dimensioning.

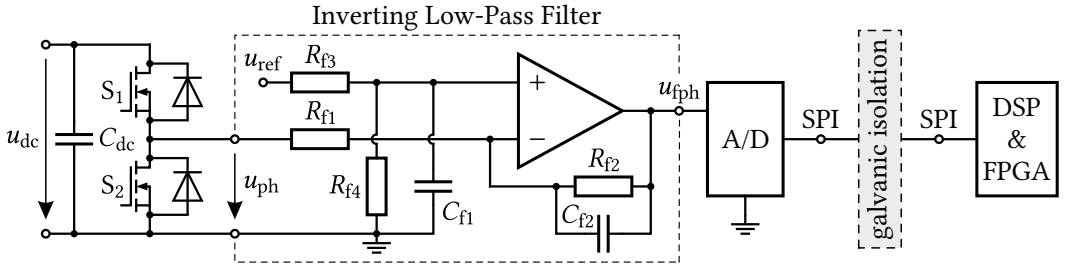

Fig. 5.14: Circuit diagram of the voltage measurement circuit with inverting LPF and A/D conversion on the high-voltage side. The phase voltage is measured across the low-side switch S_2.

independent solution can be found which is given in Fig. 5.13. With the help of the graphs, the LPF can be dimensioned for any constant-switching-frequency PWM based VSI system by the following design procedure:

Step 1: Selection of a suitable stator fundamental frequency for which the LPF is optimized. During operation below that frequency, the resulting worst-case measurement error is lower and above it is higher, according to (5.4). Afterwards, the abscissa is calculated as

$$\frac{f_s}{f_{sw}} = \frac{\text{design stator fundamental frequency}}{\text{PWM switching frequency}}.$$

Step 2: The optimal time-constant-to-sampling-period ratio is taken from the left ordinate and multiplied with T_a to obtain the error optimal LPF time constant τ_f.

Step 3: Reading of the error ratio from the right ordinate and division by the number of samples per switching period $m_a = f_a/f_{sw}$ to obtain the theoretical worst-case measurement error in p.u. of the DC-link voltage.

It should be noted, that this optimization approach is not limited to two-level VSI systems. The phase output voltage of a three-level neutral-point clamped (NPC) inverter, for example, can be described as two superimposed rectangular waveforms of half the DC-link voltage, which leads to exactly the same worst-case digital integration error. This also applies to higher-order multi-level VSI systems.

5.2.3 Gate-Driver Integrated Hardware Implementation

As depicted in Fig. 5.14, the VSI output voltage is measured across the inverter-leg bottom switch S_2, for each phase output individually. The LPF and A/D conversion are implemented on the high-voltage side, which is beneficial in terms of measuring noise. Galvanic isolation is provided on the digital side through an isolated SPI bus. Even though for most applications the differential voltage between the phases is of major interest, using three independent measurement circuits from the phase outputs to the DC-link ground – instead of only two differential measurements – has some important advantages:

TABLE 5.1
Voltage Measurement Circuit Parameters of Inverter 2

(a) System Parameters

Parameter		Value
DC-link voltage	u_{dc}	75 V
switching frequency	f_{sw}	10 kHz
sampling frequency	f_a	1 MHz
design frequency	f_s	250 Hz
LPF cutoff frequency	$1/(2\pi\tau_f)$	169 kHz
samples per PWM period	m_a	100
A/D converter resolution		14 bit

(b) LPF Parameters

Parameter		Value
reference voltage	u_{ref}	4.5 V
input resistor	R_{f1}	56 kΩ
LPF resistor	R_{f2}	1.5 kΩ
offset resistor	R_{f3}	330 Ω
offset resistor	R_{f4}	9.1 kΩ
filter capacitor	C_{f1}	100 nF
LPF capacitor	C_{f2}	570 pF

- It is an inherently modular solution and can be easily applied to multi-phase systems. Furthermore, a full integration into the gate-driver integrated circuit (IC) of the bottom switch is possible.
- Simple implementation of the analog LPF circuit using a single-ended operational amplifier with a single supply and a single-ended A/D converter – no need for analog subtraction or additional components that could be affected by temperature drift.
- Low measuring noise due to positioning close to the gate driver and common DC-link ground potential as demonstrated in Section 5.2.4.
- Implementation of additional features, such as detection of the inverter voltage distortion for online current and voltage sensor offset calibration as demonstrated in Section 5.3 or individual monitoring of the semiconductor condition as demonstrated in Section 5.4.

Due to the semiconductor voltage drop across the MOSFETs and diodes, u_{ph} ranges from a few volts negative to slightly more than the DC-link voltage u_{dc}. This measuring range can be provided by a single-supply operational amplifier and single-ended A/D converter using an inverting LPF as illustrated in Fig. 5.14. The transfer function of the filter is then given by

$$\underset{\sim}{u}_{fph} = \underbrace{\frac{R_{f4}(R_{f1}+R_{f2})}{R_{f1}(R_{f3}+R_{f4})}u_{ref}}_{\text{offset}} - \underbrace{\frac{R_{f2}}{R_{f1}}\underset{\sim}{u}_{ph}\frac{1}{1+s\tau_f}}_{\text{gain and LPF}} \quad \text{with} \quad \tau_f = R_{f2}C_{f2}. \tag{5.12}$$

u_{ref} is a constant low-noise reference voltage which is simultaneously used for A/D conversion and offset adjustment. The input resistor R_{f1} must be chosen carefully to limit the current into the analog circuit. R_{f2} and C_{f2} are then used to set the amplifier gain and LPF time constant, respectively. With R_{f3} and R_{f4} the offset can be adjusted to meet the desired measuring range. For the following considerations, Inverter 2 is used with the system properties given in Table 5.1a. With the measurement circuit parameters in Table 5.1b

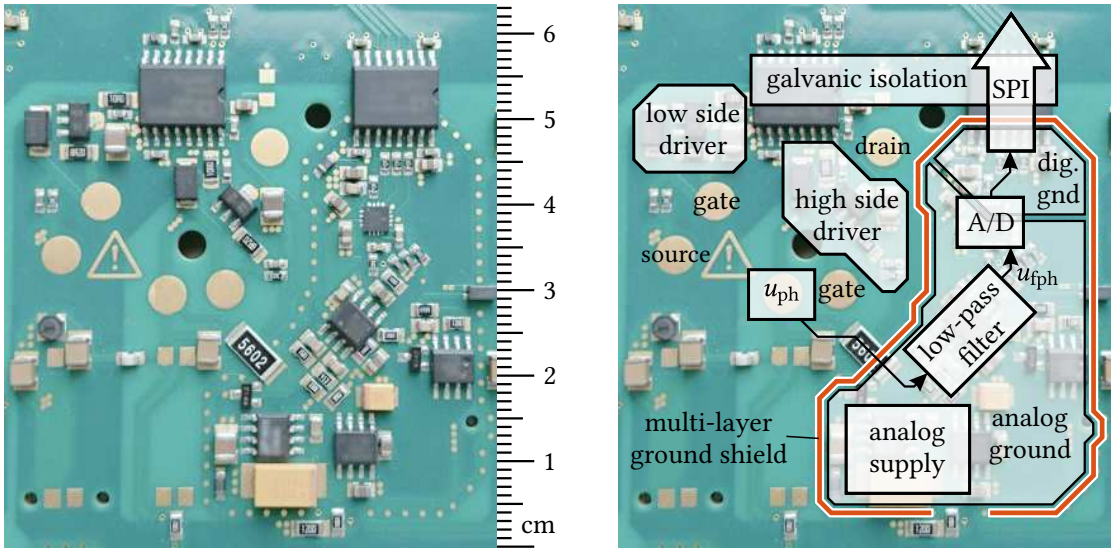

(a) photography of the PCB (b) PCB with component description

Fig. 5.15: Gate-driver integrated implementation of the measurement circuit on a six-layer printed circuit board (PCB) with dedicated grounds and voltage supplies for high-voltage, analog and digital sections.

the A/D converter input range of 0 to 4.5 V corresponds to a measuring range of −1.5 to 166.5 V. The resolution of 10 mV is defined by the 14 bit A/D converter. Inverter 1 is operated at a higher DC-link voltage of $u_{dc} = 120$ V with otherwise identical parameters and properties. Inverter 3 is a 400 V IGBT system, which is used for higher voltage validation. Further details on the hardware properties can be found in Appendix A.2.2.

Fig. 5.15a shows a photograph of the gate-driver section of the produced printed circuit board (PCB) including inverter control and drivers with the component descriptions given in Fig. 5.15b. The left upper half shows the low- and high-side gate-drivers of a single half bridge. The gold-plated pads are the gate, source and drain contacts to the MOSFETs, which are connected via springs (Inverter 1) or pogo pins (Inverter 2). The phase voltage sensing circuit is positioned close to the gate driver. It is separated from the driver circuit by a surrounding ground shield (red line) to suppress noise and contains dedicated grounds and voltage supplies for the analog and digital components. The A/D converted signals are transmitted to the FPGA via a galvanically isolated SPI bus.

5.2.4 Experimental Verification and Conclusions

The accuracy of the voltage sensing circuit is experimentally verified using Inverter 2. In a first step, the analytical solution for the digital integration error is verified. Then, the sampling of the filtered rectangular PWM voltage signal is examined and the measurement accuracy is proven for different fundamental voltage waveforms. The validity for higher voltages is proven by a comparative measurement with Inverter 3.

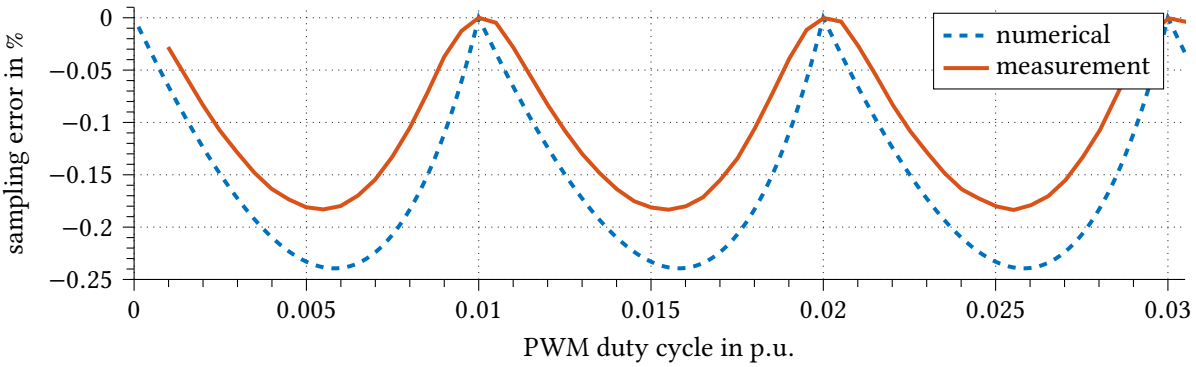

Fig. 5.16: Numerical and experimental validation of the digital integration error at very low duty cycle. Illustration according to Fig. 5.10a with $\tau_d = 0$ at the rising edge and variable at the falling edge. LPF cutoff frequency set to 322 kHz.

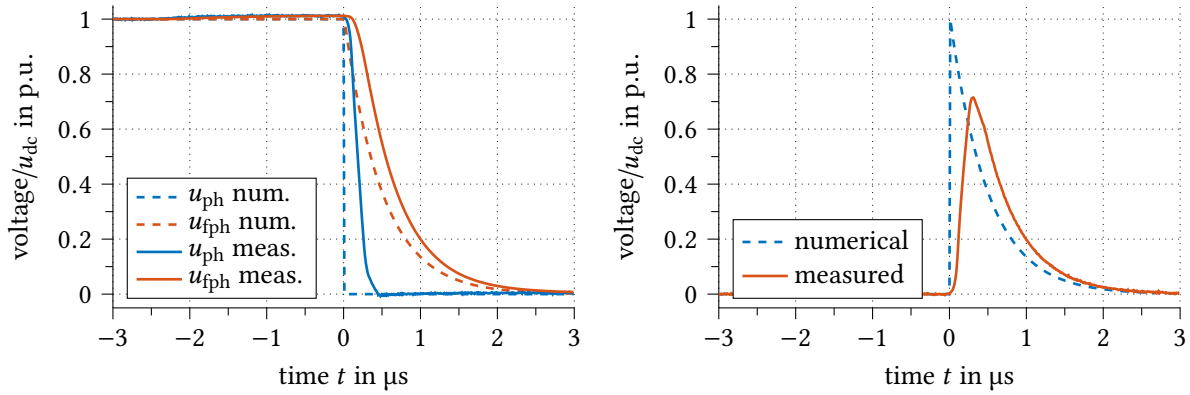

(a) output voltage

(b) voltage difference $u_{fph} - u_{ph}$

Fig. 5.17: Comparison of the ideal rectangular voltage waveform used for numerical calculation and the measured voltage signal. Due to the finite voltage slope of the measured signal, the maximum deviation between the u_{fph} and u_{ph} is generally lower.

5.2.4.1 Validation of the Analytical Solution for the Digital Integration Error

In Section 5.2.1.1 assumption were made to derive the worst-case integration error. To verify the generality of the analytical approach, the worst-case integration error according to Fig. 5.12a on page 107 has been compared to a more time-consuming numerical simulation approach. The results show a negligible absolute deviation of less than 0.001 % [SD18].

At very low duty cycle, the LPF time constant is no longer small compared to the PWM pulse width and the assumptions on page 103 are violated. However, the error at the rising edge caused by a too small pulse width is fully compensated by the error at the falling edge due to a lower voltage magnitude. The validity of the analytical solution can be experimentally verified, as shown in Fig. 5.16. Therefore, the position of the rising edge is set to $\tau_d = 0$ and the duty cycle is manipulated by moving the falling edge. For better illustration, the LPF time constant has been reduced. The figure shows, that the digital integration error periodically follows the theoretical minimum calculated in Fig. 5.10b

down to zero duty cycle. Consequently, the analytical solution is generally valid.

Furthermore, the measured error magnitude in Fig. 5.16 is always lower than the theoretically calculated error. This is caused by the limited slope of the actual VSI output voltage as depicted in Fig. 5.17a. A finite voltage slope generally leads to lower measurement error. This becomes particularly clear when considering the voltage difference in Fig. 5.17b. Due to the reduced voltage slope, the maximum instantaneous deviation of the filtered signal from the original is decreased, as well. The perfectly rectangular voltage waveform assumed for the calculation can thus be seen as the worst case.

5.2.4.2 Sampling of the LPF filtered PWM Voltage Signal

For accurate measurement of the switching-period average voltage, precise sampling of the filtered PWM waveform before digital integration is crucial. For experimental verification, in Fig. 5.18a, the captured voltage waveform $u_{\mathrm{fph}}^{\diamond}$ – which was digitally read from the FPGA buffer using XILINX Chip Scope Pro [XIL13] – is compared to the original phase voltage u_{ph} recorded by an oscilloscope. The filtered signal is precisely captured including the voltage drop of the free-wheeling diode during dead time. The magnified view proves very low measuring noise of the driver-integrated analog circuit, which is below the least-significant bit (LSB) or 10 mV, respectively. The steady-state value is reached after 9 µs.

The LPF time constant can be modified by only changing the LPF capacitor C_{f2}, which keeps offset and gain unchanged. In Fig. 5.18b this has been done for an LPF cutoff frequency of 27 kHz. As expected, the voltage slope at the edges is further reduced which decreases the digital integration error but increases the fundamental signal distortion.

To demonstrate the functionality at higher voltages the experiment was repeated with Inverter 3 at $u_{\mathrm{dc}} = 400\,\mathrm{V}$. The measurement resolution has been set to 80 mV which allows a voltage range from −10 to 1300 V. The target application is an 800 V DC-link voltage VSI with IGBT-based NPC and silicon carbide MOSFET-based B6 configuration. The results show identical behavior and precise sampling with noise below the LSB. The increased noise in u_{ph} is caused by the additional differential probe which was used for the oscilloscope measurement and was not required with Inverter 2.

Since the acquisition of the raw voltage data is performed with identical accuracy and quality for both VSI systems, the following experimental results produced using Inverter 2 may be considered to be valid in general.

5.2.4.3 Verification of the Switching-Period Average Voltage Measurement

For experimental verification of the switching-period average measurement, the captured and digitally integrated FPGA internal signal is compared to a synchronized reference measurement recorded with a 12 bit oscilloscope (type LeCroy HDO6104) at a sampling rate of 100 MS s^{-1} using a 350 MHz passive probe. The switching-period average of the oscilloscope measurement is obtained by piece-wise integration during post-processing.

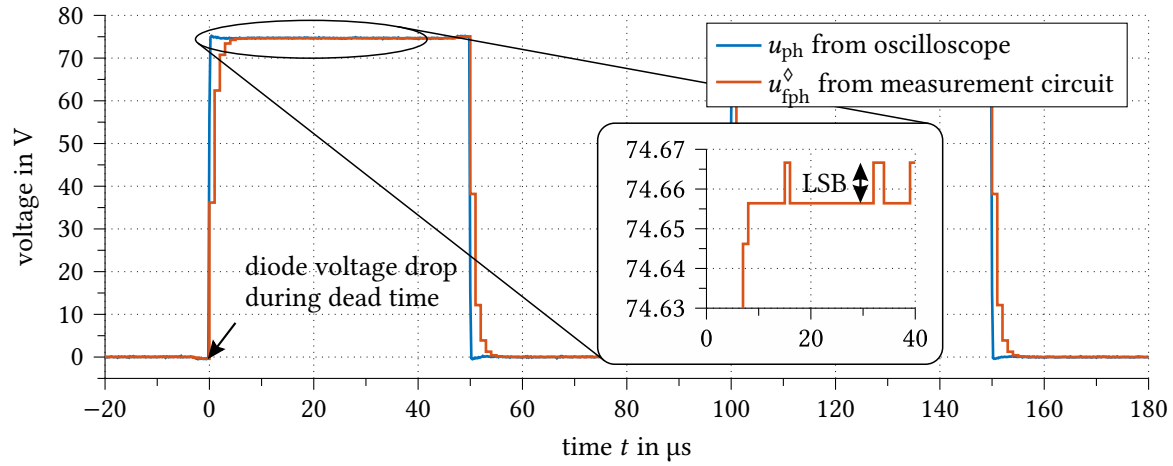

(a) Inverter 2, LPF cutoff frequency: 169 kHz, u_{dc} = 75 V

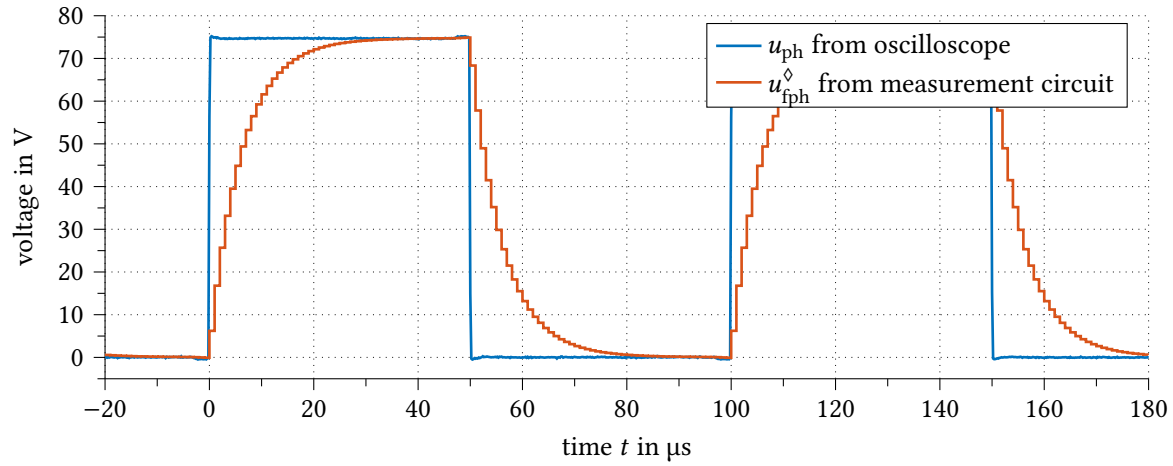

(b) Inverter 2, LPF cutoff frequency: 27 kHz, u_{dc} = 75 V

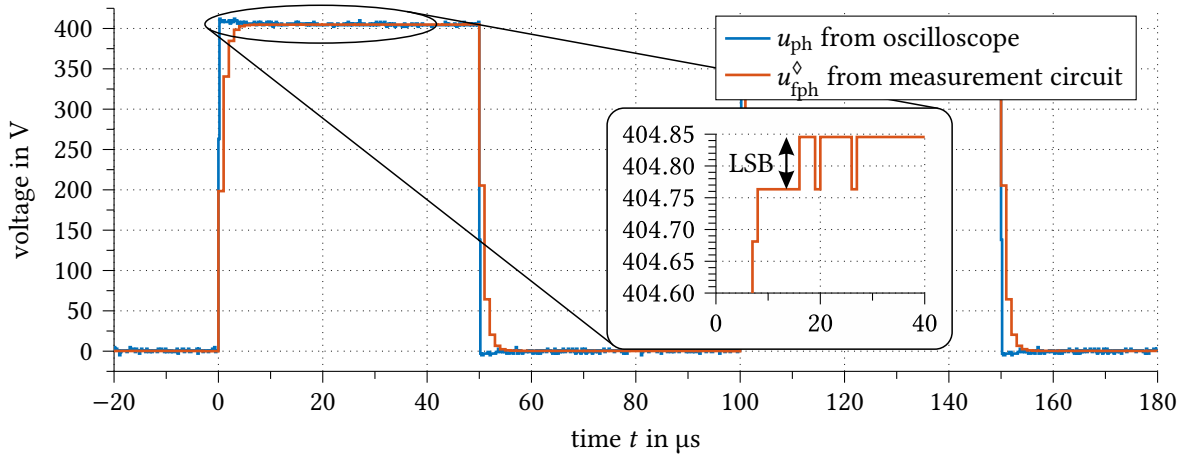

(c) Inverter 3, LPF cutoff frequency: 169 kHz, u_{dc} = 400 V

Fig. 5.18: Experimental results of the sampled phase voltage $u^{\diamond}_{fph}$ with different LPF time-constant before digital integration.

To benchmark the dynamic performance and accuracy of the measurement circuit, in Fig. 5.19, a fundamental voltage signal with the shape of Aachen Cathedral has been generated, which contains significant transients. The three outputs of the VSI were connected to IM750 and operated to generate a 10 A DC current through the investigated phase. The switching-period average of the original phase voltage signal u_{ph} is accurately captured by the measurement circuit. It precisely reproduces the voltage signal given to the PWM modulator from the phase voltage. The comparison with the reference measurement indicates an instantaneous error of less than 0.1 % of u_{dc}, except during transients where the error increases to a maximum of 0.25 %. This is within the limits of the theoretical worst-case analysis presented in Fig. 5.12a on page 107.

Fig. 5.20 shows experimental results of the voltage-sensing circuit under realistic operating conditions. IM750 is driven by a 50 Hz alternating three-phase system generated by Inverter 2. To demonstrate the instantaneous sensing of the inverter distortion voltage, the dead-time compensation has been switched off. It appears in the measurement as a voltage distortion at the current zero crossing at 8 and 18 ms and is precisely captured. In the case of sine-triangle modulation according to Fig. 5.20a, the maximum deviation from the reference measurement is below 0.15 % of u_{dc} and shows a fundamental frequency component, which is correlated with the slope of the captured voltage signal. This observation is in perfect agreement with the considerations made in Section 5.2.1.2 and is caused by the LPF group delay. The results for SVM are given in Fig. 5.20b and show a slightly increased deviation in the region of the first harmonic zero crossing. This is related to the increased voltage slope due to the superimposed triangular wave that is applied for better voltage utilization in conjunction with the LPF group delay.

It should be noted, that the digitally-integrated signal is a sum of $m_{\mathrm{a}} = 100$ 14 bit samples and thus a 21 bit signal. However, since the noise is lower than the LSB, the measurement resolution of 10 mV remains unchanged [LWV92]. The quantization error of the integrated measurement circuit is in the range of ±5 mV and ±20 mV for the reference measurement, which is about 0.03 % of u_{dc} and is thus partially responsible for the noise present in $\Delta\bar{u}^{\Diamond}_{\mathrm{ph}}$.

5.2.4.4 Conclusions

The maximum instantaneous measurement error of the digital integration PWM inverter output voltage sensing method can be significantly reduced by a high-cutoff-frequency analog LPF before A/D conversion. The introduced analytical worst-case error assessment provides a sufficient approach for optimal dimensioning of the LPF time constant. It resulted in a generalized easy-to-use graphical solution for first-order LPF parameterization and can be applied to two-level and multi-level VSI systems. Because the rate-limiting properties of the LPF are of major interest, a first-order filter is preferable. It is easy to implement and leads to a low distortion due to its lower group delay compared to higher-order filters.

Close integration to the gate driver in conjunction with phase to DC ground measurement leads to very low measuring noise and enables additional features as described below.

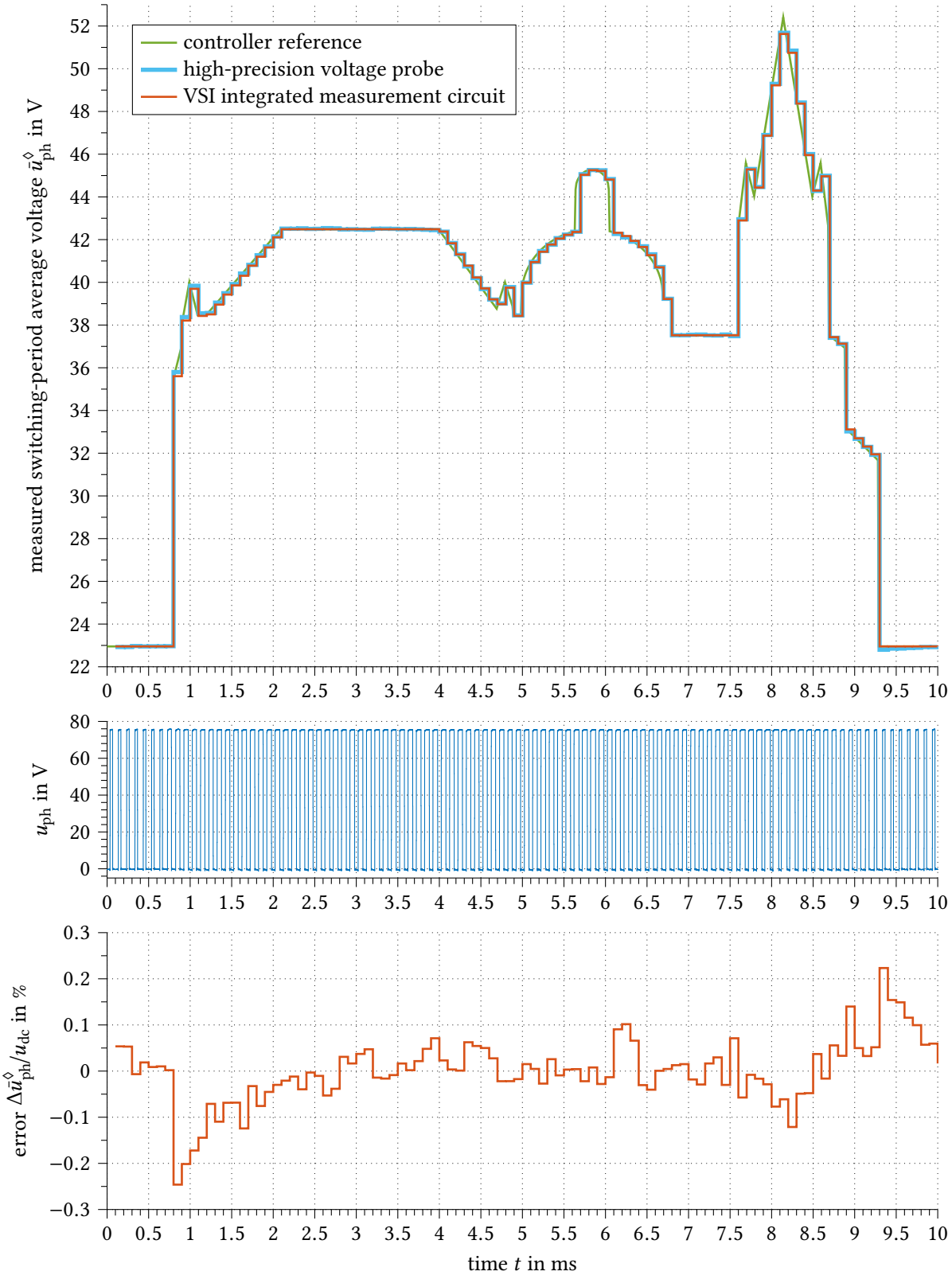

Fig. 5.19: Experimental verification of the instantaneous switching-period average voltage measurement using an Aachen-Cathedral-shaped fundamental voltage signal which contains high transients. The measurement error is less than 0.25 % of u_{dc} and only exceeds 0.1 % during high transients.

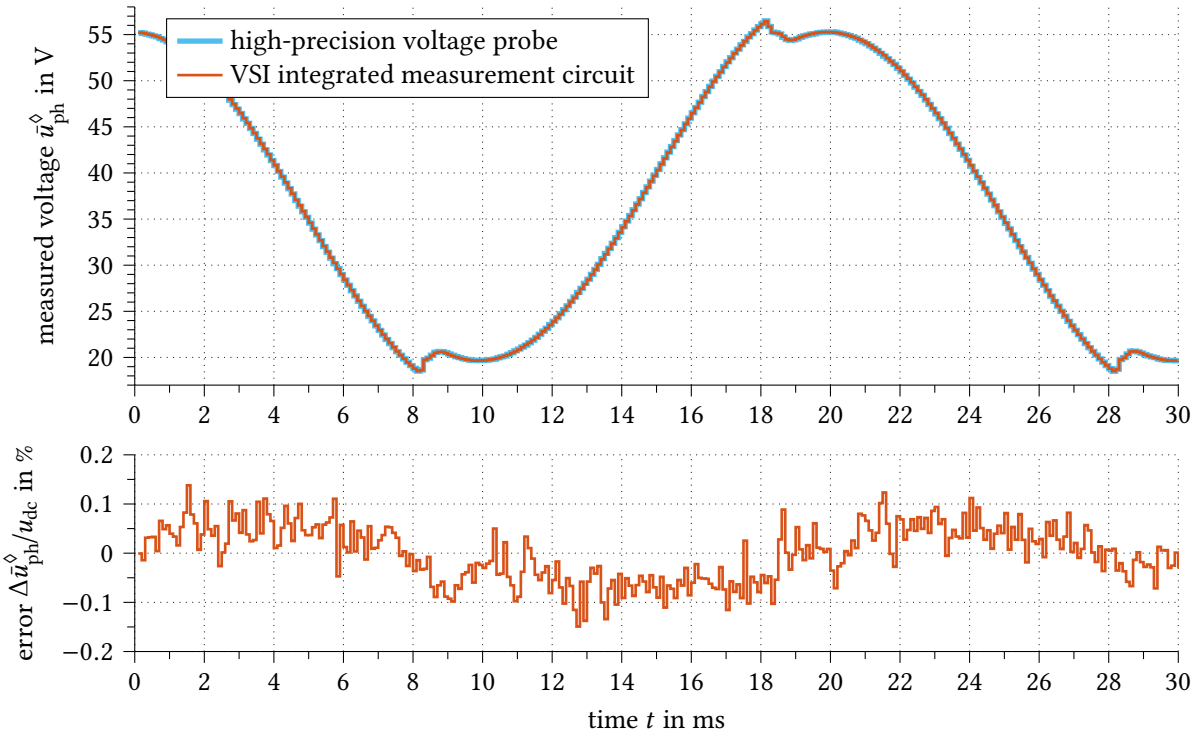

(a) sine-triangle modulation

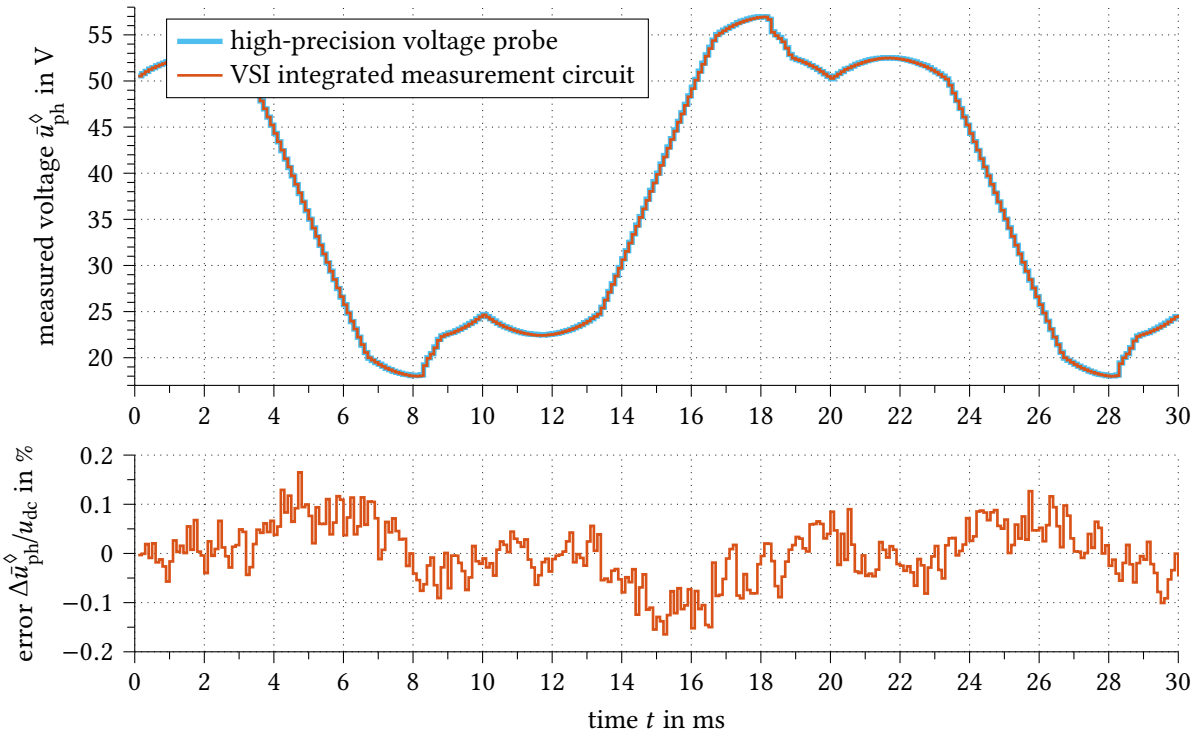

(b) space-vector modulation (SVM)

Fig. 5.20: Experimental results for a 50 Hz sinusoidal voltage reference signal. The measured voltage signal is distorted at the current zero crossing at 8 and 18 ms due to dead-time effect. The measurement error has a fundamental frequency component caused by the LPF group delay.

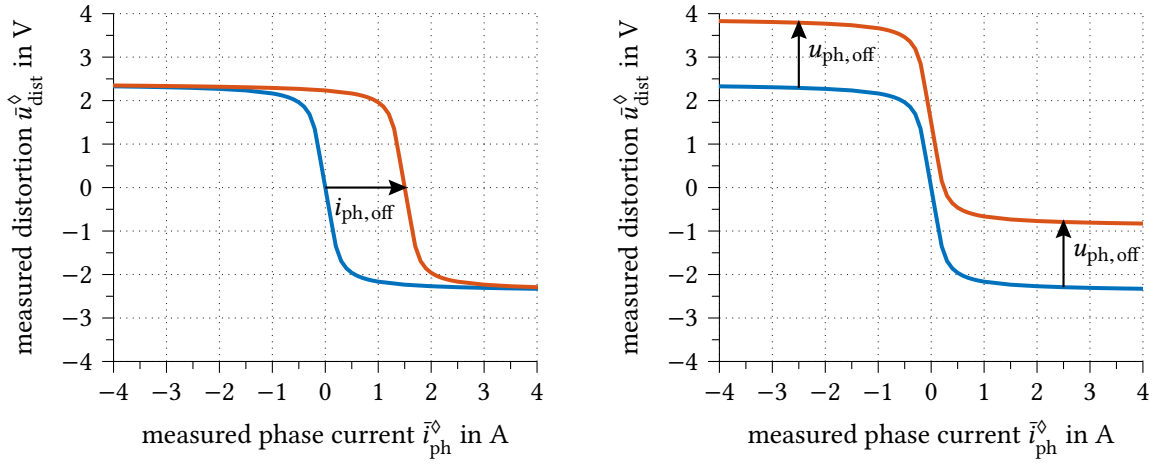

(a) current sensor offset

(b) voltage sensor offset

Fig. 5.21: The influence of current and voltage sensor offsets on the measured inverter voltage distortion curve for a single phase.

5.3 Online Current and Voltage Sensor Offset Calibration based on Inverter Voltage Distortion

In Section 4.1.2, the influence of sensor errors on the flux-linkage estimation and torque production has been discussed. Sensor-offset errors are critical especially when using the voltage-model flux-linkage observer, since they cause high relative errors at low speeds when the back-EMF magnitude is small. This is why sensor offsets are usually calibrated during startup of the VSI. However, sensors – including the one introduced in the previous chapter – are sensitive to thermal offset drift during operation. Online sensor offset calibration methods are an active field of research. Existing solutions have been discussed in Section 4.1.2, but they usually interfere with the machine control algorithm, are sensitive to load parameter variations or require signal injection.

In the following, a novel sensor calibration method is introduced, which is fully decoupled from the control algorithm and load parameters. It allows individual offset calibration of each phase voltage and current sensor during operation and is based on the instantaneous measurement of the inverter distortion voltage which can be obtained from the previously described sensing circuit and the reference voltage as

$$\bar{u}^{\diamond}_{\mathrm{dist}} = \bar{u}^{\diamond}_{\mathrm{ph}} - \bar{u}^{\star}_{\mathrm{ph}}. \tag{5.13}$$

As described in Section 2.3.2, the inverter voltage distortion curve is point-symmetric with respect to the origin. However, if the curve is measured with a phase current and voltage sensor, in the presence of sensor offsets it is shifted along the current axis by the current offset and along the voltage axis by the voltage offset, as illustrated in Fig. 5.21. This effect can be utilized for direct sensor offset detection and calibration. The online

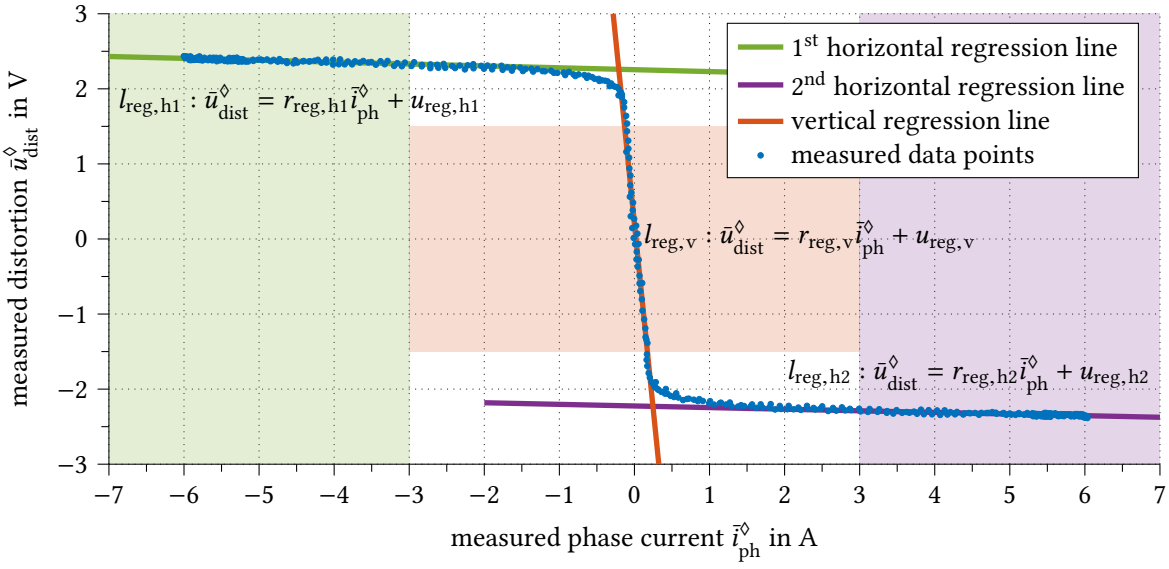

Fig. 5.22: Regression lines for measured voltage distortion data, captured during a single period of a sinusoidal current wave with 6 A amplitude and 20 Hz stator fundamental frequency.

offset calibration algorithm is applicable to systems which meet certain requirements:

- Each inverter leg must be equipped with instantaneous voltage and current sensing.
- The voltage must be measured from the phase terminal output to the DC ground in order to be comparable to the phase reference voltage and to calculate (5.13).
- The output phase current must be an alternating signal with repetitive zero crossings for the detection of the inverter voltage distortion curve.

The former two are satisfied by the voltage sensing circuit in Section 5.2 and the latter is particularly fulfilled for most three-phase drive systems as those considered in this work.

5.3.1 Theoretical Approach for the Offset Calibration Algorithm

To determine the current and voltage sensor offsets, detection of the entire inverter voltage distortion curve is required. Since in real-time implementation only a single data point of the voltage distortion curve can be obtained during each PWM cycle, an effective mathematical representation and acquisition process must be found. As described in Section 2.3.2, the inverter voltage distortion curve comprises three nearly linear regions which are now utilized for this purpose. Linear approximation by three lines as illustrated in Fig. 5.22 promises a simple mathematical representation with a small number of variables. It significantly reduces the memory consumption in the microcontroller and offers effective suppression of measuring noise.

In the following, a sequential algorithm for adding sampled data information to the regression lines $l_{\mathrm{reg,h1}}$, $l_{\mathrm{reg,v}}$ and $l_{\mathrm{reg,h2}}$ of the linearized curve and the adaptive mechanism

for offset calibration is introduced. The algorithm is executed for each phase individually and is divided into three major steps:

Step 1: Real-time detection and linear approximation of the inverter voltage distortion curve.

Step 2: Determination of the point of symmetry of the inverter voltage distortion curve to calculate the current and voltage sensor offsets.

Step 3: Adaptive calibration of the sensor offsets during operation.

5.3.1.1 Real-Time Detection of the Voltage Distortion Curve and Offsets

For the linear approximation of the inverter voltage distortion curve, only the sampled data points that are located within the linear regions may be used. The three regions are illustrated by the shaded areas in Fig. 5.22 and are referred to as the data windows of the lines $l_{\mathrm{reg,h1}}$, $l_{\mathrm{reg,v}}$ and $l_{\mathrm{reg,h2}}$. If a data point is sampled within one of these windows it is considered to contribute to the corresponding line. Otherwise, it is discarded.

With the k^{th} data point that is sampled within a window, the corresponding regression line $l_{\mathrm{reg}} : \bar{u}^{\Diamond}_{\mathrm{dist}} = r_{\mathrm{reg}} \bar{i}^{\Diamond}_{\mathrm{ph}} + u_{\mathrm{reg}}$ can be calculated using the least square method by minimizing

$$\sum_{j=1}^{k} \left(r_{\mathrm{reg}} \bar{i}^{\Diamond}_{\mathrm{ph}}(t_j) + u_{\mathrm{reg}} - \bar{u}^{\Diamond}_{\mathrm{dist}}(t_j) \right)^2 \quad \text{with} \quad k, j \in \mathbb{N}. \tag{5.14}$$

According to [Ler12, pp. 474–476], the coefficients r_{reg} and u_{reg} can be identified by a simple calculation scheme in k steps. It is described below and has been modified to allow a step-wise calculation on a microcontroller. To determine the coefficients for the k^{th} sampling point, first, the arithmetic mean of the data points is calculated as

$$\overline{\bar{i}^{\Diamond}_{\mathrm{ph}}}(t_k) = \frac{1}{k} \sum_{j=1}^{k} \bar{i}^{\Diamond}_{\mathrm{ph}}(t_j) = \frac{1}{k} \left((k-1) \overline{\bar{i}^{\Diamond}_{\mathrm{ph}}}(t_{k-1}) + \bar{i}^{\Diamond}_{\mathrm{ph}}(t_k) \right) \quad \text{with} \quad k \in \mathbb{N} \tag{5.15a}$$

$$\text{and} \quad \overline{\bar{u}^{\Diamond}_{\mathrm{dist}}}(t_k) = \frac{1}{k} \sum_{j=1}^{k} \bar{u}^{\Diamond}_{\mathrm{dist}}(t_j) = \frac{1}{k} \left((k-1) \overline{\bar{u}^{\Diamond}_{\mathrm{dist}}}(t_{k-1}) + \bar{u}^{\Diamond}_{\mathrm{dist}}(t_k) \right), \tag{5.15b}$$

which are based on the results of the previous step. With the help of the mean of squares

$$\overline{\bar{i}^{\Diamond 2}_{\mathrm{ph}}}(t_k) = \frac{1}{k} \sum_{j=1}^{k} \bar{i}^{\Diamond 2}_{\mathrm{ph}}(t_j) = \frac{1}{k} \left((k-1) \overline{\bar{i}^{\Diamond 2}_{\mathrm{ph}}}(t_{k-1}) + \bar{i}^{\Diamond 2}_{\mathrm{ph}}(t_k) \right) \quad \text{and} \tag{5.16a}$$

$$\overline{\bar{i}^{\Diamond}_{\mathrm{ph}} \bar{u}^{\Diamond}_{\mathrm{dist}}}(t_k) = \frac{1}{k} \sum_{j=1}^{k} \bar{i}^{\Diamond}_{\mathrm{ph}}(t_j) \bar{u}^{\Diamond}_{\mathrm{dist}}(t_j) = \frac{1}{k} \left((k-1) \overline{\bar{i}^{\Diamond}_{\mathrm{ph}} \bar{u}^{\Diamond}_{\mathrm{dist}}}(t_{k-1}) + \bar{i}^{\Diamond}_{\mathrm{ph}}(t_k) \bar{u}^{\Diamond}_{\mathrm{dist}}(t_k) \right), \tag{5.16b}$$

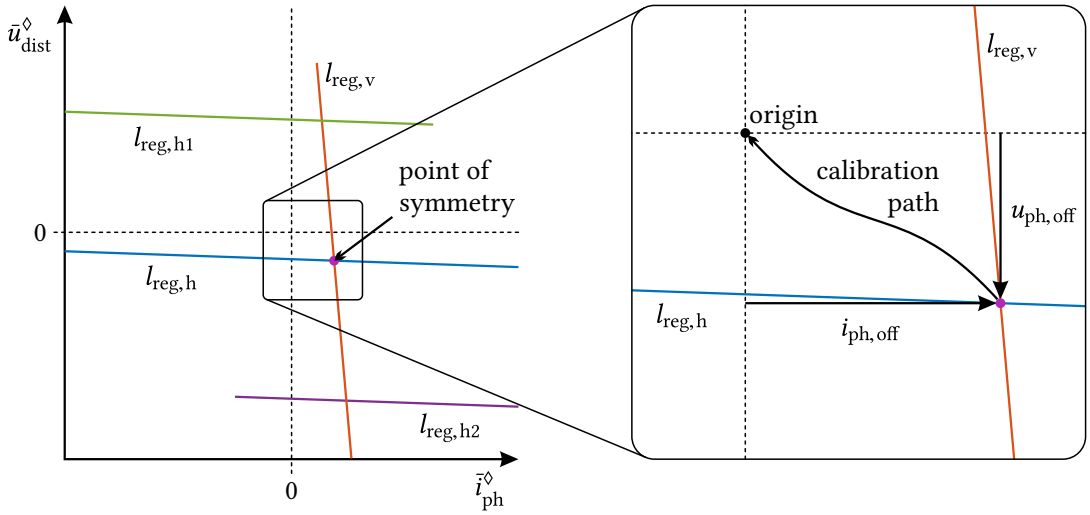

Fig. 5.23: Determination of the current and voltage sensor offsets and the calibration path.

and with the Steiner translation theorem, the sample variance of the measured current and the covariance

$$\sigma_{\mathrm{i}}^2(t_k) = \frac{1}{k}\sum_{j=1}^{k}\left(\bar{i}^{\diamond}_{\mathrm{ph}}(t_j) - \overline{\bar{i}^{\diamond}_{\mathrm{ph}}}(t_k)\right)^2 = \overline{\bar{i}^{\diamond 2}_{\mathrm{ph}}}(t_k) - \overline{\bar{i}^{\diamond}_{\mathrm{ph}}}^{2}(t_k) \quad \text{and} \tag{5.17}$$

$$q_{\mathrm{iu}}(t_k) = \frac{1}{k}\sum_{j=1}^{k}\left(\bar{i}^{\diamond}_{\mathrm{ph}}(t_j) - \overline{\bar{i}^{\diamond}_{\mathrm{ph}}}(t_k)\right)\left(\bar{u}^{\diamond}_{\mathrm{dist}}(t_j) - \overline{\bar{u}^{\diamond}_{\mathrm{dist}}}(t_k)\right) = \overline{\bar{i}^{\diamond}_{\mathrm{ph}}\bar{u}^{\diamond}_{\mathrm{dist}}}(t_k) - \overline{\bar{i}^{\diamond}_{\mathrm{ph}}}(t_k)\overline{\bar{u}^{\diamond}_{\mathrm{dist}}}(t_k) \tag{5.18}$$

can be found. The coefficients of the regression line after capturing the k^{th} sampling point are then determined by

$$r_{\mathrm{reg}}(t_k) = \frac{q_{\mathrm{iu}}(t_k)}{\sigma_{\mathrm{i}}^2(t_k)} \tag{5.19}$$

$$\text{and} \quad u_{\mathrm{reg}} = \overline{\bar{u}^{\diamond}_{\mathrm{dist}}}(t_k) - r_{\mathrm{reg}}(t_k)\cdot\overline{\bar{i}^{\diamond}_{\mathrm{ph}}}(t_k). \tag{5.20}$$

The three regression lines are determined in real time by executing (5.15) to (5.20) once per PWM period. Only the line corresponding to the last sampled data point is updated. This way, the computational effort remains low and deterministic for each PWM cycle.

To calculate the sensor offsets, a sufficient number of data points within each data window is required. This is usually fulfilled after one electrical period, provided that the stator current magnitude is high enough. However, most of the data points are generally located on the horizontal regression lines. With increasing current and fundamental frequency the number of samples available to determine $l_{\mathrm{reg,v}}$ decreases significantly. The density of sampling points at the current zero crossing is reduced especially if a dead-time compensation scheme is applied. In the case that only a few data points are captured, the calculation of a regression line is not recommended. Instead, (5.19) can be replaced by the

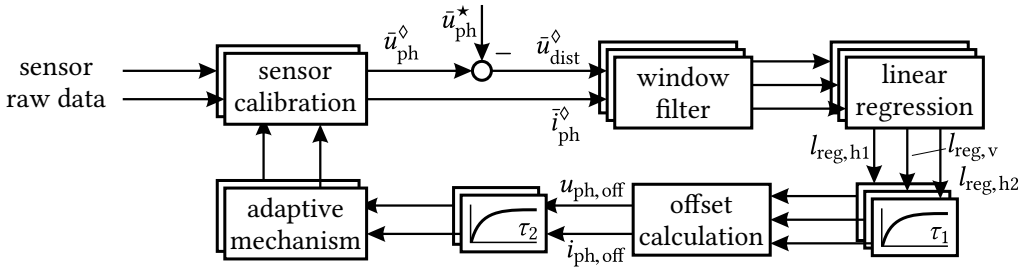

Fig. 5.24: Structure of the online sensor offset calibration algorithm.

constant gradient

$$r_{\mathrm{reg,v}} = -\frac{T_{\mathrm{dt}}^2}{2C_{\mathrm{out}}T_{\mathrm{sw}}} - R_{\mathrm{ds,on}} \tag{5.21}$$

which is taken from the inverter model according to Equation (2.45) on page 40. This way, only one data point is required to determine $l_{\mathrm{reg,v}}$.

After capturing the regression lines, the sensor offsets can be obtained from the point of symmetry of the linearized voltage distortion curve. Therefore, $l_{\mathrm{reg,h1}}$ and $l_{\mathrm{reg,h2}}$ are combined to a new horizontal line $l_{\mathrm{reg,h}}$ with

$$r_{\mathrm{reg,h}} = \frac{r_{\mathrm{reg,h1}} + r_{\mathrm{reg,h2}}}{2} \quad \text{and} \quad u_{\mathrm{reg,h}} = \frac{u_{\mathrm{reg,h1}} + u_{\mathrm{reg,h2}}}{2}. \tag{5.22}$$

The offsets are then conveniently defined by the intersection of $l_{\mathrm{reg,h}}$ and $l_{\mathrm{reg,v}}$, as illustrated in Fig. 5.23, and are calculated as

$$i_{\mathrm{ph,off}} = \frac{u_{\mathrm{reg,h}} - u_{\mathrm{reg,v}}}{r_{\mathrm{reg,v}} - r_{\mathrm{reg,h}}} \quad \text{and} \quad u_{\mathrm{ph,off}} = \frac{u_{\mathrm{reg,h}} r_{\mathrm{reg,v}} - u_{\mathrm{reg,v}} r_{\mathrm{reg,h}}}{r_{\mathrm{reg,v}} - r_{\mathrm{reg,h}}}. \tag{5.23}$$

5.3.1.2 Adaptive Mechanism for the Sensor Offsets Calibration

Before the continuous calibration process can be started, the sensor offsets must be accurately determined. This requires a sufficient number of samples and robust continuous detection of the regression lines. In this work, the proof of concept is provided using a discontinuous regression-line calculation method with the structure given in Fig. 5.24. (5.15) and (5.16) are executed for all consecutive data points within the corresponding data window. If a point outside the window is captured, the detection is completed, and a regression line is calculated using (5.17) to (5.20). With the first consecutive data point within a data window, k is reset to one and the previous regression line is discarded. To ensure stability and robustness, only those horizontal lines which are based on a minimum of 20 data points and have reached a certain current magnitude are considered. The vertical line is determined analogously with a reduced minimum number of data points.

The coefficients of the three lines are filtered by an LPF before they are used for calculation of the sensor offsets. The discrete LPF is updated after each successful line detection.

A weighting factor, proportional to the time between two successful detected lines, ensures a constant and deterministic dynamic response. To increase the robustness of the regression line filters, the ordinates of the horizontal regression lines are shifted to half the corresponding minimum current magnitude.

After filtering, the offsets can directly be used for offset adaption. If a PI-controller is used to drive the offsets to zero, an additional filter is not required. However, special attention must be given to the choice of the adaption gains. The dynamics of the adaptive mechanism must be chosen sufficiently lower than those of the previous LPFs. Since the lines $l_{\mathrm{reg,h}}$ and $l_{\mathrm{reg,v}}$ are not exactly orthogonal, a cross coupling between current and voltage sensor offsets exists. Even though current and voltage should be fully decoupled by (5.23), slight deviations of the line gradients can introduce small coupling effects. Nevertheless, if the adaption process is sufficiently slow, the resulting coupling is negligible.

An alternative continuous approach is the continuous calculation of (5.15) and (5.16) with simply limiting the number of samples k. This way, k is counted up during startup until it reaches its target value. Then, the calibration process is started, and k remains constant which results in a first-order LPF characteristic. However, the last sampled value is always weighted higher, which differs from the least square method in Equation (5.14). Furthermore, a sufficient distribution of the samples along the regression line cannot be guaranteed. This particularly becomes a problem at low electrical frequency when many samples are taken for the same current value. The latter problem can be solved by only considering data points after a certain minimum change of $\bar{i}_{\mathrm{ph}}^{\Diamond}$. However, this alternative solution requires further investigation and is beyond the scope of this work.

5.3.2 Experimental Results and Discussion

To verify the novel offset calibration approach, first, the instantaneous detection of the inverter voltage distortion curve is experimentally investigated. For better illustration, measurements were carried out at a low current magnitude using Inverter 2. The results of the adaptive calibration process in Section 5.3.2.3 were measured using Inverter 1.

All experimental results were captured and processed by the inverter-integrated measurement circuit and the microcontroller. The presented data has been provided by CAN communication or by the inverter-integrated digital-to-analog (D/A) converters and were recorded using a data logger or oscilloscope.

5.3.2.1 Detection of the Inverter Voltage Distortion Curve and Sensor Offsets

The acquired inverter distortion voltage $\bar{u}_{\mathrm{dist}}^{\Diamond}$ and the phase current $\bar{i}_{\mathrm{ph}}^{\Diamond}$ are plotted in Fig. 5.25 for three different stator frequencies over time. The experiments prove precise capturing of the distortion voltage using the instantaneous output voltage sensing circuit introduced in Section 5.2.

In Fig. 5.26, the first electrical period of the measured data for 25 Hz and 99 Hz are plotted

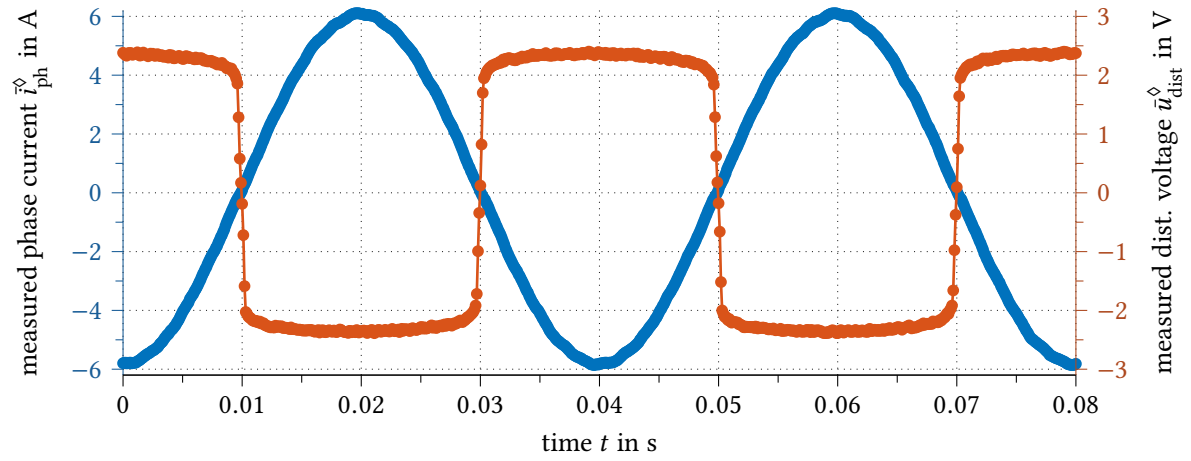

(a) $f_{\mathrm{s}} = 25\,\mathrm{Hz}$

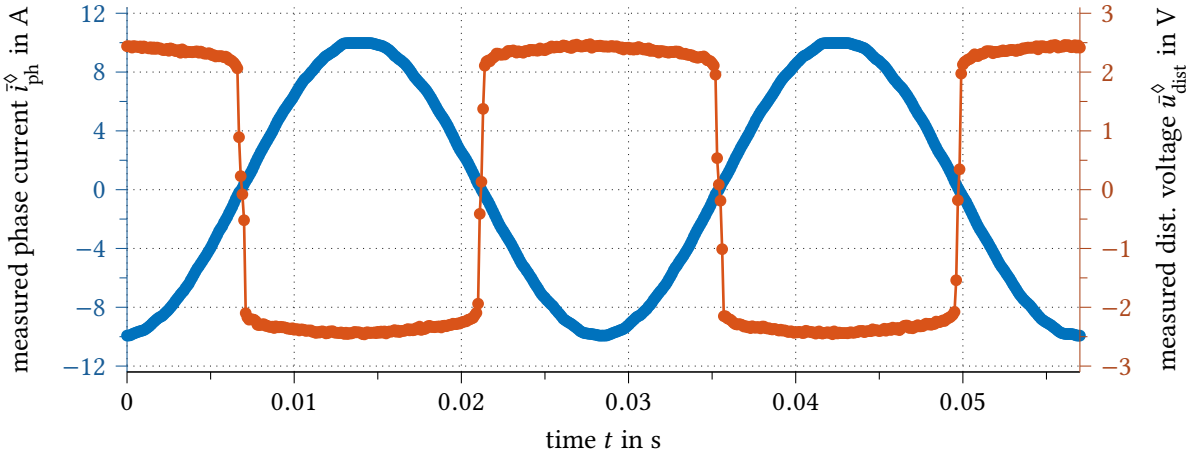

(b) $f_{\mathrm{s}} = 35\,\mathrm{Hz}$

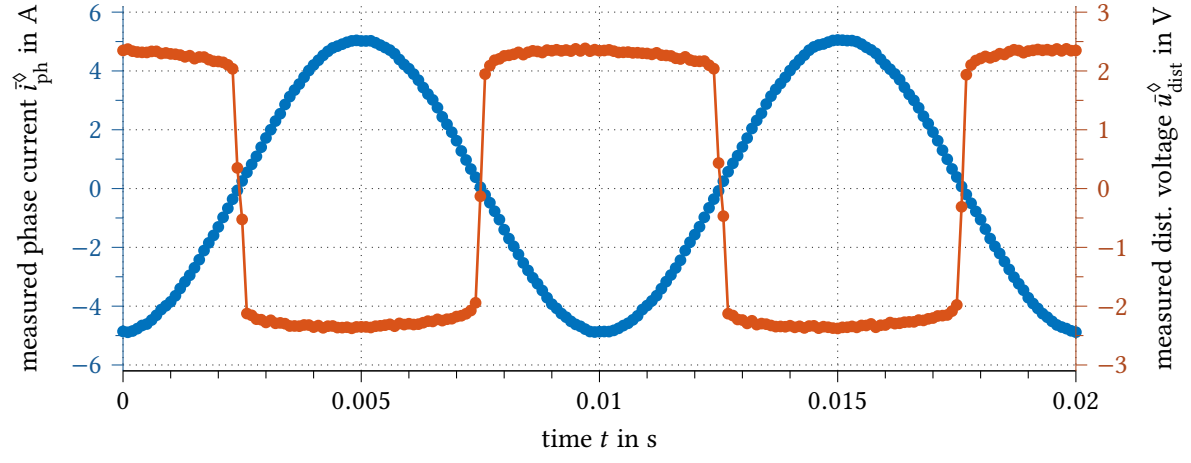

(c) $f_{\mathrm{s}} = 99\,\mathrm{Hz}$

Fig. 5.25: Experimental results for the inverter integrated measurement of the phase current and the inverter distortion voltage at different stator electrical frequencies using Inverter 2 with enabled dead-time compensation.

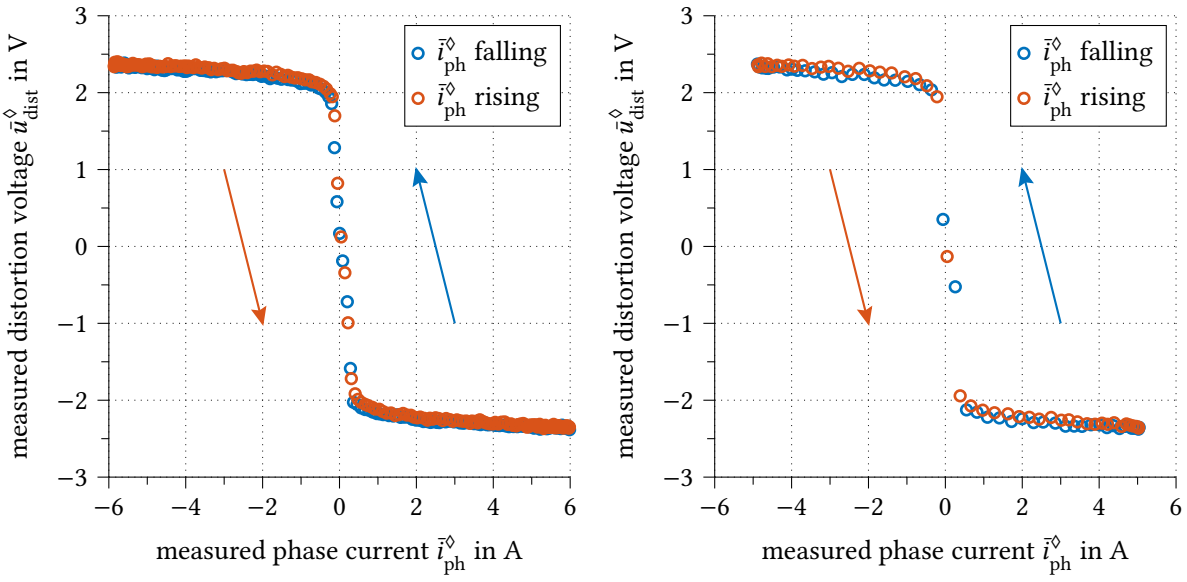

(a) $f_{\mathrm{s}} = 25\,\mathrm{Hz}$ (b) $f_{\mathrm{s}} = 99\,\mathrm{Hz}$

Fig. 5.26: Experimental results for the inverter integrated measurement of the voltage distortion curve. The data points are identical to the first electrical period in Fig. 5.25.

again as current dependent voltage distortion curve. Data points measured during the rising half period are illustrated in red and those captured during the falling half period are blue. The curve is precisely detected by the inverter integrated measurement. Compared to Fig. 5.22, the number of data points in the data window of $l_{\mathrm{reg,v}}$ is significantly reduced by the dead-time compensation scheme. As expected, the number further decreases with increasing frequency or current magnitude. At 25 Hz, only six samples are available per zero crossing. However, with at least one sample present at 99 Hz, detection of the vertical regression line is still possible using the simplification according to (5.21). At 99 Hz, a slight hysteresis is noticeable which is caused by the LPF group delay of the voltage measurement circuit. With sufficiently slow offset adaption and filtering of the regression line coefficients, this effect may be neglected.

It should be noted that especially at low frequency and low current magnitude – when offset errors are mainly critical and other calibration methods fail – the conditions for the inverter voltage distortion based offset calibration algorithm are ideal.

5.3.2.2 Special Constraints and Characteristics of the Offset Detection Method

With the proposed approach, the detection of the inverter voltage distortion curve and offsets is reliable and stable. However, certain constraints exist that must be considered to avoid unexpected behavior:

Current sensor offset detection at high frequency and current magnitude becomes increasingly difficult. With enabled dead-time compensation scheme, there are elec-

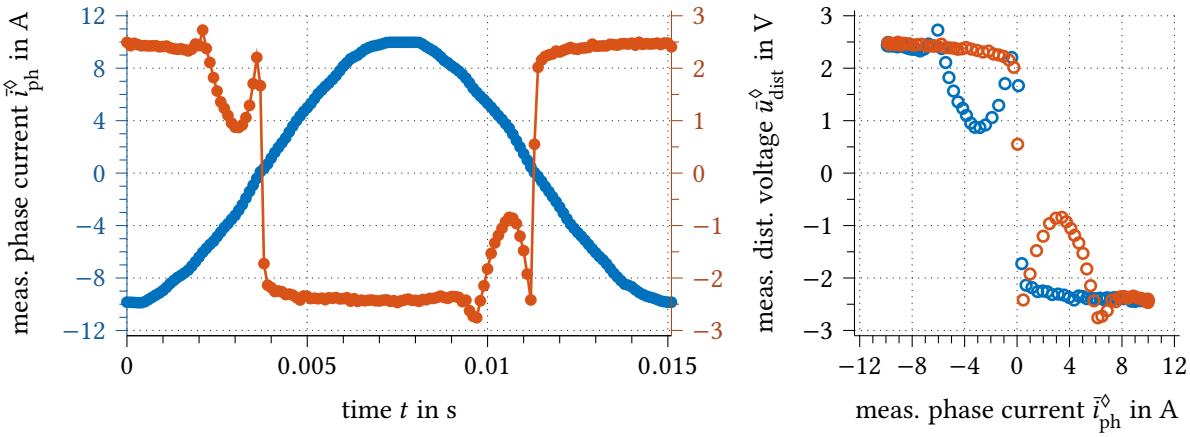

(a) captured period with $f_{\mathrm{s}} = 66\,\mathrm{Hz}$ (b) corresponding distortion curve

Fig. 5.27: The effect of PWM overmodulation near maximum and minimum duty cycle.

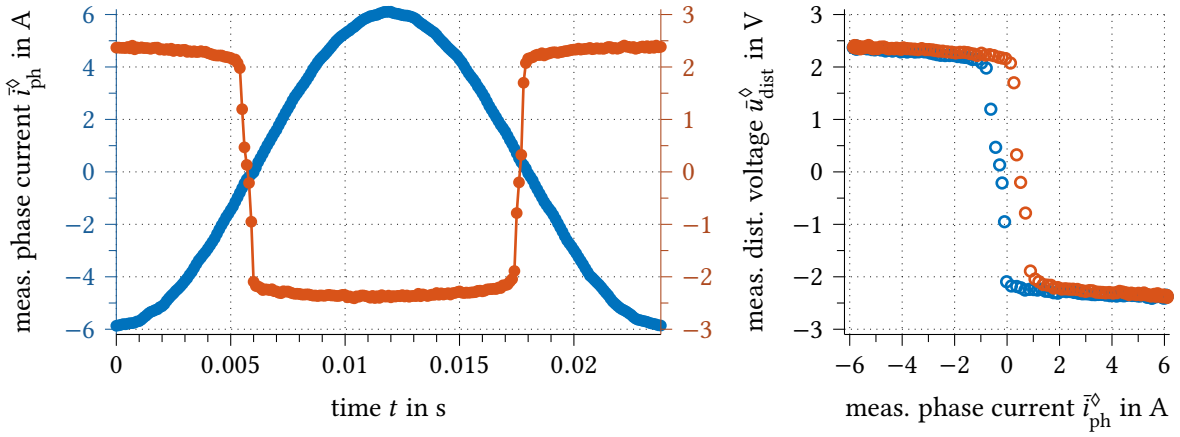

(a) captured period with $f_{\mathrm{s}} = 42\,\mathrm{Hz}$ (b) corresponding distortion curve

Fig. 5.28: The effect of current sensor delay on the inverter voltage distortion curve. The current sensor signal is delayed by 300 µs.

trical periods in which no measure data point for $l_{\mathrm{reg,v}}$ is available. In this case, the algorithm will automatically suspend the detection of the vertical line and thus the calibration of the current sensor offset without any risk of instability.

Overmodulation of the PWM modulator occurs at very high or low duty cycle. The PWM modulator then becomes nonlinear and Equation (5.13) leads to a wrong voltage, as illustrated in Fig. 5.27. The effect can be compensated by taking this effect in (5.13) into account. But, the linearization is dependent on the dead time T_{dt} and is sensitive to model deviations. A simpler solution is to discard data points below and above a certain duty cycle. Since the current zero crossing is of major interest, this typically does not affect the offset detection as long as the power factor $\cos\varphi$ is sufficiently high. This is because for $\cos\varphi = 1$ the nonlinear influence of overmodulation

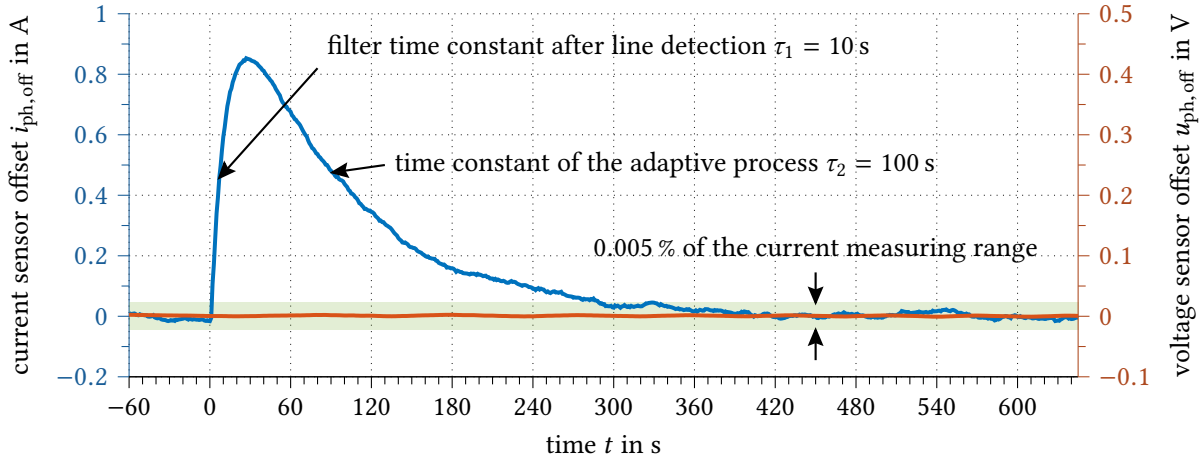

(a) introduced current sensor offset of 1 A, sensing range ±900 A

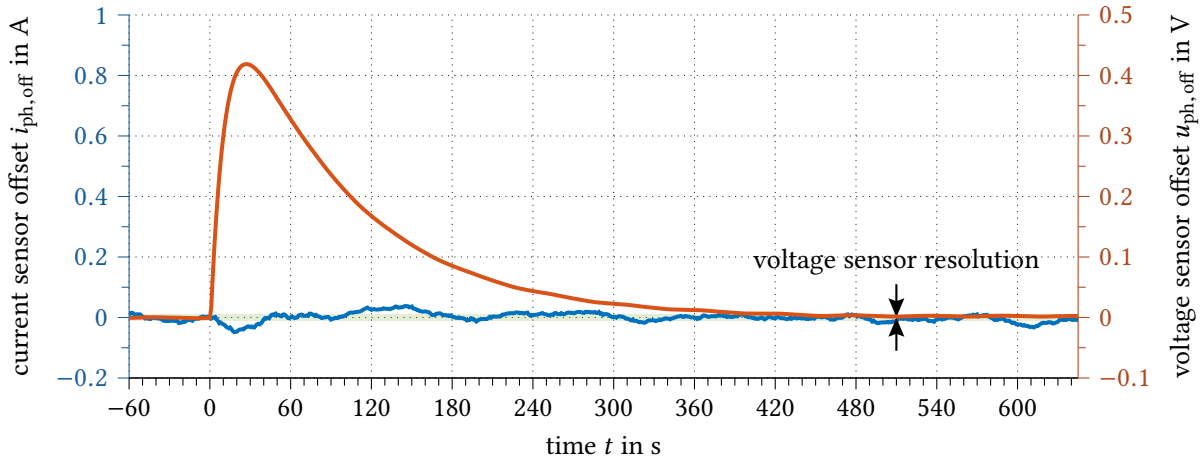

(b) introduced voltage sensor offset of 0.5 V, sensing range −1.5 to 166.5 V

Fig. 5.29: Experimental results for the adaptive calibration process after artificially introduced sensor offsets. Constant operating point at 23.5 Hz and 100 A.

present in Fig. 5.27 is located at the current peaks at zero and 7.5 µs. The captured data during the current zero crossing is then undisturbed.

Current sensor delay causes a deterministic hysteresis in the voltage distortion curve, as illustrated in Fig. 5.28. Synchronous sensing of voltage and current is crucial for proper functionality of the calibration algorithm. In the presence of current sensor delay, synchronization can be restored by applying the same delay to the measured voltage distortion.

5.3.2.3 Experimental Results for the Online Offset Calibration and Discussion

The adaptive calibration process is experimentally investigated by the step-response measurements shown in Fig. 5.29. In Fig. 5.29a, a current sensor offset of 1 A is introduced

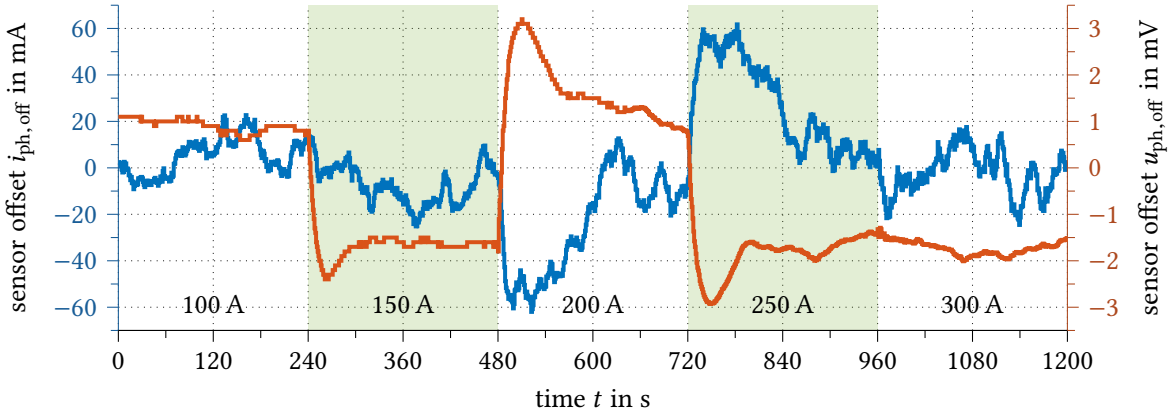

(a) online detected sensor offsets after the first LPF in Fig. 5.24

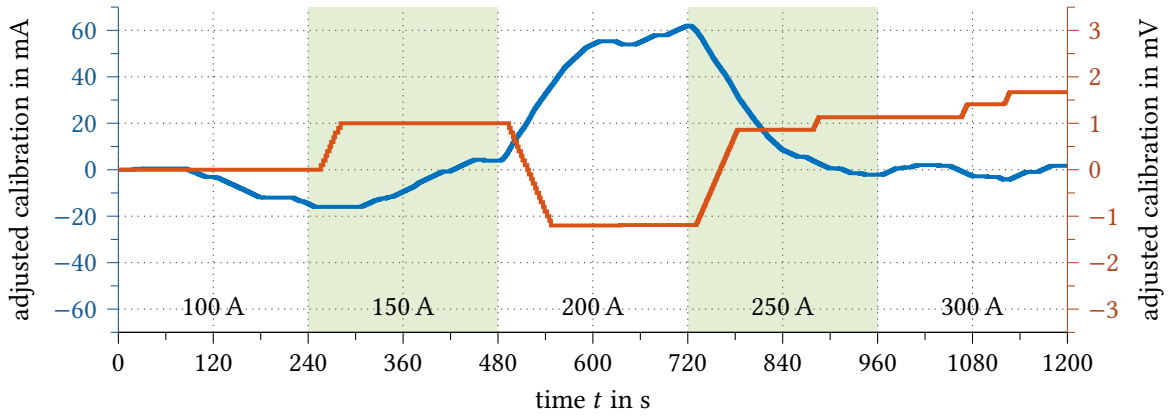

(b) adjustment of the calibration offsets

Fig. 5.30: Experimental results of the detected sensor offsets and adjusted calibration offsets as a function of the stator current magnitude at a constant frequency of 12.75 Hz.

at time instant zero. The offset is precisely detected with a time constant of 10 s, which is defined by the regression line LPFs. The adaption time constant is set to 100 s. After 330 s, the current sensor offset is driven below 45 mA which is 0.005 % of the current measuring range. A cross coupling to the voltage sensor offset is not present. In Fig. 5.29b the experiment is repeated for the voltage sensor with an offset of 0.5 V. The results are comparable to those of the current sensor. After 500 s the offset decreases to less than the sensor resolution of 10 mV. The cross coupling to the current sensor is negligible.

The verification was performed at a constant fundamental frequency and current magnitude of 23.5 Hz and 100 A. To validate the algorithm for all operating points, in Fig. 5.30 and Fig. 5.31, the detected sensor offsets and adjusted calibration values were logged as a function of the stator current magnitude and the fundamental frequency. Fig. 5.30a shows that the current magnitude has negligible influence on the detected sensor offsets which remain below 60 mA and 3 mV. The resulting adaption of the calibration values is given in Fig. 5.30b. Compared to the measuring ranges of ±900 A and -1.5 to 166.5 V, the offset drift is very low. The sensitivity of the offset detection algorithm to the stator frequency is given

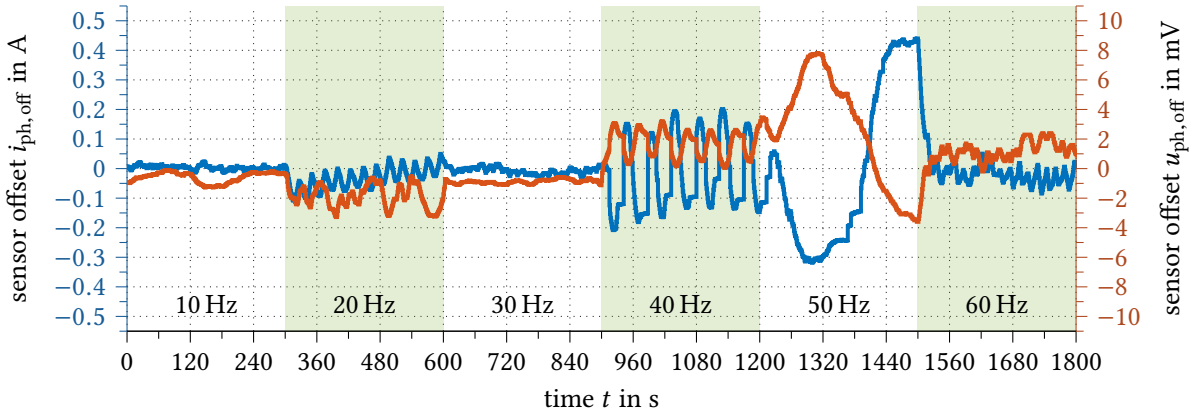

(a) online detected sensor offsets

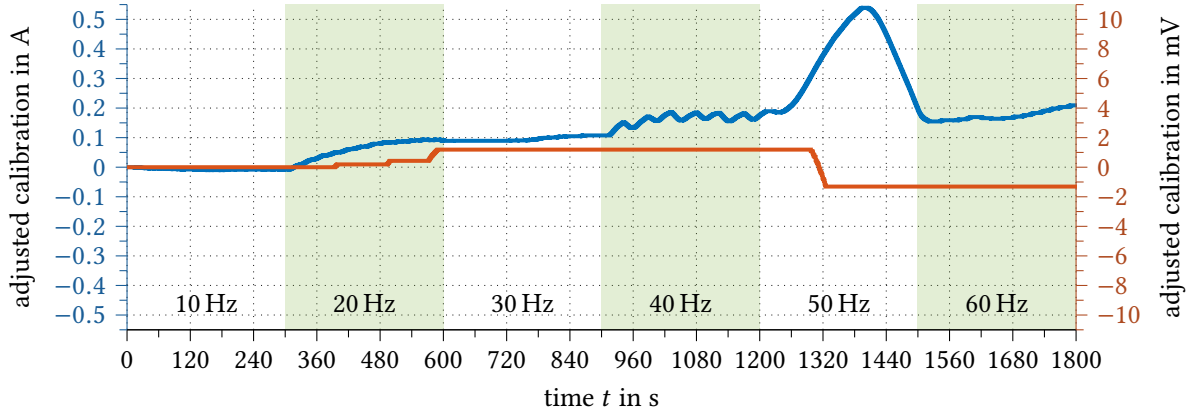

(b) adjustment of the calibration offsets

Fig. 5.31: Experimental results of the detected sensor offsets and adjusted calibration offsets as a function of the stator fudamental frequency at a constant current magnitude of 100 A.

in Fig. 5.31a. Below 20 Hz and at 30 and 60 Hz, the detection of the sensor offsets is accurate and smooth. At 20, 40 and 50 Hz, small oscillations occur, which are caused by aliasing effects during the detection of the vertical line $l_{\mathrm{reg,v}}$. Since in these cases the fundamental frequency is an integer divider of the switching frequency, the locations of the sampling points remain constant. If the number of available samples for the detection of $l_{\mathrm{reg,v}}$ is limited, the sampling points are statistically not evenly distributed and the detection of the vertical regression line is inaccurate. The aliasing effect is mostly filtered out by the large time constant of the adaptive calibration process. However, low frequency disturbance can cause deviations of up to 0.5 A. The influence on the voltage sensor is below its resolution and therefore negligible.

In conclusion, the experimental results prove the feasibility of the proposed sensor-offset calibration approach, which is based on the continuous detection of the inverter voltage distortion curve. It allows individual sensor offset calibration during operation and is fully decoupled from the drive control algorithm. The stability of the algorithm is ensured at any time due to the definite shape of the inverter voltage distortion curve.

Limitations exist at high fundamental frequency, when the number of sampling points for the vertical regression line is limited. If the fundamental frequency is an integer divider of the switching frequency, aliasing effects can then cause an alternating current offset deviation. However, the maximum error is limited to about 0.5 % of the measuring range and only occurs at a constant fundamental frequency. In variable speed drives this case can be considered as extremely unlikely.

5.4 Online Semiconductor Condition Monitoring

High efficiency requirements and the demand for increased power density are stimulating the use of power electronics in general [Sti+17]. This development usually comes along with an increased system complexity and a higher susceptibility to failures. Condition monitoring can counteract this issue and improves the reliability of the system [Ave+15]. On the one hand, it can be used to collect data on the sources of failures, on the other hand, it allows to monitor the state of health, such that components can be replaced before they fail [HCB18]. This so-called predictive maintenance is also beneficial from an economical point of view, since maintenance can be carried out as required instead of regularly, and breakdowns can be prevented.

One of the major aging effects in power electronic systems is bond-wire lift-off caused by mechanical stress due to thermal cycling. In [Bab+14; Ped+17] an 'on'-state voltage-drop measurement was proposed to detect the increased resistance due to bond-wire failure during operation. Experimental results in [DBS16] showed, that the health state of the devices can also be extracted from the temperature profile at low fundamental frequency of the phase current. In [FKP05], a thermal model is used to estimate the junction temperature. The model is in good agreement with measurements obtained using an infrared camera. The idea is improved in [vCD15; van+17], where a 3D spatial LPTN similar to Section 4.2.2 is proposed using a real-time finite differential approach. Consequently, it is shown in [vLD18] how this 3D thermal model can be combined with a junction temperature measurement in a thermal observer structure. The model offers accurate real-time monitoring of the spatial temperature distribution within power electronic modules and can be used for thermal control of power devices [van+18]. Accurate junction temperature sensing is required in most thermal monitoring solutions and various techniques have been proposed [ADK12; Bak+14; vGD18]. However, most of these approaches require additional sensor circuitry.

The instantaneous phase voltage measurement circuit presented in this chapter can be utilized for 'on'-state voltage-drop measurement and temperature sensing. Thus, condition monitoring can be implemented without extra circuitry. The additional functionality can be used simultaneously with stator voltage sensing and sensor offset calibration. This section describes the required modifications which are only related to the FPGA and DSP software. Experimental results demonstrate the feasibility of this solution.

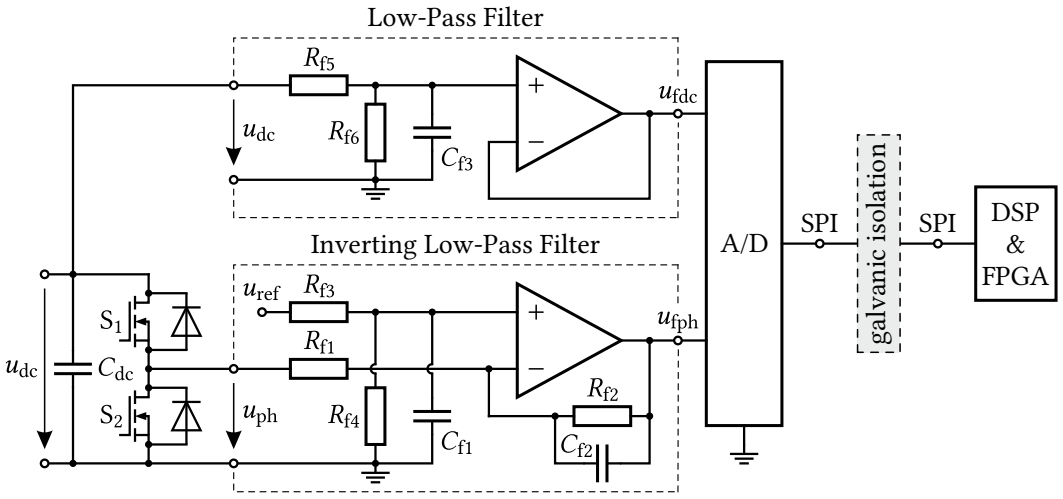

Fig. 5.32: Circuit diagram of the voltage measurement circuit with DC-link voltage measurement.

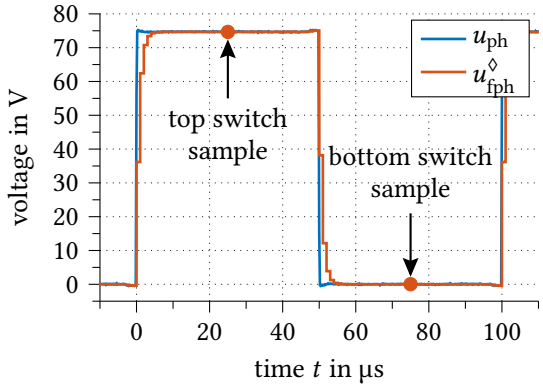

Fig. 5.33: Sampling points for semiconductor voltage drop detection.

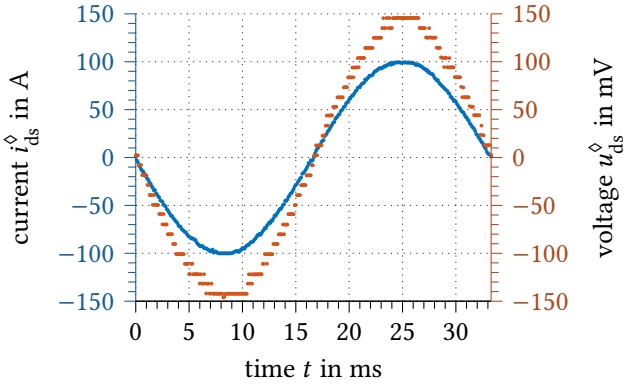

Fig. 5.34: Experimentally captured 2nd phase bottom switch 'on'-state voltage drop and current.

5.4.1 Implementation Details and Experimental Evaluation

As described in Section 5.2, the proposed phase-voltage measurement circuit is based on digital integration of the voltage across the bottom switch. Thus, the 'on'-state voltage drop of the switch S_2 can be directly obtained by taking a single sample when the switch is conducting. The voltage drop across the top switch can be determined with the help of the DC-link voltage measurement. According to Fig. 5.32, the sensing circuit introduced in Fig. 5.14 is equipped with a two-channel A/D converter per phase. At phase 1, the second channel is used to measure the DC-link voltage, and at phase 3, the direct bonded copper (DBC) substrate temperature at phase 2 is captured. Consequently, the voltage drop and current through each MOSFET is obtained using only existing sensors with

$$u^{\diamond}_{ds} = \begin{cases} u^{\diamond}_{fph} & \text{at the bot. switch,} \\ u^{\diamond}_{fdc} - u^{\diamond}_{fph} & \text{at the top switch,} \end{cases} \quad \text{and} \quad i^{\diamond}_{ds} = \begin{cases} -i^{\diamond}_{ph} & \text{at the bot. switch,} \\ i^{\diamond}_{ph} & \text{at the top switch.} \end{cases} \tag{5.24}$$

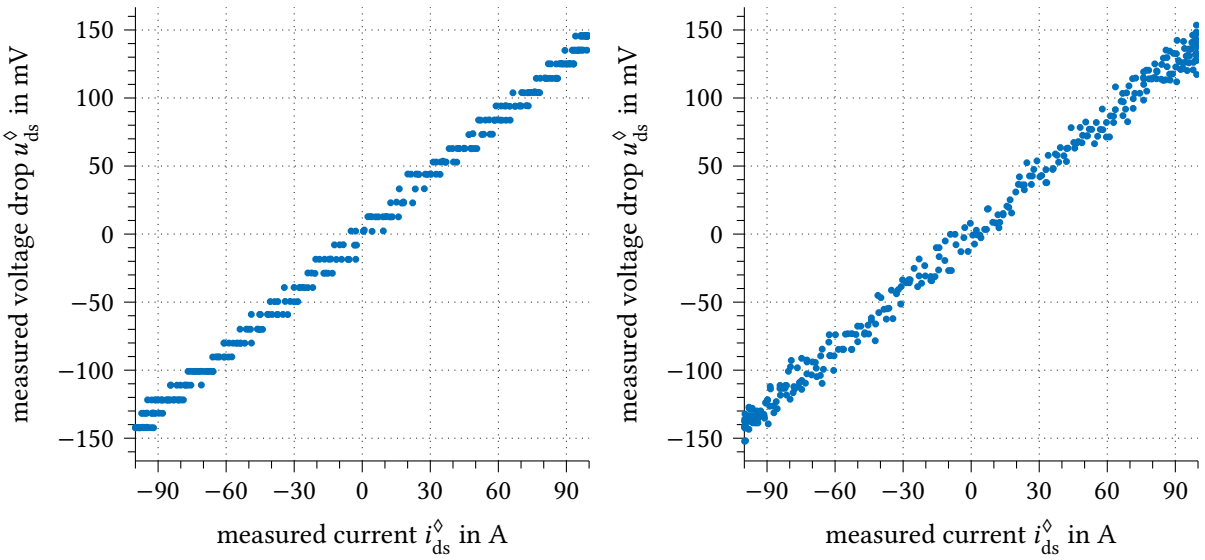

(a) bottom switch voltage drop

(b) top switch voltage drop

Fig. 5.35: Measured MOSFET 'on'-state voltage drop plotted over current for an operating point of 100 A and 30 Hz using the internal measuring circuit of Inverter 1.

The voltage drop across the top switch and the current are obtained by simultaneously sampling u_{fdc}, u_{fph} and i_{ph} at the center of the high potential, as illustrated in Fig. 5.33. $u_{\mathrm{fdc}}^{\diamond}$ is only measured at the driver circuit of phase 1. The LPF time constants should be chosen equally. This is achieved with $R_{\mathrm{f5}} = R_{\mathrm{f1}}$, $C_{\mathrm{f3}} = C_{\mathrm{f1}}$ and $R_{\mathrm{f6}} \approx R_{\mathrm{f2}}$ in Fig. 5.32, since $R_{\mathrm{f1}} \gg R_{\mathrm{f2}}$. The quantities of the bottom switch are obtained during the low potential, accordingly. Both is realized by software modification on the FPGA. Due to the LPF and the dead time, the voltage signal can be distorted at duty cycles near zero and 100 %. Thus, sampling points at these duty cycles must be discarded. However, since the proposed circuit uses a high-cutoff-frequency LPF, this limitation is minimal.

Experimental results of the sampled voltage drop and current of the bottom switch are given in Fig. 5.34. Since the measuring range has to cover the full output-voltage span of the VSI from -1.5 to 166.5 V, the quantization steps of 10 mV become visible in $u_{\mathrm{ds}}^{\diamond}$. This is also the case when the voltage drop is plotted over current in Fig. 5.35a. At the top switch in Fig. 5.35b, the quantization error of the DC-link voltage measurement is superimposed on that of $u_{\mathrm{fdc}}^{\diamond}$, which results in quantization noise. However, the resistive nature of the MOSFET can clearly be recognized although the current magnitude is comparably low.

The limited resolution of the A/D converter makes the detection of the 'on'-state resistance rather difficult. However, with (5.15) to (5.20) on page 119, the voltage drop in Fig. 5.35 can be described by a regression line, which makes the detection more robust. $R_{\mathrm{ds,on}}^{\diamond}$ is then equal to the gradient r_{reg}. According to Section 2.3.1, the anti-parallel body diode is not conducting in reverse direction during the 'on' state, because the voltage drop across the MOSFET is always lower. Thus, Fig. 5.35 is only defined by the 'on'-state resistance, which makes the linear approximation a valid representation.

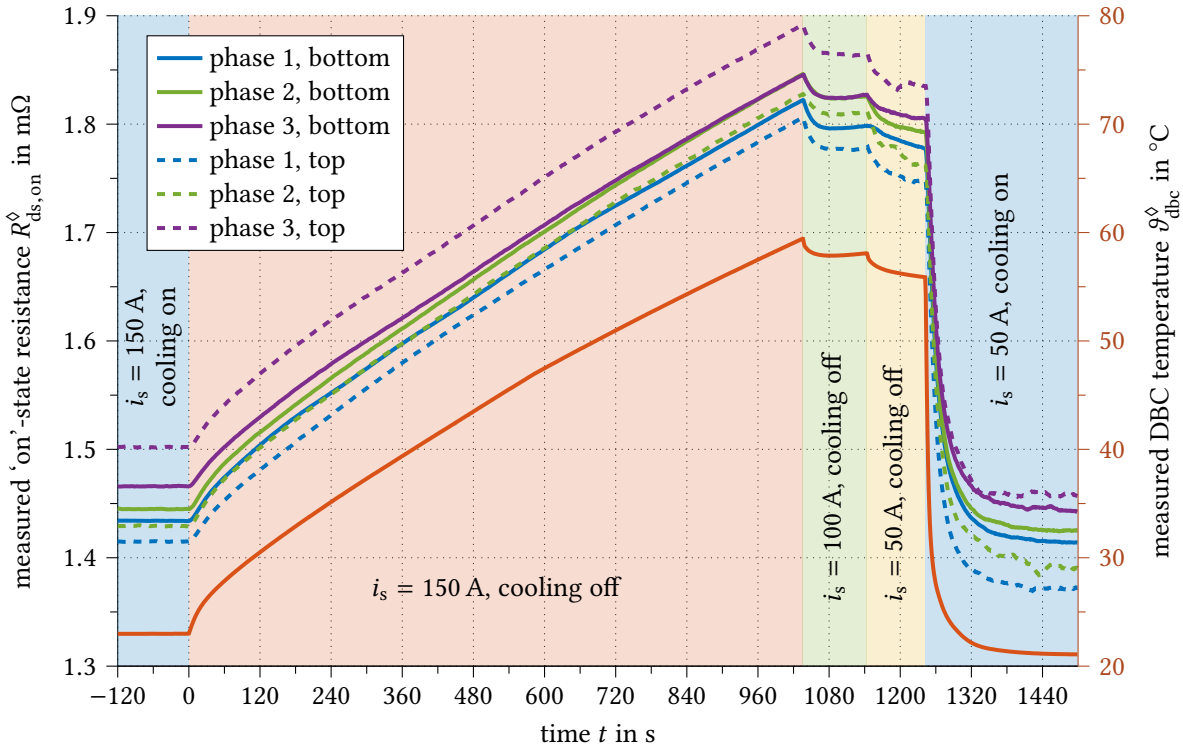

Fig. 5.36: Measurement of the 'on'-state resistance and the DBC temperature over time using the VSI-integrated measurement circuit of Inverter 1 at 10 Hz fundamental frequency.

5.4.2 Monitoring of the MOSFET Junction Temperature and Resistance

It was shown in Fig. 2.27 on page 39, that the 'on'-state resistance is temperature dependent with a positive temperature coefficient. $R_{ds,on}$ is directly related to the MOSFET junction temperature and can thus be used for temperature monitoring. Fig. 5.36 demonstrates the temperature dependency of $R_{ds,on}$. Therefore, the DBC temperature and all six MOSFET resistances have been captured simultaneously by the VSI integrated circuit as previously described. The drive was operated at 150 A and 10 Hz. At time instant zero, the water cooling was switched off and the temperature started to rise. At $\vartheta^{\Diamond}_{dbc}$ = 60 °C, the current was reduced in two steps before the cooling was switched on again. It can be seen, that the resistances $R^{\Diamond}_{ds,on}$ change proportionally with the DBC temperature. The results of the bottom switches are very close to each other, which proves a homogeneous temperature distribution on the mutual cooling plate. The top switches show more dispersion, which can be explained by the fact, that the DC-link voltage is only captured at phase 1 and the sampled voltage includes the measuring and quantization errors of two measurements. Overall, the relative resistance deviation remains within an acceptable range of ±3 %.

It is noted, that the measured resistance is about 0.9 mΩ lower than the datasheet value given in Table 2.3 on page 38. This is because the voltage is measured directly at the gate driver and thus the resistance of the bus bars and terminal is not included. Furthermore, the datasheet value includes a safety margin and is considered as the worst case.

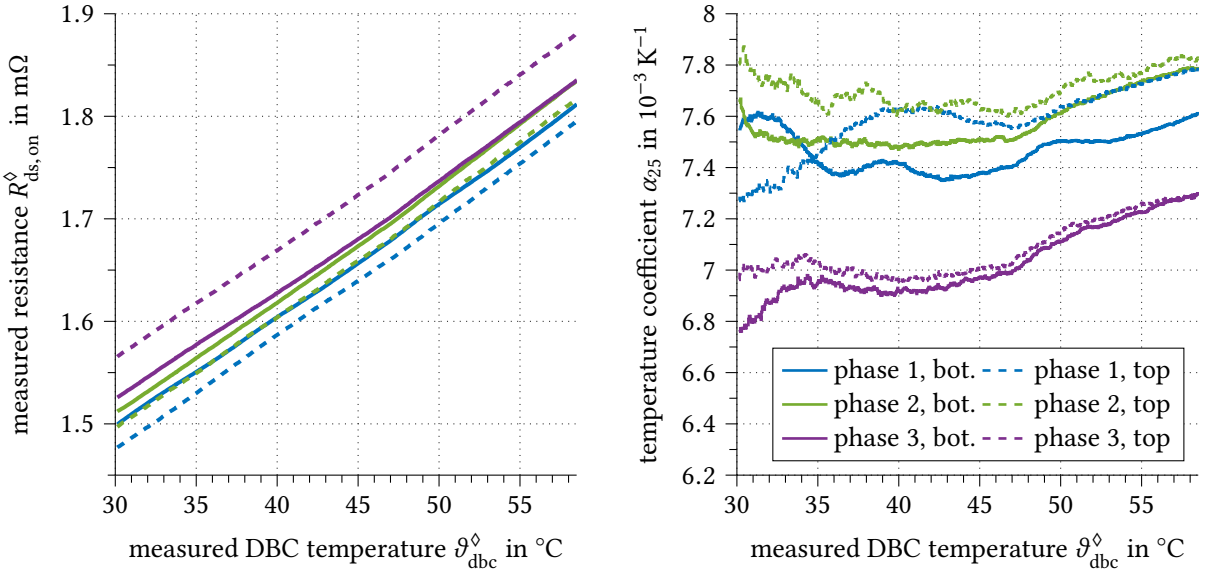

(a) 'on'-state resistances $R^{\Diamond}_{\mathrm{ds,on}}\left(\vartheta^{\Diamond}_{\mathrm{dbc}}\right)$ (b) temperature coefficients $\alpha_{25}\left(\vartheta^{\Diamond}_{\mathrm{dbc}}\right)$

Fig. 5.37: MOSFET 'on'-state resistances and coefficients as a function of the DBC temperature measured at phase 2.

Temperature Coefficient and Operating-Point Dependency

To determine the $R_{\mathrm{ds,on}}$ temperature coefficients, in Fig. 5.37a the resistances are plotted as a function of the DBC temperature. Therefore, the data recorded in Fig. 5.36 between 120 and 1000 s is used. In this interval the temperature is increased slowly compared to the thermal time constant between the semiconductor and the DBC. Thus, steady-state conditions may be assumed. The resistances show a linear dependency on the measured DBC temperature $\vartheta^{\Diamond}_{\mathrm{dbc}}$, which can be described using Equation (2.17) on page 18.

The resulting temperature coefficient with respect to 25 °C is given in Fig. 5.37b. For phases 1 and 2 the coefficient is about $7.5 \cdot 10^{-3}\,\mathrm{K}^{-1}$ and $7 \cdot 10^{-3}\,\mathrm{K}^{-1}$ for the 3rd phase. The deviation of the latter might be caused by the spatial distance to the DC-link voltage detection at phase 1 and the temperature sensor being located at phase 2. Furthermore, at higher temperature, the coefficient increases slightly. However, the deviation is within ±5 % which is low for the internal measuring circuit. In the following the value $\alpha_{25} = 7.5 \cdot 10^{-3}\,\mathrm{K}^{-1}$ is used.

The dependency of the 'on'-state resistance detection on the operating point is evaluated based on the experiments conducted in Fig. 5.38. In Fig. 5.38a, the drive is operated at 10 Hz fundamental frequency. The current is increased to 300 A in steps of 50 A. Above 100 A the resistance in smoothly captured, whereas below it is slightly distorted. This is caused by the low signal-to-noise ratio at low current magnitude due to the limited A/D-converter resolution. The temperature rises due to the quadratically increasing losses. Overall, the influence of the current magnitude is marginal and can be neglected.

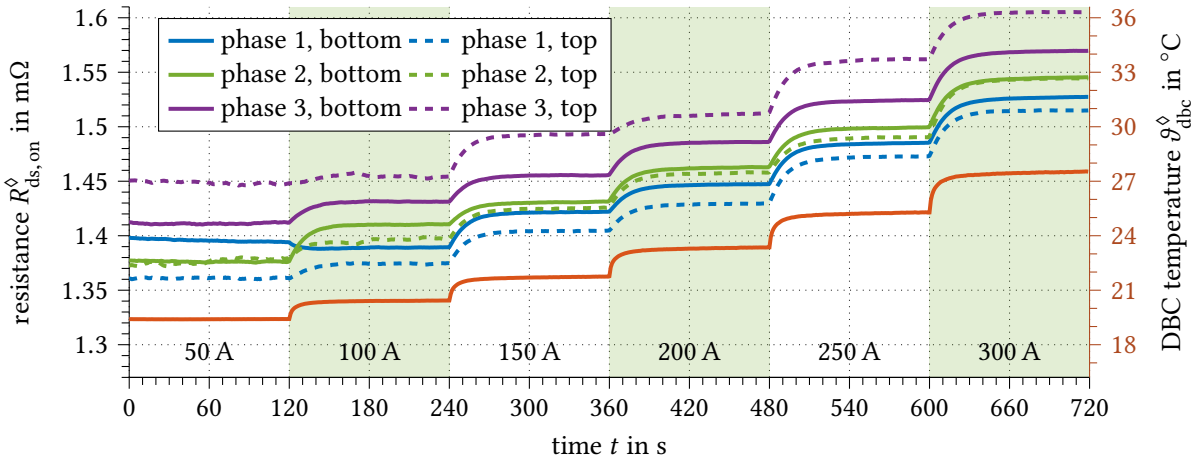

(a) dependency on the current magnitude

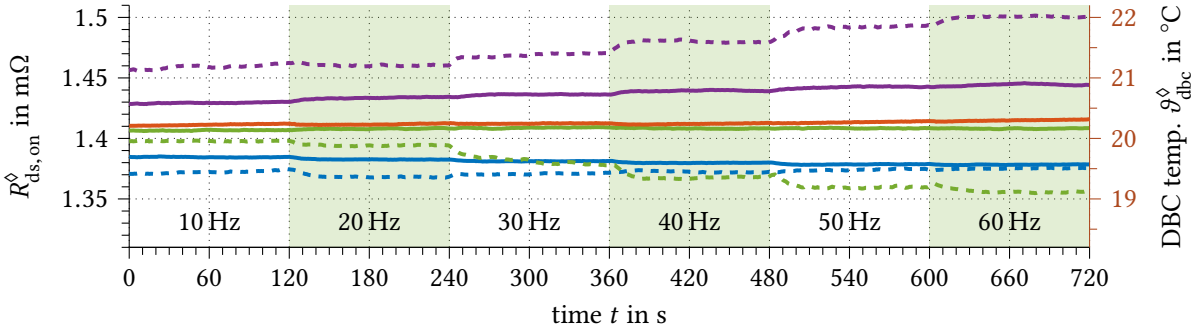

(b) dependency on the current fundamental frequency

Fig. 5.38: Experimental evaluation of the influence of current magnitude and fundamental frequency on the detection of $R^{\Diamond}_{ds,on}$. All data captured using the VSI internal sensing circuit of Inverter 1.

In Fig. 5.38b, the sensitivity to the fundamental frequency is investigated. For this purpose, a current magnitude of 100 A is applied and the frequency is varied from 10 to 60 Hz in steps of 10 Hz. The DBC temperature at phase 2 remains relatively constant during the entire procedure, so the resistance values are expected to remain constant, too. However, the captured resistances vary slightly. At the bottom switches the maximum drift is <1.4 %, which can be neglected. But at the top switches the resistances change by up to 6 %. It is noted, that phase 1 – where the DC-link voltage measurement is located – is almost not affected by this. Thus, the drift is most likely caused by the physical distance of the other two phases to the DC-link voltage measurement and the resulting voltage drop across the bus bar. Overall, compared to the temperature dependency, the influence of the current magnitude and fundamental frequency on $R^{\Diamond}_{ds,on}$ is sufficiently low.

Online Detection of Bond-Wire Faults

The effect of bond-wire fault is demonstrated using a modified MOSFET module with Inverter 1. As illustrated in Fig. 5.39, each switch of the B6 circuit consists of seven parallel

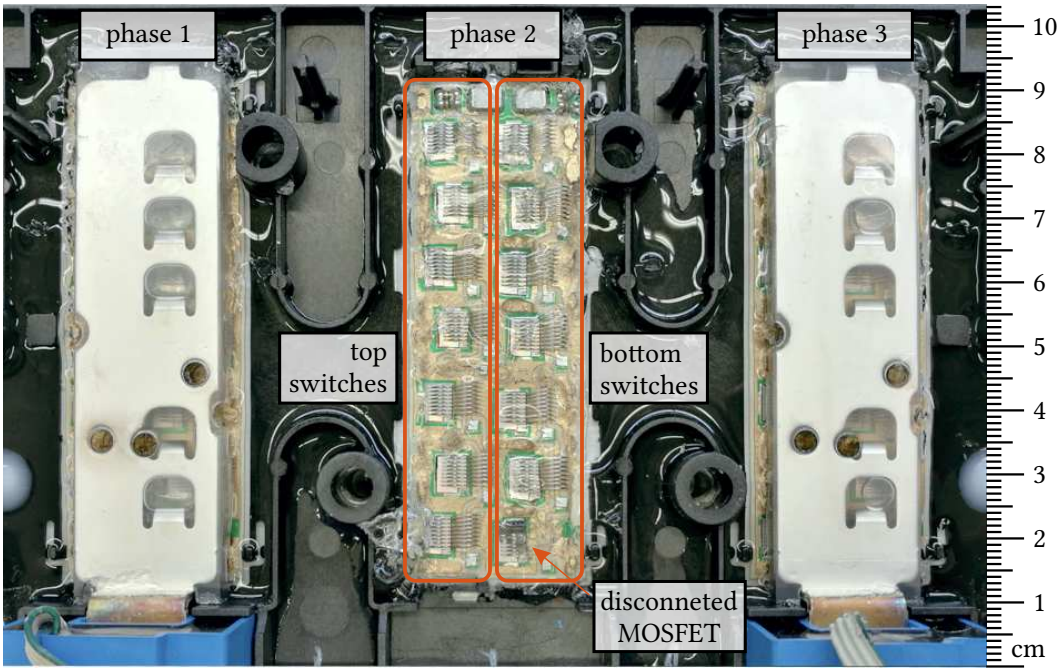

Fig. 5.39: Photograph of the opened power MOSFET module of Inverter 1. Each phase has an individual DBC on a common water cooling plate. The top and bottom switches consist of 7 parallel MOSFETs. At phase 2, one MOSFET is defective and the bond wires have been removed.

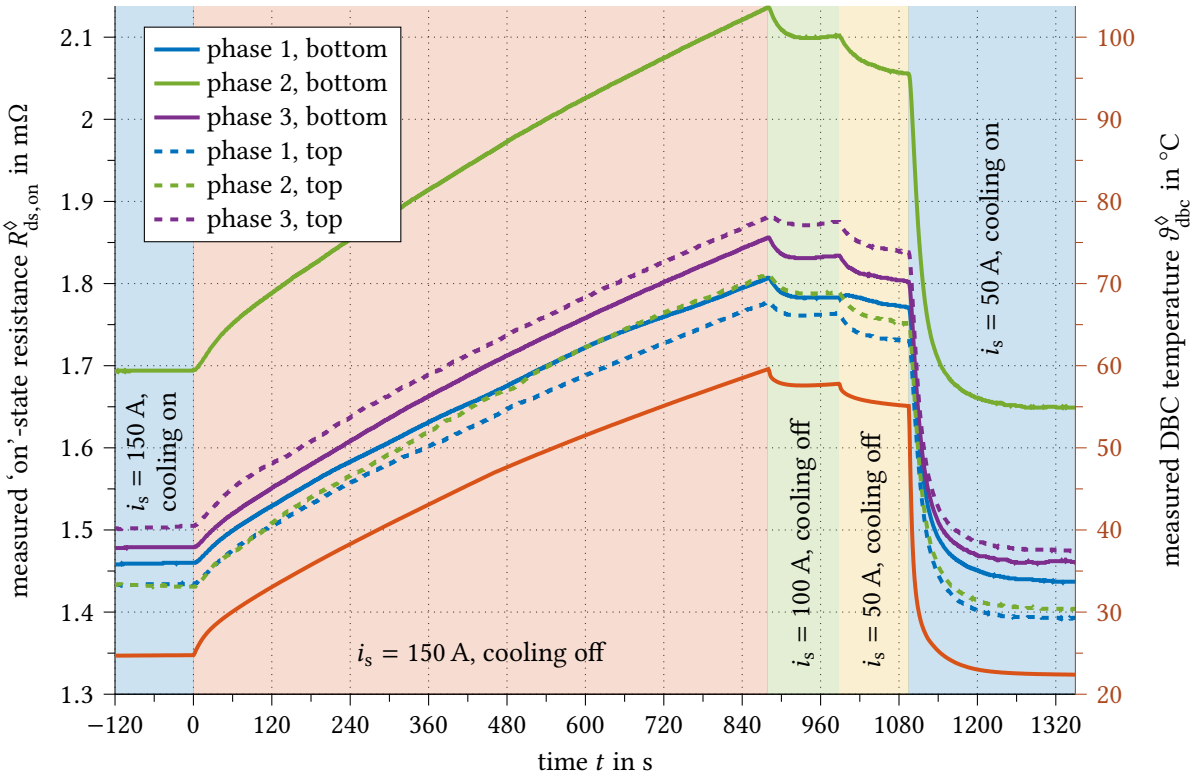

Fig. 5.40: Measurement of the 'on'-state resistance and the DBC temperature over time with removed defective MOSFET at phase 2 of Inverter 1. Captured using the VSI-integrated measurement circuit at 10 Hz fundamental frequency.

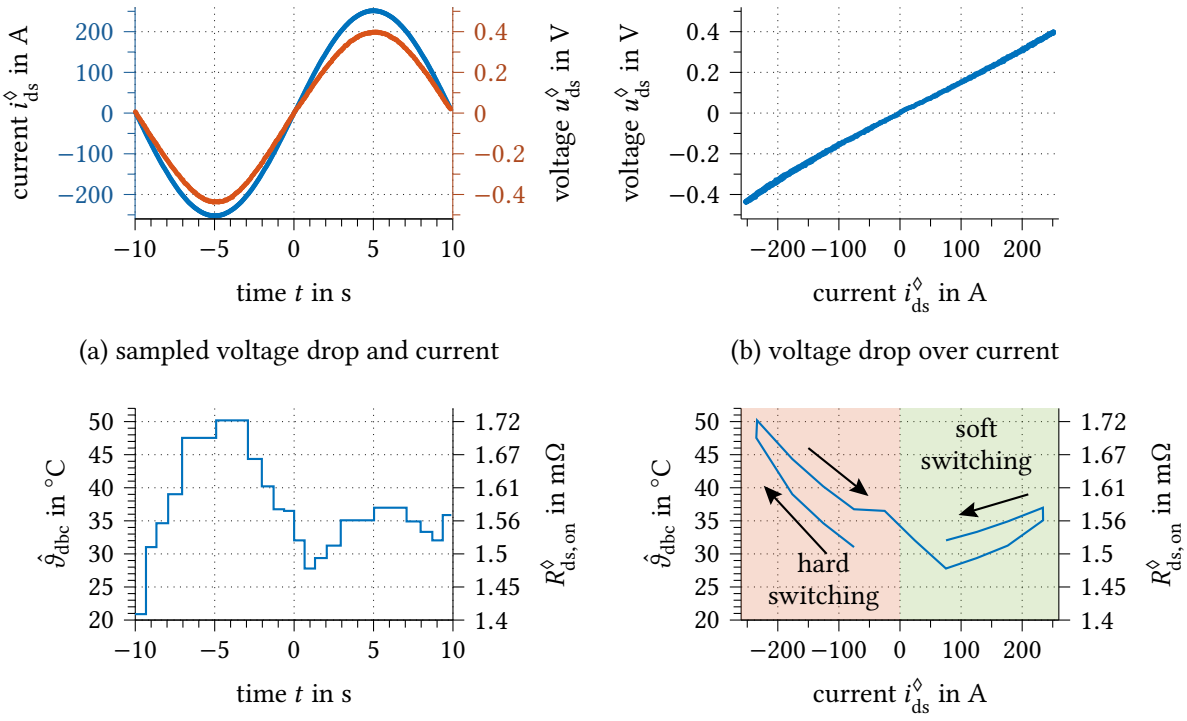

(a) sampled voltage drop and current

(b) voltage drop over current

(c) transient resistance

(d) resistance over current

Fig. 5.41: Estimation of thermal micro cycles of twice the fundamental frequency using the internal measuring circuit of Inverter 1 at 0.05 Hz and 250 A.

MOSFET chips. In this experiment, one of the parallel switches at the bottom side of phase 2 is defective and has been disconnected by removing the bond wires. This has direct influence on the 'on'-state resistance as demonstrated by the measurements in Fig. 5.40. Compared to the results in Fig. 5.36, the corresponding $R_{ds,on}^{\Diamond}$ of phase 2 is now significantly increased. It is about 16 % higher than for the other switches. This way, the missing bond-wire connection can be detected as an abnormal resistance increase and the module can be changed before complete failure.

Detection of Fundamental-Frequency Thermal Cycles

As the current through the MOSFETs is alternating with the fundamental frequency, the switches experience two thermal micro cycles per electrical period. This becomes notable especially at very low speed and is demonstrated in Fig. 5.41. In Fig. 5.41a, a current of 250 A and 0.05 Hz fundamental frequency is applied. It can be seen, that the voltage sine wave captured across the 2nd phase bottom switch is slightly distorted by the transient change of $R_{ds,on}$. This causes a nonlinearity in Fig. 5.41b. In Fig. 5.41c, the resistance is piece-wise calculated in averaged intervals of 50 A. The junction temperature is determined from the resistance using the temperature coefficient α_{25}. As expected, two thermal cycles per electrical period occur. The first cycle is significantly higher because the bottom switch experiences increased switching losses caused by hard switching during the negative half-

wave. This effect becomes particularly clear when plotted as a function of the current, as in Fig. 5.41d. The thermal micro cycle follows a temperature hysteresis, which is defined by the thermal time constants of the module.

At higher fundamental frequencies, the detection of thermal micro cycle becomes more difficult due to the limited voltage measurement resolution. However, as previously mentioned, the measurement circuit can be combined with a real-time thermal observer and used as a closed-loop feedback [vLD18]. Furthermore, the measurement circuit can be utilized for the detection of thermal time constants and thermal model parameterization.

The online sensor-offset calibration and the 'on'-state resistance monitoring are simultaneously executed along with the instantaneous phase-voltage sensing. The adaption of the three sensor-offset pairs took 7.75 µs and the simultaneous detection of the six $R^{\Diamond}_{\mathrm{ds,on}}$ values consumed 1.88 µs computation time of the control interrupt on the DSP.

5.5 Torque Control without dedicated Speed Transducer

Even though torque control without speed transducer is out of focus of this work, it is a good benchmark for the instantaneous voltage-sensing circuit and is thus used for experimental evaluation. The measurement results in Fig. 5.42 demonstrate the problem of detecting the stator terminal voltage at low stator frequencies. A constant stator-current magnitude of 55 A and 1 Hz stator frequency is applied to IM26kA. At this frequency, the induced EMF is very low and the signal-to-noise ratio can become too small for stable voltage-model-based flux-linkage estimation. The figure shows a comparison between the stator voltage obtained from the reference voltage $\bar{\vec{u}}^{\star}_{\mathrm{s}}$ – with and without dead-time compensation – and from the previously introduced measuring circuit. The measured stator voltages and currents are given as space vectors in the 'αβ'-reference frame and should consequently form a circle.

Without dead-time compensation, the voltage $\bar{\vec{u}}^{\star}_{\mathrm{s}}$ follows a hexagonal trajectory, as shown in Fig. 5.42a. When compared to the measurement in Fig. 5.42d, its magnitude is about ten times higher and is dominated by the dead-time-related voltage error. In Fig. 5.42b a simple dead-time compensation scheme is activated, but C_{out} and $R_{\mathrm{ds,on}}$ are neglected. The average magnitude is now closer to the measurement but significant distortion occurs during the current zero crossing. As shown in Fig. 5.42c, considering C_{out} and $R_{\mathrm{ds,on}}$ notably improves the stator voltage estimation. However, the signal is still deformed and distorted by modeling errors and asymmetries. The voltage signal provided by the instantaneous voltage-sensing circuit is given in Fig. 5.42d. It is a smooth circle as expected. Only slight distortion occurs, which is mainly caused by the quantization noise of the A/D conversion. Therefore, it can be expected that the region of stable operation without dedicated speed transducer is extended by the voltage measurement towards lower speeds.

Fig. 5.43 demonstrates the low-speed operation of the IM drive without speed transducer but with the proposed voltage-sensing circuit. The torque is controlled in motoring mode

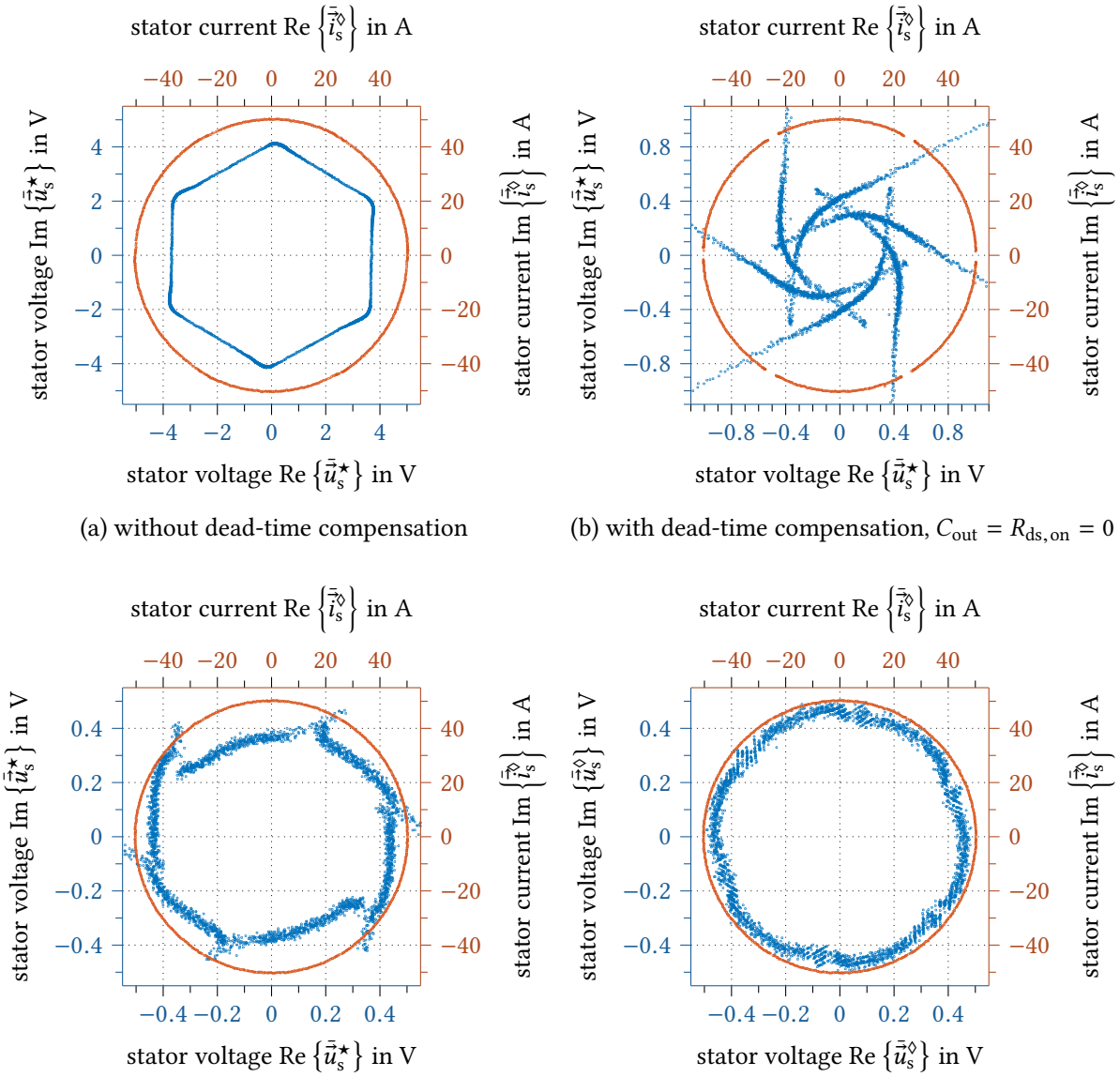

(a) without dead-time compensation

(b) with dead-time compensation, $C_{out} = R_{ds,on} = 0$

(c) with dead-time compensation and VSI model

(d) with instantaneous voltage sensing

Fig. 5.42: Comparison between the instantaneous stator-voltage sensing circuit and reference-voltage-based detection in the complex 'αβ'-reference frame. Experimental results at 55 A and 1 Hz.

by direct FOC using the inherently sensorless stator flux-linkage oberserver introduced in Section 3.2.2.3. The observer poles are chosen according to the proportional pole-placement method described in Appendix A.5.1, with $g = 5$. Starting from zero torque and 300 rpm, the torque is first increased in steps of 10 Nm. The controller precisely sets the requested torque. At 50 Nm, the torque command is kept constant, whereas the speed is reduced in steps of 50 rpm. With decreasing speed, the influence of parameter mismatch increases and causes a torque deviation of up to 5 Nm. At standstill, the torque is decreased again in steps of 10 Nm. Throughout the whole experiment, with the voltage-sensing circuit, the controller does not lose its field orientation and the torque is stably applied – even at zero

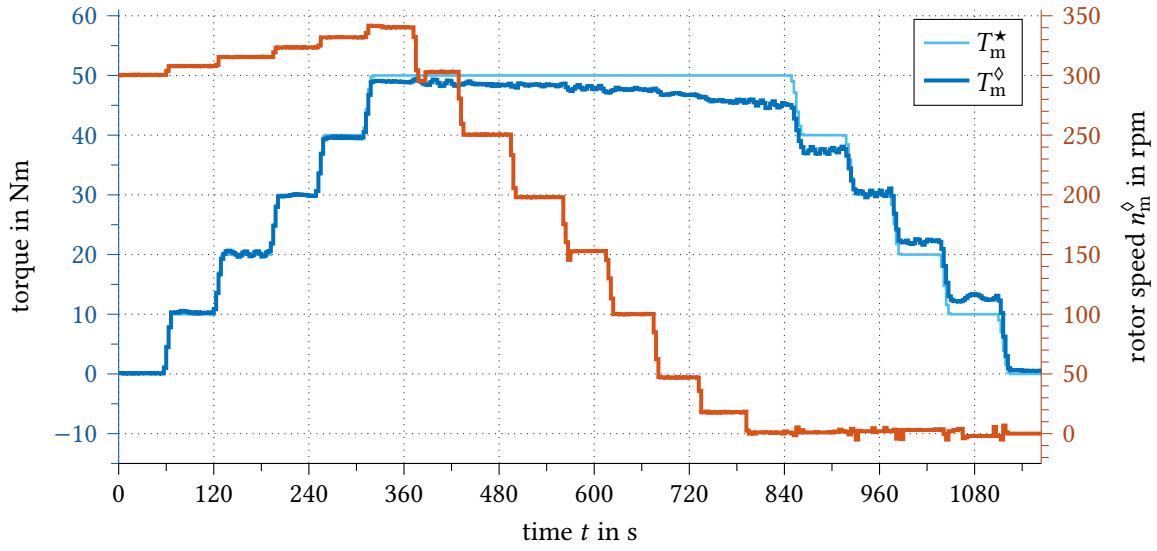

Fig. 5.43: Low-speed motoring operation of the IM drive without dedicated speed tranducer using the sliding-mode inherently sensorless stator flux-linkage observer. Experiment performed using IM26kA and Inverter 1 with the torque captured by TS200.

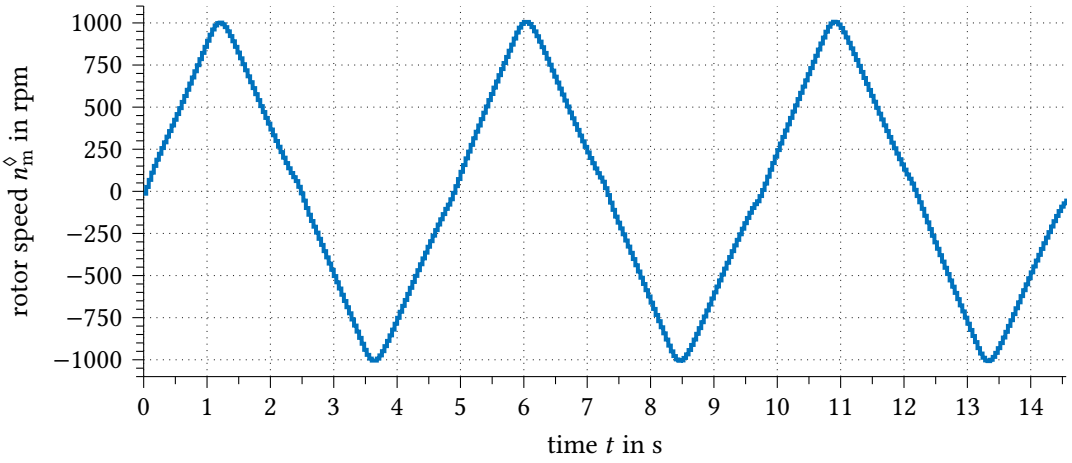

Fig. 5.44: Speed reversals using the sliding-mode inherently sensorless stator flux-linkage observer with a torque reference of ±3 Nm. Experiment done with IM26kA and Inverter 1.

rotor speed and even though all online parameter adaption schemes are deactivated.

It should however be noted, that the stable operation region does not cover the generating mode at zero stator frequency, as the induced voltage then becomes zero. In this case, other techniques, such as exploiting artificially introduced rotor saliencies [JL95; LM17] or saturation and slot effects [JL96; LKM16] must be applied. Since control without dedicated speed transducer is out of focus of this work, such methods are not further investigated.

A common experiment to evaluate the low-speed generating-mode performance of the controller are speed reversals as conducted in Fig. 5.44. Between ±1000 rpm, an alternating torque request of ±3 Nm is applied. The rotor speed smoothly crosses the zero stator frequency point and the controller maintains its field orientation.

5.6 Summary

In the previous chapters it was pointed out, that the back-EMF-based voltage-model flux-linkage observer shows substantial advantages over the current model in terms of parameter independence. To extend its stable operating region to low or zero speed, precise detection of the stator terminal voltage is required. In this chapter, various approaches for instantaneous detection of the PWM-period average voltage were discussed. A gate-driver-integrated voltage-measurement circuit was proposed, that allows to capture the drain–source voltage of each low-side MOSFET at a high sampling rate of 1 MHz. The PWM-period average is obtained by digital integration performed on an FPGA. To improve the measurement accuracy, an analog high-cutoff-frequency LPF (169 kHz) was introduced before A/D conversion. The LPF was analytically optimized with respect to maximum measurement accuracy. A general solution for two and multi-level PWM-based VSIs was given. For the 120 V system used in this work, a measurement resolution of 10 mV was achieved. Experimental results showed a maximum instantaneous measurement error of less than 0.25 % of the DC-link voltage, which is a notable improvement over common solutions without additional high-cutoff-frequency LPF. The analog noise of the circuit is lower than 10 mV. Thus, the measuring noise is only defined by the quantization error.

Experiments with FOC without dedicated speed transducer demonstrated the benefit of using the instantaneous stator-voltage sensing. Stable torque control at low speed, and even at zero rotor speed, was achieved.

The proposed instantaneous phase-voltage measurement offers precise online detection of the inverter distortion voltage for each phase, individually. In this chapter, this feature was utilized for a novel sensor-offset calibration technique that allows decoupled online calibration of all phase-voltage and current sensor offsets. The method is independent of the control and is based on parallel zero-crossing detection using the inverter voltage-distortion curve. Experimental results prove the feasibility of the new method and show outstanding precision. Especially at low speed, when other offset calibration techniques fail, the proposed scheme performs reliably.

Since the voltage measuring circuit captures the voltages across the low-side switch, together with the measurement of the DC-link voltage, direct detection of the semiconductor voltage drop is possible. In this chapter, simultaneous online monitoring of the ‘on’-state resistance of all six MOSFETs was experimentally demonstrated. Due to the nearly linear temperature dependency of $R_{\mathrm{ds,on}}$, this enables individual monitoring of the MOSFET junction temperatures. Furthermore, detection of an abnormal resistance increase due to bond-wire lift-off is possible and has been experimentally verified.

6 Torque Dynamics of the Efficiency-Optimized Induction Machine Drive

As described in Section 2.2.1, the efficiency of the IM drive is improved by the operating-point-dependent adjustment of the flux-linkage magnitude. For this purpose, a lookup table was derived in Fig. 2.20, which assigns an efficiency-optimized flux-linkage magnitude to each combination of torque reference and stator frequency.

This chapter focuses on the dynamic limitations associated with the efficiency-enhancing reduction of the flux-linkage magnitude at light loads. As illustrated in Fig. 6.1a, then, a change of the operating point not only requires a different torque-producing current i_{sq} but also a modification of the flux-linkage magnitude. However, due to the rotor time constant, the flux-linkage reacts relatively slowly to changes in the flux-producing current i_{sd}. If a straight current trajectory – such as ① in Fig. 6.1b – is used, the LPF-type link between current and flux linkage limits the dynamic performance of the drive system and leads to violations of the dynamic requirements stated in Fig. 1.5. By correct decoupling according to Section 2.2.2 and application of a closed-loop flux-linkage regulator, this negative effect can be eliminated. However, the decoupler or regulator can cause a high flux-producing current during transients ②, that violates the maximum current constraint of the VSI.

In the following, control approaches for improved torque dynamics are investigated that ensure a dynamic torque response within the requirements of the MAs:Stab project while not violating the defined constraints. The desired current trajectory in the RFO

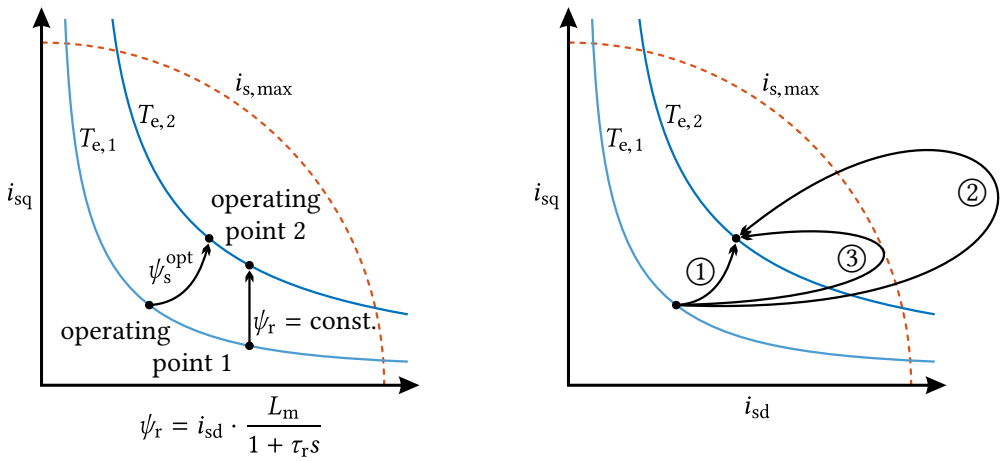

(a) operating point trajectory

(b) different stator current trajectories

Fig. 6.1: Trajectories of the operating point and stator current in RFO coordinates.

reference frame is supposed to touch and travel along the maximum current circle as long as the reference torque is not reached ③. To achieve this, in Section 2.2.3, the direct SFO controller was extended by an input trajectory filter and a current limiter. In conjunction with the flux-linkage PI regulator, they can be utilized to manipulate the dynamic current sharing during transients. In Section 6.1, this approach is implemented in C++ and analyzed in simulations using the software-in-the-loop simulation model given in Appendix A.4. Experimental results show the feasibility of this solution on the test bench using IM26kA.

Even though the dynamic requirements are fulfilled, the resulting current trajectory of the direct FOC controller may not be considered as an optimal solution. This also applies to the few publications that are available on this topic. In [Mat+99], the maximum available stator current is utilized by the flux-producing current component during transients. This way, the flux-linkage build-up is accelerated. However, since the maximum current $i_{\mathrm{s,max}}$ is a mutual constraint for flux-producing and torque-producing current, the latter is suspended and an optimal dynamic distribution between both is not achieved. Instead, [VL03a] proposes an analytical approach to minimize the resulting speed error after a sudden load step, which is equivalent to maximum torque dynamics. The current share is described by the current space-vector angle $\measuredangle \vec{i}_{\mathrm{s}}^{\,\mathrm{dq}}$ which is calculated during each sampling time step. Even though the dynamic response is improved, the future trajectory and control actions are not taken into account, which leads to a solution different from the global optimum. Furthermore, operating-point-dependent parameter variations such as magnetic saturation cannot be considered. In [SK13; SDK13], the trajectory is calculated offline by numerically solving a second-order nonlinear time-varying boundary value problem. However, the optimization goal is the minimization of dynamic losses, which is different from the objective in this work.

To find the theoretical optimum with respect to dynamic torque response, in Section 6.2, a current trajectory optimizer is developed which finds a dynamically optimized solution based on the theory of model-predictive control (MPC). The offline-computed results are used to derive a lookup-table-based trajectory planner which can be implemented on a low-cost microcontroller. The basic principle has been published in the course of this work under [SGD17] and is further developed in this chapter including magnetic saturation.

For better visualization and comparability, in the following, all quantities and figures are referred to the RFO reference frame. Results obtained from the direct SFO controller are transformed to RFO coordinates, accordingly.

6.1 Dynamics of the Direct SFO controller

The decoupler and the closed-loop flux-linkage regulator enable a fast torque response of the SFO controller, even with efficiency-optimized flux manipulation. Fig. 6.2 shows the simulated step response from zero to 100 Nm with an input rate limiter of $4\,\mathrm{Nm\,ms^{-1}}$. Without constraints handling, a stator current overshoot of up to 750 A occurs. With

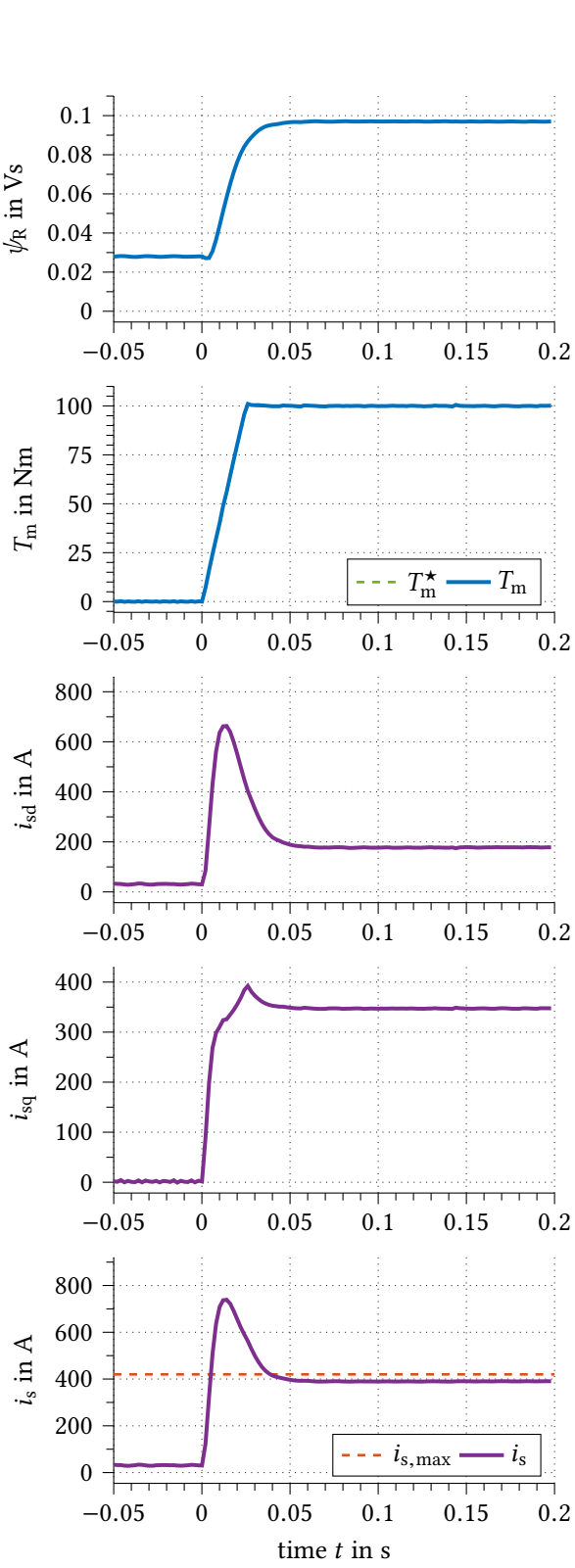

Fig. 6.2: Decoupling and flux-linkage regulation without considering the maximum current constraint. Case ② in Fig. 6.1b.

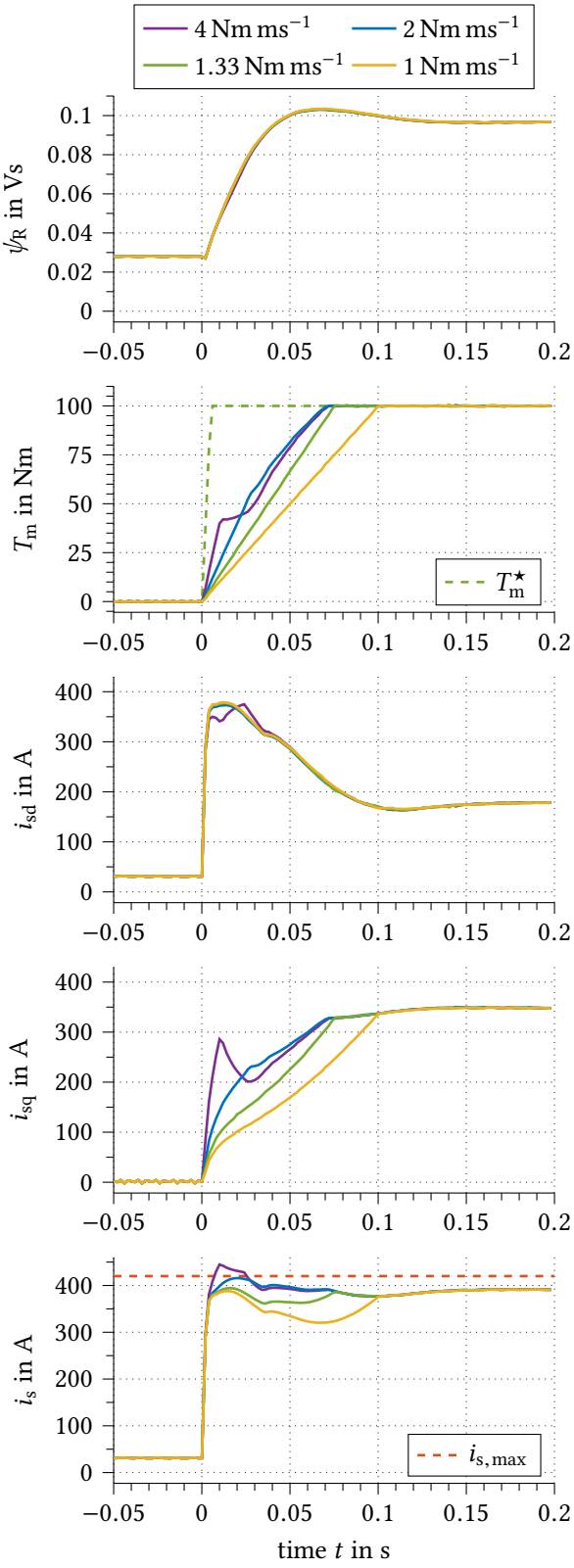

Fig. 6.3: Step response as a function of the torque reference input trajectory filter with a 10 Hz flux-linkage PI-controller.

the constraints handling of Fig. 2.23 enabled, this current overshoot is prevented at the cost of degraded torque dynamics. However, the dynamic response can be influenced by sufficient selection of the input trajectory filter, the flux-linkage controller bandwidth and an additional flux-producing current constraint:

The torque-reference rate limiter defines the maximum slope of the torque-producing current component. Since in Fig. 2.23 the torque-reference rate limiter is placed behind the flux-linkage lookup table, the flux-producing current i_{sd} is almost not affected by the rate limiter. As illustrated by the simulation results in Fig. 6.3, with a slope of 1 or $1.33\,\mathrm{Nm\,ms^{-1}}$, the flux-production is sufficiently fast compared to the torque slope and the maximum stator-current magnitude is not reached. At a higher slope, the torque-producing current i_{sq} is limited by the current constraint which reduces the torque slope. Since the flux-producing current – according to Section 2.2.3 – is prioritized, the rate limiter does not influence the current sharing. However, it can be used to ensure that sufficient flux-linkage magnitude is present before torque is produced, which leads to a smoother torque response. A reasonable choice for the case shown in Fig. 6.3 is $2\,\mathrm{Nm\,ms^{-1}}$.

The flux-linkage controller bandwidth defines the dynamic response of the flux-producing current on the flux-linkage reference. As shown in Fig. 6.4, the PI-controller bandwidth is directly related to the stator current sharing. A higher bandwidth leads to an increased flux-producing current i_{sd} and reduced torque-producing current i_{sq} during transients. This influences the torque dynamics. The simulation results show, that a bandwidth between 5 and 10 Hz leads to smooth and fast torque production.

The additional flux-producing current constraint offers a second way of influencing the stator-current sharing during transients and can be implemented as output limitation of the flux-linkage PI controller in conjunction with an anti-windup mechanism. Since the controller is implemented in SFO, the simulation results in Fig. 6.5 – which have been transformed to RFO – do not show a constant additional current constraint. Instead, it manifests itself in a negative slope in i_{sd} between 0 and 0.04 s. The results show, that with $\max(i_{\mathrm{sd}}) = 300\,\mathrm{A}$ a further improvement is possible. Then, in i_{sd} a second local maximum becomes present, which boosts the flux-production after the desired torque has been reached.

The simulation results with IM26kA proof, that the dynamic torque requirements defined in Fig. 1.5 can be fulfilled with the direct SFO controller and the proposed constraints handling without violating the maximum stator-current constraint. The simulations have been conducted using the software-in-the-loop simulation model described in Appendix A.4. Thus, the control algorithm – which has been implemented in C++ – can directly be downloaded to the DSP of the VSI. The experimental results are presented in the following section.

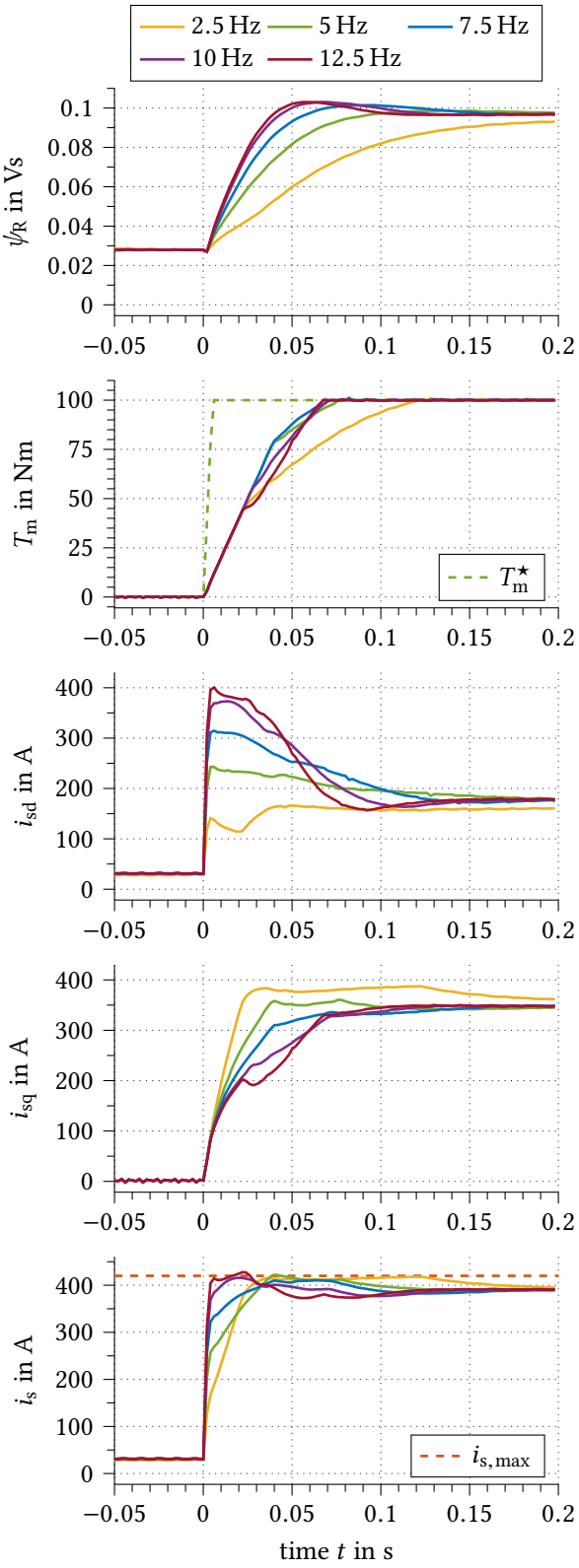

Fig. 6.4: Step response as a function of the flux-linkage PI-controller bandwidth with a $2\,\mathrm{Nm\,ms^{-1}}$ torque-reference rate limiter.

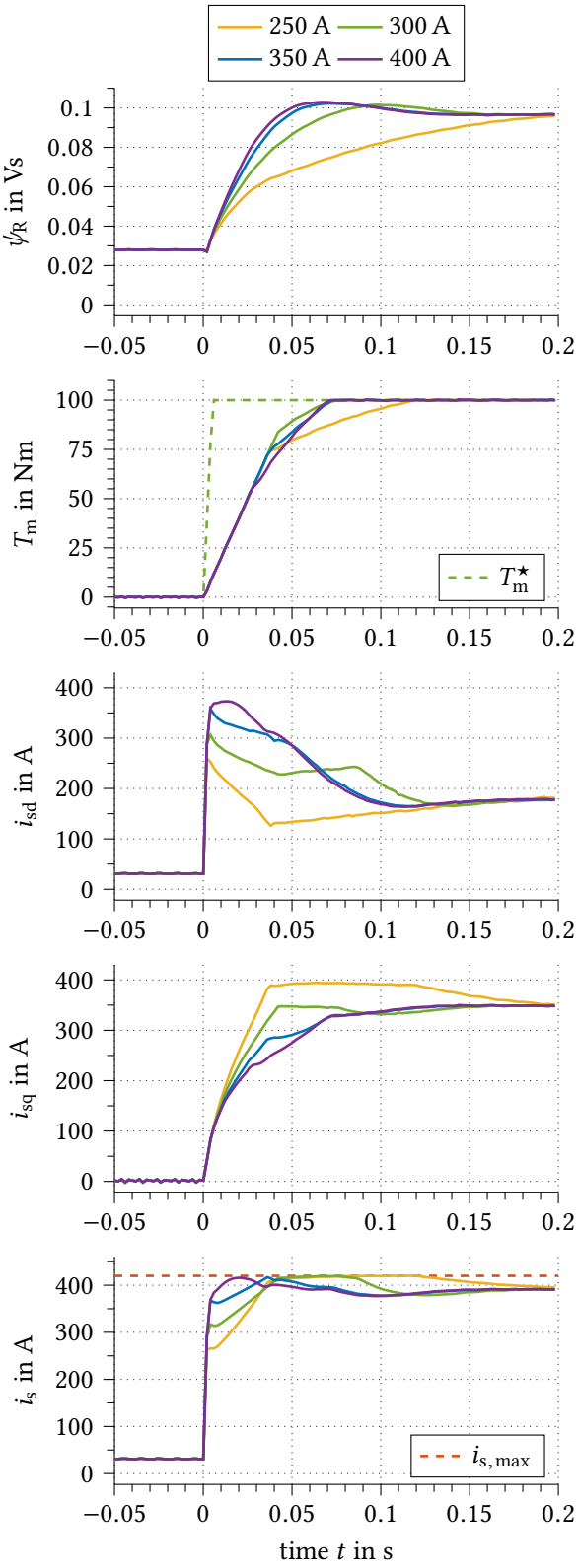

Fig. 6.5: Step response as a function of an additional i_{sd} current constraint with 10 Hz PI controller a $2\,\mathrm{Nm\,ms^{-1}}$ rate limiter.

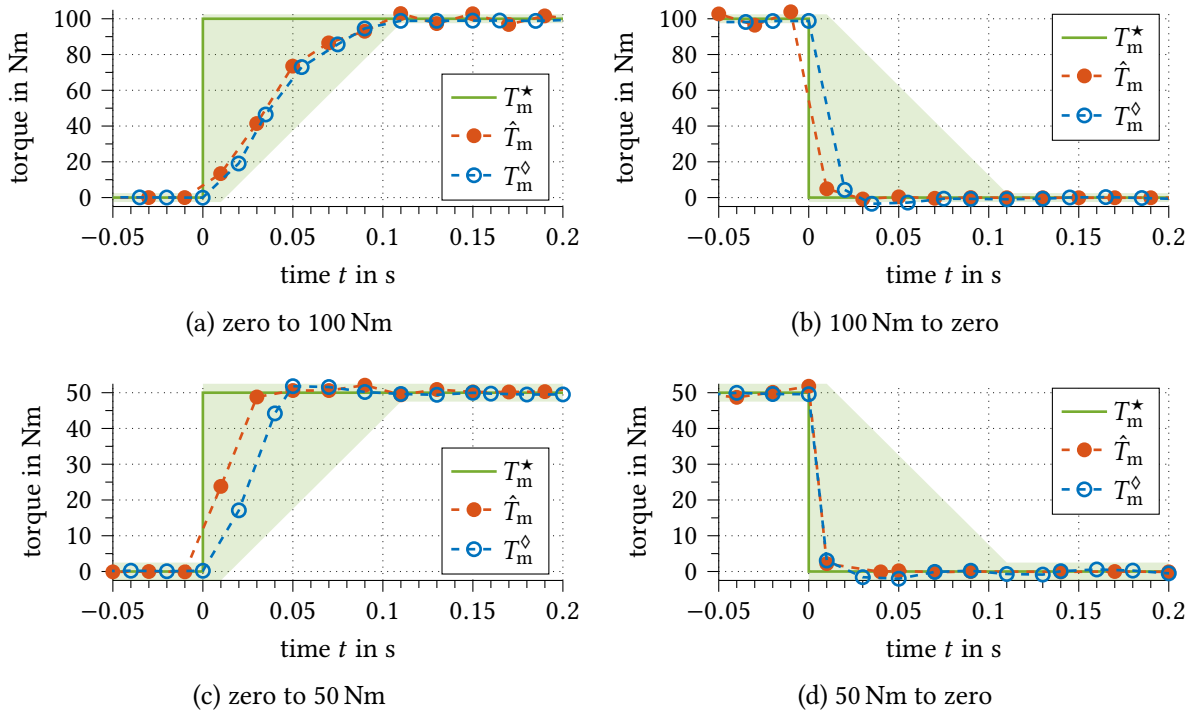

(a) zero to 100 Nm

(b) 100 Nm to zero

(c) zero to 50 Nm

(d) 50 Nm to zero

Fig. 6.6: Experimental step-response results of the efficiency-optimized direct SFO controller with input trajectory filter. Data recorded from CAN with 20 ms update rate using IM26kA.

6.1.1 Experimental Results and Conclusions

To obtain realistic experimental results, the hardware setup and the communication interface are chosen identical to the final EV setup which is described in Fig. 1.4. The MABX sends a torque request $T_\mathrm{m}^\star$ via CAN to the drive and receives an estimated torque feedback $\hat{T}_\mathrm{m}$. The messages are exchanged at a constant update rate of 20 ms. The torque $T_\mathrm{m}^\diamond$ is measured using the torque sensor TS290 with the specifications given in Appendix A.2.3. All signals are recorded using a CAN data logger.

Fig. 6.6a shows the experimental step response of the efficiency-enhanced IM26kA drive for a reference $T_\mathrm{m}^\star$ from zero to maximum torque. The flux controller bandwidth has been set to 10 Hz and the trajectory filter was set to 0.15 Nm ms^{-1}. The direct SFO controller meets the requirements of the MAs:Stab project, which are represented by the shaded area. Until 0.05 s the torque follows the input reference ramp. Between 0.05 and 0.1 s the current is limited and the slope is reduced. The request of 50 Nm (c) is fulfilled faster because less flux is required. Due to the reference rate limiter, the flux-linkage magnitude is always sufficiently high to produce the desired torque. A step to zero torque - as depicted in (b) and (d) - is always instantly possible, because i_sq can be set to zero only limited by the current controller bandwidth which has been chosen to 500 Hz. A negative flux-producing current to accelerate the flux adaption is not required. Instead, a lower boundary of zero or more should be applied to i_sd in order to improve the transient efficiency.

It is concluded, that the direct SFO controller meets the dynamic requirements stated

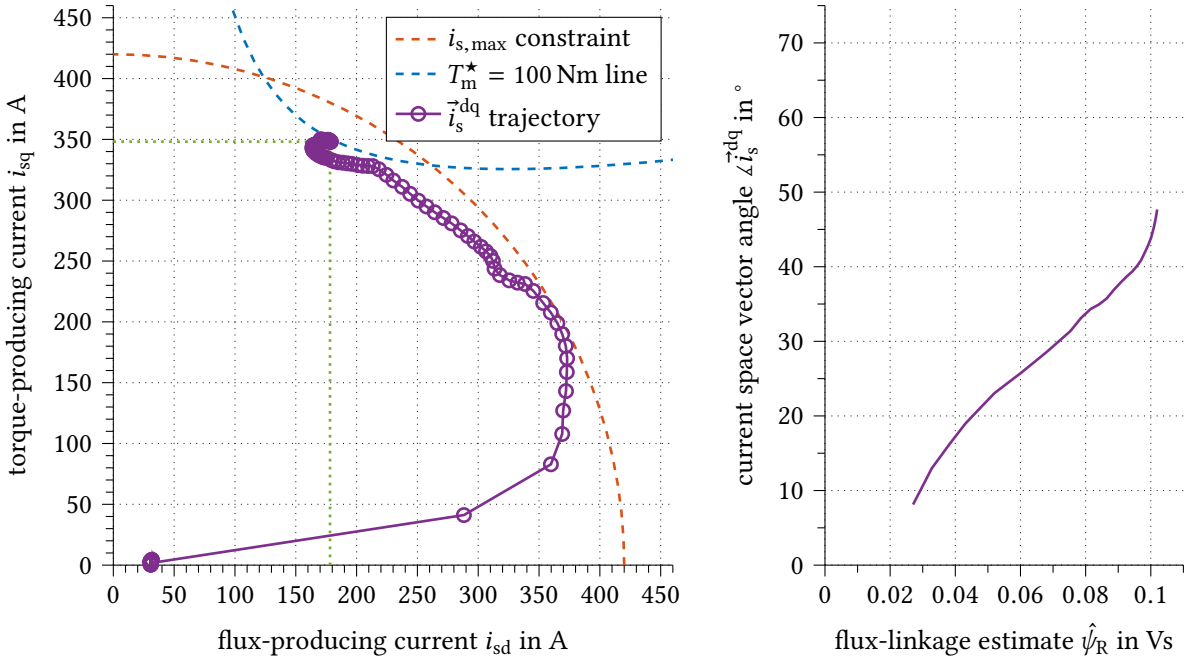

(a) current locus in RFO

(b) current vector angle in RFO

Fig. 6.7: Simulated RFO current locus diagram. Step response from zero torque to 100 Nm with a rate limiter of 0.2 Nm ms^{-1}, 10 Hz flux-controller bandwidth and max(i_{sd}) = 400 A.

in Fig. 1.5. The major limitation is caused by the CAN communication which is part of the higher-level TV control loop, implemented on the MABX. The constant refresh rate of 20 ms causes a feedback delay of up to 40 ms and is thus in the same order of magnitude as the delay caused by the flux-linkage build-up. However, from a theoretical point of view, there is still a margin for dynamic improvement of the torque controller. The simulation results show, that during build-up of the flux-linkage, the maximum stator current is not fully utilized. Thus, in the current locus diagram of Fig. 6.7a, the constraint is not reached. An improved solution for optimal dynamic response is derived in Section 6.2.

6.2 Dynamically-Optimized Current Sharing in FOC drives

To find the optimal current trajectory for a maximum dynamic response, a two-dimensional nonlinear optimization problem with mutual constraint must be solved. This exceeds the capabilities of conventional linear control theory. Instead, a control algorithm is required, which optimizes the current trajectory taking future control actions and the maximum current constraint into account. An effective, systematic approach for this type of optimization problem is described by the theory of MPC [Ros04].

In this section, an MPC-based trajectory planner is developed. Therefore, the decoupling equations and the constraints handling of the direct SFO controller are replaced according to Fig. 6.8 and the reference current $\vec{i}_s^{dq}$ is obtained from the trajectory planner.

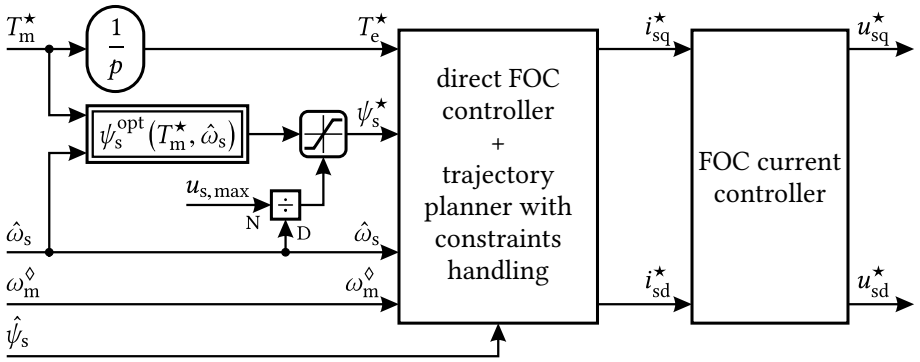

Fig. 6.8: Signal-flow diagram of the modified FOC controller with stator current trajectory planner.

6.2.1 RFO Current Model of the IM in State-Space Representation

In a first step, a linearized state-space current model of the IM is derived. This way, the future system states and outputs can be predicted using the prediction matrices (A.20) and (A.21) in Appendix A.7 [Ros04, p. 32]. By choosing the RFO reference frame, the system reduces to only a single state variable and the results can be illustrated more intuitively.

Based on (2.28), the rotor flux linkage $\psi_\mathrm{R} = L_\mathrm{m}/L_\mathrm{r}\psi_\mathrm{r}$ is chosen as the only state variable of the RFO state-space model. ψ_R is also chosen as the output of the model, along with the air-gap torque T_m. As system input, the stator current space vector $\vec{i}_\mathrm{s}^{\,\mathrm{dq}}$ is selected, which will later be the output of the MPC-based trajectory planner. To ensure integral action with zero steady-state error, the state-space representation with steady-state estimates – which are denoted by the superscript 'ss' – is used [MR93]. The system variables are then given by

$$\boldsymbol{u}_\mathrm{rfo} = \begin{bmatrix} i_\mathrm{sd} - i_\mathrm{sd}^\mathrm{ss} \\ i_\mathrm{sq} - i_\mathrm{sq}^\mathrm{ss} \end{bmatrix}, \quad \boldsymbol{x}_\mathrm{rfo} = \psi_\mathrm{R} - \psi_\mathrm{R}^\mathrm{ss} \quad \text{and} \quad \boldsymbol{y}_\mathrm{rfo} = \begin{bmatrix} \psi_\mathrm{R} - \psi_\mathrm{R}^\mathrm{ss} \\ T_\mathrm{m} - T_\mathrm{m}^\mathrm{ss} \end{bmatrix}. \tag{6.1}$$

Since in (2.25) the torque is defined as the product of a state variable ψ_R and an input variable i_sq, the system is nonlinear. However, for model representation, the torque can be linearized with

$$T_\mathrm{m} - T_\mathrm{m}^\mathrm{ss} = \frac{3p}{2}\Big(i_\mathrm{sq}^\mathrm{ss}\big(\psi_\mathrm{R} - \psi_\mathrm{R}^\mathrm{ss}\big) + \hat{\psi}_\mathrm{R}\Big(i_\mathrm{sq} - i_\mathrm{sq}^\mathrm{ss}\Big)\Big), \tag{6.2}$$

where $\hat{\psi}_\mathrm{R}$ is the estimated rotor flux linkage calculated during the previous calculation step. The system matrices are then derived from (2.28) and (6.2) as

$$\boldsymbol{A}_\mathrm{rfo} = -\frac{1}{\tau_\mathrm{r}}, \quad \boldsymbol{B}_\mathrm{rfo} = \begin{bmatrix} R_\mathrm{R} & 0 \end{bmatrix}, \quad \boldsymbol{C}_\mathrm{rfo} = \begin{bmatrix} 1 \\ \frac{3p}{2} i_\mathrm{sq}^\mathrm{ss} \end{bmatrix} \quad \text{and} \quad \boldsymbol{D}_\mathrm{rfo} = \frac{3p}{2}\begin{bmatrix} 0 & 0 \\ 0 & \hat{\psi}_\mathrm{R} \end{bmatrix}. \tag{6.3}$$

The system matrix $\boldsymbol{A}_\mathrm{rfo}$ and the feed-through matrix $\boldsymbol{D}_\mathrm{rfo}$ are time-varying and need to be updated each prediction time step to consider magnetic saturation and to linearize the torque equation according to (6.2). It can be shown, that since $\hat{\psi}_\mathrm{R}$ changes relatively slowly, the optimizer remains stable and converges to the correct solution.

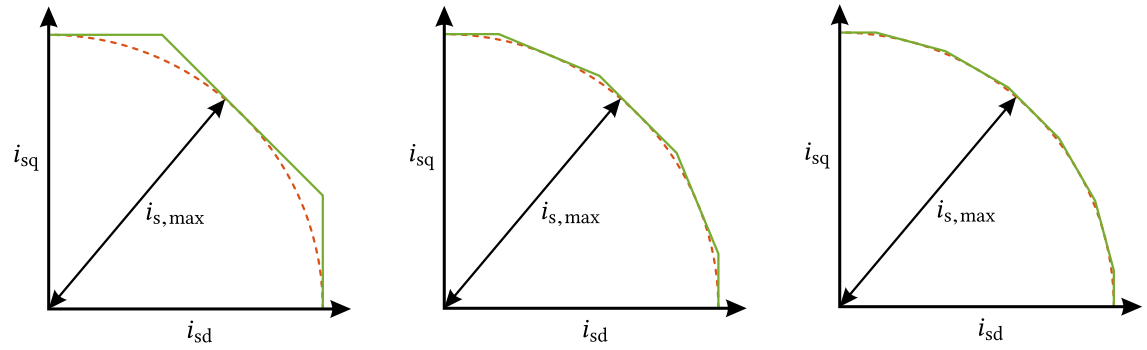

(a) three constraints (b) five constraints (c) seven constraints

Fig. 6.9: Linearized maximum current constraint as a function of the number of constraints.

6.2.2 MPC-based Trajectory-Optimization Algorithm

The MPC algorithm optimizes the manipulated variable – $\boldsymbol{u}_{\mathrm{rfo}}$ in this case – based on the minimization of a performance index[(i)] which considers future system outputs over a prediction horizon N_{p} and future control actions over a control horizon N_{c}.

Formulation of the Performance Index

The performance index is formulated to penalize the quadratic output error and the quadratic steady-state input error [Di 97] as

$$J_{\mathrm{p}}(t_k) = \sum_{k=1}^{N_{\mathrm{p}}} \hat{\boldsymbol{y}}_{\mathrm{rfo}}^{\mathsf{T}}(t_k)\boldsymbol{Q}_{\mathrm{y}}\hat{\boldsymbol{y}}_{\mathrm{rfo}}(t_k) + \sum_{k=1}^{N_{\mathrm{c}}} \hat{\boldsymbol{u}}_{\mathrm{rfo}}^{\mathsf{T}}(t_{k-1})\boldsymbol{Q}_{\mathrm{u}}\hat{\boldsymbol{u}}_{\mathrm{rfo}}(t_{k-1}). \tag{6.4}$$

$\hat{\boldsymbol{y}}_{\mathrm{rfo}}$ and $\hat{\boldsymbol{u}}_{\mathrm{rfo}}$ are predicted future values of the system output and input errors. $\boldsymbol{Q}_{\mathrm{y}}$ and $\boldsymbol{Q}_{\mathrm{u}}$ are the output and input error weighting matrices, which define the dynamic response and the optimization goals. It can be seen, that J_{p} becomes zero only when the input reaches its steady-state value and the output reaches the reference setpoint.

Equation (6.4) is a quadratic programming problem which can be solved numerically using MATLAB/Simulink and the predefined quadratic programming function `quadprog` [Mat16]. With the matrices and quantities defined in Appendix A.7, (6.4) can be written in a compact form

$$\begin{aligned} \min_{\boldsymbol{u}_{\mathrm{p}}} J_{\mathrm{p}} &= \frac{1}{2}\boldsymbol{u}_{\mathrm{p}}^{\mathsf{T}}\boldsymbol{H}\boldsymbol{u}_{\mathrm{p}} + \boldsymbol{f}^{\mathsf{T}}\boldsymbol{u}_{\mathrm{p}}, \\ \text{with} \quad \boldsymbol{H} &= 2 \cdot \boldsymbol{H}_{\mathrm{p}}^{\mathsf{T}}\boldsymbol{Q}_{\mathrm{y}}'\boldsymbol{H}_{\mathrm{p}} + 2 \cdot \boldsymbol{Q}_{\mathrm{u}}' \\ \text{and} \quad \boldsymbol{f} &= 2 \cdot \boldsymbol{H}_{\mathrm{p}}^{\mathsf{T}}\boldsymbol{Q}_{\mathrm{y}}'\boldsymbol{P}_{\mathrm{p}}\hat{\boldsymbol{x}}_{\mathrm{rfo}}\boldsymbol{u}_{\mathrm{p}}, \end{aligned} \tag{6.5}$$

which is suitable for the `quadprog` function [Di 13].

[(i)] also referred to as *cost function*

TABLE 6.1
MPC Optimization Parameters

parameter	symbol	unit	value
prediction horizon	N_p		50
control horizon	N_c		50
number of constraints			50
input weighting matrix	$\boldsymbol{Q}_\mathrm{u}$	A^{-2}	$\mathrm{diag}(0.5, 0.1)\left(\psi_\mathrm{R}^{ss} - \psi_\mathrm{R}(t=0)\right)$
output weighting matrix	$\boldsymbol{Q}_\mathrm{y}$	$\mathrm{diag}\left(\mathrm{V}^{-2}\,\mathrm{s}^{-2}, \mathrm{N}^{-2}\,\mathrm{m}^{-2}\right)$	$\mathrm{diag}\left(10^7, 10^3\right)$
sampling period		ms	1

Definition of the Maximum Current Constraint

The maximum current that can be delivered by the VSI is defined as

$$\sqrt{i_\mathrm{sd}^2 + i_\mathrm{sq}^2} \leq i_\mathrm{s,max}, \tag{6.6}$$

which represents a circle in the 'dq'-reference frame. The constraint is quadratic in nature and cannot be formulated into a general form of the quadratic programming problem. However, the circle can be linearized as a multitude of linear constraints according to Fig. 6.9, which can directly be given as a parameter to the `quadprog` function.

6.2.3 Simulation Results and Trajectory-Planner Synthesis

The output of the optimizer for a requested step from zero to 50 Nm and 100 Nm is depicted in Fig. 6.10. The parameters of the MPC algorithm are given in Table 6.1. The number of constrains is selected comparably high to obtain a precise circle approximation. The prediction and control horizons are chosen to cover half the rotor time constant. It can be seen, that in both cases the maximum stator-current magnitude is immediately fully utilized. First, the majority of the current is used for flux production, then, the torque-producing share is increased until the torque reaches its setpoint. Finally, the flux-producing current is increased again until the desired flux-linkage magnitude is obtained.

Compared to the direct SFO controller with input trajectory filter discussed in Section 6.1, the MPC algorithm generates the desired torque in about half the time. In the flux-linkage magnitude, no overshoot occurs. Instead, the flux linkage is only raised until just enough magnetization is available to generate the requested torque. This way, the desired torque is reached earlier, even before the flux linkage is raised to the optimum value.

Simulation-based Parameter-Sensitivity Analysis

For a deeper understanding of the dynamically optimized stator-current trajectory, the optimizer results are further investigated as a function of the flux linkage and torque references, and the flux linkage and torque initial values. By only varying a single parameter at

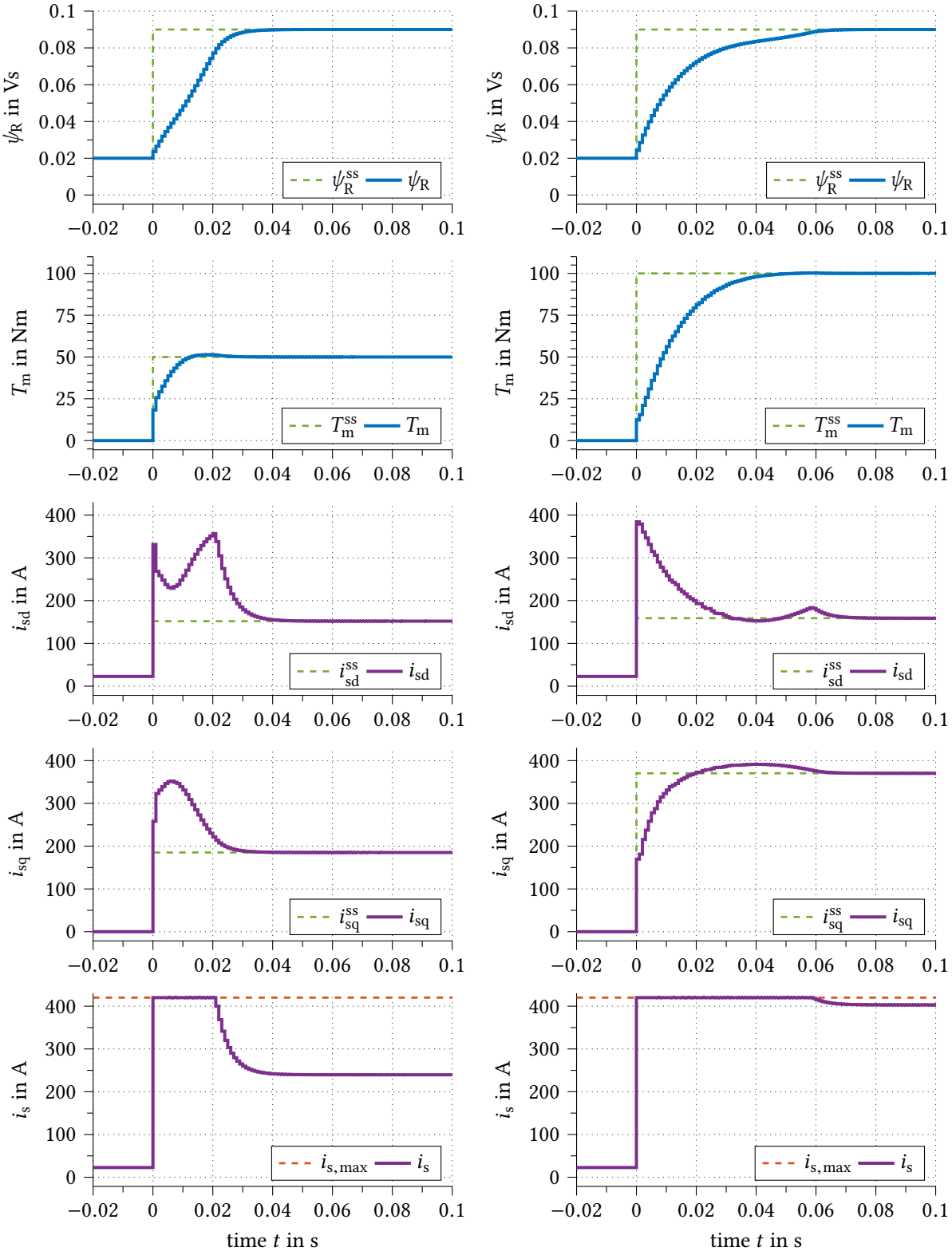

(a) zero to 50 Nm (b) zero to 100 Nm

Fig. 6.10: Simultaneous torque and flux-linkage step response with MPC based optimal current sharing.

a time, the influence of each parameter can be analyzed separately. The resulting current trajectories are plotted in the RFO reference frame, which offers a more insightful illustration of the trajectory and the current sharing. However, time-related information is lost. As a single quantity for the current share, the current space vector angle $\measuredangle \vec{i}_\mathrm{s}^{\,\mathrm{dq}}$ is plotted as a function of the estimated rotor flux linkage $\hat{\psi}_\mathrm{R}$. Since the torque is only limited when the current travels along the maximum current constraint, only the points located on the $i_\mathrm{s,max}$ circle need to be considered.

The flux-linkage-reference dependency of the current trajectory is studied using Fig. 6.11. The target value has been varied from 0.04 to 0.09 Vs, while a torque reference step from zero to 40 Nm is applied. It is observed, that the initial current share or space-vector angle on the current-constraint circle is identical for each case. All trajectories travel along the circle, first in counterclockwise and afterwards in clockwise direction, before they leave the circle at an individual angle. When described as a function of $\hat{\psi}_\mathrm{R}$, the current angle is very similar for all cases. Notable difference only occurs at the point of reversal. Since a lower flux linkage leads to a higher torque-producing current, the maximum angle increases with decreasing reference flux-linkage. However, it should be noted that the trajectory is a result of the selection of the weighting factors and thus a compromise between torque and flux-linkage dynamics. With shifting the priority further towards torque dynamics, the curves of the space-vector angle become closer to each other. But, the flux-linkage dynamics degrade significantly, whereas the improvement in torque dynamics is disproportionately small or even negligible.

The torque-reference influence is shown in Fig. 6.12. The requested torque has been varied between 20 and 100 Nm with a target flux linkage of 0.09 Vs. As in the previous case, the trajectories start with an identical current share and move along the $i_\mathrm{s,max}$ circle. It can be seen in the angle plot, that for a higher torque reference, the current angle increases more slowly. Thus, for a longer time a larger share is given to the flux-producing current. This is explained by the higher flux-linkage magnitude that is required to produce the desired torque. For a lower torque reference, less magnetization is required, and it is beneficial to increase i_sq earlier. Compared to the previous case in Fig. 6.11, the torque reference has a considerably higher influence on the dynamic current sharing.

The initial flux-linkage influence on the stator current trajectory is given in Fig. 6.13. The initial value is varied from 0 to 0.08 Vs for the target operating point of 100 Nm and 0.09 Vs. The initial angle in the maximum current circle increases with increasing initial flux linkage. Other than that, the trajectories are very similar. When described as a function of the estimated rotor flux linkage, the current angle is identical. Thus, the angle is not a function of the initial flux-linkage magnitude. However, for a

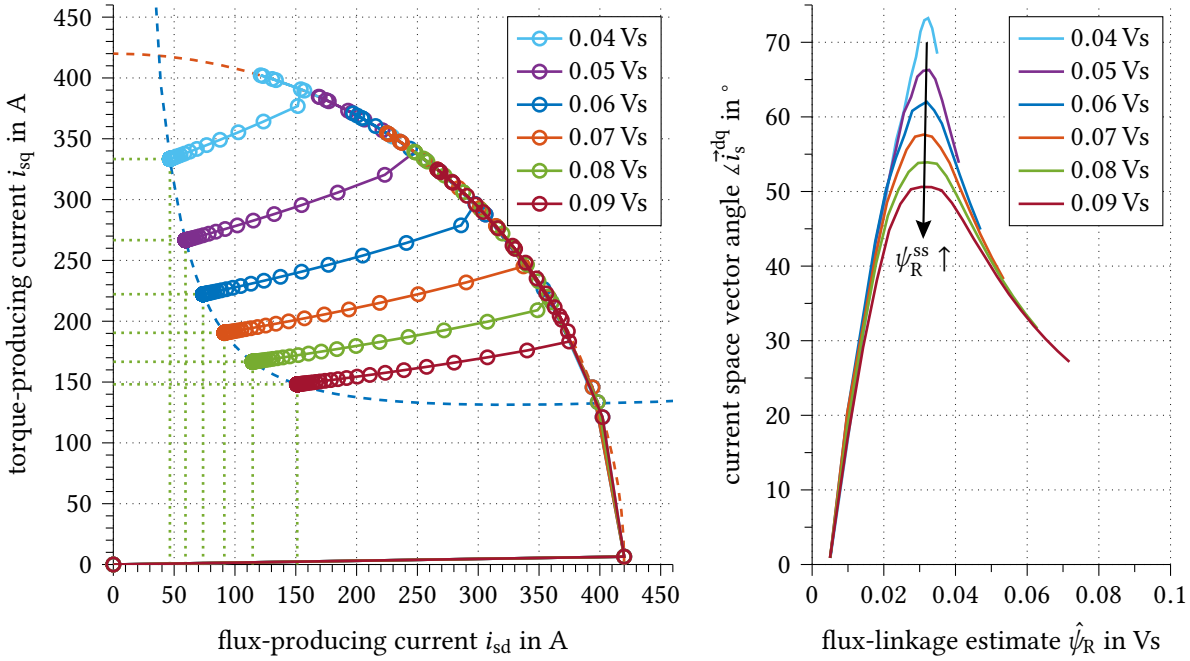

(a) current locus (b) current vector angle

Fig. 6.11: RFO current locus diagram as a function of the reference flux-linkage magnitude. Step response from zero flux and zero torque to 40 Nm.

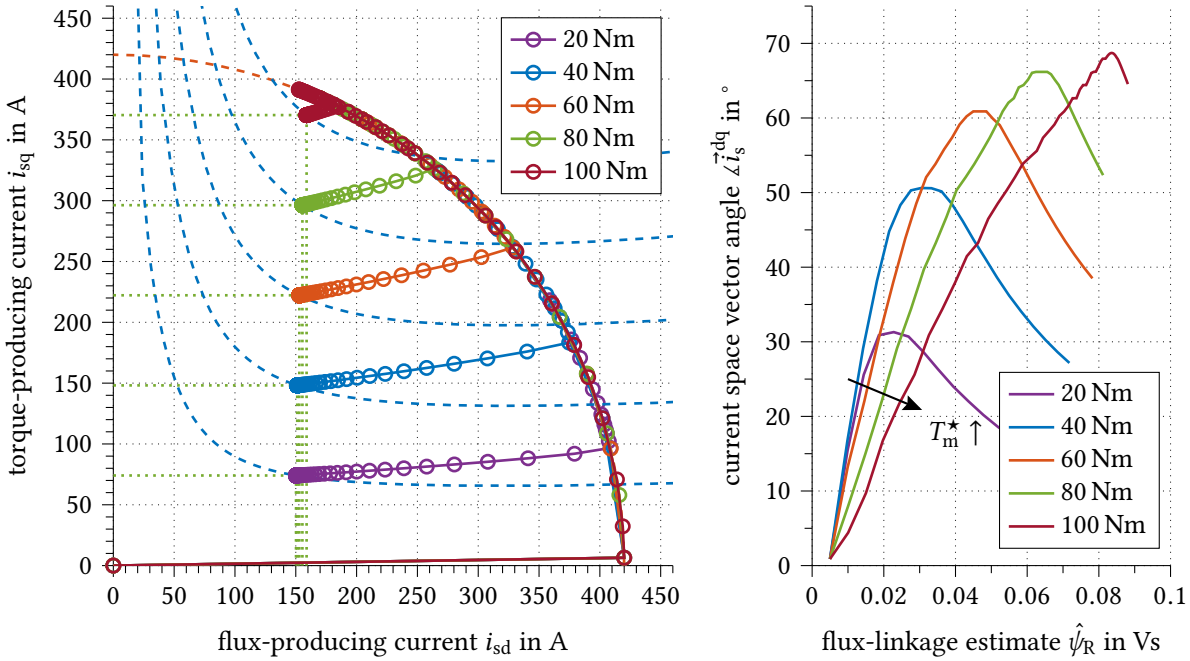

(a) current locus (b) current vector angle

Fig. 6.12: RFO current locus diagram as a function of the reference air-gap torque. Step response from zero torque and zero flux and 0.09 Vs.

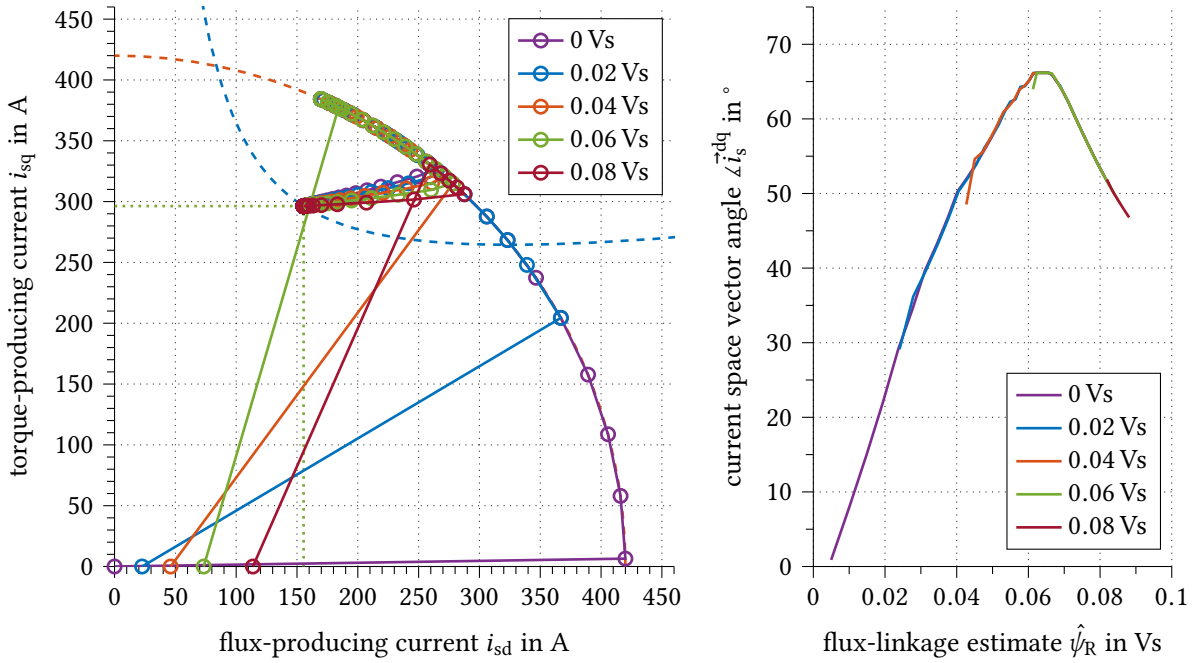

(a) current locus (b) current vector angle

Fig. 6.13: RFO current locus diagram as a function of the initial flux-linkage magnitude. Step response from zero torque to 80 Nm and 0.09 Vs.

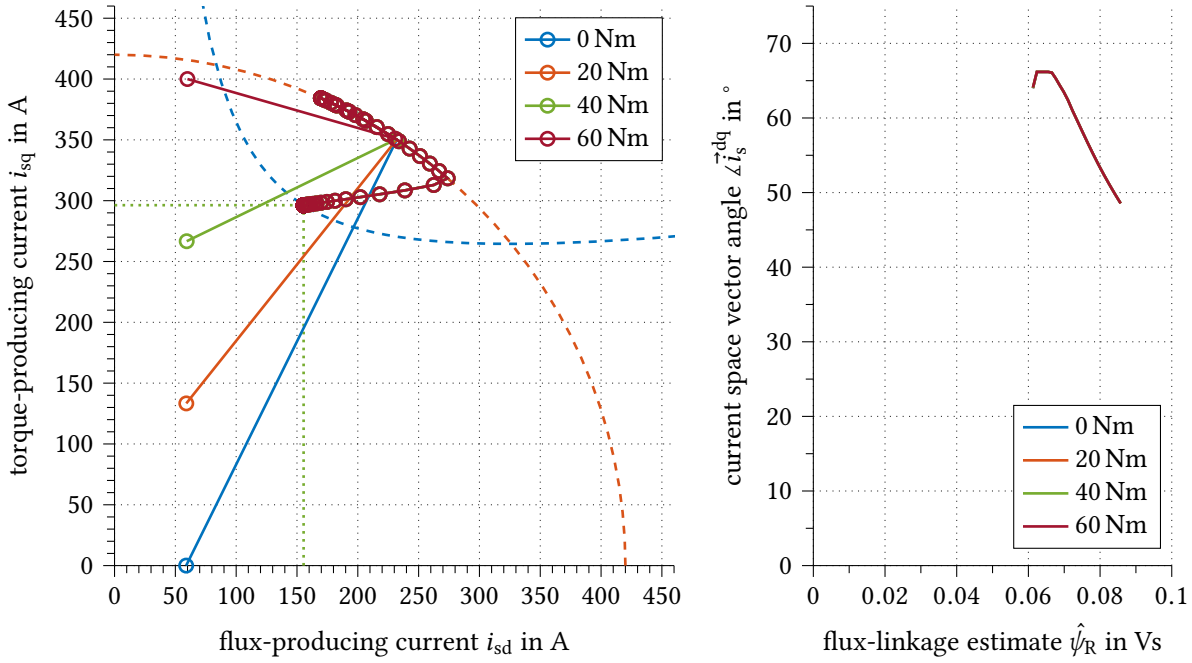

(a) current locus (b) current vector angle

Fig. 6.14: RFO current locus diagram as a function of the initial flux-linkage magnitude. Step response from 0.05 Vs to 80 Nm and 0.09 Vs.

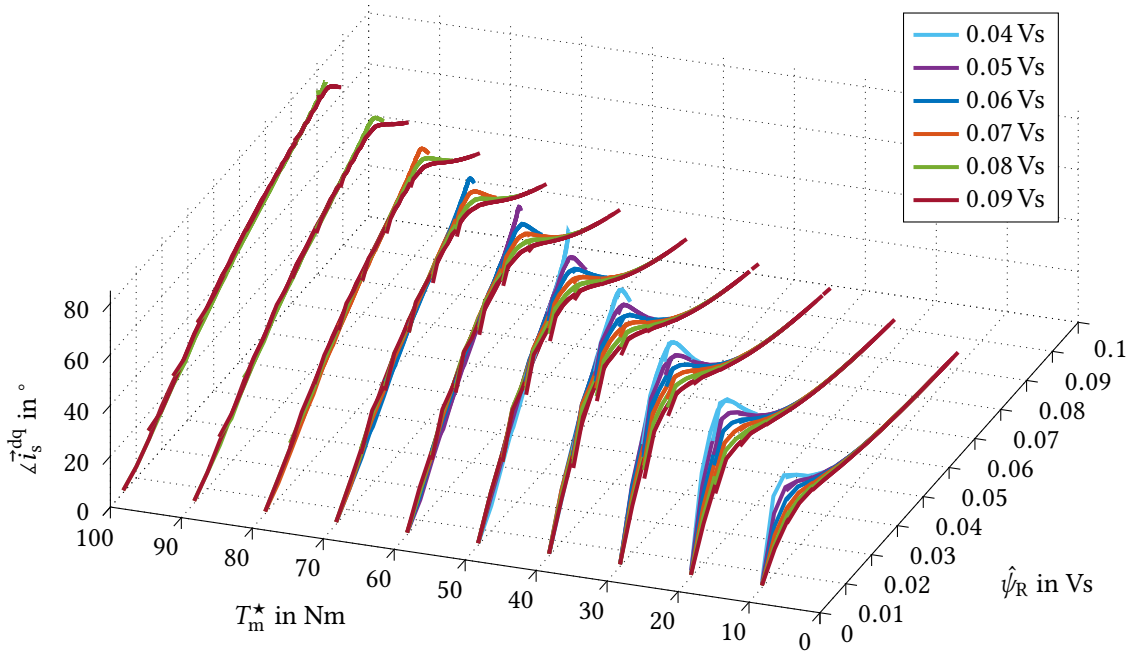

Fig. 6.15: Simulation results of the stator current space-vector angle as a function of reference torque and estimated rotor flux linkage. Only points on the maximum current constraint $i_s = i_{s,max}$ are considered. Step-response data of 403 different operating-point changes.

higher initial flux, the movement along the maximum current circle starts and ends at a higher estimated flux linkage.

The initial torque is varied from 0 to 60 Nm in Fig. 6.14. It can be seen, that – except for the first sampling step – the current trajectory is identical. The initial torque has no effect on the future current trajectory. This behavior is natural, since the initial torque value has no influence on the state variable ψ_R.

Synthesis of a Lookup-Table-based Trajectory Planner and Implementation

From the parameter sensitivity analysis, it is concluded that the current sharing during transients with limited stator current can be described by the RFO current space-vector angle as a function of the estimated rotor flux linkage. Only the flux-linkage and torque reference values have an influence on the optimal current sharing. The space-vector angle is not affected by the initial values.

Compared to the torque reference, the flux-linkage reference has only minor influence on the optimal current sharing. Thus, a lookup table can be created, which describes the angle as a function of the reference torque and the estimated rotor flux linkage. Fig. 6.15 shows the resulting data taken from 403 calculated trajectories which cover all possible initial and reference value combinations. As expected, a representation by a two-dimensional lookup table is possible. As previously mentioned, ambiguous data only occurs at the maximum angle point and at reduced torque where the dynamic response is less critical.

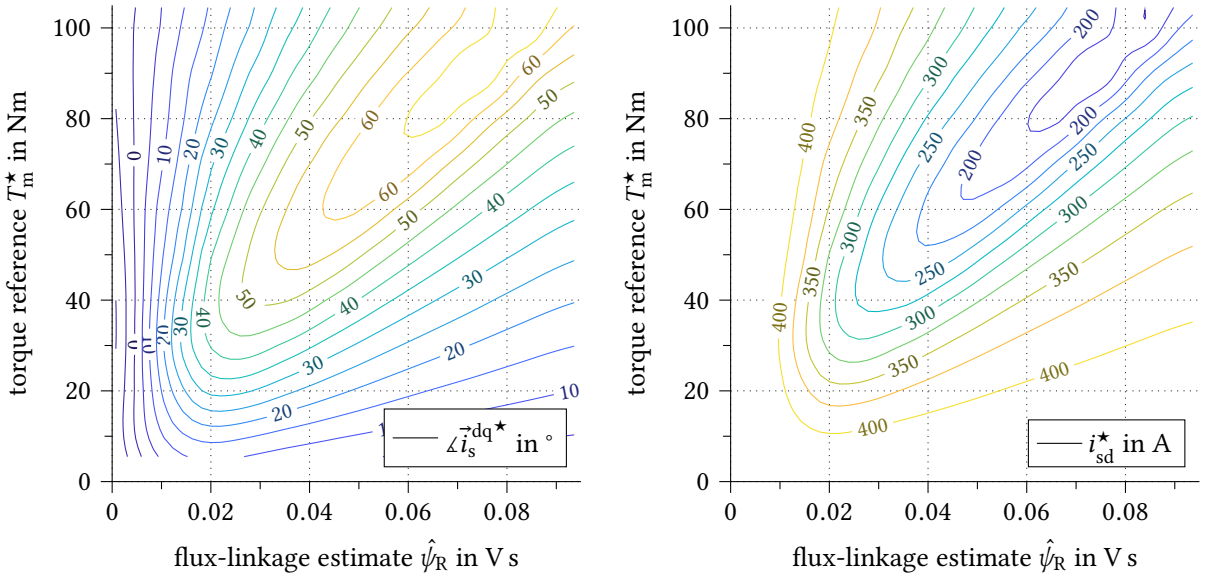

(a) current space-vector angle

(b) direct axis current in RFO

Fig. 6.16: Lookup table for the current vector angle generated from Fig. 6.15 using thin-plate spline interpolation and resulting lookup table for the dynamic flux-producing current constraint.

Fig. 6.16a shows the created lookup table for the reference current angle using a thin-plate spline interpolation. A trajectory planner according to Fig. 6.8 can be implemented by minor modification of the direct FOC algorithm. Since $i_{sd}^\star$ is already prioritized by the constraints handling, the desired behavior is obtained by applying a time-varying current limit to $i_{sd}^\star$, which is obtained by conversion of the lookup table as given in Fig. 6.16b.

6.3 Summary

In this chapter, the constraints handling of the direct SFO controller has been improved to enhance the dynamic torque response of efficiency-optimized IM drives while not violating the maximum VSI current constraint. Experimental results show that the dynamic requirements of the higher-level torque vectoring (TV) controller can be fulfilled. A further contribution of this chapter is the dynamic optimization of a direct RFO controller. Based on an MPC algorithm, the controller finds an optimal current trajectory during load transients, which considers future control actions and magnetic saturation. A lookup-table based solution was proposed that allows simple implementation on low-cost microcontrollers.

The proposed algorithm improves the dynamic torque response significantly. Even though EV traction drives usually have moderate dynamic requirements, for implementation of TV functions and modern safety features such as ESC and other ADAS, fast torque response is essential [Kra+17]. Furthermore, with the proposed solution, active damping of torsional drive-train oscillations as described in [MD00; GD04; SD15] can be applied using efficiency-optimized IM drives.

7 Conclusions and Future Work

This work presented a systematic approach to improve the torque accuracy and the dynamics of an efficiency-enhanced IM traction drive for EVs. A gate-driver-integrated phase-voltage-sensing circuit was proposed and novel sensor-offset compensation and condition-monitoring schemes were developed and experimentally demonstrated.

Parameter Uncertainty in the Component Models of the Drive System

The torque deviation of the IM drive is mainly caused by parameter uncertainty of its component models. When considering the common T-type transformer model of the IM, all parameters are time-varying quantities that change with magnetic saturation, thermal drift, rotor deep-bar effect, iron losses and other influences. Some of them can be precisely identified during parameterization and adapted during operation, others remain uncertain. The rotor resistance and the leakage inductances, for example, are not accessible for independent detection. Consequently, the control algorithm should be rather insensitive to these uncertain parameters. The main inductance, however, can be precisely determined by no-load tests and can be adapted as a function of the flux-linkage. With a temperature sensor at the stator-winding, also stator resistance adaption is possible.

Sensitivity of the Flux-Linkage Observer to Parameter Drift and Sensor Error

Analytical assessment of the sensitivity of the flux-linkage observer to parameter variations gives an insightful prognosis for the resulting torque deviation. The analysis is based on the frequency-response function approach introduced by Jansen et al. in [JL94], which has been extended in this work to investigate the influence of current and voltage sensor errors, of iron losses, and the rejection of higher-order harmonics. The latter is caused by sensor offset, imbalanced sensor gains and inverter dead-time effect.

The analysis reveals that the voltage-model observer with current-model corrective feedback – also referred to as Gopinath-style observer – outperforms the Luenberger-type and sliding-mode full-order observers. The torque deviation caused by current-sensor error is less then half of that resulting from the other observers. The sensitivity to higher-order harmonics and parameter drift is also lower. Especially for main and leakage inductance variations, the influence on the torque error using the Gopinath-style observer remains sufficiently small. Thus, for further improvement, only the stator and rotor resistances must be focused.

Since the resistance drift is mainly caused by temperature variations, adaption using a thermal model is most suitable. The advantage compared to other electromagnetic-model-based methods, such as the common MRAS, is, that the resistance adaption is decoupled from magnetic saturation and other non-thermal effects. It is inherently stable and leads to physically reasonable values – even at standstill. Using a spatially-resolved LPTN, the temperature distribution in the stator slots and the end-winding, as well as the rotor bars and the end ring, can be accurately determined. This results in a better resistance estimation than using only a single temperature sensor at the end-winding.

Experimental results using direct FOC with the Gopinath-style stator flux-linkage observer and the LPTN-based thermal resistance adaption resulted in a torque error below 1 % of the maximum torque for the entire operating range.

Gate-Driver-Integrated Sensing of the Inverter Output Voltage

The voltage-model-based stator flux-linkage observer is only dependent on the stator resistance and does not require rotor speed information. This makes it the favored observer for direct FOC. However, with decreasing speed, the back EMF reduces and the signal-to-noise ratio becomes insufficiently small. To extend the stable operating range of the observer to low and zero speed, precise sensing of the stator voltage is necessary.

Since the voltage is a switched, rectangular-shaped quantity, its PWM-period average value is of major interest. This makes instantaneous sensing quite challenging. A gate-driver-integrated voltage sensing circuit was proposed, that measures the drain–source voltage across the bottom switch of each inverter leg. The PWM-period average is obtained by digital integration using a sampling rate of 1 MHz. This solution offers:

- Possible integration into the gate-driver ICs.
- Simple implementation with single-ended analog components.
- Instantaneous measurement with low measuring noise.
- Additional features, such as online sensor-offset calibration and semiconductor condition monitoring without additional hardware effort.

The instantaneous measuring error is reduced by means of an analog LPF with a cutoff frequency higher than the switching frequency and lower than the sampling rate. By analytical error minimization, a general optimal solution for dimensioning the LPF was found, that can be applied to any PWM-based VSI, including multi-level systems. Experimental results show a maximum instantaneous voltage error of 0.25 % of the DC-link voltage.

Decoupled Online Sensor-Offset Calibration

Instantaneous output-voltage sensing across the bottom switches of each inverter leg allows precise measurement of the dead-time and semiconductor voltage-drop-related

voltage distortion. The distinctive S-shaped curve – when described as a function of the phase current – is used for continuous zero-crossing detection of the measured currents and the voltages. A sensor-offset drift is recognized as a displacement of the S-shaped distortion curve and is driven to zero by the adaption algorithm proposed in this work.

The method is applied to each pair of phase current and voltage sensors, individually. It only requires consecutive zero-crossings of the phase current and is otherwise fully decoupled from the control algorithm or application. Experimental verification shows the feasibility of the proposed method.

Limitations exist at high fundamental frequency and high current magnitude, as then, the detection of current zero-crossings becomes more difficult. However, the method is always stable and performs increasingly well at low frequencies where offset compensation is most important and other methods fail.

Online Semiconductor Condition Monitoring

Besides instantaneous phase-voltage sensing and online sensor-offset calibration, the voltage-sensing circuit is simultaneously used for monitoring the 'on'-state resistance of each B6 MOSFET switch. Based on this, individual junction-temperature sensing was experimentally demonstrated. Furthermore, the effect bond-wire lift-off was tested. It can be recognized during operation as an abnormal resistance increase.

The measuring range of the voltage-sensing circuit has to cover the full output-voltage span of the VSI from below zero to above the DC-link voltage. This is not optimal for the semiconductor voltage-drop sensing, as the measurement resolution is limited to 10 mV for the considered system. This problem is resolved using an online least-square fitting algorithm. By piece-wise linear regression thermal micro cycles can be detected.

Current-Trajectory Planner for Improved Torque Dynamics

With flux present in the electrical machine, the dynamic torque response using FOC is only limited by the bandwidth of the current regulator. However, to achieve maximum efficiency, in partial load, IM drives are operated with reduced flux-linkage. Consequently, after a suddenly increased torque demand, the flux linkage must first be built-up, before the increased torque can be generated. This process is limited by the rotor time constant which can be in the range of 100 ms and more. By applying a higher flux-producing current for a short time, the process can be accelerated. However, the current is limited by the maximum current that can be delivered by the VSI. Since it is a mutual constraint for flux- and torque-producing current, an optimum current trajectory exists that leads to maximum torque dynamics.

By appropriate dimensioning of the flux-controller bandwidth and the torque-reference rate limiter, the dynamic torque response can be significantly improved. Experimental results from zero to full torque meet the requirements for the TV controller, as initially

formulated in Section 1.2. 75 % of the full torque is reached after 50 ms, 100 % after 100 ms.

To find the current trajectory of maximum torque dynamics, a complex optimization problem with nonlinear constraint must be solved. An MPC-based trajectory optimizer was developed, that takes into account future control actions and magnetic saturation. The trajectories have been calculated offline and were analyzed in terms of their dependency on the initial and target operating points. It was found, that the optimal current share is almost only dependent on the reference torque and the actual flux-linkage. Based on these results, a two-dimensional lookup table was generated, and a trajectory planner was designed that can be implemented on low-cost microcontrollers. Simulation results promise an improved dynamic response with 75 % of the full torque after 18 ms and 100 % after 40 ms from zero.

7.1 Open Issues and Future Work

As the scope of this work is limited, naturally, some aspects remain open. Moreover, new topics were identified, that require further investigation. Some of them are listed below.

Modeling of Induction Machine Drives

Accurate model representation of the leakage inductances remains problematic. Due to the low parameter sensitivity of the Gopinath-style observer, it was not a serious issue in this work. But for IMs with closed rotor slots, the cross saturation can lead to fluctuations by a factor of ten. Then, saturation of the leakage path may not be neglected. This also includes proper division between the stator and rotor leakage inductance.

Another aspect is the modeling of increased iron losses caused by slot harmonics in the field-weakening region. They are not represented by the fundamental-frequency lumped-parameter model, yet. Since it does not affect the efficiency enhancement, this was a negligible issue in this work. But the losses can become significant in other machines and then contribute to the torque deviation.

Precise Torque Control of Induction Machine Drives

The torque-accuracy analysis was performed for a limited number of open and closed-loop observers. The analytic methodology is generally applicable to any linear time-invariant observer structure and should thus be used for further investigation of alternative observers.

Thermal resistance adaption was implemented using a spatially-resolved LPTN with 46 thermal units in an open loop manner. In a next step, the available temperature sensor at the end winding should be incorporated to form a closed-loop temperature observer. Furthermore, the model was used for simultaneous hot-spot temperature estimation, which requires a high spatial resolution. For the purpose of resistance estimation, model-order

reduction, for example based on balanced truncation [BS10; Qi+16b], is recommended to decrease the computational effort.

The MPC-based current-trajectory planner for maximum torque dynamics was only analyzed in simulation. For the implementation on a microcontroller, a lookup-table-based solution was derived. For experimental verification, a test bench is required that features a stiff shaft that shifts the torsional resonance frequency to a sufficiently high value.

Instantaneous Phase-Voltage Sensing

The proposed phase-voltage sensing is based on oversampling and digital integration. As the analog noise is lower than the LSB, the resolution is equal to that of the 14 bit A/D converter. Introducing an additional dither should be investigated to further improve the measurement resolution [LWV92]. However, this does not increase the resolution for the 'on'-state resistance monitoring. Therefore, a higher-resolution A/D converter is required.

The voltage-sensing circuit was implemented using discrete electronic components. To reduce the number of components and thus the total system cost, integration into the gate-driver IC should be targeted.

The novel online sensor-offset calibration technique was successfully demonstrated in this work but showed limitations at high fundamental frequencies. The digital filtering during post processing plays a major role for the precise detection of the current and voltage sensor offsets. Alternative filtering methods should be investigated to improve the current zero crossing detection at high fundamental frequencies and high current magnitudes, when only few sampling points are available.

Semiconductor condition monitoring using the integrated voltage-sensing was briefly examined. The proof of concept has been provided. Further investigations should focus on dynamic variations of the 'on'-state resistance to detect thermal micro cycles and to monitor the thermal impedances of power electronic modules. Therefore, the filtering during post processing must be improved and an increased resolution of the A/D-converter might be required.

A Final Word

The author is confident, that the methods and solutions presented in this work improve the precision and dynamics of IM drives and make the IM a competitive option for efficient and highly-dynamic traction applications. The proposed phase-voltage-sensing method has the potential to significantly improve the low-speed performance of electrical drive systems, while enabling valuable features, such as decoupled online sensor-offset calibration and semiconductor condition monitoring, without additional hardware effort.

A Appendix

A.1 Mathematical Conventions

For better illustration, in this work, superscripts and diacritical marks are added to physical quantities to emphasize their type or relation to a reference frame. Space vectors are depicted in vector and complex representation simultaneously and common simplifications are used for mathematical space-vector operations. Details about the applied notation and simplified calculation rules are given in the following.

A.1.1 Superscripts and Diacritical Marks

$x^{\star}$	reference value
x^{ss}	steady-state value
$x^{\lozenge}$	measured quantity
x^{*}	complex conjugate
$\vec{x}$	space vector in stator coordinates
$\vec{x}^{\alpha\beta}$	space vector in stator coordinates
$\vec{x}^{\mathrm{xy}}$	space vector in rotor coordinates
$\vec{x}^{\mathrm{dq}}$	space vector in field coordinates
$\hat{x}$	estimated quantity
$\bar{x}$	switching-period average
$\underset{\sim}{x}$	Laplace-transformed quantity
$\underline{x}$	phasor or Fourier-transformed quantity
$\underline{X}$	complex variable
$\underline{X}(\mathrm{j}\omega_{\mathrm{s}})$	transfer function in the frequency domain
$\boldsymbol{X}$	matrix
$\boldsymbol{x}$	vector

A.1.2 Space Vector Arithmetic and Reference Frame Transformations

Space vectors are widely used to describe quantities of a symmetrical three-phase system in a more intuitive two-dimensional reference frame. Space vectors are time-domain quantities and may not be confused with phasors in the frequency domain.

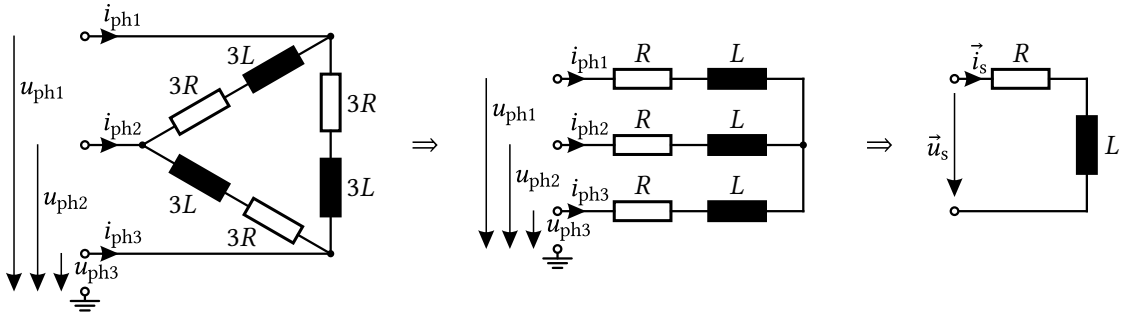

Fig. A.1: Single-phase representation of symmetrical three-phase systems using space vectors.

Space Vector Representation of Three Phase Systems

Voltages and currents of an electrical machine with 120° symmetrical arranged three-phase windings may be transformed into two-dimensional quantities without zero-sequence component using the simplified Clarke transformation

$$\vec{u}_\mathrm{s} = \vec{u}_\mathrm{s}^{\alpha\beta} = \begin{bmatrix} u_{\mathrm{s}\alpha} \\ u_{\mathrm{s}\beta} \end{bmatrix} = \frac{2}{3} \begin{bmatrix} 1 & -\frac{1}{2} & -\frac{1}{2} \\ 0 & \frac{\sqrt{3}}{2} & -\frac{\sqrt{3}}{2} \end{bmatrix} \begin{bmatrix} u_{\mathrm{ph1}} \\ u_{\mathrm{ph2}} \\ u_{\mathrm{ph3}} \end{bmatrix}. \tag{A.1}$$

In this work, space vectors are amplitude invariant and those without superscript refer to the stator-aligned ‘αβ’-reference frame. Space vectors may be written as complex numbers $\vec{u}_\mathrm{s}^{\alpha\beta} = u_{\mathrm{s}\alpha} + \mathrm{j}u_{\mathrm{s}\beta}$. For reference-frame transformation, the multiplication with $\mathrm{e}^{\mathrm{j}\theta_\mathrm{s}}$ is then equivalent to the multiplication with the rotation matrix

$$\vec{u}_\mathrm{s}^{\alpha\beta}\mathrm{e}^{\mathrm{j}\theta_\mathrm{s}} \quad \hat{=} \quad \begin{bmatrix} \cos\theta_\mathrm{s} & -\sin\theta_\mathrm{s} \\ \sin\theta_\mathrm{s} & \cos\theta_\mathrm{s} \end{bmatrix} \begin{bmatrix} u_{\mathrm{s}\alpha} \\ u_{\mathrm{s}\beta} \end{bmatrix}. \tag{A.2}$$

The multiplication with the imaginary number is analogously defined as

$$\mathrm{j}\vec{u}_\mathrm{s}^{\alpha\beta} \quad \hat{=} \quad \mathbf{J} \begin{bmatrix} u_{\mathrm{s}\alpha} \\ u_{\mathrm{s}\beta} \end{bmatrix} = \begin{bmatrix} -u_{\mathrm{s}\beta} \\ u_{\mathrm{s}\alpha} \end{bmatrix} \quad \text{with} \quad \mathbf{J} = \begin{bmatrix} 0 & -1 \\ 1 & 0 \end{bmatrix}. \tag{A.3}$$

Both space-vector notations, complex numbers and vectors are used interchangeably throughout this work.

As Fig. A.1 indicates, the space-vector notation allows to describe symmetrical three-phase systems as single-phase systems. However, this representation is not power invariant. Power-related quantities are obtained by multiplication with a power factor as

$$P = \frac{3}{2} \operatorname{Re}\left\{ \vec{u}_\mathrm{s} \vec{i}_\mathrm{s}^{\,*} \right\}. \tag{A.4}$$

All quantities described in this work are given as amplitude-invariant numbers.

Cross Product of Space Vectors

According to the Lorenz force, the torque produced by the induction machine can be defined as the cross product of magnetic flux linkage and current. When applied to the space-vector notation, this is not mathematically precise, as the cross product is only applicable to three-dimensional quantities. According to common practice and to the IRTF modeling concept introduced by Veltman et al. [Vv91], the cross product of two-dimensional space vectors is a scalar. It can be computed as the determinant of a 2×2 matrix formed by the four space vector coefficients. In this work, a new cross-product operator $|\times|$ for two-dimensional space vectors is introduced which is accordingly defined as

$$\vec{\psi}_\mathrm{s} \,|\times|\, \vec{i}_\mathrm{s} = \det \begin{bmatrix} \psi_{\mathrm{s}\alpha} & i_{\mathrm{s}\alpha} \\ \psi_{\mathrm{s}\beta} & i_{\mathrm{s}\beta} \end{bmatrix} = \begin{vmatrix} \psi_{\mathrm{s}\alpha} & i_{\mathrm{s}\alpha} \\ \psi_{\mathrm{s}\beta} & i_{\mathrm{s}\beta} \end{vmatrix} = \psi_{\mathrm{s}\alpha} i_{\mathrm{s}\beta} - \psi_{\mathrm{s}\beta} i_{\mathrm{s}\alpha}, \tag{A.5a}$$

$$\text{or} \quad \vec{\psi}_\mathrm{s} \,|\times|\, \vec{i}_\mathrm{s} = \mathrm{Im}\left\{ \vec{\psi}_\mathrm{s}^{*} \vec{i}_\mathrm{s} \right\} = \psi_{\mathrm{s}\alpha} i_{\mathrm{s}\beta} - \psi_{\mathrm{s}\beta} i_{\mathrm{s}\alpha} \tag{A.5b}$$

in complex space-vector notation.

Fourier and Laplace Transform of Space Vectors

In steady-state conditions, the electrical quantities of the IM are sinusoidal with

$$\vec{u}_\mathrm{s} = u_\mathrm{s} \mathrm{e}^{\mathrm{j}\theta_\mathrm{s}} = u_\mathrm{s} \mathrm{e}^{\mathrm{j}(\omega_\mathrm{s} t + \rho)} = \underbrace{u_\mathrm{s} \sin(\omega_\mathrm{s} t + \rho)}_{u_{\mathrm{s}\alpha}} + \mathrm{j} \underbrace{u_\mathrm{s} \cos(\omega_\mathrm{s} t + \rho)}_{u_{\mathrm{s}\beta}}. \tag{A.6}$$

They can be represented by complex phasors in the frequency domain where $\mathrm{d}/\mathrm{d}t \mathrel{\hat{=}} \mathrm{j}\omega$ using the Fourier transformation according to

$$\vec{u}_\mathrm{s} = u_\mathrm{s} \mathrm{e}^{\mathrm{j}(\omega_\mathrm{s} t + \rho)} \quad \overset{\mathcal{F}}{\circ\!\!-\!\!\bullet} \quad \mathcal{F}\{\vec{u}_\mathrm{s}\} = \underline{u}_\mathrm{s} = u_\mathrm{s} \mathrm{e}^{\mathrm{j}\rho}. \tag{A.7}$$

The complex phasors and transfer functions in the frequency domain are notated using the underline diacritic.

In control theory, systems are often described in the complex frequency domain with $\mathrm{d}/\mathrm{d}t \mathrel{\hat{=}} s$. Therefore, the quantities are transformed using the Laplace transformation as

$$\vec{u}_\mathrm{s} \quad \overset{\mathcal{L}}{\circ\!\!-\!\!\bullet} \quad \mathcal{L}\{\vec{u}_\mathrm{s}\} = \underline{\underline{u}}_\mathrm{s}. \tag{A.8}$$

A.2 Experimental Test Setups

For the experimental verification in this work, two dedicated test benches have been constructed and built. Test Bench 1 is shown in Fig. A.2 and consists of two air-cooled

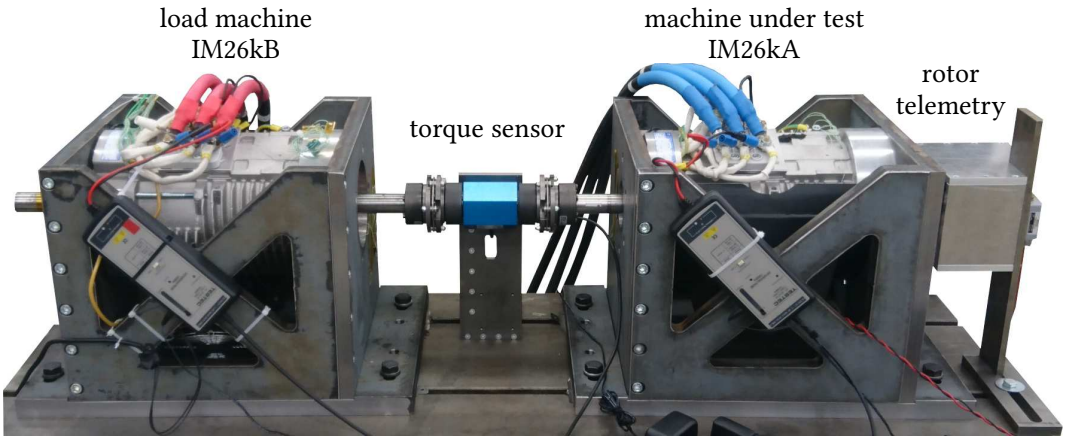

Fig. A.2: Test Bench 1 with two 26 kW induction machines and TS200 torque sensor. IM26kB is star-connected and IM26kA is in delta configuration and equipped with four rotor temperature sensors.

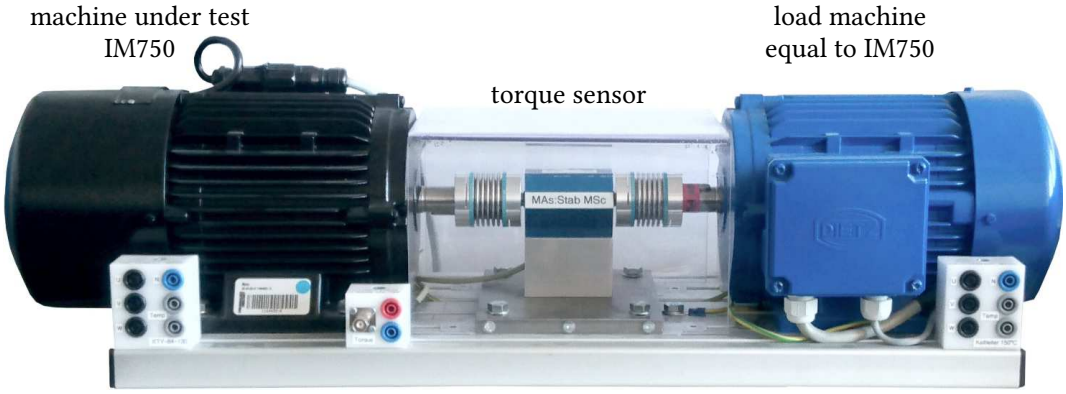

Fig. A.3: Test Bench 2 with two 750 W IMs of type IM750 and TS10 torque sensor. The left machine is equipped with a 720 pulses incremental encoder.

automotive IMs with 15 kW rated power and 26 kW maximum power. IM26kA is delta-connected and mostly operated as the device under test (DUT), and IM26kB is in star connection and used as the load machine. Both machines are identical except for the winding configuration and the additional rotor temperature sensing in IM26kA.

Test Bench 2 in Fig. A.3 is a reduced power configuration with two identical 750 W IMs. The black machine IM750 on the left is equipped with a 720 pulses incremental encoder, whereas the blue on the right has a fan for cooling, instead. Both test benches are equipped with the same type of torque transducer. Further details on the test bench components are given in the following.

A.2.1 Induction Machines under Test

The nameplate data of the three IMs used in this work are given in Fig. A.4. IM26kA is the traction machine of the first-generation StreetScooter vehicle series production. Its

(a) IM26kA (b) IM26kB (c) IM750

Fig. A.4: Nameplate data of the investigated IMs.

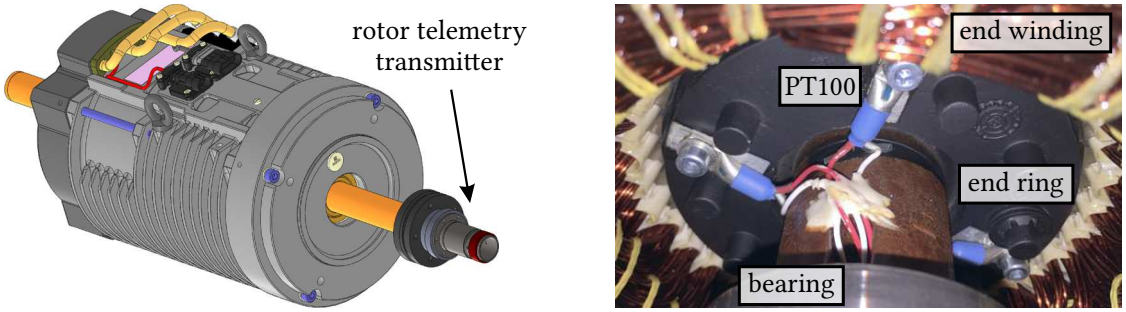

(a) CAD model of IM26kA with rotor telemetry (b) locations of the PT100 rotor-temperature sensors

Fig. A.5: IM26kA is equipped with four PT100 temperature sensors screwed to the aluminum rotor end ring in steps of 90°.

TABLE A.2
IM26kA Datasheet Values

quantity	symbol	unit	max. torque	rated power	max. speed
speed	n_m	rpm	2460	5140	8000
torque	T_m	N m	100	27.87	11.94
mech. power	P_m	kW	25.76	15	10
RMS current[(i)]	I_RMS	A	293.3	161.3	111.8
power factor[(i)]	$\cos\varphi$		0.82	0.86	0.84
efficiency[(i)]	η_im	%	86	86.8	85.5
RMS voltage	U_RMS	V	72	72	72
stator frequency	f_s	Hz	86	178	274
IEC duty cycle			S2 – 5 min	S2 – 30 min	S2 – 30 min

datasheet values are given in Table A.2. To fit the test bench, the 30 mm shaft has been lengthened and is exposed on both sides. Fig. A.5a shows the corresponding computer-aided design (CAD) model with attached transmitter for the rotor-temperature measurement. The IM is equipped with four PT100 temperature sensors attached to the end ring as depicted in Fig. A.5b. The sensors have been placed in cable shoes and screwed to the aluminum end ring by the manufacturer ABM Greiffenberger Antriebstechnik. The datasheet values of IM26kA are given in [ABM12].

IM26kB is a modified version of IM26kA. The number of turns has been reduced from six to four and the coils are now star-connected instead of delta-connected. The machines

[(i)]root mean square (RMS) current, power factor and efficiency are estimated values [ABM12].

TABLE A.3
Induction Machine Model Parameters

parameter	symbol	unit	IM26kA	IM26kB	IM750
number of pole pairs	p		2	2	2
stator resistance	$R_\mathrm{s}(20\,^\circ\mathrm{C})$	mΩ	6.25	8.3	195
stator temperature coefficient	α_{20}	$10^{-3}\,\mathrm{K}^{-1}$	3.5	3.5	
rotor resistance	$R_\mathrm{r}(80\,^\circ\mathrm{C})$	mΩ	7.5	7.5	100
stator leakage inductance	$L_{\sigma\mathrm{s}}$	µH	31.3	44.7	650
rotor leakage inductance	$L_{\sigma\mathrm{r}}$	µH	35	35	650
unsaturated stator inductance	$L_{\mathrm{s}1}$	mH	0.948	1.246	12.13
saturation model factor	$l_{\mathrm{s}2}$	$\mathrm{mH\,(V\,s)}^{-e_{\mathrm{s}2}}$	783.5	560.8	147.2
saturation model exponent	$e_{\mathrm{s}2}$		3.437	3.42	1.851
Steinmetz equation factor	k_fe	$\mathrm{W\,s}^{a_\mathrm{fe}}\,\mathrm{(V\,s)}^{-b_\mathrm{fe}}$	1.777	0.399	0.479
Steinmetz equation exponent	a_fe		1.305	1.43	1.168
Steinmetz equation exponent	b_fe		1.592	1.541	1.69
maximum stator current	$i_{\mathrm{s},\max}$	A	420	420	20.5
number of encoder pulses			64	64	720
winding configuration			delta	star	star

are not fully interchangeable as IM26kB requires a 15.5 % higher DC-link voltage to cover the same operating range. Since with Test Bench 1 both drives share the same DC-link, the maximum achievable torque in the field-weakening region of IM26kA is always higher than with IM26kB. Other than that, both machines are identical.

IM750 is a standard 750 W IM used for both drives in Test Bench 2. The winding configuration has been modified to fit a DC-link voltage of 85 V. The reduced-power test bench is beneficial for the first experimental evaluation and implementation of new control algorithms. All implemented functions have been evaluated using IM750 before they were tested on the final target IM26kA.

The components of the extended nonlinear IM model according to Section 2.1.3 have been parameterized in experiments. The resulting parameters for the three machines are given in Table A.3.

A.2.2 Inverters under Test

For the integration of two IM drives at the rear axle of the StreetScooter C16, in the project MAs:Stab, a compact and sealed 40 kW VSI was required, that is compatible to the 120 V battery system. As the commercially available SKAI 120V MOSFET inverter from Semikron fulfills these requirement, it was chosen as the basis for the inverter developed in this work. The system is equipped with a single PCB which includes the controller, the communication interfaces, the gate drivers and all other electronics. Since in this work a new and more-advanced control algorithm was implemented, a freely programmable, higher-performance microcontroller was needed. Therefore, the original PCB was replaced

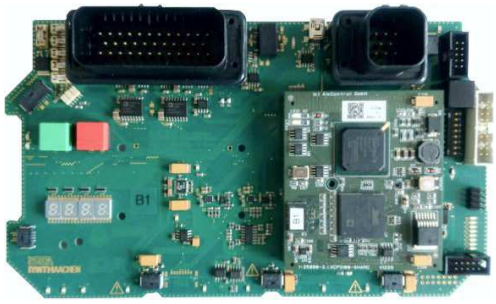

(a) main controller board, front

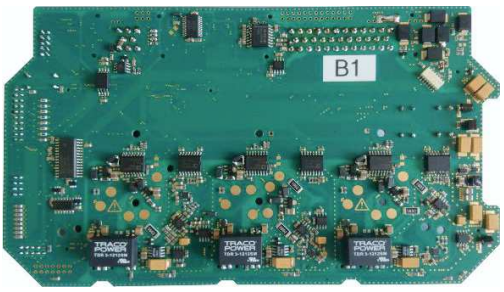

(b) main controller board, back

(c) Inverter 1

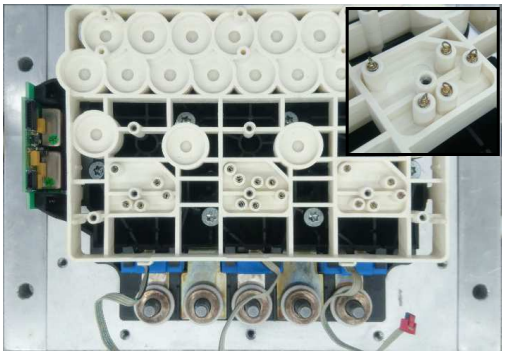

(d) gate-driver contacts of Inverter 1

(e) Inverter 2

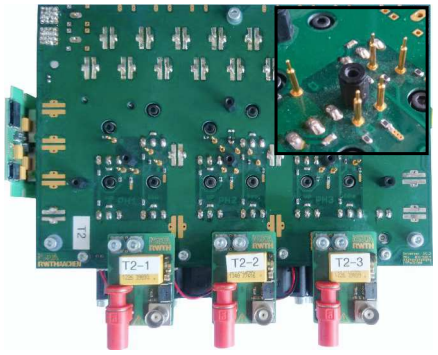

(f) gate-driver contacts of Inverter 2

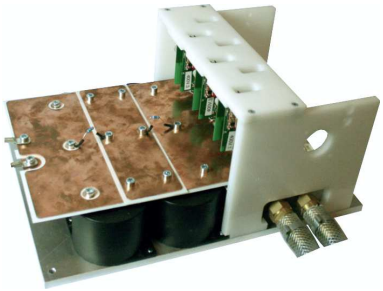

(g) Inverter 3

(h) control rack of Inverter 3

Fig. A.6: VSIs developed and used for testing in this work. All systems are equipped with instantaneous output voltage sensing and use the same software developed in this work.

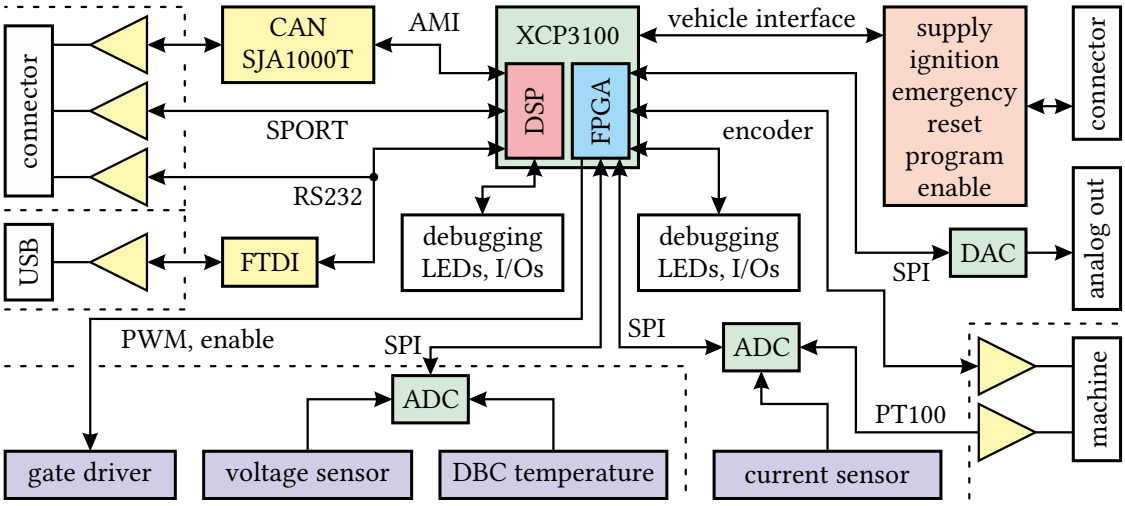

Fig. A.7: Simplified structure of the developed inverter control and driver PCB.

by a newly developed controller and driver board.

Fig. A.6d shows the opened SKAI 120V VSI with removed PCB. The remaining unit is equivalent to a B6 power module with attached DC-link capacitor and current sensors. The power MOSFETs are contacted via springs pushing on pads on the controller board, as shown in Fig. A.6b. The structure of the developed six-layer PCB is given in Fig. A.7. Beside communication, encoder and current sensor interfaces, it contains gate-driver-integrated voltage measurement circuits for the instantaneous phase-voltage sensing. The central component is the controller platform XCP3100 from AixControl, which – together with the new PCB – fits into the original, sealed housing of the SKAI 120V inverter. The resulting liquid-cooled VSI is depicted in Fig. A.6c and is referred to as Inverter 1. Both machines of Test Bench 1 are driven by this system.

For software implementation and initial testing, it is often beneficial to use a test environment of reduced voltage and reduced power. This is why for Test Bench 2, the air-cooled Inverter 2, given in Fig. A.6e, was developed. The system is based on discrete MOSFETs and uses the same controller and driver board as Inverter 1. Instead of springs, the gate drivers are connected via pogo pins, as shown in Fig. A.6f.

After project completion, the MAs:Stab inverter system was adapted for higher voltages up to 800 V. In this work, it was used for verification of the voltage-sensing circuit at 400 V. It is equipped with the same controller platform and software and is referred to as Inverter 3. Fig. A.6g shows a photograph of the system. More detailed information about the inverters used in this work can be found in Table A.4.

A.2.3 Measuring Equipment

As this work focuses on the torque accuracy of IM drives, the accuracy of the torque sensors used for experimental verification must be considered. Fig. A.8 shows the torque

TABLE A.4
INVERTER DATA

Values @ 25 °C	Inverter 1	Inverter 2	Inverter 3
semiconductor device	SKAI 120V	2× IRFP4668 (parallel)	SKM 600GB066D
device manufacturer	Semikron	Infineon	Semikron
max. blocking voltage	200 V	200 V	600 V
max. RMS phase current	385 A	260 A	760 A
'on'-state resistance $R_{\mathrm{ds,on}}$	2.4 mΩ (MOSFET)	4 mΩ (MOSFET)	0.9 mΩ (IGBT)
forward voltage drop	0.58 V @ 240 A	0.32 V @ 81 A	1.45 V @ 600 A
body-diode voltage drop	0.88 V @ 240 A	1.3 V @ 81 A	1.4 V @ 600 A
DC-link voltage	120 V	75 V	400 V
PWM switching frequency	10 kHz	10 kHz	10 kHz
dead time	2.5 µs	3.15 µs	3 µs
current sensor type	LEM HAFS 600	CDS4015ABC	LEM HO 250-P
sensor bandwidth	50 kHz (−3 dB)	400 kHz (−1 dB)	100 kHz (−3 dB)
sensor nom. RMS current	600 A	15 A	250 A
voltage sensor resolution	10 mV	10 mV	80 mV
sensor measuring range	−1.5 V to 166.5 V	−1.5 V to 166.5 V	−10 V to 1300 V
sampling frequency	1 MHz	1 MHz	1 MHz
control platform	AixControl XCP3100	AixControl XCP3100	AixControl XCP3100

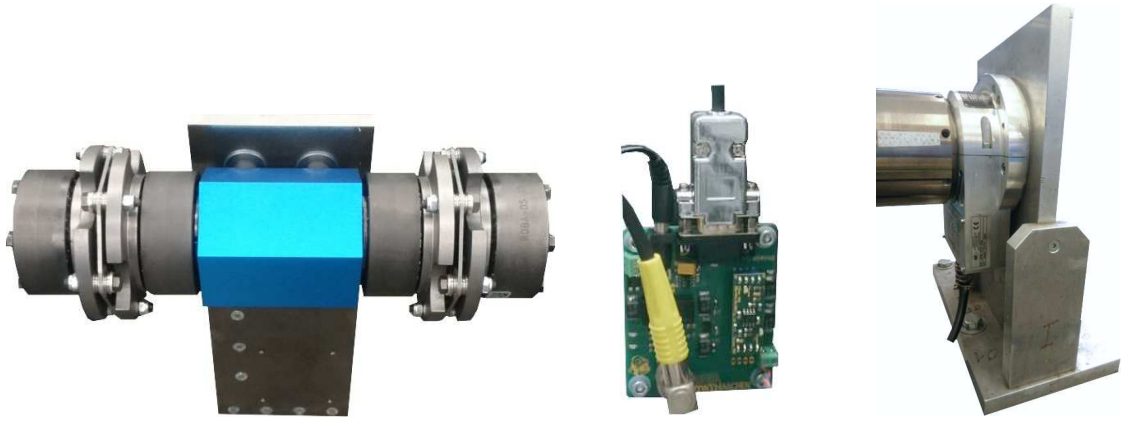

(a) TS200 with couplings (b) supply and filter (c) TS290

Fig. A.8: Torque sensors used in this work. TS200 is used in Test Bench 1 and is of the same type as TS10 used in Test Bench 2. The Experimental results given in Chapter 4 were recorded with TS290.

TABLE A.5
TORQUE-SENSOR SPECIFICATIONS

quantity	unit	TS290	TS200	TS10
brand		GIF	Lorenz Messtechnik	Lorenz Messtechnik
type		FLFMI1–290	DR–2477	DR–2477
nominal torque	N m	±290	±200	±10
output signal	V	CAN	±10	±10
accuracy class	%	0.1	0.25	0.25

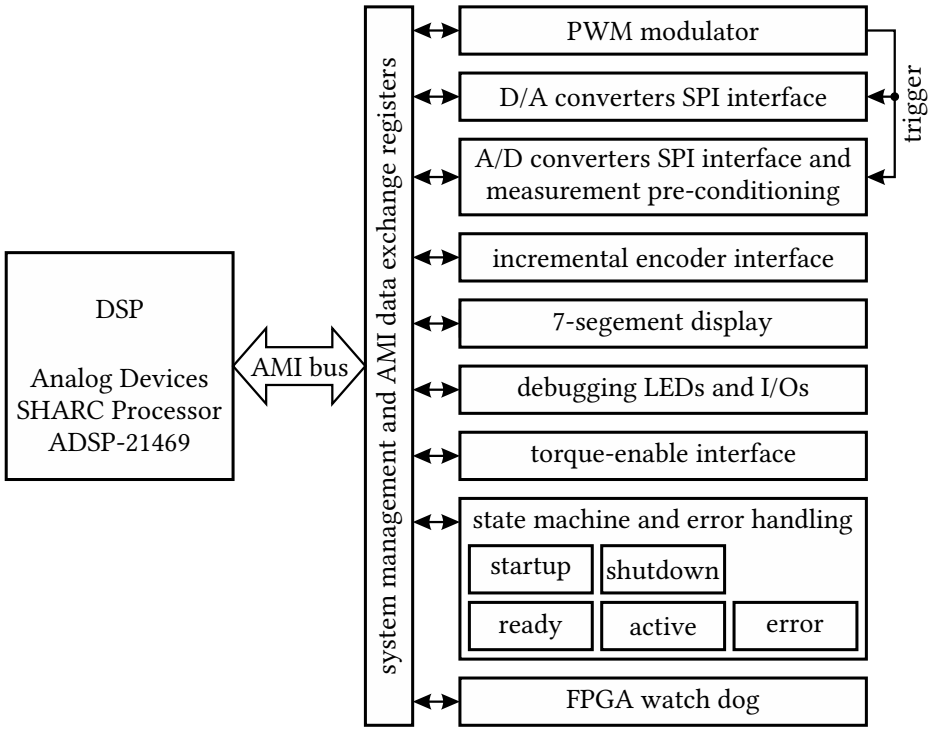

Fig. A.9: Simplified structure of the FPGA functional components implemented in VHDL.

sensors used in this work. Detailed information is given in Table A.5. TS200 and TS10 are cost effective torque sensors of the type DR-2477 from Lorenz Messtechnik. Both have a ±10 V analog output. To optimize the signal quality, the dedicated noise-suppressing voltage supply given in Fig. A.5 was developed. It offers an plug-in interface for additional active filters. However, all experimental results given in this work were recorded using the high-precision torque sensor TS290 shown in Fig. A.8c.

A.3 Inverter Control Framework

Introducing a new control platform, such as the AixControl XCP3100, at ISEA comes along with a lot of necessary software development. Besides the actual control procedure, the majority of the code belongs to measurement-data acquisition, error handling, safety features, communication interfaces and other supporting functions. However, it also gives the opportunity to implement new features, such as the instantaneous phase voltage measurement, and to develop a flexible testing environment that also allows safe and reliable operation within an electric vehicle.

The XCP3100 controller board is equipped with an Analog Devices SHARC Processor (ADSP-21469) and a XILINX Spartan-6 (XC6SLX45) FPGA, which communicate through an AMI-bus using memory registers implemented on the FPGA, as illustrated in Fig. A.9. A brief description of the DSP and FPGA software structure is given in the following.

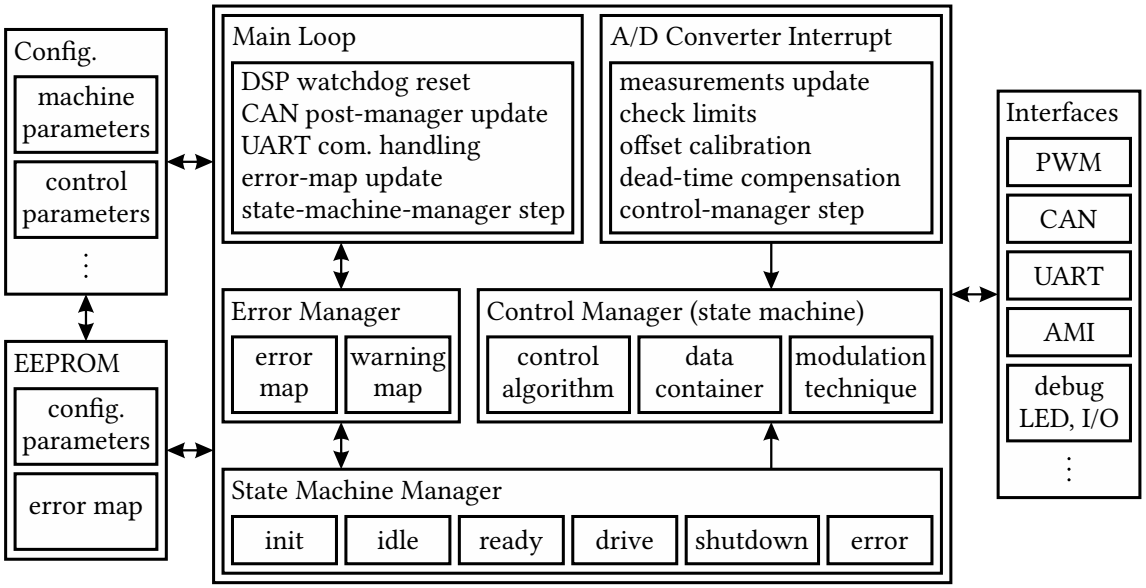

Fig. A.10: Simplified structure of the DSP functional components implemented in C++.

A.3.1 Structure of the FPGA Framework

Since the DSP does not offer a PWM unit or analog input/outputs (I/Os), these functions must be provided externally. Therefore, the PWM modulator has been implemented in the FPGA. A/D and D/A converters are integrated using dedicated SPI interfaces implemented on the FPGA. In the same unit, the switching-period averaging of the sampled signals for the instantaneous output voltage sensing is performed. The incremental encoder of the IM is connected to an FPGA block, where position and speed is directly calculated.

The FPGA contains a dedicated state machine, which controls the signals of the vehicle interface described in Fig. A.7 and enables or disables the gate drivers and FPGA functional units described above. For debugging, unused pins have been connected to 7-segment displays and status light-emitting diodes (LEDs). 16 additional I/Os are available for extension of the system. For example, based on Inverter 2, an NPC inverter has been built, where six additional gate drives were connected.

A.3.2 Structure of the DSP Framework

The structure of the implemented DSP software framework is given in Fig. A.10. One of the main components is the main loop where the communication via CAN and universal asynchronous receiver transmitter (UART) is managed. Furthermore, the state machine and the error map stored in the error manager are updated. During initialization, the configuration parameters of the system are loaded from an external electrically erasable programmable read-only memory (EEPROM) into the internal memory. Additionally, error codes written to the EEPROM during a former system halt are loaded. This way, debugging is possible even if the system was stopped due to a communication error.

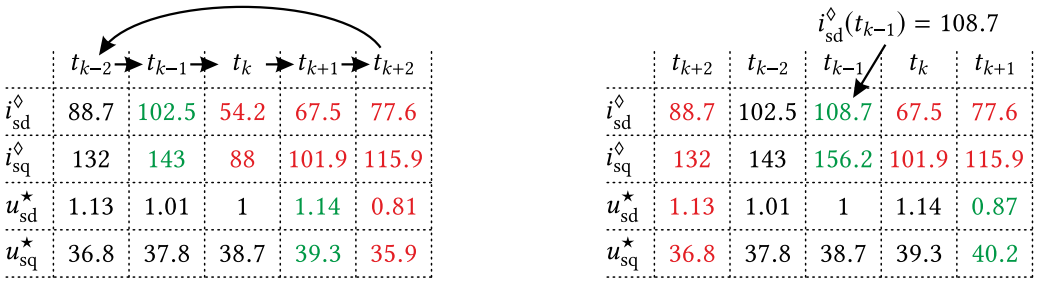

	t_{k-2}	t_{k-1}	t_k	t_{k+1}	t_{k+2}
$i^{\Diamond}_{\mathrm{sd}}$	88.7	102.5	54.2	67.5	77.6
$i^{\Diamond}_{\mathrm{sq}}$	132	143	88	101.9	115.9
$u^{\star}_{\mathrm{sd}}$	1.13	1.01	1	1.14	0.81
$u^{\star}_{\mathrm{sq}}$	36.8	37.8	38.7	39.3	35.9

(a) previous time step

	t_{k+2}	t_{k-2}	t_{k-1}	t_k	t_{k+1}
$i^{\Diamond}_{\mathrm{sd}}$	88.7	102.5	108.7	67.5	77.6
$i^{\Diamond}_{\mathrm{sq}}$	132	143	156.2	101.9	115.9
$u^{\star}_{\mathrm{sd}}$	1.13	1.01	1	1.14	0.87
$u^{\star}_{\mathrm{sq}}$	36.8	37.8	38.7	39.3	40.2

(b) current time step

Fig. A.11: Concept of the time-resolved data container. All variables used in the control loop are stored in the data container, which simplifies access to previous samples. It also serves as an interface to the simulation environment and allows flexible access to internal control variables for debugging during operation on the test bench. New values are green, invalid are red.

The major control task is performed within the interrupt routine, triggered by the A/D converters. First the measurement samples stored in the FPGA registers are loaded before they are checked and a warning or error is triggered if the safety current and voltage limits are exceeded. Then the online offset-calibration algorithm is executed and the dead time related voltage error is compensated. The actual control is executed during a control-manager step. The control manager is a state machine that handles the switching between different control strategies, such as FOC, DB-DTFC and direct torque control (DTC). Furthermore, the modulation strategy can be chosen between sine-triangle modulation, SVM and third-harmonic injection.

The majority of variables used by the control algorithm is stored in a time-resolved data container as described in Fig. A.11. Each variable is assigned 5 values, which belong to consecutive time steps. This allows convenient discrete-time implementation of the observers and controllers. For example, the measured current recorded during the previous time interval is assigned to time instant t_{k-1} whereas the calculated reference voltage for the future PWM period is written to t_{k+1}. The time assignment is realized using pointers that are shifted each step, as illustrated in the figure.

Furthermore, the data container is used as an interface to the MATLAB/Simulink simulation. This way each variable is accessible and can be analyzed during debugging of the C++ code. On the test bench, a limited number of data-container variables can be simultaneously accessed via CAN and UART by choosing from a drop down list during operation. Alternatively, they can be routed to the D/A converters.

A.4 Software-in-the-Loop Simulation Model

For control implementation and debugging, a software-in-the-loop simulation model has been implemented in MATLAB/Simulink, which precisely emulates the behavior of the crucial system components. Therefore, the IM drive has been modeled using the extended

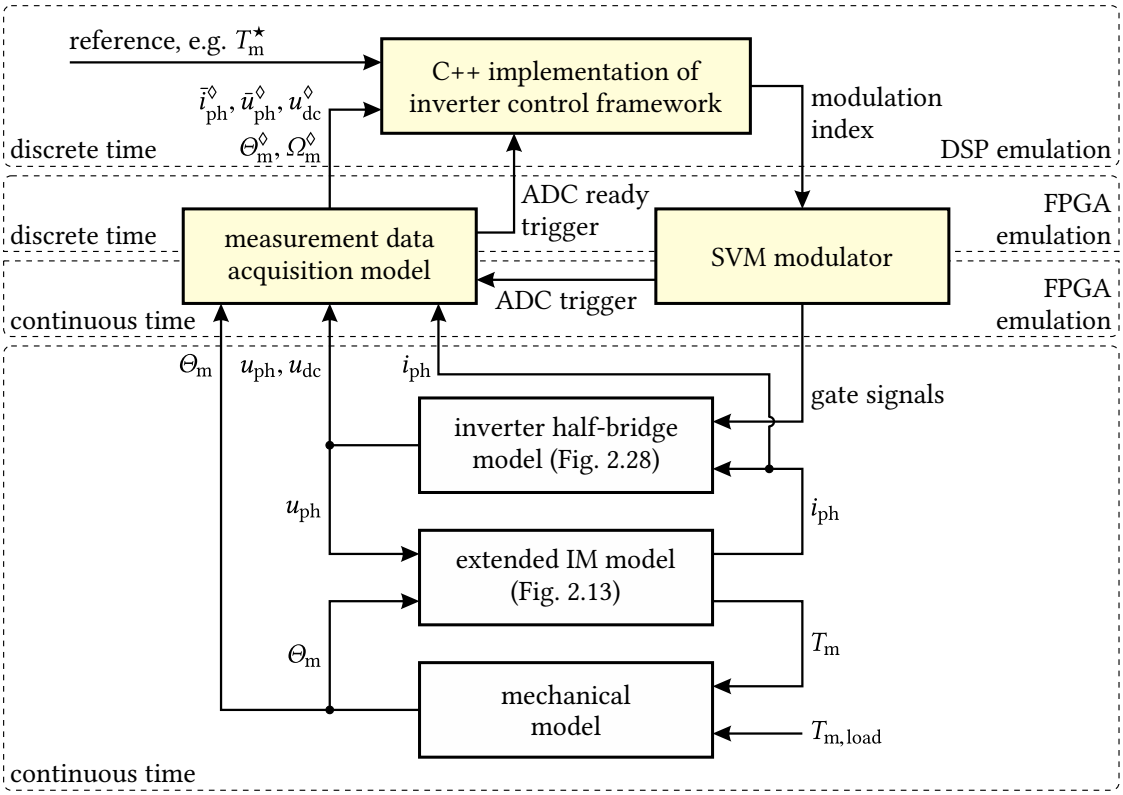

Fig. A.12: Simplified signal-flow diagram of the software in the loop simulation model.

IM model introduced in Section 2.1.3 and the inverter half-bridge model according to Section 2.3.1. Both components and a simple mechanical model are simulated using a continuous-time solver, as illustrated in Fig. A.12.

The SVM modulator and the current- and voltage-sensing circuits, including sampling and the FPGA post-processing, are also modeled in MATLAB/Simulink. Identical to the real system, they represent the interface between the continuous-time and the discrete-time domain. Modeling these components is crucial for accurate simulation and implementation of discrete-time control algorithms with proper discretization. The control algorithm is implemented in C++ and is inserted as a MATLAB/Simulink s-function. By including the DSP framework, the simulation model can be used for evaluation and debugging of the microcontroller software. This way, the majority of software bugs can be removed in a very early stage during simulation, which significantly accelerates the software development process.

A.5 Observer Gain Selection

The observer gain matrix $\boldsymbol{K}$ of the full-order stator flux-linkage observer is selected based on the pole placement of the observer poles $\hat{s}_{pn}$ in the complex s-plane. To ensure stability, the observer must converge faster than the IM, which means that the observer poles must

be located to the left of the IM poles $s_{\mathrm{p}n}$ [DB11, pp. 847–856]. In the following, mathematical expressions to determine the coefficients of the feedback gain matrix

$$\boldsymbol{K} = \begin{bmatrix} k_1\mathbf{I} + k_2\mathbf{J} \\ k_3\mathbf{I} + k_4\mathbf{J} \end{bmatrix} \tag{A.9}$$

are given for the proportional and the left-shift pole-placement methods described in Section 3.2.2.1.

A.5.1 Proportional Observer Pole Placement

A stable observer which converges faster than the IM dynamics can be achieved by placing the observer poles proportionally to the IM poles with

$$\hat{s}_{\mathrm{p}n} = g \cdot s_{\mathrm{p}n}. \tag{A.10}$$

The factor $g > 1$ defines the scaling of the observer poles in relation to the IM poles.

The resulting observer gains for the full-order observer in Section 3.2.2, with $\hat{\vec{\psi}}_{\mathrm{s}}$ and $\hat{\vec{\psi}}_{\mathrm{r}}$ as state variables, can be found by solving Equation (A.10) with (2.11) and (3.16) for the observer gains. After some mathematics the coefficients of $\boldsymbol{K}$ are obtained as

$$\begin{aligned} k_1 &= \left(g^2 - 1\right) \cdot \hat{R}_{\mathrm{s}}, & k_2 &= 0, \\ k_3 &= (g-1) \cdot \frac{g \cdot \hat{R}_{\mathrm{s}}\hat{L}_{\mathrm{r}} - \hat{R}_{\mathrm{r}}\hat{L}_{\mathrm{s}}}{\hat{L}_{\mathrm{m}}} \quad \text{and} & k_4 &= (g-1) \cdot \omega_{\mathrm{m}} \frac{\hat{\sigma}\hat{L}_{\mathrm{s}}\hat{L}_{\mathrm{r}}}{\hat{L}_{\mathrm{m}}}. \end{aligned} \tag{A.11}$$

A.5.2 Left Shift Observer Pole Placement

The proportional pole-placement method can lead to observer poles with large imaginary part. This can cause instability in digital implementation. To overcome this problem, [MM00] suggests an alternative pole placement which shifts the poles to the left according to

$$\hat{s}_{\mathrm{p}n} = s_{\mathrm{p}n} - g \cdot \frac{\hat{R}_{\mathrm{s}}\hat{L}_{\mathrm{r}} + \hat{R}_{\mathrm{r}}\hat{L}_{\mathrm{s}}}{\hat{\sigma}\hat{L}_{\mathrm{s}}\hat{L}_{\mathrm{r}}}. \tag{A.12}$$

The resulting coefficients of the feedback-gain matrix $\boldsymbol{K}$ are derived with the help the rotor angular-frequency-dependent auxiliary variable

$$f = \frac{(g+1) \cdot \dfrac{\hat{R}_{\mathrm{s}}\hat{L}_{\mathrm{r}} + \hat{R}_{\mathrm{r}}\hat{L}_{\mathrm{s}}}{\hat{\sigma}\hat{L}_{\mathrm{s}}\hat{L}_{\mathrm{r}}} - \dfrac{\hat{R}_{\mathrm{r}}}{\hat{L}_{\mathrm{r}}}}{\omega_{\mathrm{m}}^2 + \dfrac{\hat{R}_{\mathrm{r}}^2}{\hat{L}_{\mathrm{r}}^2}} \tag{A.13}$$

and are equal to

$$\begin{aligned} k_1 &= g \cdot \hat{R}_\mathrm{s}\left(1 + \frac{\hat{R}_\mathrm{r}\hat{L}_\mathrm{s}}{\hat{R}_\mathrm{s}\hat{L}_\mathrm{r}}\right)\left(1 + \frac{\hat{R}_\mathrm{r}}{\hat{L}_\mathrm{r}}f\right), & k_2 &= g \cdot \omega_\mathrm{m}\hat{R}_\mathrm{s}\left(1 + \frac{\hat{R}_\mathrm{r}\hat{L}_\mathrm{s}}{\hat{R}_\mathrm{s}\hat{L}_\mathrm{r}}\right)f, \\ k_3 &= -g \cdot \hat{R}_\mathrm{s}\frac{\hat{L}_\mathrm{r}}{\hat{L}_\mathrm{m}}\left(1 + \frac{\hat{R}_\mathrm{r}\hat{L}_\mathrm{s}}{\hat{R}_\mathrm{s}\hat{L}_\mathrm{r}}\right)\left(1 - \frac{\hat{R}_\mathrm{r}}{\hat{L}_\mathrm{r}}f\right) \quad \text{and} & k_4 &= g \cdot \omega_\mathrm{m}\hat{R}_\mathrm{s}\frac{\hat{L}_\mathrm{r}}{\hat{L}_\mathrm{m}}\left(1 + \frac{\hat{R}_\mathrm{r}\hat{L}_\mathrm{s}}{\hat{R}_\mathrm{s}\hat{L}_\mathrm{r}}\right)f. \end{aligned} \tag{A.14}$$

Unlike the previous case, the left-shift pole placement leads to constant dynamic behavior of the observer. All parameters are speed dependent, which requires more computational effort.

A.5.3 Proportional Observer Pole Placement with Rotation

In addition to the proportional gain in (A.10), [Gri+01] proposes to rotate the poles by a constant angle γ to ensure stability at higher speeds. However, this can lead to undesired poles at low speeds. To overcome this, in [GŽ10], this approach is improved by a speed-variable angle. The observer poles are then defined by

$$\hat{s}_{\mathrm{p}n} = \underline{g} \cdot s_{\mathrm{p}n} \quad \text{with} \quad \underline{g} = g_\mathrm{r} + \mathrm{j}g_\mathrm{i} = g\mathrm{e}^{\mathrm{j}\gamma}. \tag{A.15}$$

The coefficients of the feedback-gain matrix $\boldsymbol{K}$ are derived analogously to Appendix A.5.1, which leads to

$$\begin{aligned} k_1 &= \left(g_\mathrm{r}^2 - 1\right) \cdot \hat{R}_\mathrm{s} - g_\mathrm{i}^2 \cdot \hat{R}_\mathrm{s}, \\ k_2 &= 2g_\mathrm{r}g_\mathrm{i} \cdot \hat{R}_\mathrm{s}, \\ k_3 &= (g_\mathrm{r} - 1) \cdot \frac{g_\mathrm{r} \cdot \hat{R}_\mathrm{s}\hat{L}_\mathrm{r} - \hat{R}_\mathrm{r}\hat{L}_\mathrm{s}}{\hat{L}_\mathrm{m}} - g_\mathrm{i} \cdot \frac{g_\mathrm{i} \cdot \hat{R}_\mathrm{s}\hat{L}_\mathrm{r} + \omega_\mathrm{m}\hat{\sigma}\hat{L}_\mathrm{s}\hat{L}_\mathrm{r}}{\hat{L}_\mathrm{m}}, \\ \text{and} \quad k_4 &= (g_\mathrm{r} - 1) \cdot \omega_\mathrm{m}\frac{\hat{\sigma}\hat{L}_\mathrm{s}\hat{L}_\mathrm{r}}{\hat{L}_\mathrm{m}} + g_\mathrm{i} \cdot \frac{(2g_\mathrm{r} - 1) \cdot \hat{R}_\mathrm{s}\hat{L}_\mathrm{r} - \hat{R}_\mathrm{r}\hat{L}_\mathrm{s}}{\hat{L}_\mathrm{m}}. \end{aligned} \tag{A.16}$$

A.6 Special Case: Two Current Sensors

In Section 4.1.2, the robustness of the observer against measurement-feedback distortion is analyzed assuming that each phase is equipped with its own sensors. However, in common three-phase inverter systems, only two current sensors are available. The third current is then calculated from the other two currents as

$$i_{\mathrm{ph}3}^{\Diamond} = -\left(i_{\mathrm{ph}1}^{\Diamond} + i_{\mathrm{ph}2}^{\Diamond}\right). \tag{A.17}$$

Using the Clarke transformation (A.1) and with the help of the addition theorems for trigonometric functions, the real and imaginary parts of the measured stator-current space

vector are now found as

$$\begin{aligned} i_{\mathrm{s}\alpha}^{\diamondsuit} &= g_{\mathrm{ph1}} i_{\mathrm{s}} \cos(\omega_{\mathrm{s}} t) \\ \text{and} \quad i_{\mathrm{s}\beta}^{\diamondsuit} &= g_{\mathrm{ph2}} i_{\mathrm{s}} \sin(\omega_{\mathrm{s}} t) + \frac{g_{\mathrm{ph1}} - g_{\mathrm{ph2}}}{\sqrt{3}} i_{\mathrm{s}} \cos(\omega_{\mathrm{s}} t) + \frac{i_{\mathrm{ph1,off}} + 2 i_{\mathrm{ph2,off}}}{\sqrt{3}}. \end{aligned} \tag{A.18}$$

By expanding the trigonometric terms and after some rearrangements, the measured current can be written in polar form as

$$\begin{aligned} \vec{i}_{\mathrm{s}}^{\,\diamondsuit} = & \underbrace{\left(\frac{g_{\mathrm{ph1}} + g_{\mathrm{ph2}}}{2} - \mathrm{j} \frac{g_{\mathrm{ph1}} - g_{\mathrm{ph2}}}{2\sqrt{3}} \right)}_{\text{balanced error } \vec{i}_{\mathrm{s,pos}}^{\,\diamondsuit} / \vec{i}_{\mathrm{s}}} \underbrace{i_{\mathrm{s}} \mathrm{e}^{\mathrm{j}\omega_{\mathrm{s}} t}}_{\vec{i}_{\mathrm{s}}} + \underbrace{\left(\frac{g_{\mathrm{ph1}} - g_{\mathrm{ph2}}}{2} + \mathrm{j} \frac{g_{\mathrm{ph1}} - g_{\mathrm{ph2}}}{2\sqrt{3}} \right) i_{\mathrm{s}} \mathrm{e}^{-\mathrm{j}\omega_{\mathrm{s}} t}}_{\text{imbalanced sensor-gain error } \vec{i}_{\mathrm{s,neg}}^{\,\diamondsuit}} \\ & + \underbrace{i_{\mathrm{ph1,off}} + \mathrm{j} \frac{i_{\mathrm{ph1,off}} + 2 i_{\mathrm{ph2,off}}}{\sqrt{3}}}_{\text{sensor-offset error } \vec{i}_{\mathrm{s,off}}^{\,\diamondsuit}}. \end{aligned} \tag{A.19}$$

When comparing with (4.7), this result is similar to the three sensors case. The current space-vector can likewise be represented by a positive sequence, a negative sequence and an offset component. Thus, the considerations described in Section 4.1.2 are analogously valid for the case with two current sensors. But note, the positive sequence component experiences an additional angle error which also contributes to torque error and detuning.

A.7 MPC Prediction Matrices

In this work, the MPC algorithm is applied using the IM model in state-space representation. This way, the future system states up to the prediction horizon N_{p} are obtained by

$$\begin{bmatrix} \hat{\boldsymbol{x}}(t_{k+1}) \\ \hat{\boldsymbol{x}}(t_{k+2}) \\ \vdots \\ \hat{\boldsymbol{x}}(t_{k+N_{\mathrm{p}}}) \end{bmatrix} = \begin{bmatrix} \boldsymbol{A} \\ \boldsymbol{A}^2 \\ \vdots \\ \boldsymbol{A}^{N_{\mathrm{p}}} \end{bmatrix} \hat{\boldsymbol{x}}(t_k) + \begin{bmatrix} \boldsymbol{B} & \boldsymbol{0} & \boldsymbol{0} & \cdots \\ \boldsymbol{AB} & \boldsymbol{B} & \boldsymbol{0} & \cdots \\ \vdots & \vdots & \vdots & \vdots \\ \boldsymbol{A}^{N_{\mathrm{p}}-1}\boldsymbol{B} & \boldsymbol{A}^{N_{\mathrm{p}}-2}\boldsymbol{B} & \boldsymbol{A}^{N_{\mathrm{p}}-3}\boldsymbol{B} & \cdots \end{bmatrix} \begin{bmatrix} \hat{\boldsymbol{u}}(t_k) \\ \hat{\boldsymbol{u}}(t_{k+1}) \\ \vdots \\ \hat{\boldsymbol{u}}(t_{k+N_{\mathrm{p}}-1}) \end{bmatrix} \tag{A.20}$$

[Ros04, p. 32]. The future system outputs are then calculated using

$$\underbrace{\begin{bmatrix} \hat{\boldsymbol{y}}(t_{k+1}) \\ \hat{\boldsymbol{y}}(t_{k+2}) \\ \vdots \\ \hat{\boldsymbol{y}}(t_{k+N_{\mathrm{p}}}) \end{bmatrix}}_{\boldsymbol{y}_{\mathrm{p}}} = \underbrace{\begin{bmatrix} \boldsymbol{CA} \\ \boldsymbol{CA}^2 \\ \vdots \\ \boldsymbol{CA}^{N_{\mathrm{p}}} \end{bmatrix}}_{\boldsymbol{P}_{\mathrm{p}}} \hat{\boldsymbol{x}}(t_k) + \underbrace{\begin{bmatrix} \boldsymbol{CB} & \boldsymbol{D}(t_{k+1}) & \boldsymbol{0} & \cdots \\ \boldsymbol{CAB} & \boldsymbol{CB} & \boldsymbol{D}(t_{k+2}) & \cdots \\ \vdots & \vdots & \vdots & \vdots \\ \boldsymbol{CA}^{N_{\mathrm{p}}-1}\boldsymbol{B} & \boldsymbol{CA}^{N_{\mathrm{p}}-2}\boldsymbol{B} & \boldsymbol{CA}^{N_{\mathrm{p}}-3}\boldsymbol{B} & \cdots \end{bmatrix}}_{\boldsymbol{H}_{\mathrm{p}}} \underbrace{\begin{bmatrix} \hat{\boldsymbol{u}}(t_k) \\ \hat{\boldsymbol{u}}(t_{k+1}) \\ \vdots \\ \hat{\boldsymbol{u}}(t_{k+N_{\mathrm{p}}-1}) \end{bmatrix}}_{\boldsymbol{u}_{\mathrm{p}}}. \tag{A.21}$$

$\boldsymbol{H}_\mathrm{p}$ and $\boldsymbol{P}_\mathrm{p}$ are the corresponding prediction matrices, and $\boldsymbol{u}_\mathrm{p}$ and $\boldsymbol{y}_\mathrm{p}$ the vectors of future inputs and outputs.

The weighting factors in matrix notation are defined according to [Di 97] as

$$\boldsymbol{Q}'_\mathrm{u} = \begin{bmatrix} \boldsymbol{Q}_\mathrm{u} & \mathbf{0} & \cdots & \mathbf{0} \\ \mathbf{0} & \boldsymbol{Q}_\mathrm{u} & \cdots & \mathbf{0} \\ \vdots & \vdots & \ddots & \vdots \\ \mathbf{0} & \mathbf{0} & \cdots & \boldsymbol{Q}_\mathrm{u} \end{bmatrix} \quad \text{and} \quad \boldsymbol{Q}'_\mathrm{y} = \begin{bmatrix} \boldsymbol{Q}_\mathrm{y} & \mathbf{0} & \cdots & \mathbf{0} \\ \mathbf{0} & \boldsymbol{Q}_\mathrm{y} & \cdots & \mathbf{0} \\ \vdots & \vdots & \ddots & \vdots \\ \mathbf{0} & \mathbf{0} & \cdots & \boldsymbol{Q}_\mathrm{y} \end{bmatrix}. \tag{A.22}$$

List of Abbreviations

AC	alternating current 100
ACC	adaptive cruise control 1, 5, 29
A/D	analog-to-digital 53, 100–102, 108–110, 114, 130, 131, 133, 137, 140, 161, 170, 172–174, 199
ADAS	advanced driver-assistance systems 1, 5, 156
AMI	asynchronous memory interface 53, 170, 172, 173
B6	six-pulse bridge 5, 112, 134, 159, 170
CAD	computer-aided design 167
CAN	controller area network 3, 4, 122, 146, 147, 170, 171, 173, 174
D/A	digital-to-analog 122, 170, 172–174
DB-DTFC	dead-beat direct torque and flux control 1, 174
DBC	direct bonded copper 130, 132–135, 170, 200
DC	direct current 17, 18, 26, 29, 38, 46, 81, 91, 98–100, 106, 108–110, 112, 114, 118, 130–134, 140, 158, 159, 168, 170, 171, 199, 200
DSP	digital signal processor v, 53, 94, 108, 129, 130, 137, 144, 170, 172, 173, 175, 202
DTC	direct torque control 174
DUT	device under test 166
EEPROM	electrically erasable programmable read-only memory 173
EMF	electromotive force 42, 45, 57, 94, 97, 117, 137, 140, 158
ESC	electronic stability control 2, 5, 156
EV	electric vehicle 1, 2, 146, 156, 157
FEM	finite element method 16, 21, 22, 93, 195
FOC	field-oriented control 1, 5, 7, 25–28, 30, 35, 41, 42, 59, 61, 62, 75, 94, 138, 140, 142, 148, 156, 158, 159, 174, 195, 201
FOH	first-order hold 56, 197

FPGA field-programmable gate array v, 53, 108, 110, 112, 129–131, 140, 170, 172–175, 202

I/O input/output 170, 172, 173
IC integrated circuit 109, 158, 161
IEC International Electrotechnical Commission 167
IEM Institut für Elektrische Maschinen
engl.: Institute of Electrical Machines 4, 21
IGBT insulated-gate bipolar transistor 40, 110, 112, 171
IM induction machine 5–7, 9–15, 18–25, 27, 28, 30, 33, 35, 37, 41–43, 45, 47, 48, 54, 55, 59–63, 65, 67–69, 72, 73, 75, 80, 82, 86–88, 91, 92, 94–97, 99, 137, 139, 141, 148, 156, 157, 159–161, 165–168, 170, 173–176, 178, 195–198, 201–203
IoT internet of things 1
IRTF ideal rotating transformer 10–12, 15, 22, 24, 165, 195
ISEA Institut für Stromrichtertechnik und Elektrische Antriebe
engl.: Institute for Power Electronics and Electrical Drives v, vi, 2, 4, 91, 172

LED light-emitting diode 170, 172, 173
LPF low-pass filter 6, 43, 44, 55–57, 81, 99, 100, 102, 103, 105–109, 111–114, 116, 121, 122, 124, 127, 131, 140, 141, 158, 199
LPTN lumped-parameter thermal network 92–96, 129, 158, 160, 198
LSB least-significant bit 112–114, 161

MABX dSPACE MicroAutoBox 3, 4, 146, 147
MAs:Stab Modularer Antriebsstrang: Stabilität bei Mehrfachantrieben
engl.: modular drive train: stability with multiple drives
Three-years project, funded by the German Federal Ministry for Economic Affairs and Energy 2, 3, 86, 141, 146, 168, 170, 195
MOSFET metal–oxide–semiconductor field-effect transistor 5, 7, 36–39, 41, 42, 82, 109, 110, 112, 130–136, 140, 159, 168, 170, 171, 196, 200, 203
MPC model-predictive control 6, 7, 142, 147–151, 156, 160, 161, 178, 201
MRAS model-reference adaptive system 52, 86–88, 90, 91, 96, 158, 198
MTPF maximum torque per flux linkage 34

NPC neutral-point clamped 108, 112, 173

PCB printed circuit board v, 110, 168, 170, 199, 202

PMSM	permanent-magnet synchronous machine 81, 91, 100
PWM	pulse-width modulation 36–40, 53, 54, 97, 98, 100–103, 107–112, 114, 118, 120, 125, 140, 158, 171–174, 199, 200
RFO	rotor field orientation 25–29, 51, 52, 141, 142, 144, 147, 148, 152–156, 195, 201
RMS	root mean square 167, 171
RWTH	Rheinisch-Westfälische Technische Hochschule (Aachen) engl.: RWTH Aachen University v, 2, 4
SFO	stator field orientation 25–28, 30, 33–35, 41, 43, 59, 94, 95, 142, 144, 146, 147, 150, 156, 195, 196, 201
SPI	serial peripheral interface 53, 108, 110, 130, 170, 172, 173
SPORT	synchronous serial peripheral port 170
SVM	space-vector modulation 105, 106, 114, 116, 174, 175
TV	torque vectoring 2, 5, 147, 156, 159
UART	universal asynchronous receiver transmitter 173, 174
USB	universal serial bus 170
VCO	voltage-controlled oscillator 101, 102
VCU	vehicle control unit 3, 4
VHDL	very high speed integrated hardware description language 53, 172, 202
VSI	voltage-source inverter 4–6, 9, 36, 39, 42, 82, 97–99, 101, 103, 106, 108, 112, 114–117, 131, 132, 134, 135, 138, 140, 141, 144, 150, 156, 158, 159, 168–170, 200, 202
ZOH	zero-order hold 55, 57, 197

List of Symbols

$\mathbf{0}$	zero matrix 13, 178, 179
α_{20}	temperature coefficient of the electrical resistance at 20 °C 18, 19, 133, 136, 168
δ	angle of the steady-state observer flux-linkage error 61–63, 65, 68, 69, 72, 73, 76–78, 89, 197, 198
$\varepsilon_{\measuredangle}$	flux-linkage angle adaptive error feedback 87, 90
ε_{ψ}	flux-linkage magnitude adaptive error feedback 87, 90
$\underline{\varepsilon}_{\mathrm{i}}$	phasor of the observer stator-current error feedback $\hat{\underline{i}}_{\mathrm{s}} - \underline{i}_{\mathrm{s}}^{\Diamond}$ 50–52
$\vec{\varepsilon}_{\mathrm{i}}$	space vector of the observer stator-current error feedback $\hat{\vec{i}}_{\mathrm{s}} - \vec{i}_{\mathrm{s}}^{\Diamond}$ 48, 50, 52
η_{im}	efficiency of the induction machine 167
$\Theta_{\mathrm{m}}^{\Diamond}$	measured value of the mechanical rotor angle 175
Θ_{m}	mechanical angle of the rotor 5, 12, 24, 175
$\hat{\vartheta}_{\mathrm{dbc}}$	estimated DBC temperature of the power module 136
$\vartheta_{\mathrm{dbc}}^{\Diamond}$	measured DBC temperature of the power module 132–135
$\hat{\vartheta}_{\mathrm{r}}$	estimated temperature of the IM rotor cage 92
ϑ_{r}	temperature of the IM rotor cage 18, 24, 28, 92
$\hat{\vartheta}_{\mathrm{s}}$	estimated temperature of the IM stator winding 92
$\vartheta_{\mathrm{s}}^{\Diamond}$	measured temperature of the IM stator winding 86
ϑ_{sc}	temperature of the semiconductor switch 39, 41, 196
ϑ_{s}	temperature of the IM stator winding 18, 24, 28, 92
ϑ_{th}	temperature of an LPTN element 93
$\theta_{\mathrm{m}}^{\Diamond}$	measured value of the electrical angle θ_{m} 5, 44–46, 50, 55–57
θ_{m}	electrical angle $p \cdot \Theta_{\mathrm{m}}$ of the rotor 11, 12, 24, 25
$\hat{\theta}_{\mathrm{s}}$	estimated field angle θ_{s} 26, 27, 61
θ_{s}	field angle to the direct axis of the ‘dq’-reference frame 25, 51, 52, 164, 165
$\hat{\sigma}$	estimated leakage factor 35, 43–46, 48, 50–52, 54–57, 83, 176, 177
σ	leakage factor $1 - L_{\mathrm{m}}^2/L_{\mathrm{s}}L_{\mathrm{r}}$ 12–14, 26, 28, 30–32, 34, 35, 44, 45, 61, 62
σ_{i}^2	variance of the measured current used for offset calibration 120
τ_{d}	time difference between the PWM voltage edge and the previous sampling point 103–105, 111, 199
$\hat{\tau}_{\mathrm{eq}}$	equivalent estimated time constant of the current predictor 56

τ_f time constant of the first-order analog in the voltage measurement circuit 100, 103–109, 199

$\hat{\tau}_\mathrm{r}$ estimated rotor time constant 35, 43–46, 48, 50–52, 55–57, 83

τ_r rotor time constant $L_\mathrm{r}/R_\mathrm{r}$ 25–28, 30, 31, 34, 35, 44, 45, 61, 62, 141, 148

φ_f phase shift of the phase voltage caused by the 100, 105

$\hat{\psi}_\mathrm{R}$ estimated value of the virtual rotor flux linkage magnitude ψ_R 147, 148, 152–156

$\psi_\mathrm{R}^\mathrm{ss}$ steady state value of the virtual rotor flux linkage magnitude ψ_R 148, 150, 151, 153

ψ_R virtual rotor flux linkage magnitude $L_\mathrm{m}/L_\mathrm{r}\psi_\mathrm{r}$ 143, 145, 148, 150, 151, 155

$\vec{\psi}_\mathrm{m}$ space vector of the main or mutual flux linkage 9–11, 15, 23–25

$\hat{\vec{\psi}}_\mathrm{r}$ space vector of the field-oriented rotor flux linkage estimate 51

$\vec{\psi}_\mathrm{r}^\mathrm{dq}$ space vector of the rotor flux linkage in a field-oriented reference frame 25, 26

$\hat{\psi}_\mathrm{r}$ estimated rotor flux linkage magnitude 52

$\underline{\hat{\psi}}_\mathrm{r}$ phasor of the rotor flux linkage estimate 50, 51

$\psi_\mathrm{r}^\star$ reference rotor flux linkage magnitude 27

$\vec{\psi}_\mathrm{r}^*$ complex conjugate space vector of the rotor flux linkage 11

$\hat{\vec{\psi}}_\mathrm{r}$ space vector of the rotor flux linkage estimate 45, 46, 48, 50, 52, 54–57, 176

$\vec{\psi}_\mathrm{r}$ space vector of the rotor flux linkage 11–13, 15, 23–26, 28

$\vec{\psi}_\mathrm{r}^\mathrm{xy}$ space vector of the rotor flux linkage in the rotor reference frame 11, 12, 15, 24

$\hat{\psi}_\mathrm{rd}$ direct component of the field-oriented rotor flux linkage estimate 52

$\hat{\psi}_\mathrm{rq}$ quadrature component of the field-oriented rotor flux linkage estimate 52

ψ_r rotor flux linkage magnitude $|\vec{\psi}_\mathrm{r}|$ 25, 26, 28, 141, 148

$\vec{\psi}_\mathrm{s}^\mathrm{dq}$ space vector of the stator flux linkage in a field-oriented reference frame 26

$\hat{\psi}_\mathrm{s}$ estimated stator flux linkage magnitude 16, 20, 21, 27, 34, 35, 46, 61–63, 65, 68, 69, 72, 73, 76–78, 89, 90, 94, 148, 198

$\psi_\mathrm{s}^\mathrm{opt}$ efficiency optimized stator flux linkage magnitude 32, 33, 35, 141, 148

$\underline{\hat{\psi}}_\mathrm{s}$ phasor of the stator flux linkage estimate 43–45, 47, 50, 51

$\underline{\psi}_\mathrm{s}$ phasor of the stator flux linkage 43–45, 47, 51, 61, 83

$\psi_\mathrm{s}^\star$ reference stator flux linkage magnitude 27, 34, 35, 148

$\vec{\psi}_\mathrm{s}^*$ complex conjugate space vector of the stator flux linkage 165

$\hat{\vec{\psi}}_\mathrm{s}$ space vector of the stator flux linkage estimate 27, 43–46, 48, 50–52, 54–56, 61, 86, 87, 176

$\vec{\psi}_\mathrm{s}$ space vector of the stator flux linkage 9–13, 15, 21, 23–25, 28, 32, 61, 165

$\psi_{s\alpha}$ real component of the stator flux linkage space vector 165
$\psi_{s\beta}$ imaginary component of the stator flux linkage space vector 165
$\hat{\psi}_{sd}$ direct component of the field-oriented stator flux-linkage estimate 52
ψ_s stator flux linkage magnitude $|\vec{\psi}_s|$ 16, 19–21, 24–26, 28, 30–32, 35, 61–63, 65, 68, 69, 72, 73, 76–78, 89, 198
$\Omega_m^{\Diamond}$ measured value of the mechanical angular rotor frequency 139, 175
Ω_m mechanical angular frequency of the rotor $2\pi \cdot n_m/60$ 9, 61, 167, 187
$\hat{\omega}_m$ estimate of the rotor angular frequency ω_m 52, 87
$\omega_m^{\Diamond}$ measured electrical angular frequency of the rotor ω_m 27, 33, 35, 55–57, 86, 87, 148
ω_m electrical angular frequency of the rotor $p \cdot \Omega_m$ 9–11, 13–15, 22, 23, 25, 28, 43, 48, 50, 63–73, 76–78, 81, 83, 84, 92, 95, 176, 177
$\hat{\omega}_s$ estimate of the stator angular frequency ω_s 33–35, 46, 52, 86, 148
$\hat{\omega}_{sl}$ estimated value of the slip angular frequency ω_{sl} 35
$\omega_{sl}^{\star}$ reference value of the slip angular frequency ω_{sl} 27
ω_{sl} slip angular frequency $\omega_s - \omega_m$ 10, 19, 25, 26, 28, 30–32, 34, 35, 43–45, 50–52, 59–62, 83
ω_s stator angular frequency $2\pi \cdot f_s$ 9, 10, 16, 20, 21, 24, 25, 29, 35, 43–45, 47, 50, 51, 59, 61, 62, 74, 75, 82, 83, 100, 105, 163, 165, 178
a_{fe} Steinmetz equation exponent 20, 21, 24, 35, 168
$\hat{\boldsymbol{A}}_{im}$ estimated system matrix of the state space induction machine model 47, 48
$\boldsymbol{A}_{im}$ system matrix of the state space induction machine model 12–14, 47
$\boldsymbol{A}_{rfo}$ system matrix of the rotor field oriented induction machine model 148
b_{fe} Steinmetz equation exponent 20, 21, 24, 35, 168
$\boldsymbol{B}_{im}$ input matrix of the state space induction machine model 12, 13, 47
$\boldsymbol{B}_{rfo}$ input matrix of the rotor field oriented induction machine model 148
C_{dc} DC-link capacitance of the 37, 108, 130
C_{ds} drain-source capacitance of a single MOSFET 36, 37
C_f capacitor of the first-order circuit 108, 109, 112, 130, 131
C_{gd} gate-drain capacitance of a single MOSFET 37
C_{gs} gate-source capacitance of a single MOSFET 36, 37
$\hat{\boldsymbol{C}}_{im}$ estimated output matrix of the state space induction machine model 47, 48
$\boldsymbol{C}_{im}$ output matrix of the state space induction machine model 12, 13, 47
C_{out} equivalent total drain-source output capacitance of an inverter half bridge 37, 38, 40, 41, 82, 121, 137, 138
$\boldsymbol{C}_{rfo}$ output matrix of the rotor field oriented induction machine model 148

C_{th} thermal capacitance 93

$\boldsymbol{D}_{\mathrm{im}}$ feed-forward matrix of the state space induction machine model 12, 13, 47

$\boldsymbol{D}_{\mathrm{rfo}}$ feed-forward matrix of the rotor field oriented induction machine model 148

e_{s2} stator inductance saturation model exponent 16, 168

f_{a} A/D converter sampling frequency 101, 102, 106, 108, 109

$\underline{F}_{\mathrm{C}}(\mathrm{j}\omega_{\mathrm{s}})$ relative steady-state flux-linkage error of the open-loop current-model observer 44, 47, 51

$\underline{F}_{\mathrm{C}}^{\Delta\mathrm{i}}(\mathrm{j}\omega_{\mathrm{s}})$ relative steady-state flux-linkage error of the open-loop current-model observer caused by current sensor deviation 44

$\underline{F}_{\mathrm{C,h}}^{\Delta\mathrm{i}}(\mathrm{j}k\omega_{\mathrm{s}})$ normalized frequency-response function of the open-loop current-model observer for the k^{th} current harmonic 83

$\underline{F}_{\mathrm{F}}(\mathrm{j}\omega_{\mathrm{s}})$ relative steady-state flux-linkage error of the full-order Luenberger-type observer 51

$\underline{F}_{\mathrm{G}}(\mathrm{j}\omega_{\mathrm{s}})$ relative steady-state flux-linkage error of the closed-loop Gopinath-style observer 47

f_{s} electrical stator frequency 20, 29, 31–33, 54, 60, 103, 105–109, 123–125, 167, 187

f_{sw} inverter PWM switching frequency 53, 101, 102, 105–109

$\underline{F}_{\mathrm{T}}(\mathrm{j}\omega_{\mathrm{s}})$ relative steady-state torque error of the FOC controller 61, 62

$\underline{F}_{\mathrm{V}}(\mathrm{j}\omega_{\mathrm{s}})$ relative steady-state flux-linkage error of the open-loop voltage-model observer 45, 47, 51

$\underline{F}_{\mathrm{V}}^{\Delta\mathrm{i}}(\mathrm{j}\omega_{\mathrm{s}})$ relative steady-state flux-linkage error of the open-loop voltage-model observer caused by current sensor deviation 45

$\underline{F}_{\mathrm{V,h}}^{\Delta\mathrm{i}}(\mathrm{j}k\omega_{\mathrm{s}})$ normalized frequency-response function of the open-loop voltage-model observer for the k^{th} current harmonic 83

$\underline{F}_{\mathrm{V}}^{\Delta\mathrm{u}}(\mathrm{j}\omega_{\mathrm{s}})$ relative steady-state flux-linkage error of the open-loop voltage-model observer caused by voltage sensor deviation 45

$\underline{F}_{\mathrm{V,h}}^{\Delta\mathrm{u}}(\mathrm{j}k\omega_{\mathrm{s}})$ normalized frequency-response function of the open-loop voltage-model observer for the k^{th} voltage harmonic 83

g observer pole placement design factor 66–73, 77, 78, 81, 138, 176, 177, 197, 198

$\hat{\underline{G}}_{\mathrm{C}}(\mathrm{j}\omega_{\mathrm{s}})$ partial transfer function of the full-order flux-linkage observer 50, 51

g_{ph} sensor gain of the phase current or voltage sensor 74, 75, 178

$\underline{G}_{\mathrm{PI}}(\mathrm{j}\omega_{\mathrm{s}})$ transfer function of a PI-controller 47, 83

$\boldsymbol{H}_{\mathrm{p}}$ Toeplitz prediction matrix of the MPC algorithm 149, 178, 179

i_{ds} drain–source current of a conducting MOSFET 37–39, 41, 196

$i_{\mathrm{ds}}^{\Diamond}$ measured drain–source current of a conducting MOSFET 130, 131, 136

$\vec{i}_{\mathrm{fe}}$ space vector of the iron loss equivalent current 21, 24, 32, 34, 35, 94

$\mathbf{I}$ identity matrix 13, 14, 47, 48, 176

$\vec{i}_{\mathrm{m}}$ space vector of the main or mutual inductance current $\vec{i}_{\mathrm{s}} - \vec{i}_{\mathrm{r}}$ 11, 15, 23–25

i_{ph} phase output current of an inverter half bridge 36–41, 53, 82, 97, 99, 131, 164, 175, 196

$\bar{i}_{\mathrm{ph}}$ switching period average of the inverter phase output current 53

$\vec{i}^{\,\lozenge}_{\mathrm{ph}}$ switching period average of the measured inverter phase output current 53, 99, 117–125, 175

$i^{\lozenge}_{\mathrm{ph}}$ measured phase output current of an inverter half bridge 53, 74, 99, 130, 177

$i_{\mathrm{ph,off}}$ phase current sensor offset error 74, 117, 120, 121, 126–128, 178

$\vec{i}_{\mathrm{r}}^{\,\mathrm{dq}}$ space vector of the rotor current in a field-oriented reference frame 25

$\vec{i}_{\mathrm{r}}$ space vector of the rotor current 9–12, 15, 23–25, 32

$\vec{i}_{\mathrm{r}}^{\,\mathrm{xy}}$ space vector of the rotor current in the rotor reference frame 11, 12, 15, 24

i_{s} stator current magnitude $|\vec{i}_{\mathrm{s}}|$ 16, 34, 61, 62, 74, 132, 135, 143, 145, 151, 155, 178

$i_{\mathrm{s}\alpha}$ real component of the stator current space vector 165

$i^{\lozenge}_{\mathrm{s}\alpha}$ measured real component of the stator current space vector 74, 178

$i_{\mathrm{s}\beta}$ imaginary component of the stator current space vector 165

$i^{\lozenge}_{\mathrm{s}\beta}$ measured imaginary component of the stator current space vector 74, 178

i_{sd} flux-producing direct current component 19, 25, 26, 28–30, 35, 141, 143–151, 153, 154, 201

$i^{\lozenge}_{\mathrm{sd}}$ measured flux-producing direct current component 26, 94

$\vec{i}_{\mathrm{s}}^{\,\mathrm{dq}}$ space vector of the stator current in a field-oriented reference frame 25, 26, 142, 147, 148, 152–156

$\vec{i}_{\mathrm{s}}^{\,\mathrm{dq}\star}$ stator current reference in a field-oriented reference frame 26, 27

$i^{\star}_{\mathrm{sd}}$ reference value of the flux-producing direct current component 26, 27, 34–36, 148, 156

$i^{\mathrm{ss}}_{\mathrm{sd}}$ steady state value of the flux-producing direct current component 148, 151

$i_{\mathrm{s,max}}$ maximum stator current magnitude constraint 29, 34, 35, 141–143, 145, 147, 149–152, 155, 168

$i^{\lozenge}_{\mathrm{s}}$ measured stator current magnitude $|\vec{i}^{\,\lozenge}_{\mathrm{s}}|$ 61, 62

$\underline{i}_{\mathrm{s}}$ phasor of the stator current 44, 45, 61, 83

$\underline{i}^{\lozenge}_{\mathrm{s}}$ measured value of the stator current phasor 43–45, 47, 50, 51

i_{sq} torque-producing quadrature current component 19, 25, 26, 28–30, 35, 141, 143–154

$i^{\lozenge}_{\mathrm{sq}}$ measured torque-producing quadrature current component 26, 94

$i_{\mathrm{sq}}^{\star}$ reference value of the torque-producing quadrature current component 26, 27, 34–36, 148

$i_{\mathrm{sq}}^{\mathrm{ss}}$ steady state value of the torque-producing quadrature current component 148, 151

$\vec{i}_{\mathrm{s}}$ space vector of the stator current 5, 9–13, 15, 23–25, 28, 32, 61, 74, 75, 82, 164, 165, 178

$\hat{\vec{i}}_{\mathrm{s}}$ space vector of the stator-current estimate 48, 50, 52, 54–57

$\bar{\hat{\vec{i}}}_{\mathrm{s}}$ switching-period average of the estimated stator current space vector 55, 57

$\vec{i}_{\mathrm{s}}^{\,\Diamond}$ measured value of the stator current space vector $\vec{i}_{\mathrm{s}}$ 5, 26, 43–46, 48, 50, 52, 54, 55, 74, 86, 87, 178

$\bar{\vec{i}}_{\mathrm{s}}^{\,\Diamond}$ switching-period average of the measured stator current space vector 54, 55, 57, 138

$\vec{i}_{\mathrm{s,neg}}^{\,\Diamond}$ negative sequence component of the measured stator current $\vec{i}_{\mathrm{s}}^{\,\Diamond}$ 74, 75, 79, 80, 178

$\vec{i}_{\mathrm{s,off}}^{\,\Diamond}$ offset component of the measured stator current $\vec{i}_{\mathrm{s}}^{\,\Diamond}$ 74, 75, 178

$\vec{i}_{\mathrm{s,pos}}^{\,\Diamond}$ positive sequence component of the measured stator current $\vec{i}_{\mathrm{s}}^{\,\Diamond}$ 74, 75, 79, 178

$\mathbf{J}$ matrix notation of the imaginary number j 13, 47, 164, 176

J_{p} performance index or cost function of an optimization problem 149

$k_{\measuredangle}$ flux-linkage angle adaptive error feedback gain 87

k_{fe} Steinmetz equation factor 20, 21, 24, 35, 168

K_{I} PI-controller integral gain 46, 47

$\boldsymbol{K}$ observer gain matrix 47–49, 175–177

K_{P} PI-controller proportional gain 46, 47

$\underline{K}_{\mathrm{R}}$ weighted rotor flux linkage complex observer feedback gain $\hat{\sigma}\hat{L}_{\mathrm{s}}\hat{\tau}_{\mathrm{r}}/\hat{L}_{\mathrm{m}}\underline{K}_{\mathrm{r}}$ 50–52

$\underline{K}_{\mathrm{r}}$ rotor flux linkage complex observer feedback gain 47, 48, 50–52, 176, 177

$\underline{K}_{\mathrm{s}}$ stator flux linkage complex observer feedback gain 47, 48, 50–53, 80, 81, 176, 177, 198

L_{m} main or mutual inductance 11–16, 18, 19, 21, 24–28, 32, 35, 42, 62–65, 68, 69, 72, 73, 141, 148, 197

$\hat{L}_{\mathrm{m}}$ estimated main inductance 45, 46, 48, 50–52, 54–57, 63, 65, 68, 69, 72, 73, 87, 89, 94, 176, 177

$L_{\sigma\mathrm{r}}$ rotor stray or leakage inductance 11, 12, 15–18, 23–25, 31, 62, 63, 65, 68, 69, 72, 73, 168

$\hat{L}_{\sigma\mathrm{r}}$ estimated rotor stray or leakage inductance 63, 65, 68, 69, 72, 73, 89

$L_{\sigma\mathrm{r0}}$ partial rotor leakage inductance 15, 23, 24, 31, 42

$L_{\sigma r1}$ deep bar effect parallel network partial rotor leakage inductance 15, 23, 24, 31, 42

$L_{\sigma s}$ stator stray or leakage inductance 9, 11, 12, 15–18, 23–25, 42, 62–65, 68, 69, 72, 73, 168

$\hat{L}_{\sigma s}$ estimated stator stray or leakage inductance 63, 65, 68, 69, 72, 73, 89

L_r rotor inductance $L_m + L_{\sigma r}$ 12–14, 19, 25, 27, 28, 32, 35, 148

l_{reg} regression line $r_{reg} \cdot \vec{i}^{\,\Diamond}_{ph} + u_{reg}$ of the inverter voltage distortion curve representation 118–122, 124, 125, 128

$\hat{L}_r$ estimated rotor inductance 45, 46, 48, 50–52, 54–57, 176, 177

L_s stator inductance $L_m + L_{\sigma s}$ 12–14, 16, 19, 21, 24, 26, 28, 30–32, 34, 35, 44, 45, 61, 62, 83

$\hat{L}_s$ estimated stator inductance 16, 35, 43–46, 48, 50–52, 54–56, 94, 176, 177

L_{s1} first stator inductance saturation model parameter 16, 168

l_{s2} second stator inductance saturation model parameter 16, 168

m_a number of A/D converter samples per switching period T_{sw}/T_a 101, 104, 106–109, 114, 199

N_c control horizon of the MPC algorithm 149, 150

N_p prediction horizon of the MPC algorithm 149, 150, 178

p number of pole pairs 9, 10, 12, 24, 35, 61, 148, 168

P_{fe} iron losses of the induction machine 20–22, 32, 93

$\hat{P}_{fe}$ estimated iron losses of the IM 20–22

P_m mechanical power of the induction machine 167

P_{loss} total electromagnetic losses of the induction machine 32

$\boldsymbol{P}_p$ prediction matrix of the MPC algorithm 149, 178, 179

P_r rotor ohmic losses of the induction machine 32, 93, 94

P_s stator ohmic losses of the induction machine 32, 93, 94

Q_{th} dissipated thermal power 93, 94

$\boldsymbol{Q}_u$ input weighting matrix of the MPC algorithm 149, 150, 179

q_{iu} covariance of the measured current and distortion voltage used for offset calibration 120

$\boldsymbol{Q}_y$ output weighting matrix of the MPC algorithm 149, 150, 179

$R_{ds,on}$ MOSFET ‘on’-state resistance 37–41, 82, 121, 132, 133, 136–138, 140, 171

$R^{\Diamond}_{ds,on}$ measured MOSFET ‘on’-state resistance 131–137, 200

$\hat{R}_{eq}$ equivalent estimated resistance of the current predictor 56, 57

R_f resistor of the first-order circuit 108, 109, 130, 131

R_{fe} iron loss equivalent resistance 21, 32, 42, 44, 45, 61–63

R_R virtual rotor winding resistance $L_m^2/L_r^2 R_r$ 148

R_r rotor winding resistance 11–15, 19, 23–25, 27, 28, 31, 32, 42, 62–73, 168, 197

r_reg gradient of the regression line l_reg 118–121, 131

$\hat{R}_\mathrm{r}$ estimated rotor winding resistance 18, 48, 51, 52, 56, 63–73, 86, 87, 89, 90, 93, 94, 176, 177

R_p1 deep bar effect parallel network resistance 15, 23, 24, 31, 42

R_s stator winding resistance 10–15, 18, 24, 28, 32, 42, 45, 59, 62–73, 83, 168, 197

$\hat{R}_\mathrm{s}$ estimated stator winding resistance 18, 44–48, 50, 52, 54–56, 59, 63–73, 82, 83, 86, 89, 93, 94, 176, 177

$R_\mathrm{s}^\Diamond$ measured stator winding resistance 18

R_th thermal resistance 93

s complex variable of the Laplace transform 13, 14, 26, 28, 48, 49, 55, 56, 109, 141, 175

s_slip slip of the rotor $\omega_\mathrm{sl}/\omega_\mathrm{s}$ 10, 22, 23

S_n n^th switch of a power electronic circuit 37, 38, 40, 108, 130

$s_{\mathrm{p}n}$ n^th pole of the IM transfer function 13–15, 48, 176, 177

$\hat{s}_{\mathrm{p}n}$ n^th pole of the observer transfer function 48, 175–177

T_a A/D converter sampling period $1/f_\mathrm{a}$ 102–108

T_dt inverter dead time between 'on'-states of lower and upper half-bridge switches 37, 38, 40, 41, 82, 121, 125

T_e electrical air-gap torque of the electrical machine 9, 11, 12, 15, 24, 25, 31, 34, 35, 141

$\hat{T}_\mathrm{e}$ estimated value of the air-gap torque T_e 52

$T_\mathrm{e}^\star$ electrical air-gap torque reference 27, 35, 148

T_m mechanical air-gap torque $p \cdot T_\mathrm{e}$ 4, 5, 9, 12, 22–24, 61, 63–73, 76–78, 143, 145, 148, 151, 167, 175

$\bar{T}_\mathrm{m}$ averaged mechanical air-gap torque 86, 90

$\hat{T}_\mathrm{m}$ estimated value of the mechanical air-gap torque T_m 61, 63–73, 76–78, 146

$T_\mathrm{m}^\Diamond$ measured value of the mechanical air-gap torque T_m 92, 95, 139, 146

$T_\mathrm{m}^\star$ mechanical air-gap torque reference 4, 5, 29, 31–33, 35, 36, 60, 95, 139, 143, 145–148, 153, 155, 156, 175

T_m^ss steady state value of the mechanical air-gap torque 148, 151

T_s electrical period $1/f_\mathrm{s}$ 105

T_sw inverter PWM switching period $1/f_\mathrm{sw}$ 37, 40, 41, 53–57, 82, 98–105, 121

u_dc DC-link voltage of the inverter system 34, 37, 38, 40, 82, 99–106, 108–116, 130, 175

$u_\mathrm{dc}^\Diamond$ measured DC-link voltage of the inverter system 175

u_{dist} voltage distortion caused by dead time and inverter voltage drop 97

$\bar{u}_{\mathrm{dist}}$ switching-period average value of the voltage distortion caused by dead time and inverter voltage drop 36–41, 99, 196

$\hat{\bar{u}}_{\mathrm{dist}}$ switching-period average estimate of the voltage distortion caused by dead time and inverter voltage drop 99

$\bar{u}^{\Diamond}_{\mathrm{dist}}$ measured switching-period average value of the voltage distortion caused by dead time and inverter voltage drop 117–125

u_{ds} drain–source voltage drop of a conducting MOSFET 37–39, 41

$u^{\Diamond}_{\mathrm{ds}}$ measured drain–source voltage drop of a conducting MOSFET 130, 131, 136

u_{fdc} filtered DC-link voltage 130, 131

$u^{\Diamond}_{\mathrm{fdc}}$ measurement value of the filtered DC-link voltage 130, 131

u_{fph} filtered phase voltage 99, 100, 102–104, 108, 111, 130, 131

$\bar{u}_{\mathrm{fph}}$ switching-period average of the filtered phase voltage 105

$\Delta\bar{u}_{\mathrm{fph}}$ switching-period average of the induced measurement error 103, 105–107

$\Delta\bar{u}^{\Diamond}_{\mathrm{fph}}$ switching-period average of the backward-Euler digital integration error 103, 105, 107

$\Delta\bar{u}^{\Diamond}_{\mathrm{fph,FE}}$ switching-period average of the backward-Euler digital integration error at the falling voltage edge 104

$\Delta\bar{u}^{\Diamond}_{\mathrm{fph,RE}}$ switching-period average of the backward-Euler digital integration error at the rising voltage edge 104

$u^{\Diamond}_{\mathrm{fph}}$ A/D converter sampled signal of the filtered phase voltage 103, 104, 112, 113, 130, 199

$\boldsymbol{u}_{\mathrm{im}}$ input vector of the induction machine model 12, 13, 47

u_{ph} phase output voltage of an inverter half bridge 36, 37, 40, 53, 82, 97–99, 102, 103, 108–115, 130, 164, 175

$\bar{u}_{\mathrm{ph}}$ switching period average value of the output voltage of a single inverter phase 36, 53, 98, 99, 105, 106

$\bar{u}^{\Diamond}_{\mathrm{ph}}$ measured switching-period average of the phase-to-ground voltage u_{ph} 53, 97, 98, 115–117, 121, 175

$\Delta\bar{u}^{\Diamond}_{\mathrm{ph}}$ switching-period average of the total instantaneous measurement error 101, 103, 107, 114–116

$\bar{u}^{\star}_{\mathrm{ph}}$ switching period average value of the reference voltage of a single inverter phase 36, 53, 97–99, 117, 121

$u_{\mathrm{ph,off}}$ phase voltage sensor offset error 117, 120, 121, 126–128

$\boldsymbol{u}_{\mathrm{p}}$ input prediction matrix of the MPC algorithm 149, 178, 179

u_{ref} reference voltage for the A/D conversion 108, 109, 130

u_{reg} y-intercept of the regression line l_{reg} 118–121

$\boldsymbol{u}_{\mathrm{rfo}}$ input vector of the rotor field oriented induction machine model 148, 149
$\hat{\boldsymbol{u}}_{\mathrm{rfo}}$ predicted future input vector of the RFO induction machine model 149
u_{s} magnitude of the stator voltage space vector 165
$u_{\mathrm{s}\alpha}$ real component of the stator voltage space vector 164, 165
$\bar{u}_{\mathrm{s}}$ switching period average of the stator voltage magnitude 100
$u_{\mathrm{s}\beta}$ imaginary component of the stator voltage space vector 164, 165
$u^{\star}_{\mathrm{sd}}$ reference value direct voltage component 26, 35, 148
$u_{\mathrm{s,max}}$ maximum stator voltage magnitude constraint 29, 34, 35, 148
$\bar{u}^{\Diamond}_{\mathrm{s}}$ switching period average of the measured stator voltage magnitude 100
$\underline{u}_{\mathrm{s}}$ amplitude invariant stator voltage phasor 45, 83, 165
$\underline{u}^{\Diamond}_{\mathrm{s}}$ measured value of the stator voltage phasor 44, 45, 47, 50
$u^{\star}_{\mathrm{sq}}$ reference value quadrature voltage component 26, 35, 148
$\vec{u}_{\mathrm{s}}$ space vector of the stator voltage 5, 10–13, 15, 24, 28, 164, 165
$\vec{u}^{\Diamond}_{\mathrm{s}}$ measured value of the stator voltage space vector $\vec{u}_{\mathrm{s}}$ 5, 44–46, 48, 50, 52, 54, 86, 87
$\bar{\vec{u}}^{\Diamond}_{\mathrm{s}}$ switching-period average of the measured stator voltage space vector 54
$\vec{u}^{\star}_{\mathrm{s}}$ space vector of the reference stator voltage 5, 26, 56, 97
$\bar{\vec{u}}^{\star}_{\mathrm{s}}$ switching-period average of the reference stator voltage space vector 54, 55, 57, 98, 99, 137, 138
$\hat{\boldsymbol{x}}_{\mathrm{im}}$ estimated state vector of the induction machine model 47
$\boldsymbol{x}_{\mathrm{im}}$ state vector of the induction machine model 12, 13, 47
$\boldsymbol{x}_{\mathrm{rfo}}$ state vector of the rotor field oriented induction machine model 148
$\hat{\boldsymbol{x}}_{\mathrm{rfo}}$ predicted future state vector of the RFO induction machine model 149
$\boldsymbol{y}_{\mathrm{im}}$ output vector of the induction machine model 12, 13, 47
$\boldsymbol{y}_{\mathrm{p}}$ output prediction matrix of the MPC algorithm 178, 179
$\boldsymbol{y}_{\mathrm{rfo}}$ output vector of the rotor field oriented induction machine model 148
$\hat{\boldsymbol{y}}_{\mathrm{rfo}}$ predicted future output vector of the RFO induction machine model 149

List of Figures

1.1 Drive train of the electric vehicle with two independent electrical drives at the rear axle. . . . 2
1.2 StreetScooter C16 with two independent single-wheel drives at the rear axle. 3
1.3 New torque vectoring functions developed in the project MAs:Stab. . . . 3
1.4 Configuration of the drive system with higher-level torque-vectoring and stability control. . . . 3
1.5 Torque accuracy and dynamics requirement for the electrical traction drives. 4
1.6 System overview of an IM drive train with functional components. . . . 5
1.7 Structure of the main contents of this work. Main contributions in light green. . . . 7

2.1 Cross section of an IM with squirrel-cage rotor and two pole pairs. . . . 10
2.2 Equivalent circuit of the IM with ideal rotating transformer (IRTF). . . . 11
2.3 Signal-flow diagram of the IM with ideal rotating transformer (IRTF). . . . 12
2.4 Generel state-space representation of a linear time-invariant system. . . . 13
2.5 Root locus diagrams of the IM with two poles and one zero. . . . 14
2.6 Extended nonlinear induction machine model with IRTF. . . . 15
2.7 The influence of magnetic saturation on the stator inductance and the dependency of the stray inductances on current magnitude and frequency. 16
2.8 Measured sum of leakage inductances as a function of the magnetizing current and field angle. Detected by signal injection. . . . 17
2.9 Temperature drift of the stator and rotor resistance for IM26kA. . . . 18
2.10 Iron core losses of IM26kA measured by no-load tests and fitted using Steinmetz's equation. . . . 20
2.11 Comparison of calculated iron losses using FEM and iron-loss model using fitted data from no-load tests. . . . 22
2.12 Influence of the rotor bar shape on the torque production [HVB99]. . . . 23
2.13 Signal-flow diagram of the extended IM model with IRTF. . . . 24
2.14 Space-vector diagram with stator ($\alpha\beta$), rotor (xy) and field-oriented (dq) reference frame. . . . 25
2.15 Structure of FOC with current regulators and reference frame transformations. . . . 26
2.16 Structure of the indirect RFO and direct SFO decoupling networks. . . . 27
2.17 Steady-state current locus diagram in RFO with current and voltage constraints. . . . 29

2.18 Equivalent slip-frequency-dependent rotor parameters due to rotor deep-bar effect. . . . 31
2.19 Electromagnetic losses as a function of the stator flux-linkage. . . . 32
2.20 Efficiency optimal stator flux linkage as a function of stator frequency and torque reference. . . . 33
2.21 Implementation of the direct SFO controller with decoupling using the estimated stator frequency. . . . 35
2.22 Signal-flow diagram of the steady-state iron-loss compensation implementation within the direct SFO controller. . . . 35
2.23 Constraints handling of the direct SFO controller with input trajectory filter. 35
2.24 The inverter as nonlinear actuator within the drive control loop with disturbance caused by dead time and semiconductor voltage drop. . . . 36
2.25 Parasitic capacitances of a power MOSFET and simplified inverter half-bridge model with parasitic drain–source capacitance. . . . 37
2.26 Simplified waveforms of the inverter half bridge output voltage with dead time and parasitic capacitor effect. . . . 37
2.27 Power MOSFET and body diode voltage drop as a function of the current i_{ds} and the semiconductor temperature ϑ_{sc}. . . . 39
2.28 Signal-flow diagram of the inverter half-bridge model with semiconductor voltage drop and dead-time effect. . . . 40
2.29 Measured reverse voltage drop of two parallel 'on'-state MOSFETs and the body diode at $\vartheta_{sc} = 95\,^{\circ}\mathrm{C}$. . . . 41
2.30 Distortion voltage $\bar{u}_{dist}$ as a function of the phase current i_{ph} with three linear regions. . . . 41

3.1 Structure of the open-loop current-model stator flux-linkage observer. . . . 44
3.2 Structure of the open-loop voltage-model stator flux-linkage observer with open integration. . . . 45
3.3 Structure of the closed-loop voltage-model observer with open-loop current-model corrective feedback. . . . 46
3.4 General structure of a Luenberger observer in state-space representation. 47
3.5 Root-locus diagrams of the full-order observer poles for IM26kA, using different pole placement methods. . . . 49
3.6 Structure of the closed-loop Luenberger-type stator flux-linkage observer with modified voltage model. . . . 50
3.7 Structure of the sliding-mode inherently speed-sensorless flux-linkage observer with modified voltage and current models. . . . 52
3.8 Discrete-time representation of measured currents and voltages in the inverter system with sampled and switching-period average quantities. . . . 53
3.9 Optimal discrete-time voltage model of the IM using the backward-Euler method on switching-period average quantities. . . . 54

3.10 Optimal discrete-time current model of the IM using the zero-order hold (ZOH) method for switching-period average input quantities. 55
3.11 Discrete-time inverse current model of the full-order observer using the first-order hold (FOH) method. 56
3.12 Discrete-time single-step current predictor using the stator voltage reference [WL09]. 57

4.1 Slip frequency as a function of the operating point of the efficiency-optimized IM drive. 60
4.2 Chosen slip frequency used for the worst-case torque accuracy analysis and the corresponding torque as a function of the stator electrical frequency for IM26kA. 60
4.3 Definition of the flux-linkage estimation error angle δ. 61
4.4 Steady-state error of the open-loop flux-linkage observers and resulting torque error as a function of the IM parameter for IM26kA with $X = R_\mathrm{s}, R_\mathrm{r}, L_\mathrm{m}$, ... 63
4.5 Steady-state torque error caused by stator- and rotor-resistance drift as a function of the observer PI controller bandwidth for IM26kA. 64
4.6 Steady-state error of the Gopinath-style flux-linkage observer and resulting torque error as a function of the IM parameter for IM26kA. 65
4.7 Steady-state torque error caused by stator- and rotor-resistance drift as a function of the observer proportional pole-placement design factor g for IM26kA. 66
4.8 Steady-state torque error caused by stator- and rotor-resistance drift as a function of the observer left-shift pole-placement design factor g for IM26kA. 67
4.9 Steady-state error of the full-order flux-linkage observer with proportional pole placement ($g = 10$) and resulting torque error as a function of the IM parameter for IM26kA. 68
4.10 Steady-state error of the full-order flux-linkage observer with left-shift pole placement ($g = 0.3$) and resulting torque error as a function of the IM parameter for IM26kA. 69
4.11 Steady-state torque error caused by stator- and rotor-resistance drift as a function of the sliding-mode observer proportional pole-placement design factor g for IM26kA. 70
4.12 Steady-state torque error caused by stator- and rotor-resistance drift as a function of the sliding-mode observer left-shift pole-placement design factor g for IM26kA. 71
4.13 Steady-state error of the sliding-mode flux-linkage observer with proportional pole placement ($g = 5$) and resulting torque error as a function of the IM parameter for IM26kA. 72

4.14 Steady-state error of the sliding-mode flux-linkage observer with left-shift pole placement ($g = 0.3$) and resulting torque error as a function of the IM parameter for IM26kA. 73
4.15 Offset, positive and negative-sequence components of the measured stator-current space vector, caused by sensor offset and imbalanced sensor-gain errors. 75
4.16 Steady-state error of the Gopinath-style flux-linkage observer and the resulting torque deviation caused by balanced current- and voltage-sensor deviation. 76
4.17 Steady-state error of the full-order flux-linkage observer and the resulting torque deviation caused by balanced current- and voltage-sensor deviation. 77
4.18 Steady-state error of the sliding-mode flux-linkage observer and the resulting torque deviation caused by balanced current- and voltage-sensor deviation. 78
4.19 Absolute value of the voltage-model feedback gain $\underline{K}_\mathrm{s}$ for proportional ($g = 5$) and left-shifted ($g = 0.3$) pole placement as a function of the rotor rotational speed. 81
4.20 Normalized flux-linkage frequency response of the Gopinath-style and Luenberger-type observers with proportional and left-shifted poles for harmonics in the voltage and current signal caused by offset, differential gain error and dead-time effect. 84
4.21 Model-based open-loop resistance estimation and adaption using the measured stator-winding temperature and the measured slip frequency. . . . 86
4.22 Simulation results of the model-based open-loop rotor-resistance estimation using Equation (2.18) without stator-resistance adaption. 86
4.23 MRAS-based parameter adaption. 87
4.24 Parameter sensitivity of the stator flux-linkage magnitude $\hat{\psi}_\mathrm{s}/\psi_\mathrm{s} - 1$ in %. 89
4.25 Parameter sensitivity of the stator flux-linkage angle δ in electrical degrees (°). 89
4.26 Simulation results of the MRAS-based rotor-resistance adaption as a function of the error feedback and speed. 90
4.27 Geometric structure of the LPTN. 92
4.28 Comparison between measured and simulated stator and rotor temperatures using the LPTN. 92
4.29 LPTN unit with heat input, consisting of thermal lumped parameters [Qi+17]. 93
4.30 Structure of the LPTN thermal-model-based resistance-adaption scheme. 93
4.31 Measured absolute torque deviation of the IM drive with IM26kA. 95

5.1 Scheme of the drive system with instantaneous voltage sensing. 97
5.2 Definition of the switching-period average voltage and notation of the voltage quantities. 98

5.3 Feed-forward dead time and semiconductor voltage drop compensation scheme by open-loop linearization of the inverter transfer function. . . . 99
5.4 Voltage measurement using the integrating behavior of a low-cutoff-frequency low-pass filter (LPF) and center-aligned sampling. 99
5.5 Pulse-width detection and calculation using the measured DC-link voltage. 100
5.6 Switching-period average voltage measurement using an analog integrator. 100
5.7 Detection of the switching-period average by oversampling and digital integration. 101
5.8 Significant reduction of the digital integration error using a first-order high-cutoff-frequency LPF. Error at rising and falling edge are canceled out. 102
5.9 Digital integration error at the rising and falling PWM voltage edge using the backward Euler method. 103
5.10 Digital integration error at the rising and falling edge as a function of the edge position τ_d (a) and total integration error as a function of τ_d and τ_f (b). The number of samples per switching period is set to $m_\mathrm{a} = 100$. . . . 104
5.11 Switching period average of the original and the filtered voltage signal (a). The LPF phase delay causes an angle dependent error (b). 105
5.12 Worst-case integration, phase-shift and resulting total error. 107
5.13 General solution for the optimal LPF time-constant and the resulting reduction of the measurement error. 107
5.14 Circuit diagram of the voltage measurement circuit with inverting LPF and A/D conversion on the high-voltage side. 108
5.15 Gate-driver integrated implementation of the measurement circuit on a six-layer printed circuit board (PCB). 110
5.16 Numerical and experimental validation of the digital integration error at very low duty cycle. 111
5.17 Comparison of the ideal rectangular voltage waveform used for numerical calculation and the measured voltage signal. 111
5.18 Experimental results of the sampled phase voltage $u^{\Diamond}_{\mathrm{fph}}$ with different LPF time-constant before digital integration. 113
5.19 Experimental verification of the instantaneous switching-period average voltage measurement using an Aachen-Cathedral-shaped fundamental voltage signal which contains high transients. 115
5.20 Experimental results for a 50 Hz sinusoidal voltage reference signal. . . . 116
5.21 The influence of current and voltage sensor offsets on the measured inverter voltage distortion curve for a single phase. 117
5.22 Regression lines for measured voltage distortion data, captured during a single period of a sinusoidal current wave with 6 A amplitude and 20 Hz stator fundamental frequency. 118

5.23 Determination of the current and voltage sensor offsets and the calibration path. . . . 120
5.24 Structure of the online sensor offset calibration algorithm. . . . 121
5.25 Experimental results for the inverter integrated measurement of the phase current and the inverter distortion voltage at different stator electrical frequencies using Inverter 2 with enabled dead-time compensation. . . . 123
5.26 Experimental results for the inverter integrated measurement of the voltage distortion curve. The data points are identical to the first electrical period in Fig. 5.25. . . . 124
5.27 The effect of PWM overmodulation near maximum and minimum duty cycle. . . . 125
5.28 The effect of current sensor delay on the inverter voltage distortion curve. The current sensor signal is delayed by 300 µs. . . . 125
5.29 Experimental results for the adaptive calibration process after artificially introduced sensor offsets. . . . 126
5.30 Experimental results of the detected sensor offsets and adjusted calibration offsets as a function of the stator current magnitude at a constant frequency of 12.75 Hz. . . . 127
5.31 Experimental results of the detected sensor offsets and adjusted calibration offsets as a function of the stator fudamental frequency at a constant current magnitude of 100 A. . . . 128
5.32 Circuit diagram of the voltage measurement circuit with DC-link voltage measurement. . . . 130
5.33 Sampling points for semiconductor voltage drop detection. . . . 130
5.34 Experimentally captured 2^{nd} phase bottom switch 'on'-state voltage drop and current. . . . 130
5.35 Measured MOSFET 'on'-state voltage drop plotted over current for an operating point of 100 A and 30 Hz using the internal measuring circuit of Inverter 1. . . . 131
5.36 Measurement of the 'on'-state resistance and the DBC temperature over time using the VSI-integrated measurement circuit of Inverter 1. . . . 132
5.37 MOSFET 'on'-state resistances and coefficients as a function of the DBC temperature measured at phase 2. . . . 133
5.38 Experimental evaluation of the influence of current magnitude and fundamental frequency on the detection of $R^{\Diamond}_{\text{ds,on}}$. . . . 134
5.39 Photograph of the opened power MOSFET module of Inverter 1. . . . 135
5.40 Measurement of the 'on'-state resistance and the DBC temperature over time with removed defective MOSFET at phase 2 of Inverter 1. . . . 135
5.41 Estimation of thermal micro cycles of twice the fundamental frequency using the internal measuring circuit of Inverter 1 at 0.05 Hz and 250 A. . . . 136

5.42 Comparison between the instantaneous stator-voltage sensing circuit and reference-voltage-based detection in the complex 'αβ'-reference frame. . 138
5.43 Low-speed motoring operation of the IM drive without dedicated speed tranducer. 139
5.44 Speed reversals using the sliding-mode inherently sensorless stator flux-linkage observer with a torque reference of ±3 Nm. Experiment done with IM26kA and Inverter 1. 139

6.1 Trajectories of the operating point and stator current in RFO coordinates. 141
6.2 Decoupling and flux-linkage regulation without considering the maximum current constraint. 143
6.3 Step response as a function of the torque reference input trajectory filter. 143
6.4 Step response as a function of the flux-linkage PI-controller bandwidth. . 145
6.5 Step response as a function of an additional i_{sd} current constraint 145
6.6 Experimental step-response results of the efficiency-optimized direct SFO controller with input trajectory filter. 146
6.7 Simulated RFO current locus diagram. Step response from zero torque to 100 Nm. 147
6.8 Signal-flow diagram of the modified FOC controller with stator current trajectory planner. 148
6.9 Linearized maximum current constraint as a function of the number of constraints. 149
6.10 Simultaneous torque and flux-linkage step response with MPC based optimal current sharing. 151
6.11 RFO current locus diagram as a function of the reference flux-linkage magnitude. 153
6.12 RFO current locus diagram as a function of the reference air-gap torque. 153
6.13 RFO current locus diagram as a function of the initial flux-linkage magnitude. 154
6.14 RFO current locus diagram as a function of the initial flux-linkage magnitude. 154
6.15 Simulation results of the stator current space-vector angle as a function of reference torque and estimated rotor flux linkage. 155
6.16 Lookup table for the current vector angle generated from Fig. 6.15 using thin-plate spline interpolation and resulting lookup table for the dynamic flux-producing current constraint. 156

A.1 Single-phase representation of symmetrical three-phase systems using space vectors. 164
A.2 Test Bench 1 with two 26 kW induction machines and TS200 torque sensor. IM26kB is star-connected and IM26kA is in delta configuration and equipped with four rotor temperature sensors. 166

A.3 Test Bench 2 with two 750 W IMs of type IM750 and TS10 torque sensor. The left machine is equipped with a 720 pulses incremental encoder. . . . 166
A.4 Nameplate data of the investigated IMs. 167
A.5 IM26kA is equipped with four PT100 temperature sensors screwed to the aluminum rotor end ring in steps of 90°. 167
A.6 VSIs developed and used for testing in this work. All systems are equipped with instantaneous output voltage sensing and use the same software developed in this work. 169
A.7 Simplified structure of the developed inverter control and driver PCB. . . 170
A.8 Torque sensors used in this work. 171
A.9 Simplified structure of the FPGA functional components implemented in VHDL. 172
A.10 Simplified structure of the DSP functional components implemented in C++. 173
A.11 Concept of the time-resolved data container. 174
A.12 Simplified signal-flow diagram of the software in the loop simulation model. 175

List of Tables

2.1 Stator and Rotor Resistance Temperature Coefficients 19
2.2 Parameter Dependencies of Basic Field Oriented IM Controllers 28
2.3 MOSFET Voltage Drop Datasheet Values 38
2.4 Overview of the IM Model Parameter Uncertainties 42

4.1 Assumed Worst-Case Parameter Deviation 62

5.1 Voltage Measurement Circuit Parameters of Inverter 2 109

6.1 MPC Optimization Parameters 150

A.2 IM26kA Datasheet Values 167
A.3 Induction Machine Model Parameters 168
A.4 Inverter Data 171
A.5 Torque-Sensor Specifications 171

Bibliography

[ABM12] ABM Greiffenberger Antriebstechnik. *DG112M-4 EL: 3-phase induction motor*. datasheet. 2012 (cit. on p. 167).

[Abr02] Abrahamsen, F. 'Energy Optimal Control of Induction Motor Drives'. In: *Control in Power Electronics*. Elsevier, 2002, pp. 209–224. ISBN: 9780124027725. DOI: 10.1016/B978-012402772-5/50007-7 (cit. on p. 30).

[Ave+15] Avenas, Y., Dupont, L., Baker, N., Zara, H., and Barruel, F. 'Condition Monitoring: A Decade of Proposed Techniques'. In: *IEEE Industrial Electronics Magazine* 9.4 (2015), pp. 22–36. ISSN: 1932-4529. DOI: 10.1109/MIE.2015.2481564 (cit. on p. 129).

[ADK12] Avenas, Y., Dupont, L., and Khatir, Z. 'Temperature Measurement of Power Semiconductor Devices by Thermo-Sensitive Electrical Parameters—A Review'. In: *IEEE Transactions on Power Electronics* 27.6 (2012), pp. 3081–3092. ISSN: 08858993. DOI: 10.1109/TPEL.2011.2178433 (cit. on p. 129).

[Bab+14] Babel, A., Muetze, A., Seebacher, R., Krischan, K., and Strangas, E. G. 'Condition monitoring and failure prognosis of IGBT inverters based on on-line characterization'. In: *2014 IEEE Energy Conversion Congress and Exposition (ECCE)*. IEEE, 2014, pp. 3059–3066. ISBN: 978-1-4799-5776-7. DOI: 10.1109/ECCE.2014.6953816 (cit. on p. 129).

[Bak+14] Baker, N., Liserre, M., Dupont, L., and Avenas, Y. 'Improved Reliability of Power Modules: A Review of Online Junction Temperature Measurement Methods'. In: *IEEE Industrial Electronics Magazine* 8.3 (2014), pp. 17–27. ISSN: 1932-4529. DOI: 10.1109/MIE.2014.2312427 (cit. on p. 129).

[BC07] Batzel, T. D. and Comanescu, M. 'Instantaneous voltage measurement in PWM voltage source inverters'. In: *2007 International Aegean Conference on Electrical Machines and Power Electronics (ACEMP) and Electromotion '07*. 2007, pp. 168–173. DOI: 10.1109/ACEMP.2007.4510497 (cit. on p. 100).

[BCP14] Bedetti, N., Calligaro, S., and Petrella, R. 'Accurate modeling, compensation and self-commissioning of inverter voltage distortion for high-performance motor drives'. In: *2014 IEEE Applied Power Electronics Conference and Exposition - APEC 2014*. 2014, pp. 1550–1557. DOI: 10.1109/APEC.2014.6803513 (cit. on p. 40).

[BS10] Benner, P. and Schneider, A. 'Balanced Truncation Model Order Reduction for LTI Systems with many Inputs or Outputs'. In: *19th International Symposium on Mathematical Theory of Networks and Systems, MTNS 2010. 5 - 9 July, 2010, Budapest, Hungary ; proceedings*. Ed. by Edelmayer, A. Budapest, 2010, pp. 1971–1974. ISBN: 978-963-311-370-7 (cit. on pp. 93, 161).

[Bla74] Blaschke, F. 'Das Verfahren der Feldorientierung zur Regelung der Drehfeldmaschine'. PhD thesis. Technische Universität Braunschweig, 1974 (cit. on pp. 1, 25).

[BM07] Böcker, J. and Mathapati, S. 'State of the Art of Induction Motor Control'. In: *2007 IEEE International Electric Machines & Drives Conference*. IEEE, 2007, pp. 1459–1464. ISBN: 1-4244-0742-7. DOI: 10.1109/IEMDC.2007.383643 (cit. on p. 85).

[CNH97] Chin, T.-H., Nakano, M., and Hirayama, T. 'Accurate measurement of instantaneous voltage for power electronics circuits'. In: *Power Conversion Conference - PCC '97*. 1997, pp. 881–884. DOI: 10.1109/PCCON.1997.638361 (cit. on p. 100).

[CJR97] Chis, M., Jayaram, S., and Rajashekara, K. 'Neural network-based efficiency optimization of EV drive'. In: *CCECE '97. Canadian Conference on Electrical and Computer Engineering. Engineering Innovation: Voyage of Discovery. Conference Proceedings*. IEEE, 1997, pp. 454–461. ISBN: 0-7803-3716-6. DOI: 10.1109/CCECE.1997.608256 (cit. on p. 30).

[CS08] Cho, K.-R. and Seok, J.-K. 'Correction on Current Measurement Errors for Accurate Flux Estimation of AC Drives at Low Stator Frequency'. In: *IEEE Transactions on Industry Applications* 44.2 (2008), pp. 594–603. ISSN: 00939994. DOI: 10.1109/TIA.2008.916730 (cit. on pp. 80, 81).

[CS98] Chung, D.-W. and Sul, S.-K. 'Analysis and compensation of current measurement error in vector-controlled AC motor drives'. In: *IEEE Transactions on Industry Applications* 34.2 (1998), pp. 340–345. ISSN: 0093-9994. DOI: 10.1109/28.663477 (cit. on pp. 79, 80).

[CD03] Clegg, A. G. and Dovaston, N. G. 'Conductors and Superconductors'. In: *Electrical engineer's reference book*. Ed. by Laughton, M. A. and Warne, D. J. Oxford: Newnes, 2003. ISBN: 0750646373 (cit. on p. 19).

[Dav+12] Davari, S. A., Khaburi, D. A., Wang, F., and Kennel, R. M. 'Using Full Order and Reduced Order Observers for Robust Sensorless Predictive Torque Control of Induction Motors'. In: *IEEE Transactions on Power Electronics* 27.7 (2012), pp. 3424–3433. ISSN: 08858993. DOI: 10.1109/TPEL.2011.2179812 (cit. on p. 49).

[De 91] De Doncker, R. W. 'Parameter sensitivity of indirect universal field oriented controllers'. In: *PESC '91 Record 22nd Annual IEEE Power Electronics Specialists Conference* (Cambridge, MA, USA). IEEE, 1991, pp. 605–612. ISBN: 0-7803-0090-4. DOI: 10.1109/PESC.1991.162737 (cit. on p. 27).

[DBG85] De Doncker, R. W., Brijs, B., and Geysen, W. 'Thermal models of inverter fed asynchronous machines suited for an adaptive control of the digital feed forward circuits of the inverter; Theory and simulation'. In: *11th IMACS World Congress*. 1985, pp. 311–314 (cit. on p. 91).

[DN88] De Doncker, R. W. and Novotny, D. W. 'The universal field oriented controller'. In: *Conference Record of the 1988 IEEE Industry Applications Society Annual Meeting*. Conference Record of the 1988 IEEE Industry Applications Society Annual Meeting (Pittsburgh, PA, USA). IEEE, 1988, pp. 450–456. DOI: 10.1109/IAS.1988.25099 (cit. on p. 26).

[DN94] De Doncker, R. W. and Novotny, D. W. 'The universal field oriented controller'. In: *IEEE Transactions on Industry Applications* 30.1 (1994), pp. 92–100. ISSN: 00939994. DOI: 10.1109/28.273626 (cit. on p. 26).

[DVG86a] De Doncker, R. W., Vandenput, A., and Geysen, W. 'A digital field oriented controller using the double cage induction motor model'. In: *1986 17th Annual IEEE Power Electronics Specialists Conference*. 1986 17th Annual IEEE Power Electronics Specialists Conference (Vancouver, Canada). IEEE, 1986, pp. 502–509. ISBN: 978-9-9963-2327-0. DOI: 10.1109/PESC.1986.7415600 (cit. on p. 23).

[DVG86b] De Doncker, R. W., Vandenput, A., and Geysen, W. 'Thermal models of inverter fed asynchronous machines suited for adaptive temperature compensation of field oriented controllers'. In: *Conf. Rec. IEEE-IAS Annual. Meeting*. Vol. 1. 1986, pp. 132–139 (cit. on p. 91).

[De 92] De Doncker, R. W. 'Field-oriented controllers with rotor deep bar compensation circuits (induction machines)'. In: *IEEE Transactions on Industry Applications* 28.5 (1992), pp. 1062–1071. ISSN: 0093-9994. DOI: 10.1109/28.158830 (cit. on pp. 23, 27).

[DPV11] De Doncker, R. W., Pulle, D. W., and Veltman, A. *Advanced Electrical Drives: Analysis, Modeling, Control*. Power Systems. Dordrecht: Springer Science + Business Media B.V., 2011. ISBN: 978-94-007-0181-6 (cit. on pp. 10, 23, 26).

[DBS16] Denk, M., Bakran, M. M., and Schafferhans, S. 'Case Sensitive Condition Monitoring of an IGBT Inverter in a Hybrid Car'. In: *CIPS 2016 - 9th International Conference on Integrated Power Electronics Systems*. Piscataway, NJ: IEEE, 2016. ISBN: 978-3-8007-4171-7 (cit. on p. 129).

[Di 97] Di Ruscio, D. 'Model predictive control and identification: A linear state space model approach'. In: *Proceedings of the 36th IEEE Conference on Decision and Control*. IEEE, 1997, pp. 3202–3209. ISBN: 0-7803-4187-2. DOI: 10.1109/CDC.1997.652336 (cit. on pp. 149, 179).

[Di 13] Di Ruscio, D. 'Model Predictive Control with Integral Action: A simple MPC algorithm'. In: *Modeling, Identification and Control: A Norwegian Research Bulletin* 34.3 (2013), pp. 119–129. ISSN: 0332-7353. DOI: 10.4173/mic.2013.3.2 (cit. on p. 149).

[Dit98] Dittrich, A. 'Model based identification of the iron loss resistance of an induction machine'. In: *Seventh International Conference on Power Electronics and Variable Speed Drives*. 1998, pp. 500–503. DOI: 10.1049/cp:19980577 (cit. on p. 21).

[DB11] Dorf, R. C. and Bishop, R. H. *Modern control systems*. 12th ed. Upper Saddle River, NJ: Prentice Hall Pearson, 2011. ISBN: 9780136024583 (cit. on pp. 14, 48, 176).

[DU95] Drakunov, S. and Utkin, V. 'Sliding mode observers. Tutorial'. In: *Proceedings of 1995 34th IEEE Conference on Decision and Control*. IEEE, 1995, pp. 3376–3378. ISBN: 0-7803-2685-7. DOI: 10.1109/CDC.1995.479009 (cit. on p. 52).

[FO93] Fetz, J. and Obayashi, K. 'High efficiency induction motor drive with good dynamic performance for electric vehicles'. In: *Proceedings of IEEE Power Electronics Specialist Conference - PESC '93*. IEEE, 1993, pp. 921–927. ISBN: 0-7803-1243-0. DOI: 10.1109/PESC.1993.472031 (cit. on p. 30).

[FKP05] Franke, U., Kruemmer, R., and Petzoldt, J. 'Online diagnostics and condition monitoring in voltage source inverters'. In: *2005 European Conference on Power Electronics and Applications*. IEEE, 2005, 6 pp–P.6. ISBN: 90-75815-09-3. DOI: 10.1109/EPE.2005.219318 (cit. on p. 129).

[FPW02] Franklin, G. F., Powell, J. D., and Workman, M. L. *Digital control of dynamic systems*. 3rd ed. Menlo Park, Calif.: Addison-Wesley, 2002. ISBN: 978-0201331530 (cit. on pp. 55, 56).

[GŽ10] Gacho, J. and Žalman, M. 'IM Based Speed Servodrive with Luenberger Observer'. In: *Journal of Electrical Engineering* 61.3 (2010), p. 31. ISSN: 1335-3632. DOI: 10.2478/v10187-011-0021-8 (cit. on pp. 49, 177).

[Ger+07] Gerada, C., Bradley, K. J., Sumner, M., and Sewell, P. 'Evaluation and Modeling of Cross Saturation Due to Leakage Flux in Vector-Controlled Induction Machines'. In: *IEEE Transactions on Industry Applications* 43.3 (2007), pp. 694–702. ISSN: 0093-9994. DOI: 10.1109/TIA.2007.895741 (cit. on p. 17).

[Gia14] Giancoli, D. C. *Physics for scientists & engineers with modern physics*. Fourth edition, Pearson New International edition. Pearson custom library. Harlow, Essex: Pearson Education Limited, 2014. ISBN: 9781292034010 (cit. on p. 18).

[Gop71] Gopinath, B. 'On the Control of Linear Multiple Input-Output Systems*'. In: *Bell System Technical Journal* 50.3 (1971), pp. 1063–1081. ISSN: 00058580. DOI: 10.1002/j.1538-7305.1971.tb01896.x (cit. on p. 46).

[GD04] Götting, G. and De Doncker, R. W. 'Active drive control of electric vehicles using a modal state observer'. In: *2004 IEEE 35th Annual Power Electronics Specialists Conference*. 2004, pp. 4585–4590. DOI: 10.1109/PESC.2004.1354810 (cit. on p. 156).

[Gri+01] Griva, G., Ferraris, P., Profumo, F., Bojoi, R., Maceratini, R., and Barba, G. 'Luenberger Observer for High Speed Induction Machine Drives based on a New Pole Placement Method'. In: *9th European Conference on Power Electronics and Applications*. Brussels: EPE Association, 2001, pp. 1–6. ISBN: 9075815069 (cit. on pp. 49, 177).

[GKP05] Gu, D.-W., Konstantinov, M. M., and Petkov, P. H. *Robust Control Design with MATLAB*. Advanced Textbooks in Control and Signal Processing. London: Springer-Verlag London Limited, 2005. ISBN: 1852339837. DOI: 10.1007/b135806 (cit. on p. 49).

[HCB18] Haque, M. S., Choi, S., and Baek, J. 'Auxiliary Particle Filtering-Based Estimation of Remaining Useful Life of IGBT'. In: *IEEE Transactions on Industrial Electronics* 65.3 (2018), pp. 2693–2703. ISSN: 02780046. DOI: 10.1109/TIE.2017.2740856 (cit. on p. 129).

[Har+08] Harke, M. C., Guerrero, J. M., Degner, M. W., Briz, F., and Lorenz, R. D. 'Current Measurement Gain Tuning Using High-Frequency Signal Injection'. In: *IEEE Transactions on Industry Applications* 44.5 (2008), pp. 1578–1586. ISSN: 0093-9994. DOI: 10.1109/TIA.2008.2002170 (cit. on p. 80).

[HL08] Harke, M. C. and Lorenz, R. D. 'The Spatial Effect and Compensation ofCurrent Sensor Differential Gains for Three-Phase Three-Wire Systems'. In: *IEEE Transactions on Industry Applications* 44.4 (2008), pp. 1181–1189. ISSN: 0093-9994. DOI: 10.1109/TIA.2008.926208 (cit. on p. 80).

[HVB99] Hering, E., Vogt, A., and Bressler, K. 'Elektrische Maschinen und Antriebe'. In: *Handbuch der elektrischen Anlagen und Maschinen*. Ed. by Hering, E., Vogt, A., and Bressler, K. Berlin, Heidelberg: Springer Berlin Heidelberg, 1999, pp. 1–298. ISBN: 978-3-642-63592-2. DOI: 10.1007/978-3-642-58433-6 (cit. on p. 23).

[Hol06] Holtz, J. 'Sensorless Control of Induction Machines - With or Without Signal Injection?' In: *IEEE Transactions on Industrial Electronics* 53.1 (2006), pp. 7–30. ISSN: 02780046. DOI: 10.1109/TIE.2005.862324 (cit. on p. 85).

[Int08] International Rectifier. *IRFP4668PbF: HEXFET Power MOSFET*. datasheet. 2008 (cit. on p. 39).

[JL94] Jansen, P. L. and Lorenz, R. D. 'A physically insightful approach to the design and accuracy assessment of flux observers for field oriented induction machine drives'. In: *IEEE Transactions on Industry Applications* 30.1 (1994), pp. 101–110. ISSN: 0093-9994. DOI: 10.1109/28.273627 (cit. on pp. 43, 46, 57, 157).

[JL95] Jansen, P. L. and Lorenz, R. D. 'Transducerless position and velocity estimation in induction and salient AC machines'. In: *IEEE Transactions on Industry Applications* 31.2 (1995), pp. 240–247. ISSN: 00939994. DOI: 10.1109/28.370269 (cit. on p. 139).

[JL96] Jansen, P. L. and Lorenz, R. D. 'Transducerless field orientation concepts employing saturation-induced saliencies in induction machines'. In: *IEEE Transactions on Industry Applications* 32.6 (1996), pp. 1380–1393. ISSN: 0093-9994. DOI: 10.1109/28.556642 (cit. on pp. 17, 139).

[JLN94] Jansen, P. L., Lorenz, R. D., and Novotny, D. W. 'Observer-based direct field orientation: Analysis and comparison of alternative methods'. In: *IEEE Transactions on Industry Applications* 30.4 (1994), pp. 945–953. ISSN: 0093-9994. DOI: 10.1109/28.297911 (cit. on pp. 28, 46, 64).

[Jun+06] Jung, H.-S., Hwang, S.-H., Kim, J.-M., Kim, C.-U., and Choi, C. 'Diminution of Current-Measurement Error for Vector-Controlled AC Motor Drives'. In: *IEEE Transactions on Industry Applications* 42.5 (2006), pp. 1249–1256. ISSN: 00939994. DOI: 10.1109/TIA.2006.880904 (cit. on p. 80).

[Ken01] Kenny, B. H. 'Deadbeat direct torque control of induction machines using self-sensing at low and zero speed'. PhD thesis. University of Wisconsin–Madison, 2001 (cit. on p. 1).

[KSL14] Kim, M., Sul, S.-K., and Lee, J. 'Compensation of Current Measurement Error for Current-Controlled PMSM Drives'. In: *IEEE Transactions on Industry Applications* 50.5 (2014), pp. 3365–3373. ISSN: 00939994. DOI: 10.1109/TIA.2014.2301873 (cit. on p. 81).

[KNL85] Kirschen, D. S., Novotny, D. W., and Lipo, T. A. 'On-Line Efficiency Optimization of a Variable Frequency Induction Motor Drive'. In: *IEEE Transactions on Industry Applications* IA-21.3 (1985), pp. 610–616. ISSN: 0093-9994. DOI: 10.1109/TIA.1985.349717 (cit. on p. 30).

[KNL87] Kirschen, D. S., Novotny, D. W., and Lipo, T. A. 'Optimal Efficiency Control of an Induction Motor Drive'. In: *IEEE Transactions on Energy Conversion* EC-2.1 (1987), pp. 70–76. ISSN: 0885-8969. DOI: 10.1109/TEC.1987.4765806 (cit. on p. 30).

[KLM15] Koupeny, J., Lucke, S., and Mertens, A. 'Observer-based online parameter estimation of squirrel-cage induction machines based on the gradient descent method'. In: *2015 17th European Conference on Power Electronics and Applications (EPE'15 ECCE-Europe)*. IEEE, 2015, pp. 1–10. ISBN: 978-9-0758-1522-1. DOI: 10.1109/EPE.2015.7309099 (cit. on p. 91).

[KLM16] Koupeny, J., Lucke, S., and Mertens, A. 'Extended observer-based simultaneous online parameter estimation of inverter-fed squirrel-cage induction machines considering the influence of current and speed measurement errors'. In: *2016 18th European Conference on Power Electronics and Applications (EPE'16 ECCE Europe)*. IEEE, 2016, pp. 1–10. ISBN: 978-9-0758-1524-5. DOI: 10.1109/EPE.2016.7695353 (cit. on p. 91).

[Kra+17] Kraaijeveld, R., Dorn, M., Wolff, K., and Schubert, M. 'New torque vectoring functions for modular electrical propulsion'. In: *8th International Munich Chassis Symposium 2017*. Ed. by Pfeffer, P. P. E. Proceedings. Wiesbaden: Springer Fachmedien Wiesbaden, 2017, pp. 447–464. ISBN: 978-3-658-18458-2. DOI: 10.1007/978-3-658-18459-9_29 (cit. on pp. 3, 4, 156).

[KMN93] Kubota, H., Matsuse, K., and Nakano, T. 'DSP-based speed adaptive flux observer of induction motor'. In: *IEEE Transactions on Industry Applications* 29.2 (1993), pp. 344–348. ISSN: 0093-9994. DOI: 10.1109/28.216542 (cit. on p. 48).

[LA06] Lascu, C. and Andreescu, G.-D. 'Sliding-mode observer and improved integrator with DC-offset compensation for flux estimation in sensorless-controlled induction motors'. In: *IEEE Transactions on Industrial Electronics* 53.3 (2006), pp. 785–794. ISSN: 02780046. DOI: 10.1109/TIE.2006.874275 (cit. on pp. 53, 81).

[LBB05] Lascu, C., Boldea, I., and Blaabjerg, F. 'Very-Low-Speed Variable-Structure Control of Sensorless Induction Machine Drives Without Signal Injection'. In: *IEEE Transactions on Industry Applications* 41.2 (2005), pp. 591–598. ISSN: 0093-9994. DOI: 10.1109/TIA.2005.844398 (cit. on pp. 51, 52).

[LBB06] Lascu, C., Boldea, I., and Blaabjerg, F. 'Comparative study of adaptive and inherently sensorless observers for variable-speed induction-motor drives'. In: *IEEE Transactions on Industrial Electronics* 53.1 (2006), pp. 57–65. ISSN: 02780046. DOI: 10.1109/TIE.2005.862314 (cit. on p. 53).

[LBB09] Lascu, C., Boldea, I., and Blaabjerg, F. 'A Class of Speed-Sensorless Sliding-Mode Observers for High-Performance Induction Motor Drives'. In: *IEEE Transactions on Industrial Electronics* 56.9 (2009), pp. 3394–3403. ISSN: 0278 0046. DOI: 10.1109/TIE.2009.2022518 (cit. on p. 53).

[Ler12] Lerch, R. 'Regression, lineare Korrelation und Hypothesen-Testverfahren'. In: *Elektrische Messtechnik*. Ed. by Lerch, R. Springer-Lehrbuch. Berlin, Heidelberg: Springer Berlin Heidelberg, 2012, pp. 473–496. ISBN: 978-3-642-22608-3. DOI: 10.1007/978-3-642-22609-0_14 (cit. on p. 119).

[Lev97] Levi, E. 'Impact of cross-saturation on accuracy of saturated induction machine models'. In: *IEEE Transactions on Energy Conversion* 12.3 (1997), pp. 211–216. ISSN: 0885-8969. DOI: 10.1109/60.629705 (cit. on p. 17).

[LWV92] Lipshitz, S. P., Wannamaker, R. A., and Vanderkooy, J. 'Quantization and Dither: A Theoretical Survey'. In: *J. Audio Eng. Soc* 40.5 (1992), pp. 355–375. URL: http://www.aes.org/e-lib/browse.cfm?elib=7047 (cit. on pp. 114, 161).

[LN90] Lorenz, R. D. and Novotny, D. W. 'Saturation effects in field-oriented induction machines'. In: *IEEE Transactions on Industry Applications* 26.2 (1990), pp. 283–289. ISSN: 00939994. DOI: 10.1109/28.54254 (cit. on p. 15).

[LKM16] Luecke, S., Koupeny, J., and Mertens, A. 'Induction machine speed tracking based on rotor slot harmonics using a modified PLL approach'. In: *2016 18th European Conference on Power Electronics and Applications (EPE'16 ECCE Europe)*. IEEE, 2016, pp. 1–10. ISBN: 978-9-0758-1524-5. DOI: 10.1109/EPE.2016.7695518 (cit. on p. 139).

[LM17] Luecke, S. and Mertens, A. 'Self-sensing control of induction machines using an additional short-circuited rotor coil'. In: *2017 IEEE International Symposium on Sensorless Control for Electrical Drives (SLED)*. IEEE, 2017, pp. 13–18. ISBN: 978-1-5090-6587-5. DOI: 10.1109/SLED.2017.8078420 (cit. on p. 139).

[Lue64] Luenberger, D. G. 'Observing the State of a Linear System'. In: *IEEE Transactions on Military Electronics* 8.2 (1964), pp. 74–80. ISSN: 0536-1559. DOI: 10.1109/TME.1964.4323124 (cit. on p. 47).

[MM00] Maes, J. and Melkebeek, J. A. 'Speed-sensorless direct torque control of induction motors using an adaptive flux observer'. In: *IEEE Transactions on Industry Applications* 36.3 (2000), pp. 778–785. ISSN: 0093-9994. DOI: 10.1109/28.845053 (cit. on pp. 49, 52, 176).

[MVZ15] Magee, D. P., Veltman, A., and Zambada, J. 'STATOR RESISTANCE ESTIMATION FOR ELECTRIC MOTORS'. U.S. pat. US2015097500 (A1). 2015 (cit. on pp. 42, 91).

[Mat16] MathWorks. *MATLAB*. Version 2016a. Natick, MA: MathWorks, 2016. URL: https://www.mathworks.com (cit. on p. 149).

[Mat+99] Matsuse, K., Yoshizumi, T., Katsuta, S., and Taniguchi, S. 'High-response flux control of direct-field-oriented induction motor with high efficiency taking core loss into account'. In: *IEEE Transactions on Industry Applications* 35.1 (1999), pp. 62–69. ISSN: 00939994. DOI: 10.1109/28.740846 (cit. on p. 142).

[MD00] Menne, M. and De Doncker, R. W. 'Active damping of electric vehicle drivetrain oscillations'. In: *Proceedings / 9th International Conference and Exhibition on Power Electronics and Motion Control, EPE-PEMC 2000*. 2000. ISBN: 80-88922-18-6 (cit. on p. 156).

[MR93] Muske, K. R. and Rawlings, J. B. 'Model predictive control with linear models'. In: *AIChE Journal* 39.2 (1993), pp. 262–287. ISSN: 0001-1541. DOI: 10.1002/aic.690390208 (cit. on p. 148).

[Ped+17] Pedersen, K. B., Kristensen, P. K., Pedersen, K., Uhrenfeldt, C., and Munk-Nielsen, S. 'Vce as early indicator of IGBT module failure mode'. In: *2017 IEEE International Reliability Physics Symposium (IRPS)*. IEEE, 2017, FA-1.1–FA-1.6. ISBN: 978-1-5090-6641-4. DOI: 10.1109/IRPS.2017.7936371 (cit. on p. 129).

[PZ10] Peretti, L. and Zigliotto, M. 'FPGA-based voltage measurements in AC drives'. In: *2010 XIX International Conference on Electrical Machines (ICEM)*. 2010, pp. 1–6. DOI: 10.1109/ICELMACH.2010.5608153 (cit. on p. 101).

[PHH15] Pfingsten, G. V., Hombitzer, M., and Hameyer, K. 'Influence of production uncertainties and operational conditions on torque characteristic of an induction machine'. In: *2015 5th International Electric Drives Production Conference (EDPC)*. IEEE, 2015, pp. 1–5. ISBN: 978-1-4673-7511-5. DOI: 10.1109/EDPC.2015.7439558 (cit. on p. 4).

[Qi+16a] Qi, F., Ralev, I., Klein-Hessling, A., and De Doncker, R. W. 'Online temperature estimation of an automotive switched reluctance motor using space-resolved lumped parameter network'. In: *2016 19th International Conference on Electrical Machines and Systems (ICEMS)*. IEEE, 2016, pp. 1–6. ISBN: 978-4-88686-098-9 (cit. on p. 93).

[QSD14] Qi, F., Schenk, M., and De Doncker, R. W. 'Discussing details of lumped parameter thermal modeling in electrical machines'. In: *7th IET International Conference on Power Electronics, Machines and Drives (PEMD 2014)*. Institution of Engineering and Technology, 2014, pp. 2.11.04–2.11.04. ISBN: 978-1-84919-815-8. DOI: 10.1049/cp.2014.0479 (cit. on p. 93).

[Qi+16b] Qi, F., Ly, D. A., van der Broeck, C., Yan, D., and De Doncker, R. W. 'Model order reduction suitable for online linear parameter-varying thermal models of electric motors'. In: *2016 IEEE 2nd Annual Southern Power Electronics Conference (SPEC)*. IEEE, 2016, pp. 1–6. ISBN: 978-1-5090-1546-7. DOI: 10.1109/SPEC.2016.7846147 (cit. on pp. 93, 161).

[Qi+17] Qi, F., Scharfenstein, D., Schubert, M., and De Doncker, R. W. 'Precise field oriented torque control of induction machines using thermal model based resistance adaption'. In: *2017 IEEE 12th International Conference on Power*

Electronics and Drive Systems (PEDS). IEEE, 2017, pp. 1, 055–1, 061. ISBN: 978-1-5090-2364-6. DOI: 10.1109/PEDS.2017.8289166 (cit. on pp. 91–93).

[Qi+14] Qi, F., Stippich, A., Guettler, M., Neubert, M., and De Doncker, R. W. 'Methodical considerations for setting up space-resolved lumped-parameter thermal models for electrical machines'. In: *2014 17th International Conference on Electrical Machines and Systems (ICEMS)*. IEEE, 2014, pp. 651–657. ISBN: 978-1-4799-5162-8. DOI: 10.1109/ICEMS.2014.7013567 (cit. on p. 93).

[Qi+15] Qi, F., Stippich, A., Koschik, S., and De Doncker, R. W. 'Model predictive overload control of induction motors'. In: *2015 IEEE International Electric Machines & Drives Conference (IEMDC)*. IEEE, 2015, pp. 999–1005. ISBN: 978-1-4799-7941-7. DOI: 10.1109/IEMDC.2015.7409183 (cit. on p. 93).

[RT97] Rasmussen, K. and Thøgersen, P. 'Model based energy optimizer for vector controlled induction motor drives'. In: *EPE '97*. Brussels: EPE Association, 1997, pp. 3711–3716. ISBN: 9075815026 (cit. on p. 30).

[RBD01] Reinert, J., Brockmeyer, A., and De Doncker, R. W. 'Calculation of losses in ferro- and ferrimagnetic materials based on the modified Steinmetz equation'. In: *IEEE Transactions on Industry Applications* 37.4 (2001), pp. 1055–1061. ISSN: 0093-9994. DOI: 10.1109/28.936396 (cit. on p. 20).

[Rei96] Reinold, H. *Optimierung dreiphasiger Pulsdauermodulationsverfahren: Zugl.: Aachen, Techn. Hochsch., Diss., 1995*. 1. Aufl. Vol. 15. Aachener Beiträge des ISEA. Aachen: Verl. der Augustinus-Buchh, 1996. ISBN: 3-86073-235-8 (cit. on p. 106).

[Ros04] Rossiter, J. A. *Model-Based Predictive Control: A Practical Approach*. Control series. Boca Raton, FL: CRC Press, 2004. ISBN: 0-8493-1291-4 (cit. on pp. 147, 148, 178).

[Sch92] Schauder, C. 'Adaptive speed identification for vector control of induction motors without rotational transducers'. In: *IEEE Transactions on Industry Applications* 28.5 (1992), pp. 1054–1061. ISSN: 0093-9994. DOI: 10.1109/28.158829 (cit. on p. 52).

[SD15] Schubert, M. and De Doncker, R. W. 'Redundancy of angular speed sensors in a double induction machine rear drive for EV'. In: *2015 IEEE 11th International Conference on Power Electronics and Drive Systems*. 2015, pp. 1144–1151. DOI: 10.1109/PEDS.2015.7203450 (cit. on p. 156).

[SD18] Schubert, M. and De Doncker, R. W. 'Instantaneous Phase Voltage Sensing in PWM Voltage Source Inverters'. In: *IEEE Transactions on Power Electronics* 33.8 (2018), pp. 6926–6935. ISSN: 08858993. DOI: 10.1109/TPEL.2017.2759662 (cit. on pp. 97, 101, 111).

[SGD17] Schubert, M., Girigoudar, K., and De Doncker, R. W. 'MPC based current sharing for maximum torque dynamics in efficiency optimized field oriented induction machine control'. In: *2017 IEEE 12th International Conference on Power Electronics and Drive Systems (PEDS)*. IEEE, 2017, pp. 932–939. ISBN: 978-1-5090-2364-6. DOI: 10.1109/PEDS.2017.8289146 (cit. on p. 142).

[SJD16] Schubert, M., Jebe, L., and De Doncker, R. W. 'Gate driver integrated instantaneous phase voltage measurement in PWM voltage source inverters'. In: *2016 IEEE International Telecommunications Energy Conference (INTELEC)*. 2016, pp. 1–8. DOI: 10.1109/INTLEC.2016.7749120 (cit. on p. 97).

[Sch+17] Schubert, M., Jebe, L., Gossen, M., and De Doncker, R. W. 'Online phase current and voltage offset calibration using inverter voltage distortion'. In: *2017 IEEE 12th International Conference on Power Electronics and Drive Systems (PEDS)*. IEEE, 2017, pp. 721–727. ISBN: 978-1-5090-2364-6. DOI: 10.1109/PEDS.2017.8289267 (cit. on p. 97).

[SKD13] Schubert, M., Koschik, S., and De Doncker, R. W. 'Fast optimal efficiency flux control for induction motor drives in electric vehicles considering core losses, main flux saturation and rotor deep bar effect'. In: *2013 IEEE Applied Power Electronics Conference and Exposition - APEC 2013*. 2013, pp. 811–816. DOI: 10.1109/APEC.2013.6520303 (cit. on p. 30).

[SSD16] Schubert, M., Scharfenstein, D., and De Doncker, R. W. 'On the torque accuracy of stator flux observer based induction machine control'. In: *2016 IEEE Symposium on Sensorless Control for Electrical Drives (SLED)*. 2016, pp. 1–8. DOI: 10.1109/SLED.2016.7518791 (cit. on pp. 19, 59).

[SK11] Schweizer, M. and Kolar, J. W. 'High efficiency drive system with 3-level T-type inverter'. In: *Proceedings of the 2011 14th European Conference on Power Electronics and Applications (EPE 2011)*. Piscataway, NJ: IEEE, 2011. ISBN: 978-90-75815-15-3 (cit. on p. 30).

[Sem13] Semikron. *SKAI 120V BO-W single*. datasheet. Version Rev.00 - DRAFT. 2013 (cit. on p. 39).

[Sht+14] Shtessel, Y., Edwards, C., Fridman, L., and Levant, A. 'Conventional Sliding Mode Observers'. In: *Sliding Mode Control and Observation*. Ed. by Shtessel, Y., Edwards, C., Fridman, L., and Levant, A. Control Engineering. New York, NY: Springer New York, 2014, pp. 105–141. ISBN: 978-0-8176-4892-3. DOI: 10.1007/978-0-8176-4893-0_3 (cit. on p. 52).

[SL96] Sokola, M. and Levi, E. 'Combined impact of iron loss and main flux saturation on operation of vector controlled induction machines'. In: *6th International Conference on Power Electronics and Variable Speed Drives*. 1996, pp. 36–41. DOI: 10.1049/cp:19960884 (cit. on p. 21).

[SBS02] Son, Y.-C., Bae, B.-H., and Sul, S.-K. 'Sensorless operation of permanent magnet motor using direct voltage sensing circuit'. In: *2002 IEEE Industry Applications Society Annual Meeting*. 2002, pp. 1674–1678. DOI: 10.1109/IAS.2002.1043759 (cit. on p. 100).

[SBC95] Sousa, G., Bose, B. K., and Cleland, J. G. 'Fuzzy logic based on-line efficiency optimization control of an indirect vector-controlled induction motor drive'. In: *IEEE Transactions on Industrial Electronics* 42.2 (1995), pp. 192–198. ISSN: 02780046. DOI: 10.1109/41.370386 (cit. on p. 30).

[Sou+92] Sousa, G., Bose, B. K., Cleland, J., Spiegel, R. J., and Chappell, P. J. 'Loss modeling of converter induction machine system for variable speed drive'. In: *1992 International Conference on Industrial Electronics, Control, Instrumentation, and Automation*. 1992, pp. 114–120. DOI: 10.1109/IECON.1992.254595 (cit. on p. 30).

[Ste92] Steinmetz, C. P. 'On the Law of Hysteresis'. In: *Transactions of the American Institute of Electrical Engineers* IX.1 (1892), pp. 1–64. ISSN: 0096-3860. DOI: 10.1109/T-AIEE.1892.5570437 (cit. on p. 20).

[Sti+17] Stippich, A., van der Broeck, C. H., Sewergin, A., Wienhausen, A. H., Neubert, M., Schülting, P., Taraborrelli, S., v. Hoek, H., and De Doncker, R. W. 'Key Components of Modular Propulsion Systems for Next Generation Electric Vehicles'. In: *CPSS Transactions on Power Electronics and Applications* 2.4 (2017), pp. 249–258. ISSN: 2475742X. DOI: 10.24295/CPSSTPEA.2017.00023 (cit. on pp. 1, 129).

[SDK13] Stumper, J.-F., Dotlinger, A., and Kennel, R. 'Loss Minimization of Induction Machines in Dynamic Operation'. In: *IEEE Transactions on Energy Conversion* 28.3 (2013), pp. 726–735. ISSN: 0885-8969. DOI: 10.1109/TEC.2013.2262048 (cit. on p. 142).

[SK13] Stumper, J.-F. and Kennel, R. 'Real-time dynamic efficiency optimization for induction machines'. In: *2013 American Control Conference*. IEEE, 2013, pp. 6589–6594. ISBN: 978-1-4799-0178-4. DOI: 10.1109/ACC.2013.6580873 (cit. on p. 142).

[Tal+16] Tallam, R., Busse, D. F., Brown, B. P., and Kerkman, R. J. 'PWM OUTPUT VOLTAGE MEASUREMENT APPARATUS AND METHOD'. U.S. pat. US937 4021 (B2). 2016 (cit. on p. 102).

[TAN13] Tamura, H., Ajima, T., and Noto, Y. 'A torque ripple reduction method by current sensor offset error compensation'. In: *2013 15th European Conference on Power Electronics and Applications (EPE)*. 2013, pp. 1–10. DOI: 10.1109/EPE.2013.6631858 (cit. on p. 81).

[Tam+14] Tamura, H., Ajima, T., Noto, Y., and Itoh, J.-i. 'A compensation method for a motor phase current sensor offset error using a voltage-source-inverter output voltage reference value'. In: *2014 16th European Conference on Power Electronics and Applications (EPE'14-ECCE Europe)*. 2014, pp. 1–10. DOI: 10.1109/EPE.2014.6910700 (cit. on p. 81).

[TIN15] Tamura, H., Itoh, J.-i., and Noto, Y. 'Two methods for compensating motor-current-sensor offset error by using DC-voltage component included in phase-voltage command for current-controlled PMSM drive'. In: *2015 17th European Conference on Power Electronics and Applications (EPE'15 ECCE-Europe)*. 2015, pp. 1–10. DOI: 10.1109/EPE.2015.7309276 (cit. on p. 81).

[Tex13] Texas Instruments. *InstaSPIN-FOC™ and InstaSPIN-MOTION™: User's Guide*. manual. 2013 (cit. on p. 99).

[USO10] Uenaka, Y., Sazawa, M., and Ohishi, K. 'Fine self-tuning method of both current sensor offset and electrical parameter variations for SPM motor'. In: *IECON 2010 - 36th Annual Conference of IEEE Industrial Electronics*. 2010, pp. 841–846. DOI: 10.1109/IECON.2010.5675177 (cit. on p. 81).

[Utk77] Utkin, V. 'Variable structure systems with sliding modes'. In: *IEEE Transactions on Automatic Control* 22.2 (1977), pp. 212–222. ISSN: 0018-9286. DOI: 10.1109/TAC.1977.1101446 (cit. on p. 52).

[vCD15] van der Broeck, C. H., Conrad, M., and De Doncker, R. W. 'A thermal modeling methodology for power semiconductor modules'. In: *Microelectronics Reliability* 55.9-10 (2015), pp. 1938–1944. ISSN: 00262714. DOI: 10.1016/j.microrel.2015.06.102 (cit. on p. 129).

[vGD18] van der Broeck, C. H., Gospodinov, A., and De Doncker, R. W. 'IGBT Junction Temperature Estimation via Gate Voltage Plateau Sensing'. In: *IEEE Transactions on Industry Applications* (2018), p. 1. ISSN: 0093-9994. DOI: 10.1109/TIA.2018.2836362 (cit. on p. 129).

[vLD18] van der Broeck, C. H., Lorenz, R. D., and De Doncker, R. W. 'Methods for monitoring 3-D temperature distributions in power electronic modules'. In: *2018 IEEE Applied Power Electronics Conference and Exposition (APEC)*. IEEE, 2018, pp. 3022–3030. ISBN: 978-1-5386-1180-7. DOI: 10.1109/APEC.2018.8341531 (cit. on pp. 129, 137).

[van+17] van der Broeck, C. H., Ruppert, L. A., Hinz, A., Conrad, M., and De Doncker, R. W. 'Spatial Electro-Thermal Modeling and Simulation of Power Electronic Modules'. In: *IEEE Transactions on Industry Applications* (2017), p. 1. ISSN: 0093-9994. DOI: 10.1109/TIA.2017.2757898 (cit. on p. 129).

[van+18] van der Broeck, C. H., Ruppert, L. A., Lorenz, R. D., and De Doncker, R. W. 'Active thermal cycle reduction of power modules via gate resistance manipulation'. In: *2018 IEEE Applied Power Electronics Conference and Exposition (APEC)*. IEEE, 2018, pp. 3074–3082. ISBN: 978-1-5386-1180-7. DOI: 10.1109/APEC.2018.8341539 (cit. on p. 129).

[vSS88] van der Broeck, H. W., Skudelny, H.-C., and Stanke, G. V. 'Analysis and realization of a pulsewidth modulator based on voltage space vectors'. In: *IEEE Transactions on Industry Applications* 24.1 (1988), pp. 142–150. ISSN: 00939994. DOI: 10.1109/28.87265 (cit. on p. 106).

[VVL03] Vasic, V., Vukosavic, S. N., and Levi, E. 'A stator resistance estimation scheme for speed sensorless rotor flux oriented induction motor drives'. In: *IEEE Transactions on Energy Conversion* 18.4 (2003), pp. 476–483. ISSN: 0885-8969. DOI: 10.1109/TEC.2003.816595 (cit. on p. 88).

[Vv91] Veltman, A. and van den Bosch, P. P. J. 'A universal method for modelling electrical machines'. In: *Electrical Machines and Drives, 1991. Fifth International Conference on (Conf. Publ. No. 341)*. 1991, pp. 193–197. ISBN: 0-85296-520-6 (cit. on pp. 10, 11, 165).

[vPSH17] V. Pfingsten, G., Steentjes, S., and Hameyer, K. 'Operating Point Resolved Loss Calculation Approach in Saturated Induction Machines'. In: *IEEE Transactions on Industrial Electronics* 64.3 (2017), pp. 2538–2546. ISSN: 02780046. DOI: 10.1109/TIE.2016.2597761 (cit. on pp. 21, 22, 42).

[VL03a] Vukosavic, S. N. and Levi, E. 'A method for transient torque response improvement in optimum efficiency induction motor drives'. In: *IEEE Transactions on Energy Conversion* 18.4 (2003), pp. 484–493. ISSN: 0885-8969. DOI: 10.1109/TEC.2003.816599 (cit. on p. 142).

[VL03b] Vukosavic, S. N. and Levi, E. 'Robust DSP-based efficiency optimization of a variable speed induction motor drive'. In: *IEEE Transactions on Industrial Electronics* 50.3 (2003), pp. 560–570. ISSN: 02780046. DOI: 10.1109/TIE.2003.812468 (cit. on p. 30).

[WL16] Wang, Y. and Lorenz, R. D. 'Using Volt-sec. sensing to extend the low speed range and the disturbance rejection capability of back-EMF-based self-sensing'. In: *2016 18th European Conference on Power Electronics and Applications (EPE'16 ECCE Europe)*. 2016, pp. 1–10. DOI: 10.1109/EPE.2016.7695488 (cit. on p. 101).

[Wan+17] Wang, Y., Xu, Y., Niimura, N., Rudolph, B. D., and Lorenz, R. D. 'Using Volt-Second Sensing to Directly Improve Torque Accuracy and Self-Sensing at Low Speeds'. In: *IEEE Transactions on Industry Applications* (2017), p. 1. ISSN: 0093-9994. DOI: 10.1109/TIA.2017.2702752 (cit. on p. 101).

[WL09] West, N. T. and Lorenz, R. D. 'Digital Implementation of Stator and Rotor Flux-Linkage Observers and a Stator-Current Observer for Deadbeat Direct Torque Control of Induction Machines'. In: *IEEE Transactions on Industry Applications* 45.2 (2009), pp. 729–736. ISSN: 00939994. DOI: 10.1109/TIA.2009.2013567 (cit. on pp. 56, 57).

[XIL13] XILINX. *ISE Design Suite*. Version 14.7. San José, CA: XILINX, 2013. URL: https://www.xilinx.com/ (cit. on p. 112).

[XDN88a] Xu, X., De Doncker, R. W., and Novotny, D. W. 'A stator flux oriented induction machine drive'. In: *PESC '88 Record., 19th Annual IEEE Power Electronics Specialists Conference*. 1988, pp. 870–876. DOI: 10.1109/PESC.1988.18219 (cit. on pp. 28, 34).

[XDN88b] Xu, X., De Doncker, R. W., and Novotny, D. W. 'Stator flux orientation control of induction machines in the field weakening region'. In: *Conference Record of the 1988 IEEE Industry Applications Society Annual Meeting*. IEEE, 1988, pp. 437–443. DOI: 10.1109/IAS.1988.25097 (cit. on p. 34).

[YC90] Yang, G. and Chin, T. H. 'Instantaneous output voltage detector for voltage source inverter'. In: *Proceedings of the IEEJ National Conference*. Vol. 5. 1990, p. 41 (cit. on p. 100).

[ZES12] ZES Zimmer. *LMG500: Precision Power Analyzer*. datasheet. 2012 (cit. on p. 101).

Curriculum Vitae

Michael Schubert

Personal Information

Date of birth	October 7, 1985
Place of birth	Leverkusen, Germany
Nationality	German

Education

10/2006–01/2012	Studies in Electrical Engineering and Information Technology at RWTH Aachen University, Germany; Diploma degree
08/1996–06/2005	Otto-Hahn-Gymnasium in Monheim am Rhein, Germany (high school)

Professional Experience

since 03/2018	Chief Engineer at the Institute for Power Electronics and Electrical Drives (ISEA) of RWTH Aachen University
07/2014–03/2017	Group Leader Electrical Drives at the Institute for Power Electronics and Electrical Drives (ISEA) of RWTH Aachen University
since 03/2012	Research Associate at the Institute for Power Electronics and Electrical Drives (ISEA) of RWTH Aachen University under the supervision of Professor Rik W. De Doncker in the Research Group Electrical Drives
10/2010–04/2011	Internship in the field of Power Electronics at ABB US Corporate Research Center in Raleigh, NC, USA
03/2009–07/2010	Student worker in the GaN Device Technology Research Group at the Institute of Electromagnetic Theory of RWTH Aachen University

Aachen, in December 2018 *Michael Schubert*

Aachener Beiträge des ISEA

ABISEA Band 1
Eßer, A.
Berührungslose, kombinierte Energie- und Informations-übertragung für bewegliche Systeme
1. Auflage 1992, 130 Seiten
ISBN 3-86073-046-0

ABISEA Band 2
Vogel, U.
Entwurf und Beurteilung von Verfahren zur Hochausnutzung des Rad-Schiene-Kraftschlusses durch Triebfahrzeuge
1. Auflage 1992, 130 Seiten
ISBN 3-86073-060-6

ABISEA Band 3
Redehorn, Th.
Stromeinprägendes Antriebssystem mit fremderregter Synchron-maschine
1. Auflage 1992, 130 Seiten
ISBN 3-86073-061-4

ABISEA Band 4
Ackva, A.
Spannungseinprägendes Antriebssystem mit Synchron-maschine und direkter Stromregelung
1. Auflage 1992, 135 Seiten
ISBN 3-86073-062-2

ABISEA Band 5
Mertens, A.
Analyse des Oberschwingungsverhaltens von taktsynchronen Delta - Modulationsverfahren zur Steuerung von Pulsstromrichtern bei hoher Taktzahl
1. Auflage 1992, 170 Seiten
ISBN 3-86073-069-X

ABISEA Band 6
Geuer, W.
Untersuchungen über das Alterungsverhalten von Bleiakkumulatoren
1. Auflage 1993, 100 Seiten
ISBN 3-86073-097-5

ABISEA Band 7
Langheim, J.
Einzelradantrieb für Elektrostraßenfahrzeuge
1. Auflage 1993, 215 Seiten
ISBN 3-86073-123-8
(vergriffen)

ABISEA Band 8
Fetz, J.
Fehlertolerante Regelung eines Asynchron-Doppelantriebes für ein Elektrospeicherfahrzeug
1. Auflage 1993, 136 Seiten
ISBN 3-86073-124-6
(vergriffen)

ABISEA Band 9
Schülting, L.
Optimierte Auslegung induktiver Bauelemente für den Mittelfrequenzbereich
1. Auflage 1993, 136 Seiten
ISBN 3-86073-174-2
(vergriffen)

ABISEA Band 10
Skudelny, H.-Ch.
Stromrichtertechnik
4. Auflage 1997, 259 Seiten
ISBN 3-86073-189-0

ABISEA Band 11
Skudelny, Ch.
Elektrische Antriebe
3. Auflage 1997, 124 Seiten
ISBN 3-86073-231-5

ABISEA Band 12
Schöpe, F.
Batterie-Management für Nickel-Cadmium Akkumulatoren
1. Auflage 1994, 156 Seiten
ISBN 3-86073-232-3
(vergriffen)

ABISEA Band 13
v. d. Weem, J.
Schmalbandige aktive Filter für Schienentriebfahrzeuge am Gleichspannungs-fahrdraht
1. Auflage 1995, 125 Seiten
ISBN 3-86073-233-1

ABISEA Band 14
Backhaus, K.
Spannungseinprägendes Direktantriebssystem mit schnelllaufender geschalteter Reluktanzmaschine
1. Auflage 1995, 156 Seiten
ISBN 3-86073-234-X
(vergriffen)

ABISEA Band 15
Reinold, H.
Optimierung dreiphasiger Pulsdauermodulations-verfahren
1. Auflage 1996, 116 Seiten
ISBN 3-86073-235-8

ABISEA Band 16
Köpken, H.-G.
Regelverfahren für Parallelschwingkreis-umrichter
1. Auflage 1996, 125 Seiten
ISBN 3-86073-236-6

ABISEA Band 17
Mauracher, P.
Modellbildung und Verbundoptimierung bei Elektrostraßenfahrzeugen
1. Auflage 1996, 192 Seiten
ISBN 3-86073-237-4

ABISEA Band 18
Protiwa, F.-F.
Vergleich dreiphasiger Resonanz-Wechselrichter in Simulation und Messung
1. Auflage 1997, 178 Seiten
ISBN 3-86073-238-2

ABISEA Band 19
Brockmeyer, A.
Dimensionierungswerkzeug für magnetische Bau-elemente in Stromrichter-anwendungen
1. Auflage 1997, 182 Seiten
ISBN 3-86073-239-0

Aachener Beiträge des ISEA

ABISEA Band 20
Apeldoorn, 0.
Simulationsgestützte Bewertung von Steuerverfahren für netzgeführte Stromrichter mit verringerter Netzrückwirkung
1. Auflage 1997, 132 Seiten
ISBN 3-86073-680-9

ABISEA Band 21
Lohner, A.
Batteriemanagement für verschlossene Blei-Batterien am Beispiel von Unterbrechungsfreien Stromversorgungen
1. Auflage 1998, 144 Seiten
ISBN 3-86073-681-7

ABISEA Band 22
Reinert, J.
Optimierung der Betriebseigenschaften von Antrieben mit geschalteter Reluktanzmaschine
1. Auflage 1998, 168 Seiten
ISBN 3-86073-682-5

ABISEA Band 23
Nagel, A.
Leitungsgebundene Störungen in der Leistungselektronik: Entstehung, Ausbreitung und Filterung
1. Auflage 1999, 160 Seiten
ISBN 3-86073-683-3

ABISEA Band 24
Menne, M.
Drehschwingungen im Antriebsstrang von Elektrostraßenfahrzeugen - Analyse und aktive Dämpfung
1. Auflage 2001, 192 Seiten
ISBN 3-86073-684-1

ABISEA Band 25
von Bloh, J.
Multilevel-Umrichter zum Einsatz in Mittelspannungs-Gleichspannungs-Übertragungen
1. Auflage 2001, 152 Seiten
ISBN 3-86073-685-X

ABISEA Band 26
Karden, E.
Using low-frequency impedance spectroscopy for characterization, monitoring, and modeling of industrial batteries
1. Auflage 2002, 154 Seiten
ISBN 3-8265-9766-4

ABISEA Band 27
Karipidis, C.-U.
A Versatile DSP/ FPGA Structure optimized for Rapid Prototyping and Digital Real-Time Simulation of Power Electronic and Electrical Drive Systems
1. Auflage 2001, 164 Seiten
ISBN 3-8265-9738-9

ABISEA Band 28
Kahlen, K.
Regelungsstrategien für permanentmagnetische Direktantriebe mit mehreren Freiheitsgraden
1. Auflage 2003, 158 Seiten
ISBN 3-8322-1222-1

ABISEA Band 29
Inderka, R.
Direkte Drehmomentregelung Geschalteter Reluktanzantriebe
1. Auflage 2003, 190 Seiten
ISBN 3-8322-1175-6

ABISEA Band 30
Schröder, S.
Circuit-Simulation Models of High-Power Devices Based on Semiconductor Physics
1. Auflage 2003, 124 Seiten
ISBN 3-8322-1250-7

ABISEA Band 31
Buller, S.
Impedance-Based Simulation Models for Energy Storage Devices in Advanced Automotive Power Systems
1. Auflage 2003, 136 Seiten
ISBN 3-8322-1225-6

ABISEA Band 32
Schönknecht, A.
Topologien und Regelungsstrategien für das induktive Erwärmen mit hohen Frequenz-Leistungsprodukten
1. Auflage 2004, 170 Seiten
ISBN 3-8322-2408-4

ABISEA Band 33
Tolle, T.
Konvertertopologien für ein aufwandsarmes, zweistufiges Schaltnetzteil zum Laden von Batterien aus dem Netz
1. Auflage 2004, 150 Seiten
ISBN 3-8322-2676-1

ABISEA Band 34
Götting, G.
Dynamische Antriebsregelung von Elektrostraßenfahrzeugen unter Berücksichtigung eines schwingungsfähigen Antriebsstrangs
1. Auflage 2004, 166 Seiten
ISBN 3-8322-2804-7

ABISEA Band 35
Dieckerhoff, S.
Transformatorlose Stromrichterschaltungen für Bahnfahrzeuge am 16 2/3Hz Netz
1. Auflage 2004, 158 Seiten
ISBN 3-8322-3094-7

ABISEA Band 36
Hu, J.
Bewertung von DC-DC-Topologien und Optimierung eines DC-DC-Leistungsmoduls für das 42-V-Kfz-Bordnetz
1. Auflage 2004, 156 Seiten
ISBN 3-8322-3201-X

Aachener Beiträge des ISEA

ABISEA Band 37
Detjen, D.-0.
Characterization and Modeling of Si-Si Bonded Hydrophobie Interfaces for Novel High-Power BIMOS Devices
1. Auflage 2004, 146 Seiten
ISBN 3-8322-2963-9

ABISEA Band 38
Walter, J.
Simulationsbasierte Zuverlässigkeitsanalyse in der modernen Leistungselektronik
1. Auflage 2004, 134 Seiten
ISBN 3-8322-3481-0

ABISEA Band 39
Schwarzer, U.
IGBT versus GCT in der Mittelspannungsanwendung - ein experimenteller und simulativer Vergleich
1. Auflage 2005, 184 Seiten
ISBN 3-8322-4489-1

ABISEA Band 40
Bartram, M.
IGBT-Umrichtersysteme für Windkraftanlagen: Analyse der Zyklenbelastung, Modellbildung, Optimierung und Lebensdauervorhersage
1. Auflage 2006, 195 Seiten
ISBN 3-8322-5039-5

ABISEA Band 41
Ponnaluri, S.
Generalized Design, Analysis and Control of Grid side converters with integrated UPS or Islanding functionality
1. Auflage 2006, 163 Seiten
ISBN 3-8322-5281-9

ABISEA Band 42
Jacobs, J.
Multi-Phase Series Resonant DC-to-DC Converters
1. Auflage 2006, 185 Seiten
ISBN 3-8322-5532-X

ABISEA Band 43
Linzen, D.
Impedance-Based Loss Calculation and Thermal Modeling of Electrochemical Energy Storage Devices for Design Considerations of Automotive Power Systems
1. Auflage 2006, 150 Seiten
ISBN 3-8322-5706-3

ABISEA Band 44
Fiedler, J.
Design of Low-Noise Switched Reluctance Drives
1. Auflage 2007, 183 Seiten
ISBN 978-3-8322-5864-l

ABISEA Band 45
Fuengwarodsakul, N.
Predictive PWM-based Direct Instantaneous Torque Control for Switched Reluctance Machines
1. Auflage 2007, 150 Seiten
ISBN 978-3-8322-6210-5

ABISEA Band 46
Meyer, C.
Key Components for Future Offshore DC Grids
1. Auflage 2007, 196 Seiten
ISBN 978-3-8322-6571-7

ABISEA Band 47
Fujii, K.
Characterization and Optimization of Soft-Switched Multi-Level Converters for STATCOMs
1. Auflage 2008, 206 Seiten
ISBN 978-3-8322-6981-4

ABISEA Band 48
Carstensen, C.
Eddy Currents in Windings of Switched Reluctance Machines
1. Auflage 2008, 190 Seiten
ISBN 978-3-8322-7118-3

ABISEA Band 49
Bohlen, 0.
Impedance-based battery monitoring
1. Auflage 2008, 200 Seiten
ISBN 978-3-8322-7606-5

ABISEA Band 50
Thele, M.
A contribution to the modelling of the charge acceptance of lead-acid batteries - using frequency and time domain based concepts
1. Auflage 2008, 168 Seiten
ISBN 978-3-8322-7659-1

ABISEA Band 51
König, A.
High Temperature DC-to-DC Converters for Downhole Applications
1. Auflage 2009, 160 Seiten
ISBN 978-3-8322-8489-3

ABISEA Band 52
Dick, C. P.
Multi-Resonant Converters as Photovoltaic Module-Integrated Maximum Power Point Tracker
1. Auflage 2010, 192 Seiten
ISBN 978-3-8322-9199-0

ABISEA Band 53
Kowal, J.
Spatially-resolved impedance of nonlinear inhomogeneous devices - using the example of lead-acid batteries -
1. Auflage 2010, 214 Seiten
ISBN 978-3-8322-9483-0

ABISEA Band 54
Roscher, M.
Zustandserkennung von LiFeP04-Batterien für Hybrid- und Elektrofahrzeuge
1. Auflage 2011, 194 Seiten
ISBN 978-3-8322-9738-l

ABISEA Band 55
Hirschmann, D.
Highly Dynamic Piezoelectric Positioning
1. Auflage 2011, 156 Seiten
ISBN 978-3-8322-9746-6

Aachener Beiträge des ISEA

ABISEA Band 56
Rigbers, K.
Highly Efficient Inverter Architectures for Three-Phase Grid Connection of Photovoltaic Generators
1. Auflage 2011, 254 Seiten
ISBN 978-3-8322-9816-9

ABISEA Band 57
Kasper, K.
Analysis and Control of the Acoustic Behavior of Switched Reluctance Drives
1. Auflage 2011, 214 Seiten
ISBN 978-3-8322-9869-2

ABISEA Band 58
Köllensperger, P.
The Internally Commutated Thyristor - Concept, Design and Application
1. Auflage 201 J, 212 Seiten
ISBN 978-3-8322-9909-5

ABISEA Band 59
Schoenen, T.
Einsatz eines DC/DC-Wandlers zur Spannungsanpassung zwischen Antrieb und Energiespeicher in Elektro-und Hybridfahrzeugen
1. Auflage 2011, 138 Seiten
ISBN 978-3-8440-0622-3

ABISEA Band 60
Hennen, M.
Switched Reluctance Direct Drive with Integrated Distributed Inverter
1. Auflage 2012, 150 Seiten
ISBN 978-3-8440-0731-2

ABISEA Band 61
van Treek, D.
Position Sensorless Torque Control of Switched Reluctance Machines
1. Auflage 2012, 144 Seiten
ISBN 978-3-8440-IO 14-5

ABISEA Band 62
Bragard, M.
Tue Integrated Emitter Turn-Off Thyristor. An Innovative MOS-Gated High-Power Device
1. Auflage 2012, 172 Seiten
ISBN 978-3-8440-1152-4

ABISEA Band 63
Gerschler, J. B.
Ortsaufgelöste Modellbildung von Lithium-Ionen-Systemen unter spezieller Berücksichtigung der Batteriealterung
1. Auflage 2012, 350 Seiten
ISBN 978-3-8440-1307-8

ABISEA Band 64
Neuhaus, C.
Schaltstrategien für Geschaltete Reluktanzantriebe mit kleinem Zwischenkreis
1. Auflage 2012, 144 Seiten
ISBN 978-3-8440-1487-7

ABISEA Band 65
Butschen, T.
Dual-ICT- A Clever Way to Unite Conduction and Switching Optimized Properties in a Single Wafer
1. Auflage 2012, 178 Seiten
ISBN 978-3-8440-1771-7

ABISEA Band 66
Plum, T.
Design and Realization of High-Power MOS Turn-Off Thyristors
1. Auflage 2013, 130 Seiten
ISBN 978-3-8440-1884-4

ABISEA Band 67
Kiel, M.
Impedanzspektroskopie an Batterien unter besonderer Berücksichtigung von Batteriesensoren für den Feldeinsatz
1. Auflage 2013, 232 Seiten
ISBN 978-3-8440-1973-5

ABISEA Band 68
Brauer, H.
Schnelldrehender Geschalteter Reluktanzantrieb mit extremem Längendurchmesserverhältnis
1. Auflage 2013, 202 Seiten
ISBN 978-3-8440-2345-9

ABISEA Band 69
Thomas, S.
A Medium-Voltage Multi-Level DC/DC Converter with High Voltage Transformation Ratio
1. Auflage 2014, 236 Seiten
ISBN 978-3-8440-2605-4

ABISEA Band 70
Richter, S.
Digitale Regelung von PWM Wechselrichtern mit niedrigen Trägerfrequenzen
1. Auflage 2014, 134 Seiten
ISBN 978-3-8440-2641-2

ABISEA Band 71
Bösing, M.
Acoustic Modeling of Electrical Drives - Noise and Vibration Synthesis based on Force Response Superposition
1. Auflage 2014, 208 Seiten
ISBN 978-3-8440-2752-5

ABISEA Band 72
Waag, W.
Adaptive algorithms for monitoring of lithium-ion batteries in electric vehicles
1. Auflage 2014, 242 Seiten
ISBN 978-3-8440-2976-5

ABISEA Band 73
Sanders, T.
Spatially Resolved Electrical In-Situ Measurement Techniques for Fuel Cells
1. Auflage 2014, 138 Seiten
ISBN 978-3-8440-3121-8

Aachener Beiträge des ISEA

ABISEA Band 74
Baumhöfer, T.
Statistische Betrachtung experimenteller Alterungsuntersuchungen an Lithium-Ionen Batterien
1. Auflage 2015, 174 Seiten
ISBN 978-3-8440-3423-3

ABISEA Band 75
Andre, D.
Systematic Characterization of Ageing Factors for High-Energy Lithium-Ion Cells and Approaches for Lifetime Modelling Regarding an Optimized Operating Strategy in Automotive Applications
1. Auflage 2015, 210 Seiten
ISBN 978-3-8440-3587-2

ABISEA Band 76
Merei, G.
Optimization of off-grid hybrid PV-wind-diesel power supplies with multi-technology battery systems taking into account battery aging
1. Auflage 2015, 194 Seiten
ISBN 978-3-8440-4148-4

ABISEA Band 77
Schulte, D.
Modellierung und experimentelle Validierung der Alterung von Blei-Säure Batterien durch inhomogene Stromverteilung und Säureschichtung
1. Auflage 2016, 168 Seiten
ISBN 978-3-8440-4216-0

ABISEA Band 78
Schenk, M.
Simulative Untersuchung der Wicklungsverluste in Geschalteten Reluktanzmaschinen
1. Auflage 2016, 142 Seiten
ISBN 978-3-8440-4282-5

ABISEA Band 79
Wang, Y.
Development of Dynamic Models with Spatial Resolution for Electrochemical Energy Converters as Basis for Control and Management Strategies
1. Auflage 2016, 198 Seiten
ISBN 978-3-8440-4303-7

ABISEA Band 80
Ecker, M.
Lithium Plating in Lithium-Ion Batteries: An Experimental and Simulation Approach
1. Auflage 2016, 170 Seiten
ISBN 978-3-8440-4525-3

ABISEA Band 81
Zhou, W.
Modellbasierte Auslegungsmethode von Temperierungssystemen für Hochvolt-Batterien in Personenkraftfahrzeugen
1. Auflage 2016, 192 Seiten
ISBN 978-3-8440-4589-5

ABISEA Band 82
Lunz, B.
Deutschlands Stromversorgung im Jahr 2050
Ein szenariobasiertes Verfahren zur vergleichenden Bewertung von Systemvarianten und Flexibilitätsoptionen
1. Auflage 2016, 196 Seiten
ISBN 978-3-8440-4627-4

ABISEA Band 83
Hofmann, A.
Direct Instantaneous Force Control Key to Low-Noise Switched Reluctance Traction Drives
1. Auflage 2016, 244 Seiten
ISBN 978-3-8440-4715-8

ABISEA Band 84
Budde-Meiwes, H.
Dynamic Charge Acceptance of Lead-Acid Batteries for Micro-Hybrid Automotive Applications
1. Auflage 2016, 168 Seiten
ISBN 978-3-8440-4733-2

ABISEA Band 85
Engel, S. P.
Thyristor-Based High-Power On-Load Tap Changers Control under Harsh Load Conditions
1. Auflage 2016, 170 Seiten
ISBN 978-3-8440-4986-2

ABISEA Band 86
VanHoek, H.
Design and Operation Considerations of Three-Phase Dual Active Bridge Converters for Low-Power Applications with Wide Voltage Ranges
1. Auflage 2017, 242 Seiten
ISBN 978-3-8440-5011-0

ABISEA Band 87
Diekhans, T.
Wireless Charging of Electric Vehicles - a Pareto-Based Comparison of Power Electronic Topologies
1. Auflage 2017, 156 Seiten
ISBN 978-3-8440-5048-6

ABISEA Band 88
Lehner, S.
Reliability Assessment of Lithium-Ion Battery Systems with Special Emphasis on Cell Performance Distribution
1. Auflage 2017, 202 Seiten
ISBN 978-3-8440-5090-5

Aachener Beiträge des ISEA

ABISEA Band 89
Käbitz, S.
Untersuchung der Alterung von Lithium-Ionen-Batterien mittels Elektroanalytik und elektrochemischer Impedanzspektroskopie
1. Auflage 2016, 258 Seiten
DOI: 10.18154/RWTH-2016-12094

ABISEA Band 90
Witzenhausen, H.
Elektrische Batteriespeichermodelle: Modellbildung, Parameteridentifikation und Modellreduktion
1. Auflage 2017, 286 Seiten
DOI: 10.18154/RWTH-2017-03437

ABISEA Band 91
Münnix, J.
Einfluss von Stromstärke und Zyklentiefe auf graphitische Anoden
1. Auflage 2017, 178 Seiten
DOI: 10.18154/RWTH-2017-01915

ABISEA Band 92
Pilatowicz, G.
Failure Detection and Battery Management Systems of Lead-Acid Batteries for Micro-Hybrid Vehicles
1. Auflage 2017, 212 Seiten
DOI: 10.18154/RWTH-2017-09156

ABISEA Band 93
Drillkens, J.
Aging in Electrochemical Double Layer Capacitors: An Experimental and Modeling Approach
1. Aufl. 2017, 179 Seiten
DOI: 10.18154/RWTH-2018-223434

ABISEA Band 94
Magnor, D.
Globale Optimierung netzgekoppelter PV-Batteriesysteme unter besonderer Berücksichtigung der Batteriealterung
1. Auflage 2017, 210 Seiten
DOI: 10.18154/RWTH-2017-06592

ABISEA Band 95
Iliksu, M.
Elucidation and Comparison of the Effects of Lithium Salts on Discharge Chemistry of Nonaqueous Li-O_2 Batteries
1. Aufl. 2018, 160 Seiten
DOI: 10.18154/RWTH-2018-223782

ABISEA Band 96
Schmalstieg, J.
Physikalisch-elektrochemische Simulation von Lithium-Ionen-Batterien: Implementierung, Parametrierung und Anwendung
1. Aufl. 2017, 176 Seiten
DOI: 10.18154/RWTH-2017-04693

ABISEA Band 97
Soltau, N.
High-Power Medium-Voltage DC-DC Converters: Design, Control and Demonstration
1. Aufl. 2017, 176 Seiten
DOI: 10.18154/RWTH-2017-04084

ABISEA Band 98
Stieneker, M.
Analysis of Medium-Voltage Direct-Current Collector Grids in Offshore Wind Parks
1. Aufl. 2017, 144 Seiten
DOI: 10.18154/RWTH-2017-04667

ABISEA Band 99
Masomtob, M.
A New Conceptual Design of Battery Cell with an Internal Cooling Channel
1. Aufl. 2017, 167 Seiten
DOI: 10.18154/RWTH-2018-223281

ABISEA Band 100
Marongiu, A.
Performance and Aging Diagnostic on Lithium Iron Phosphate Batteries for Electric Vehicles and Vehicle-to-Grid Strategies
1. Aufl. 2017, 222 Seiten
DOI: 10.18154/RWTH-2017-09944

ABISEA Band 101
Gitis, A.
Flaw detection in the coating process of lithium-ion battery electrodes with acoustic guided waves
1. Aufl. 2017, 132 Seiten
DOI: 10.18154/RWTH-2017-099519

ABISEA Band 102
Neeb, C.
Packaging Technologies for Power Electronics in Automotive Applications
1. Aufl. 2017, 132 Seiten
DOI: 10.18154/RWTH-2018-224569

ABISEA Band 103
Adler, F. S.
A Digital Hardware Platform for Distributed Real-Time Simulation of Power Electronic Systems
1. Aufl. 2017, 156 Seiten
DOI: 10.18154/RWTH-2017-10761

Aachener Beiträge des ISEA

ABISEA Band 104
Becker, J.
Flexible Dimensionierung und Optimierung hybrider Lithium-Ionenbatteriespeichersysteme mit verschiedenen Auslegungszielen
1. Aufl., 2017, 157 Seiten
DOI: 10.18154/RWTH-2017-09278

ABISEA Band 105
Warnecke, A.
Degradation Mechanisms in NMC Based Lithium-Ion Batteries
1. Aufl. 2017, 158 Seiten
DOI: 10.18154/RWTH-2017-09646

ABISEA Band 106
Taraborrelli, S.
Bidirectional Dual Active Bridge Converter using a Tap Changer for Extended Voltage Ranges
1. Aufl. 2017

ABISEA Band 107
Sarriegi, G.
SiC and GaN Semiconductors – The Future Enablers of Compact and Efficient Converters for Electromobility
1. Aufl. 2017

ABISEA Band 108
Senol, M.
Drivetrain Integrated Dc-Dc Converters utilizing Zero Sequence Currents
1. Aufl. 2017

ABISEA Band 109
Koijma, T.
Efficiency Optimized Control of Switched Reluctance Machines
1. Aufl. 2017

ABISEA Band 110
Lewerenz, M.
Dissection and Quantitative Description of Aging of Lithium-Ion Batteries Using Non-Destructive Methods Validated by Post-Mortem-Analyses
1. Aufl. 2018

ABISEA Band 111
Büngeler, J.
Optimierung der Verfügbarkeit und der Lebensdauer von Traktionsbatterien für den Einsatz in Flurförderfahrzeugen
1. Aufl. 2018

ABISEA Band 112
Wegmann, R.
Betriebsstrategien und Potentialbewertung hybrider Batteriespeichersysteme in Elektrofahrzeugen
1. Auflage 2018

ABISEA Band 113
Nordmann, H.
Batteriemanagementsysteme unter besonderer Berücksichtigung von Fehlererkennung und Peripherieanalyse
1. Aufl. 2018

ABISEA Band 114
Engelmann, G.
Reducing Device Stress and Switching Losses Using Active Gate Drivers and Improved Switching Cell Design
1. Aufl. 2018

ABISEA Band 115
Klein-Heßling, A.
Active DC-Power Filters for Switched Reluctance Drives during Single-Pulse Operation
1. Aufl. 2018

ABISEA Band 116
Burkhart, Bernhard
Switched Reluctance Generator for Range Extender Applications - Design, Control and Evaluation
1. Aufl. 2018

ABISEA Band 117
Biskoping, Matthias
Discrete Modeling and Control of a versatile Power Electronic Test Bench with Special Focus on Central Photovoltaic Inverter Testing
1. Aufl. 2018

Model inaccuracies, parameter variations and parasitic influences of the voltage source inverter can cause significant torque error and detuning in field-oriented induction machine drives.

This thesis describes an analytical minimization approach for the sensitivity of flux-linkage observers to parameter variations, measurement feedback deviation and higher-order harmonics. An extended model of the induction machine, which takes into account magnetic saturation, iron losses, rotor deep-bar effect, and temperature drift of the rotor and stator resistances is introduced. Based on an analytical sensitivity analysis, the flux-linkage observer is designed with respect to minimal sensitivity to uncertain parameters.

The low-speed accuracy is improved by an instantaneous phase voltage sensing circuit integrated with the bottom gate driver of each inverter leg. The method is based on oversampling and digital integration. A high-bandwidth low-pass filter is introduced and optimized to minimize the instantaneous measuring error. A novel sensor-offset compensation method is developed, which allows independent offset calibration for all phase voltage and current sensors during operation. The method is fully decoupled from the control algorithm.

Another very important aspect is the dynamics of efficiency-enhanced IM drives. A model-predictive approach for optimal dynamic current sharing of the flux-producing and torque-producing current is proposed. The results are transferred into a lookup table for implementation on a low-cost microcontroller.

ISSN 1437-675X